Universiteit Gent
Faculteit Wetenschappen
Vakgroep Subatomaire en Stralingsfysica
Onderzoeksgroep Elektromagnetische Reacties

Study of the helicity dependence of double pion photoproduction on the proton

Heidi Holvoet

Promotor : Prof. dr. R. Van de Vyver

Proefschrift ingediend tot het behalen van de graad van
Doctor in de Wetenschappen: Natuurkunde
Academiejaar 2000-2001

Examencommissie:

PROF. DR. H.-J. ARENDS
Universität Mainz, Duitsland

DR. N. D'HOSE,
CEA-Saclay, Frankrijk

PROF. DR. D. DRECHSEL
Universität Mainz, Duitsland

PROF. DR. K. HEYDE
Faculteit Wetenschappen, RUG

PROF. DR. P. MATTHYS, voorzitter
Faculteit Wetenschappen, RUG

PROF. DR. D. RYCKBOSCH
Faculteit Wetenschappen, RUG

DR. IR. M. VANDERHAEGHEN
Universität Mainz, Duitsland

PROF. DR. R. VAN DE VYVER, promotor
Faculteit Wetenschappen, RUG

DR. L. VAN HOOREBEKE
Faculteit Wetenschappen, RUG

PROF. DR. M. WAROQUIER
Faculteit Wetenschappen, RUG

Abstract

In this PhD thesis the helicity dependence of double pion photoproduction on the proton is studied. The subject is approached experimentally as well as theoretically. The main physical motivations are the study of the nucleon resonances and the mechanisms responsible for the observed double pion photoproduction cross sections. The emphasis is on the $\gamma p \rightarrow p\pi^+\pi^-$ and the $\gamma p \rightarrow n\pi^+\pi^0$ processes. The obtained results are the first of their kind.

The experimental part fits in with the Gerasimov-Drell-Hearn (GDH) experiment carried out at the accelerator facility MAMI in Mainz, Germany. This experiment allows to access doubly polarised observables for the pion photoproduction channels open at these energies. The data analysis for the $p\pi^+\pi^-$ and $n\pi^+\pi^0$ photoproduction reactions on the proton is performed in two steps: the development of the analysis methods for unpolarised calibration data and the application of these methods to the doubly polarised data from the GDH experiment. The analysis methods for both reaction channels are well optimised in terms of statistical and systematical errors and the results for the unpolarised total cross sections are successfully verified with existing data. The total helicity cross section difference $\sigma_{3/2} - \sigma_{1/2}$ and the separate helicity cross sections $\sigma_{1/2}$ and $\sigma_{3/2}$ are obtained for both reactions. For $p\pi^+\pi^-$, the $\sigma_{3/2}$ cross section is positive and exhibits a broad peak around 600–650 MeV, whereas $\sigma_{1/2}$ is smaller and behaves more smoothly. The $\sigma_{3/2}$ for the $n\pi^+\pi^0$ has a strong resonant peak at about 750 MeV while $\sigma_{1/2}$ is again smoother. Within the measured energy range, from threshold up to 800 MeV, the contributions of the $p\pi^+\pi^-$ and $n\pi^+\pi^0$ reactions to the GDH sum rule are $-(25.4 \pm 1 \pm 1.5)$ μb (statistical and systematical error) and $-(11.3 \pm 0.7 \pm 0.7)$ μb, respectively. Their contributions to the forward spin polarisability are $-(0.070 \pm 0.004 \pm 0.004)\, 10^{-4}$ fm^4 and $-(0.025 \pm 0.003 \pm 0.002)\, 10^{-4}$ fm^4.

In the theoretical part, a Regge Plus Resonances (RPR) model for double pion photoproduction is presented. Regge trajectory exchange provides well behaved cross sections at higher energies, i.e. the cross sections decrease with a power of the energy. In the resonance region, resonant mechanisms are added to overcome the fact that the Regge description yields only an average over all resonances (duality). The description is unitary and gauge invariant. By comparing the model predictions with the data it was found that the $p\pi^+\pi^-$ process is dominated by the non-resonant $\pi\Delta$ production via π exchange. Extra contributions stem from the non-resonant $\pi\pi$N production via π exchange, the D_{13}-resonant $\pi\Delta$ and ρN production and the non-resonant ρN production via ρ exchange. These mechanisms qualitatively describe the observed features in the measured cross sections. For the $n\pi^+\pi^0$ reaction, the non-resonant $\pi\Delta$ production via π exchange is not as predominant and the other mechanisms are relatively more important, in particular the ones involving an intermediate ρ. The contribution of double pion production to the proton GDH sum rule and its forward spin polarisability is predicted to be about 25% and 12% of the total value, respectively. These predictions represent a calculation including non-resonant $\pi\Delta$ production and D_{13}-resonant $\pi\Delta$ and ρN production.

Acknowledgement

Met veel plezier bedank ik mijn promotor Robert Van de Vyver als eerste, om mij in de groep op te nemen en mij op een goede manier te introduceren in het GDH-samenwerkingsverband. Robert, ik ben je dankbaar voor je hulp en vertrouwen en omdat je het met me eens bent dat er veel belangrijker zaken zijn dan fysica.

Bob, we zaten lange tijd in hetzelfde schuitje, en dan nog het schuitje richting Mainz en Bonn. Ik dank je voor je hulp tijdens onze analyse en je gezelschap bij die vele bezoekjes aan onze vrienden.

Tijdens onze vele discussies over DAPHNE, simulaties, fysica in het algemeen en computers heb ik veel van je geleerd, Luc, dank je wel daarvoor. Je steun was een grote hulp tijdens mijn doctoraat.

Ook elk van de overige groepsleden wil ik graag bedanken: Dirk, Michael, Natalie en Brecht —en Gert, Katty en Domi als ex-groepsleden— elk op je eigen manier heb je me het werken hier aangenaam gemaakt.

Dear Paolo, for the patience and expertise with which you introduced me to DAPHNE and guided me through the analysis, I thank you. You have always kept my interest in the data alive and each time I ran out of new ideas, you had one ready for me. I also want to thank the other members of the analysis group for the discussions that we had about the analysis.

Marc, ik wil je bedanken voor de aangename samenwerking die we in de loop van mijn doctoraat gehad hebben. Ik heb veel van je geleerd. Het staat buiten kijf dat je een grote invloed hebt gehad op de waarde van het theoretische gedeelte van deze thesis.

Op deze plaats wil ik ook graag de overige leden van de examencommissie, Prof. dr. K. Heyde, Prof. dr. P. Matthys en Prof. dr. M. Waroquier, bedanken voor de interesse die ze stellen in mijn doctoraatswerk. I also want to express my gratitude to the foreign members of the jury, Dr. Nicole d'Hose, Prof. dr. H.-J. Arends and Prof. dr. D. Drechsel for accepting to join my jury and for the interest in my work they have shown during my PhD.

Ik eindig dit dankwoordje met de mensen die eigenlijk op de eerste plaats komen.

Mijn fantastische ouders, dank je wel voor de kansen die je me gegeven hebt, van bij het begin. Voor de onvoorwaardelijke steun en alles wat voor jullie zo vanzelfsprekend is maar dat, bijvoorbeeld voor deze thesis, een wereld van verschil maakt, dank je wel.

Alex, je grote interesse en je andere kijk op de dingen waarmee ik bezig ben, verplichten me dikwijls om beter na te denken. Je grote steun en bezorgdheid zijn ook heel belangrijk voor me, dank je wel. Ook voor de vele welkome telefoontjes van jou, Veerle en de kindjes.

Tom, je bent er altijd —meestal slechts een 'talk tom' verwijderd— om me te helpen, verse courage te geven en om samen een beetje plezier te maken tussen het werken door en daarvoor wil ik je bedanken. Jou en Greetje ben ik ook dankbaar voor de vele aanmoedigingen tijdens mijn doctoraat.

Ik wil ook mijn schoonfamilie bedanken, omdat ik me ook door hen gesteund voel in wat ik doe.
Geert, je hebt me constant aangemoedigd, geholpen en je hebt deze hele thesis gelezen. Dank je wel ook voor je krachTEXe hulp aan de layout. Maar bovenal bedank ik je omdat ik bij je kan thuiskomen in een wereld die groot genoeg is zodat fysica er interessant is maar slechts een klein stukje ervan in beslag neemt.

Contents

1

Introduction and motivation

About half a century ago, physicists discovered that nucleons are non-point-like particles that can be classified within the large family of hadrons. Today, the nucleon's internal structure, and more specifically its spin structure, is still a very live topic in intermediate and high energy physics. The subject of this PhD work is situated in this field. The spin structure of the nucleon is studied through the helicity dependence of real photoabsorption processes, in particular double pion photoproduction.

Both an experimental and a theoretical approach are presented. In the experimental part, results from the Gerasimov-Drell-Hearn experiment carried out by the GDH collaboration at the accelerator facility MAMI in Mainz, are investigated. The results are the first of their kind as a similar measurement had not been done before. On the theoretical side, a Regge model to describe double pion photoproduction is developed. It provides a means to interpret the experimental data and allows to predict the observables in the unmeasured regions.

In this introduction, the physical background and motivation for the study of nucleon resonances via the helicity dependent double pion photo-production and its contribution to the GDH sum rule is discussed. A short situation of the subject within the nucleon spin structure studies of the past fifty years is given in Section 1.1. In Section 1.2 the GDH sum rule itself is treated in some detail while the GDH experiment is presented in Section 1.3. The measured data available so far for the sum rule are also shown. Nucleon resonances are considered in Section 1.4 and the status and uncertainties concerning their properties is given. An overview of the present status of the single and double pion photoproduction data measured in the GDH experiment is also presented. The Regge model for double pion production proposed in this PhD work is also introduced. Finally an overview of the thesis is given in Section 1.5.

1.1 The quest for the nucleon spin structure

In the search for the internal properties of the nucleon, many experiments using deep inelastic lepton scattering (DIS) off the nucleon were performed in the 1950's and 1960's. It soon became clear that the proton and the neutron are not unique particles but that they can be classified as members of a large family of particles named hadrons. Within the constituent quark model all hadrons are categorised according to their internal configuration of quarks. Quarks are the charged, pointlike spin-1/2 particles that, together with gluons, constitute a hadron. The family of hadrons is subdivided in two groups: the baryons —like e.g. the proton, the neutron, the Λ— that consist of three valence quarks and the mesons —like e.g. the pion, the ρ, the kaon— that are formed by a quark-antiquark pair. In the baryon, the valence quarks are those quarks that determine its static structure and its quantum numbers such as charge, mass, magnetic moment, spin, ... Within the baryon group, the nucleon can be seen as the ground state of a wide excitation spectrum of nucleon resonances. Examples of these excited nucleon states are the well-known Δ resonance, the Roper resonance P_{11}, S_{11}, D_{13}, F_{15}, ... The study of the properties of the nucleon resonances is one of the primary motivations for the research in this PhD work, as outlined further on.

The question of how the nucleon spin is built up from its constituents became very intriguing when it was found at CERN (EMC) in 1987 that the valence quarks contribute only about 30% to the total nucleon spin [47]. Several subsequent experiments at CERN, SLAC (E-142, 143, 154) and DESY (HERMES) confirmed this result and went on to search for an adequate answer [113, 68, 45]. The spin contribution from the sea quarks —virtual quark-antiquark pairs— and the gluon clouds in the nucleon are good candidates to explain the 'missing spin'. However, dedicated HERMES experiments reveal that the contribution of the sea quarks to the nucleon spin is negligible [67]. Some evidence is arising for a gluon contribution to the nucleon spin, which could solve this so-called spin crisis [69].

In the mentioned experiments the nucleon spin structure is studied via polarised lepton scattering off the nucleon. The dynamics of the virtual photoabsorption process is generally described by the spin structure functions, primarily the $g_1(x)$ function —x is the Bjorken scaling variable. From the theoretical side, several sum rules based on general assumptions have been deduced for $g_1(x)$ in the 60's and 70's. Two famous examples are the Bjorken sum rule for the proton-neutron difference $g_1^{\mathrm{p}}(x) - g_1^{\mathrm{n}}(x)$ and the Ellis-Jaffe sum rule for the proton and the neutron separately [16, 46]. The Bjorken sum rule has been verified within 10%. For the Ellis-Jaffe sum rule however, the measured data show significant disagreement with the predicted values. This again confirmed the gaps in the understanding of the nucleon spin. Solving the puzzle remains the challenge for the above listed experiments.

At the side of real photon absorption on the nucleon in the study of the nucleon spin structure, one primarily has the Gerasimov-Drell-Hearn sum rule

Figure 1.1: Illustration of the relative spin orientation of the incoming photon and the target nucleon in the GDH sum rule.

[43, 56, 57], or GDH sum rule for short. It relates the helicity dependence of the total photoabsorption by the nucleon with its static properties: its mass, its anomalous magnetic moment and its spin. The beauty of this sum rule is that it links two manifestations of the nucleon's internal structure: its excitation spectrum —a dynamical property— on the one hand and its anomalous magnetic moment —a statical property— on the other hand. The fundamental, model independent derivation of the sum rule relies on basic physical principles plus one not-verified no-subtraction hypothesis. An experimental verification of the validity of the GDH sum rule is a prerequisite to confirm the assumptions made. Even though the sum rule was derived in the late 1960's, the technical requirements for the double polarisation experiment have only recently been fulfilled. The experimental verification is the aim of the GDH experiment, the experimental framework in which this PhD work took place.

1.2 The Gerasimov-Drell-Hearn sum rule

The GDH sum rule is a very general relation that is applicable for each particle with internal structure and a non-zero spin. In its most general form it reads:

$$\int_{\nu_0}^{\infty} \frac{\sigma_{\uparrow\downarrow} - \sigma_{\uparrow\uparrow}}{\nu} \mathrm{d}\nu = -\frac{4\pi^2\alpha}{m^2}\kappa^2 S.$$

The cross sections $\sigma_{\uparrow\downarrow}$ and $\sigma_{\uparrow\uparrow}$ are the total helicity cross sections for the absorption of circularly polarised photons by longitudinally polarised target particles. The $\sigma_{\uparrow\downarrow}$ corresponds to an anti-parallel orientation of the photon and target spins whereas $\sigma_{\uparrow\uparrow}$ corresponds to the parallel relative spin orientation. The cross section difference is weighted by the photon energy and integrated over all photon energies ν, starting from the threshold energy for pion photoproduction ν_0. The mass of the target particle is denoted by m, its spin by S, κ is its anomalous magnetic moment and α is the fine structure constant. It is interesting to observe that the sum rule yields a direct link between the dynamical excitation spectrum of the target particle and its anomalous magnetic moment. This illustrates how the latter directly points towards internal structure of the target particle.

In the case of the proton and the neutron, the spin S equals $1/2$. The two spin configurations that can then be produced in combination with the photon spin are $1/2$ and $3/2$, as depicted in Figure 1.1. In the case of the nucleon, we

further write $\sigma_{1/2}$ and $\sigma_{3/2}$ for the helicity cross sections. The GDH sum rule for the nucleon reads:

$$\int_{\nu_0}^{\infty} \frac{\sigma_{1/2} - \sigma_{3/2}}{\nu} \mathrm{d}\nu = -\frac{2\pi^2\alpha}{m_{\mathrm{N}}^2}\kappa_{\mathrm{N}}^2.$$

The sum rule for the nucleon was first derived by Gerasimov [56, 57] in 1965, and soon thereafter by Drell and Hearn [43]. Its strength lies in the fact that its derivation is model independent and almost exclusively based on solid fundamental physical principles. Relying on Lorentz and gauge invariance, causality, crossing symmetry and unitarity, one can write the following dispersion relations for the scattering amplitudes f_1 and f_2 for forward Compton scattering off the nucleon:

$$\begin{aligned}
\mathrm{Re}f_1(\nu) &= \frac{1}{2\pi^2}\mathcal{P}\int_{\nu_0}^{\infty} \frac{\sigma_{\mathrm{tot}}(\nu')}{\nu'^2 - \nu^2}\nu'^2 \mathrm{d}\nu' \\
&= \frac{1}{2\pi^2}\mathcal{P}\int_{\nu_0}^{\infty} \sigma_{\mathrm{tot}}(\nu')\left(1 + \frac{\nu^2}{\nu'^2} + \cdots\right)\mathrm{d}\nu', \qquad (1.1) \\
\mathrm{Re}f_2(\nu) &= \frac{1}{4\pi^2}\mathcal{P}\int_{\nu_0}^{\infty} \frac{\sigma_{1/2}(\nu') - \sigma_{3/2}(\nu')}{\nu'^2 - \nu^2}\nu\nu' \mathrm{d}\nu' \\
&= \frac{1}{4\pi^2}\mathcal{P}\int_{\nu_0}^{\infty} (\sigma_{1/2}(\nu') - \sigma_{3/2}(\nu'))\left(\frac{\nu}{\nu'} + \frac{\nu^3}{\nu'^3} + \cdots\right)\mathrm{d}\nu'. \qquad (1.2)
\end{aligned}$$

The amplitude f_1 is the spin independent amplitude, f_2 is the polarised amplitude which can only be accessed with polarised incoming photons. The total unpolarised cross section is $\sigma_{\mathrm{tot}} = \frac{\sigma_{1/2}+\sigma_{3/2}}{2}$. For these dispersion relations to be valid, the integrand should converge for $\nu' \to \infty$.

The Low theorem provides the following series for f_1 and f_2 as a function of the photon energy ν [86]:

$$f_1(\nu) = -\frac{\alpha}{m_{\mathrm{N}}} + (\alpha_{\mathrm{N}} + \beta_{\mathrm{N}})\nu^2 + \cdots, \qquad (1.3)$$

$$f_2(\nu) = -\frac{\alpha\kappa_{\mathrm{N}}^2}{2m_{\mathrm{N}}^2}\nu + \gamma_0\nu^3 + \cdots \qquad (1.4)$$

Low's theorem is valid for small ν, where the internal nucleon structure is not probed. The expansion of the unpolarised amplitude f_1 contains the Thomson term $-\alpha/m_{\mathrm{N}}$ and the Rayleigh scattering term which is determined by the scalar electric and magnetic polarisabilities α_{N} and β_{N}. The first two terms in the f_2 series involve the anomalous magnetic moment and the forward spin polarisability of the nucleon γ_0. For the spin independent amplitude f_1, one can combine (1.1) with (1.3) to obtain the following sum rule:

$$f_1(\nu = 0) = -\frac{\alpha}{m_{\mathrm{N}}} = \frac{1}{2\pi^2}\int_{\nu_0}^{\infty} \sigma_{\mathrm{tot}}(\nu')\mathrm{d}\nu'. \qquad (1.5)$$

Since the total absorption cross section σ_{tot} is a positive quantity whereas $-\frac{\alpha}{m_{\text{N}}}$ is negative, this equation is invalid. This is related to the fact that the first term in the integrand of (1.1) does not converge since σ_{tot} becomes a slightly increasing function of photon energy at high energies. This behaviour is understood in Regge theory, where one finds the Pomeron trajectory to be dominating the total photoabsorption cross section [40]. The intercept of the Pomeron trajectory is 1.08 such that $\sigma_{\text{tot}}(\nu')$ increases as $\nu'^{0.08}$. As a consequence at least one subtraction is necessary in the f_1 dispersion relation and one writes:

$$\text{Re}f_1(\nu) = -\frac{\alpha}{m_{\text{N}}} + \frac{\nu^2}{2\pi^2}\mathcal{P}\int_{\nu_0}^{\infty}\frac{\sigma_{\text{tot}}(\nu')}{\nu'^2-\nu^2}\text{d}\nu'.$$

For the second term, in ν^2, one can obtain the Baldin sum rule for the sum of α_{N} and β_{N}:

$$\alpha_{\text{N}} + \beta_{\text{N}} = \frac{1}{2\pi^2}\int_{\nu_0}^{\infty}\frac{\sigma_{\text{tot}}(\nu')}{\nu'^2}\text{d}\nu'.$$

For the f_2 dispersion relation, there is no positive sign argument as in (1.5). The sign of the cross section difference $\sigma_{1/2}-\sigma_{3/2}$ is not a priori determined, nor is the convergence of the integrand. When deriving the GDH sum rule, this is the assumption that needs to be made: the integrand converges such that no subtraction is needed in the dispersion relation. This assumption is referred to as the *no-subtraction hypothesis* and is one important motivation for the experimental verification of the GDH sum rule. Physically, this means that the photoabsorption cross section becomes spin independent at high photon energies. Nevertheless, at lower, resonance, energies the cross section difference is an oscillating function which may change sign according to different contributing resonances. As long as the high energy behaviour is convergent, the assumption is not violated. Already, Regge theory provides a strong argument for the validity of the no-subtraction hypothesis. According to Bianchi [15], the cross section difference $\sigma_{1/2}-\sigma_{3/2}$ is governed at high energies by the a_1 meson trajectory with an intercept of -0.3, such that $\sigma_{1/2}(\nu')-\sigma_{3/2}(\nu') \sim \nu'^{-1.3}$.

Assuming the no-subtraction hypothesis, one can combine (1.2) with (1.4) to obtain:

$$\int_{\nu_0}^{\infty}\frac{\sigma_{1/2}-\sigma_{3/2}}{\nu}\text{d}\nu = -\frac{2\pi^2\alpha}{m_{\text{N}}^2}\kappa_{\text{N}}^2, \tag{1.6}$$

$$\int_{\nu_0}^{\infty}\frac{\sigma_{1/2}-\sigma_{3/2}}{\nu^3}\text{d}\nu = \gamma_0. \tag{1.7}$$

The first expression is the GDH sum rule for the nucleon. The second integral gives an expression for the nucleon forward spin polarisability. The forward spin polarisability can thus also be accessed in real photoabsorption, provided the integral converges.

	$I^{\mathrm{p}}_{\mathrm{GDH}}$ (μb)	$I^{\mathrm{n}}_{\mathrm{GDH}}$ (μb)	$I^{\mathrm{p-n}}_{\mathrm{GDH}}$ (μb)
GDH sum rule	-204	-232	$+28$
Karliner [78]	-261	-183	-78
Workman-Arndt [120]	-260	-157	-68
Burkert-Li [27]	-223	-	-
Sandorfi et al. [110]	-289	-160	-129
Drechsel-Krein [42]	-261	-180	-81
Bianchi-Thomas [15]	-207 ± 23	-226 ± 22	$+19 \pm 37$

Table 1.1: Values for the GDH integral for the proton, the neutron and the proton-neutron difference as given by the GDH sum rule and various model calculations.

The right hand side of (1.6) can be evaluated to give the GDH sum rule value and it is listed in Table 1.1 for the proton, the neutron and the difference between the proton and the neutron value. The GDH integral, the left hand side of the sum rule, is denoted $I^{\mathrm{p}}_{\mathrm{GDH}}$, $I^{\mathrm{n}}_{\mathrm{GDH}}$ and $I^{\mathrm{p-n}}_{\mathrm{GDH}}$ in the respective cases.

From the very beginning, the need for the experimental verification of the GDH sum rule was raised. Failure of such confirmation would compromise in the first place the no-subtraction hypothesis, or even more drastic, one of the assumed basic principles. While awaiting the technical improvements required to perform the GDH experiment, several model calculations have been proposed to estimate the value of the GDH sum rule. They are also given in Table 1.1. Each of the predictions listed in the table is obtained from the multipole analysis of single pion photoproduction data. For the double pion photoproduction, since less accurate data are available for the multipole analysis, all predictions rely on the rough evaluation by Karliner [78], except for [27]. The Bianchi-Thomas value includes an estimate of the contribution from multi-hadron processes obtained from an extrapolation of virtual photoabsorption results described with a Regge fit [15]. This contribution appears to be crucial to obtain a value that is compatible with the GDH sum rule value. This observation and the discrepancies with the sum rule value of most predictions shows the importance of controlling the contributions from different mechanisms. The different sign of the discrepancies for the proton and the neutron calls for an understanding of both the proton and the neutron sum rule.

The generalised GDH integral Following Anselmino [5] one defines the generalised GDH integral by extending it from the real photoabsorption point to virtual photoabsorption. It then becomes a function of the virtual momentum transfer Q^2:

$$I^*(Q^2) = \frac{2m_{\mathrm{N}}}{Q^2} \int_0^1 g_1(x)\mathrm{d}x.$$

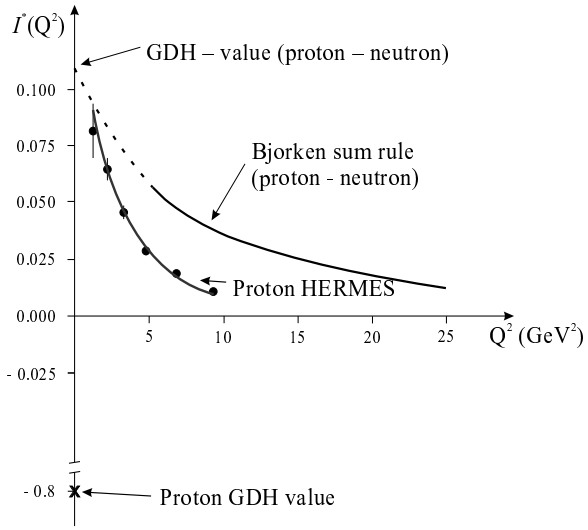

Figure 1.2: The generalised GDH integral $I^*(Q^2)$ as a function of Q^2. The values from the GDH sum rule and the Bjorken sum rule are shown. The data points for the proton are from HERMES [66].

At the real photon point where $Q^2 = 0$ one obtains:

$$I^*(Q^2 = 0) = \frac{m_{\mathrm{N}}^2}{8\pi^2\alpha} \int_{\nu_0}^{\infty} \frac{\sigma_{1/2} - \sigma_{3/2}}{\nu} \mathrm{d}\nu,$$

which contains the GDH integral. Hence one can write:

$$I^*(Q^2 = 0) = \frac{m_{\mathrm{N}}^2}{8\pi^2\alpha} I_{\mathrm{GDH}}^{\mathrm{N}} = -\frac{\kappa_{\mathrm{N}}^2}{4}.$$

From the range of DIS experiments mentioned above, data for the generalised GDH integral are available up to a Q^2 value of about 1 $(\mathrm{GeV/c})^2$. Experiments with very low Q^2 are hampered by the technical problems arising when studying very forwardly peaked processes. In Figure 1.2 recent HERMES [66] data for $I^*(Q^2)$ on the proton are shown. Also drawn is the Bjorken sum rule prediction for the proton-neutron difference and the GDH sum rule values for the proton and the proton-neutron difference. The latter seems to be in good agreement with the expectations from the Bjorken sum rule. The separate proton value, however, has a different sign and is in absolute value much larger than what one would expect from a simple extrapolation to $Q^2 = 0$ of the measured generalised integral for the proton. These observations are another strong motivation for the combined verification of the GDH sum rule on both the proton and the neutron.

1.3 The GDH experiment

1.3.1 The experimental programme of the GDH collaboration

In 1991 several physics institutes formed the GDH collaboration. Today the collaboration has grown with members from Germany, Belgium (i.e. our research group at the Universiteit Gent), Italy, France, Russia, Japan, Sweden and the United Kingdom. The primary goal was the experimental verification of the GDH sum rule. The technical knowledge and requirements to successfully carry out this experiment were becoming available at that time. As detailed in the previous sections, the motivation for this experiment was certainly strong enough.

What needs to be measured is the helicity cross section difference $\sigma_{1/2} - \sigma_{3/2}$ as a function of incoming photon energy. Weighting this difference with the inverse photon energy and integrating it from pion photoproduction threshold to infinity gives access to the GDH sum rule. A circularly polarised photon beam covering a large energy range is thus required. The target should contain polarised nucleons. Both the beam and the target polarisation degree need to be high for the experiment to be feasible and precise. Finally, also the detector system needs to satisfy high demands. A 4π acceptance and high efficiencies for both charged and uncharged hadrons are needed.

The decision was taken to perform a combined experiment at the microtron accelerator facility MAMI in Mainz [71, 70] and at the electron synchrotron ELSA in Bonn [49], both in Germany. At the former photon energies from pion production threshold (about 150 MeV) up to 800 MeV are available with a typical polarisation degree of 75%. At ELSA, photons between 500 MeV and 3 GeV can be obtained with similar polarisation features. Although 3 GeV is not infinity, the combination of these two energy ranges yields a very large energy range within which one expects to be able to observe whether or not the GDH integral converges.

The polarised nucleon target is a frozen-spin butanol target built by the Bonn, Bochum and Nagoya groups [20, 44]. By means of Dynamic Nuclear Polarisation, high polarisation degrees are reached, up to 80%. Its horizontal mechanical arrangement is one of its particular features, since it does not hinder particle emission in a large zone of the 4π acceptance.

Two different detector systems are used at the different experimental sites. In Mainz, the DAPHNE detector [10] is used as the central hadron detector. It has proven its quality in photoproduction cross section measurements on light nuclei in the Mainz energy region. DAPHNE has a large angular acceptance (94% of 4π), a large momentum acceptance and good detection efficiencies for charged and uncharged nucleon and pions. In order to complete the acceptance in the forward direction, extra detectors were designed. They are the silicon micro-strip detector MIDAS, the lead-scintillator sandwich detector FFW and the STAR detector. A threshold Čerenkov detector —built by our research group in Gent— is also added as a veto detector to suppress electromagnetic background. In Bonn, a dedicated central GDH detector was constructed [65],

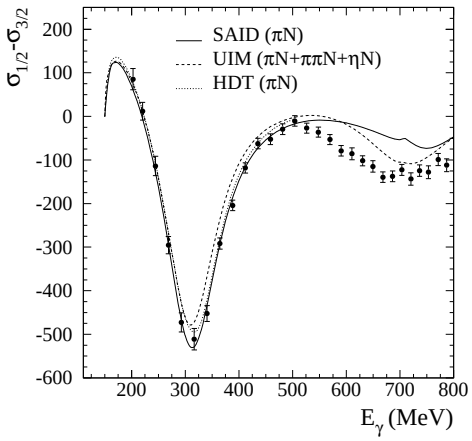

Figure 1.3: Total photoabsorption cross section difference for the proton measured in the GDH experiment, plotted as a function of incoming photon energy. The curves correspond with SAID, HDT and UIM calculations as discussed in the text.

which is also complemented in the forward direction with the FFW detector, the STAR detector and the Čerenkov detector. The Mainz detector setup is discussed in detail in Chapter 2.

After a testing phase in 1997, when a calibration measurement with unpolarised beam and target was performed, the first GDH measurements in Mainz were carried out in the summer of 1998. The measurement for the proton was completed and a short test run for the neutron was also taken. At the time of writing, the experiment in Bonn is running. Besides taking active part in the data taking at both locations, the Gent group is largely involved in the analysis of the data of the Mainz experiment.

Three other groups plan to verify experimentally the GDH sum rule. They are working at LEGS (Brookhaven, USA), GRAAL (Grenoble, France) and SPring8 (Osaka, Japan). At the moment their measurements have not started yet.

1.3.2 Measured contribution of the 200–800 MeV energy range to the GDH sum rule for the proton

The observable of immediate interest for the GDH sum rule measurement is the cross section difference $\sigma_{1/2}-\sigma_{3/2}$ for the total photoabsorption. This analysis is discussed in detail in two PhD theses, [82] and [104]. A paper with these results is submitted for publication [54]. Figure 1.3 shows the measured cross section difference for the proton as a function of photon energy. One observes a strong negative peak in the Δ resonance region, below double pion pho-

toproduction threshold, and another, smaller, peak in the second resonance region. Both point towards underlying mechanisms in which the 3/2 intermediate spin state dominates, enhancing the $\sigma_{3/2}$ cross section over $\sigma_{1/2}$. The small positive bump at pion threshold is explained by the strength of the E_{0^+} multipole stemming from the non-resonant s-wave charged pion production ($\gamma p \rightarrow n\pi^+$). The quantum numbers of this multipole correspond to an S_{11} resonance, resulting in a dominance of the $\sigma_{1/2}$ cross section. For more details about multipoles and related resonances, see Table 1.3 on p. 14. At higher energies, the M_{1^+} multipole dominates both the $\gamma p \rightarrow n\pi^+$ and $\gamma p \rightarrow p\pi^0$ single pion production processes. Its correspondence to the Δ resonance, which is a spin-3/2 state, explains the large negative signature in $\sigma_{1/2} - \sigma_{3/2}$. Three model predictions are also shown on the plot: the HDT [64] and SAID multipole analysis [9] and the Unitary Isobar Model (UIM) [41]. The latter contains a contribution from double pion photoproduction and η production, whereas the other two only contain single pion photoproduction. It is obvious from the discrepancy between the data and the SAID curve that double pion photoproduction also yields an important negative contribution. The UIM curve adds an important part by including these extra processes. However, there does not yet exist a complete understanding of the contributions from the double pion production. This supports again the dedicated study of these processes separately.

The experimental value for the GDH sum rule —from 200 to 800 MeV— is obtained by integrating the cross section difference, weighted by the photon energy. In order to examine how this integral behaves with rising photon energy, the GDH integral is plotted as a function of the upper integration limit in Figure 1.4(a). The curves are from the same model calculations as above. A fast drop due to the Δ resonance is observed. Above 550 MeV an extra decrease is found which is largely attributed to the double pion production. The full integration from 200 up to 800 MeV yields a measured value of $-(226 \pm 5 \pm 15)$ μb, the errors being statistical and systematical, respectively. The measured energy range already renders a large part of the total sum rule. However, to obtain an idea of the presently obtained agreement with the sum rule value of -204 μb we need to complete the measured value with the available model predictions for the unmeasured energy regions. Table 1.2 gives an overview of this procedure. The UIM model is used for energies below 200 MeV and between 800 and 1650 MeV. The Bianchi-Thomas contribution is added for the higher energy part. In this way a value of $-(210 \pm 5 \pm 15)$ μb is deduced. Within error bars this is in agreement with the GDH sum rule. This is already a good indication for the validity of the sum rule. However, it remains mandatory to continue the experiment towards higher energies to confirm this result. The models used for the extrapolation are not fully satisfactory yet such that a definitive conclusion can not be drawn. The measurement in Bonn is expected to give a more conclusive answer.

In the same measurement, the contribution of the 200–800 MeV energy range to the forward spin polarisability γ_0 is accessed. Weighting the cross

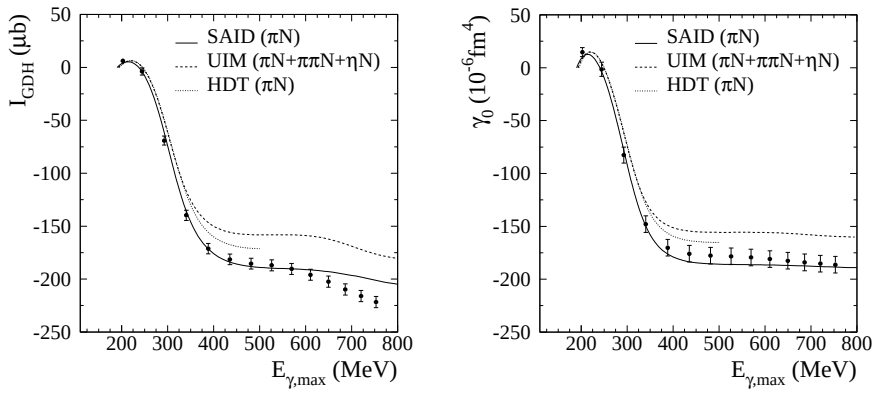

(a) (b)

Figure 1.4: (a) GDH integral for the proton as a function of its upper integration limit, (b) Forward spin polarisability for the proton as a function of its upper integration limit.

	E_γ (MeV)	$I^{\mathrm{p}}_{\mathrm{GDH}}$ (μb)	I_{γ_0} (10^{-6} fm^4)
GDH experiment	200–800	$-226 \pm 5 \pm 15$	$-187 \pm 8 \pm 13$
UIM [64]	140–200	$+30 \pm 3$	$+104 \pm 14$
UIM [64]	800–1650	-40 ± 19	-3 ± 1
Bianchi-Thomas [15]	> 1650	$+26 \pm 7$	≈ 0
SUM		$-210 \pm 5 \pm 25$	$-86 \pm 8 \pm 19$

Table 1.2: Extrapolation of the measured value for the GDH sum rule on the proton and the proton forward spin polarisability by means of the UIM and the Bianchi-Thomas predictions in the unmeasured energy regions.

section difference with the third power of the photon energy, and integrating from threshold up to the upper photon energy limit yields the desired result. The γ_0 integral is plotted as a function of the upper integration limit in Figure 1.4(b). The same model predictions as above are shown. Due to the weighting with the third power of the photon energy, this integral converges faster and the low energy part is the most important. The full measured integral is equal to $-(187 \pm 8 \pm 13)\ 10^{-6}$ fm^4. An extrapolation based on the predictions from the UIM model is also made (see Table 1.2) and this leads to a value of $-(86 \pm 8 \pm 13)\ 10^{-6}$ fm^4 for the proton forward spin polarisability. The fact that a very large contribution is expected below 200 MeV puts a serious limitation on the validity of this measurement of γ_0. Efforts are being made to extend the experimental lower integration limit below 200 MeV to cover at least part of this missing energy range. Various other model predictions exist, some of them in chiral perturbation theory and others using dispersion relations. A large range of different values, ranging from -150 to $+200\ 10^{-6}$ fm^4, is found using the different approaches. This illustrates that no conclusive result has been obtained so far. A precise (dedicated) measurement below 200 MeV would therefore not be superfluous.

1.4 Nucleon resonances

1.4.1 Introduction

In the research of the electromagnetic properties of the nucleon and its excited states, nucleon resonances have gained much interest in the past decade. Pion photo- and electro-production and pion-nucleon scattering are invaluable tools in the study of nucleon resonances. In these reactions the target nucleon can be excited to a resonant state which then decays into the final pion-nucleon state. Via this process the properties of the nucleon resonances, such as their mass, decay widths and decay amplitudes can be accessed. A lot of work has been done in this field. Many sets of experimental data are at hand and, in combination with serious theoretical efforts, this has led to a fair understanding of a range of nucleon resonances. Nevertheless, the precision with which the resonance properties are known, is not fully satisfactory. This is evident from the large ranges given by the Particle Data Group [105]. In particular this is so for resonances that occur in the second resonance region and above. Extra input which can e.g. come from doubly polarised pion photoproduction is therefore very welcome. These conclusions were the inspiration for the second goal of the GDH experiment in Mainz, i.e. the measurement of the doubly polarised asymmetry for the single and double pion photoproduction channels. Such data were not available yet and they can put new constraints on the existing theoretical models and partial-wave analyses for the nucleon multipoles and its resonant structure. Technically this is possible at the Mainz site of the GDH experiment since the DAPHNE detector is well capable of separating the different reaction channels. The main aim of this PhD work is

to improve the understanding of nucleon resonances by studying the helicity dependence of double pion photoproduction. This is done in a first step by analysing the GDH data for the double pion photoproduction. In a second step, a theoretical Regge model for these processes is developed. By means of this model, the data can then be interpreted. In the following sections the motivation is further detailed. In Section 1.4.2 it is shown where the possibilities lie to improve our knowledge of the nucleon resonances. An overview of the single and double pion photoproduction data measured in the GDH experiment is given in Section 1.4.3. Finally in Section 1.4.4 the model for double pion production is briefly introduced.

1.4.2 Room for improvement

All known baryon resonances and their properties are listed in the Review of Particle Physics (or Particle Data Book) [105]. Most of the characteristics of the resonances given have been obtained from partial-wave analyses or isobar-model analyses of electromagnetic γN and hadronic πN scattering data. Several calculations have also been made within the framework of quark models, see e.g. [2, 29, 39].

In partial-wave analysis, and also in the isobar-model analysis, the physical observables are written in terms of helicity amplitudes. The helicity amplitudes are in turn written as partial-wave expansions of multipoles. By parametrising the amplitudes one can obtain the strengths of the various multipoles that contribute to the studied process. With each multipole, specific nucleon resonances are related such that a knowledge of the multipoles allows to pin down the resonance contributions and their characteristics. In single pion photoproduction $\gamma\mathrm{N} \rightarrow \pi\mathrm{N}$ the multipoles are defined as follows. As the total angular momentum J is conserved, one has:

$$\left| L \pm \frac{1}{2} \right| = J = \left| l \pm \frac{1}{2} \right|,$$

where L is the vector sum of the photon spin and the relative angular momentum of the incoming photon and the target nucleon. The relative angular momentum of the outgoing particles is denoted by l. The parity of the final state is $(-1)^{l+1}$ since the intrinsic parity is positive for the proton and negative for the pion. Parity conservation implies that:

$$(-1)^{L} = (-1)^{l+1},$$

for electric transitions, and

$$(-1)^{L+1} = (-1)^{l+1},$$

for magnetic transitions. Table 1.3 lists the different multipoles for $l = 0$, $l = 1$ and $l = 2$. Electric multipoles are denoted by E, magnetic ones by M. One

l	J	L	Photon multipole	Pion multipole	Resonance
0	1/2	1	E1	E_{0+}	S_{11} (1535)
1	1/2	1	M1	M_{1-}	P_{11} (1440)
1	3/2	1	M1	M_{1+}	P_{33} (1232)
1	3/2	2	E2	E_{1+}	P_{33} (1232)
2	3/2	1	E1	E_{2-}	D_{13} (1520)
2	3/2	2	M2	M_{2-}	D_{13} (1520)

Table 1.3: Photon and pion multipoles in $\gamma N \rightarrow \pi N$ with corresponding nucleon resonances.

defines the photon multipoles as EL and ML and the pion multipoles as E_{lx} and M_{lx}, where x is $+$ in the case of $J = l + \frac{1}{2}$ and $-$ for $J = l - \frac{1}{2}$. Also for the nucleon resonances the classical notation is used: $L_{2I\ 2J}$ with L = S, P, D, F, ... for $l = 0$, 1, 2, 3, ... and I and J are the isospin and the angular momentum of the resonance, respectively. For $\pi N \rightarrow \pi N$ a similar procedure is used.

Via fits to existing experimental data and isobar-model calculations the different relevant multipoles can be obtained. From these the wanted observables and the resonance properties are deduced. Two examples of partial-wave analyses are SAID [9] and HDT [64], with which we compared the GDH results above. Also the Unitary Isobar Model (UIM) [41] was used for comparison with the experimental results. These nicely illustrate the status of the knowledge of the multipoles occurring in the energy range below 800 MeV.

The resonances that occur with a reasonable strength in the 200–800 MeV range are the Δ resonance ($P_{33}(1232)$), P_{11}, D_{13} and S_{11} (see also Table 1.3). Their peak position, width and relative strength is illustrated in Figure 1.5. The Δ resonance is the only important one in the first single pion resonance region, or Δ region. In the second resonance region the D_{13} is the dominating one, with overlapping though smaller, contributions from P_{11} and S_{11}. In the Δ region one finds a very nice description of the GDH data by the three predictions (see Figure 1.3 on p. 9). This demonstrates that the properties of the Δ resonance are very well known. At higher energies important discrepancies are observed, which point at a less precise knowledge of the higher lying resonances combined with larger uncertainties about the double pion production processes. These observations are understood as follows.

The large data set available for the partial-wave analyses contains many single pion production data. Unpolarised cross sections and single polarisation observables —such as beam asymmetry, target asymmetry and recoil polarisation— constitute the majority of the data, whereas almost no double polarisation observables are available. Data for double pion production are scarce and are usually not, or yet with a large uncertainty, included in the partial-wave analyses. The large single pion data set and the fact that the Δ resonance is the dominant one in this energy region have contributed to its good understanding. In the double pion region, there are several resonances

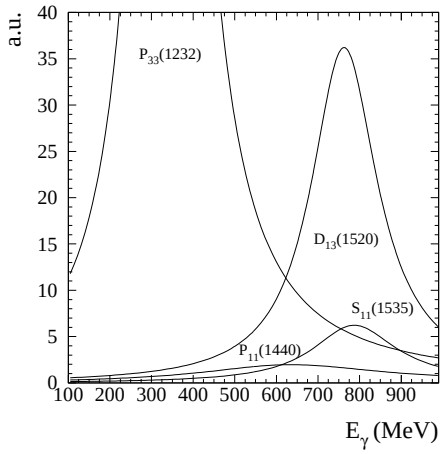

Figure 1.5: The nucleon resonances in the photon energy range below 1 GeV.

that can interfere which makes it difficult to disentangle their separate contributions. In combination with the small amount of available data, this explains why larger uncertainties are attached to the properties of these higher resonances.

An illustration of the fact that specifically the higher resonances are less precisely known and how the new measurements can improve the situation is given in Figure 1.6. Plotted are the predictions from SAID and UIM for the helicity asymmetry $\frac{d\sigma_{1/2}-d\sigma_{3/2}}{d\sigma_{1/2}+d\sigma_{3/2}}$ for the $\vec{\gamma}\vec{p} \rightarrow p\pi^0$ channel. The notation $d\sigma_{1/2}$ and $d\sigma_{3/2}$ is used to denote the angular distribution $\frac{d\sigma_{1/2}}{d\Omega}(\theta)$ and $\frac{d\sigma_{3/2}}{d\Omega}(\theta)$, respectively. The data are obtained in the GDH experiment [107]. At 300 MeV, in the Δ region, the two predictions agree very well. In the second resonance region at 720 MeV, the agreement is much poorer. At this energy, the higher resonances start to play a role and it is clear that some uncertainties remain to be solved. The data clearly favour the SAID result. This provides important new input to both SAID and UIM to tune their calculation.

Besides these uncertainties in the properties of the resonances, it is not fully understood which resonances contribute to the different double pion photoproduction processes and to what extent they do so. After the early work by Lüke and Söding [87], Oset and Laget both designed a theoretical model to describe the double pion production channels [99, 116]. The Oset model was recently revised [100]. Both these models include non-resonant and resonant terms. They do not completely agree on the issue of which resonances are predominating. For the $\gamma p \rightarrow p\pi^0\pi^0$ channel for example, the Oset model predicts a D_{13} dominance whereas in the Laget model, the P_{11} prevails. With a measurement of the helicity cross sections for this channel in the GDH ex-

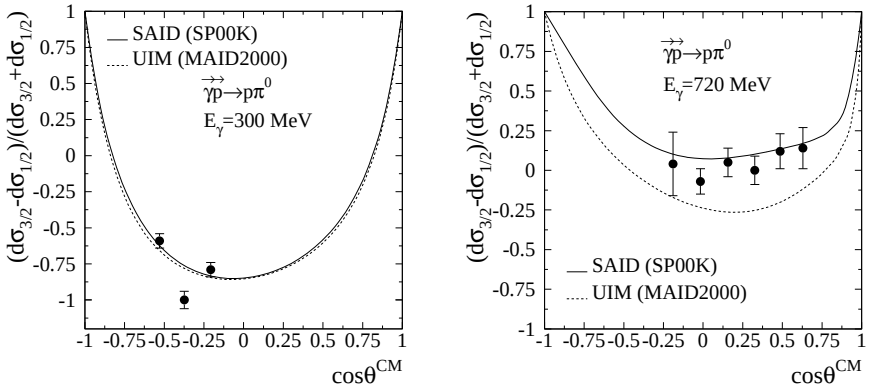

Figure 1.6: Helicity asymmetry for $\vec{\gamma}\vec{\mathrm{p}} \to \mathrm{p}\pi^0$ as a function of the center-of-mass angle as predicted by SAID and UIM at $E_\gamma = 300$ MeV in (a) and $E_\gamma = 700$ MeV in (b).

periment, one can straightforwardly distinguish between these two. A P_{11}, resp. D_{13}, dominance will be characterised by a positive, resp. negative, cross section difference $\sigma_{1/2} - \sigma_{3/2}$. The theoretical description of the $\gamma\mathrm{p} \to \mathrm{n}\pi^+\pi^0$ channel remains a challenge as it is not fully understood which mechanisms are responsible for the observed cross sections. The double polarisation measurement may also reveal new insight into this reaction by disentangling the predominant contributions.

As discussed above, it is also interesting to have an idea of the contribution of the various pion production channels to the GDH sum rule. For the single pion channels, the partial-wave analyses give adequate predictions. Few model calculations have been proposed for the double pion channels. There is the Karliner evaluation [78], the Coersmeier estimate [34] and the calculation by L'vov and Petrunkin [88]. For the contribution of double pion photoproduction to the GDH sum rule on the proton, they predict $65\ \mu$b, $83\ \mu$b an $46\ \mu$b, respectively. The large differences among these call again for an experimental constraint and a more precise model calculation.

1.4.3 Pion photoproduction in the GDH experiment at MAMI

The measurement of the helicity dependence of single and double pion photoproduction on the proton comprises the measurement of the cross section

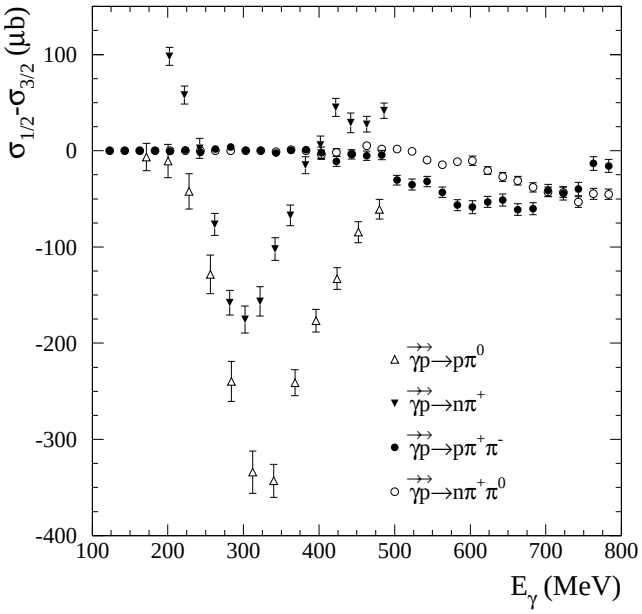

Figure 1.7: Cross section difference for the single and double pion channels measured in the GDH experiment.

difference $\sigma_{1/2} - \sigma_{3/2}$ for each of the following processes:

$$\vec{\gamma}\vec{p} \rightarrow \begin{cases} p\pi^0 \\ n\pi^+ \\ p\pi^+\pi^- \\ n\pi^+\pi^0 \\ p\pi^0\pi^0 \end{cases} .$$

Figure 1.7 gathers the present status of all GDH data analyses for the partial channels, including the new data presented in this work.

For the two single pion channels, the data have only been analysed so far in detail in the single pion region, up to 450 MeV. One observes the positive contribution to $\sigma_{1/2} - \sigma_{3/2}$ at threshold due to the E_{0^+} multipole in the $n\pi^+$ process. At higher energies the large M_{1^+} multipole of the Δ resonance dominates the cross section difference of both single pion processes. These data have recently been published by the GDH collaboration [53, 107]. They are in good agreement with the SAID and HDT predictions. Tests have already been done to incorporate the measured cross section differences in existing

partial-wave analyses. The measured contribution to the GDH sum rule in the energy range 200–450 MeV amounts to $-(144 \pm 7)$ μb for the pπ^0 channel and $-(32 \pm 7)$ μb for nπ^+.

The analysis of the data for the p$\pi^+\pi^-$ and the n$\pi^+\pi^0$ double pion reactions is the subject of this PhD thesis. Their cross section difference $\sigma_{1/2} - \sigma_{3/2}$ exhibits a rather large negative peak. The analysis of these data and the resulting cross sections are discussed in detail in Chapters 3 and 4.

The analysis of the p$\pi^0\pi^0$ channel is still ongoing [122].

1.4.4 A Regge model for double pion photoproduction

The Oset and Laget models for double pion photoproduction briefly mentioned above were developed to describe the three double pion reaction channels on the proton in the MAMI energy region, from threshold up to 800 MeV photon energy. Both calculations are tree calculations; they do not include final state interactions nor multiple intermediate states, which start to play a larger role at about 1 GeV. Particle exchanges are described as Feynman poles. These descriptions are not unitary. The consequences of this can be minimised by introducing many interfering resonances or by including absorption processes. At higher energies, however, the descriptions become unreliable.

Within the framework of this thesis, a Regge model for double pion production was designed in collaboration with Dr. Marc Vanderhaeghen. The aim is to provide a unitary model that simultaneously describes each isospin channel in a large energy range, from threshold up to several GeV incoming photon energy.

Regge theory was introduced at the end of the 1950's [108]. It has successfully been used over the years in the phenomenological description of many high energy scattering data. An example was mentioned in the discussion of the convergence of the GDH integral, with the result of a Regge fit by Bianchi. The Regge approach provides a strong argument concerning the high energy behaviour of the photoabsorption cross section.

In the Regge formalism, the partial-wave expansion of the scattering amplitude is continued into the complex plane of the angular momentum of the partial waves. This procedure ensures the unitarity of the description also at higher energies. The scattering processes are characterized by the exchange of a Regge trajectory. A Regge trajectory is a family of particles with identical quantum numbers save for their spin. This spin varies linearly with the mass squared of the particles, which corresponds to momentum transferred in the exchange mechanism. A general Regge trajectory is denoted $\alpha(t)$ with t the momentum transferred in the reaction. As detailed in Chapter 5 the angular distribution varies as:

$$\frac{\mathrm{d}\sigma}{\mathrm{d}t} \sim s^{2\alpha(t)-2},$$

with $\sqrt{s}$ the center-of-mass energy. The total cross section behaves as:

$$\sigma_{\text{tot}} \sim s^{\alpha(0)-1},$$

where $\alpha(0)$ is the intercept of the Regge trajectory at $t = 0$. These expressions hold in the kinematical region where $s \gg |t|$ and $t < 0$, the so-called Regge limit. In the model proposed here, an approach as followed by Vanderhaeghen and others for single pion production is adopted [58, 59]. From the concerned Feynman diagrams the vertex functions are derived. In the matrix element, the classical Feynman pole propagator is replaced by a Regge propagator which introduces the Regge trajectory exchange. This method has the advantage that no free parameters are used, i.e. only well known coupling constants are incorporated.

This results in a reliable high energy model. However, at lower energies, in the resonance regions, the Regge description provides only an average over all resonances, evoking the duality between resonance and Regge descriptions. Therefore, explicit resonances are also included. This explains the name of the model, *viz* Regge Plus Resonances, or RPR model for short. The RPR model is presented in detail in Chapter 6.

1.5 Overview

This thesis is organised as follows. A detailed description of the experimental setup of the GDH experiment in Mainz is given in Chapter 2. The electron and photon beams are discussed, followed by a description of the proton target. Finally the complete set of detectors is treated and a brief discussion of the data acquisition is given.

In Chapter 3 the analysis methods for the studied double pion photoproduction processes are developed. This is done by analysing the unpolarised data from the mentioned test measurement. Comparison with existing data allows to verify the proposed analysis methods and the assumed knowledge of the detector setup.

The devised analysis method is then applied to the doubly polarised data from the GDH experiment. In Chapter 4 the minor modifications with respect to the unpolarised calibration analysis are highlighted before presenting the obtained results for both $\vec{\gamma}\vec{\text{p}} \rightarrow \text{p}\pi^+\pi^-$ and $\vec{\gamma}\vec{\text{p}} \rightarrow \text{n}\pi^+\pi^0$. The helicity cross sections are shown, as well as the contribution of the studied processes to the GDH sum rule and the forward spin polarisability. A first indication for the interpretation of the data in terms of contributing resonances is also given.

As a base for the RPR model, a general introduction to Regge theory is given in Chapter 5. Via mainly phenomenological arguments the basic ideas are introduced and a formal derivation of the Regge scattering amplitude is given. Regge trajectories are also described.

In Chapter 6 the formalism of the RPR model is outlined in detail. Each contribution of both the Regge trajectory exchanges and the resonant processes is treated.

The results obtained in the RPR model are presented in Chapter 7 where they are compared with experimental data. The data are primarily the ones obtained in this work. A few data sets from literature are also added for comparing the RPR calculations in the case of reactions and kinematical regions not covered by the data presented here. This chapter gathers all main results from this thesis; an interpretation of the data is given in terms of the theoretical model and the precision of the theoretical model is tested.

Finally, in Chapter 8 a few concluding remarks are made when summarizing the presented work. An overview is also given of future topics to continue this work in the future.

The main publications of the GDH collaboration and those resulting from the research in this PhD work specifically, can be found in [53, 54, 72, 73, 74].

2

The GDH experiment at MAMI

The Mainz part of the GDH experiment was carried out at the electron accelerator facility MAMI. In this chapter the complete set of devices necessary to perform this experiment is described: the polarised electron beam (Section 2.1), the polarised photon beam obtained at the bremsstrahlung tagging spectrometer (Section 2.2), the polarised proton target (Section 2.3) and the detector setup (Section 2.4).

For testing purposes an unpolarised calibration measurement was also performed. Exactly the same setup was then used with an unpolarised beam and target, the specific features of which are also briefly discussed.

2.1 The electron beam at the Mainz Microtron MAMI

The *MAinz MIcrotron* MAMI saw the light in 1979 at the nuclear physics department of the Johannes Gutenberg University in Mainz [71, 70]. The first stage was MAMI-A1 where the exploitation of the microtron principle lead to a maximum electron energy of 14 MeV. It was followed by MAMI-A2 in 1983 when the 183 MeV facility was taken into operation. In 1991 MAMI-B was completed, producing electrons up to 855 MeV. Another upgrade, to 1.5 GeV, is planned for 2003 (MAMI-C). As the GDH measurements were performed at MAMI-B, we further concentrate on this version of the accelerator.

MAMI is a *continuous wave* electron accelerator that consists of a 3.5 MeV *LINear ACcelerator* (LINAC) which serves as an injector to three cascaded *Race-Track Microtrons* (RTM). The plan in Figure 2.1 shows the accelerator setup and the various experimental halls to which the beam can be directed (A1-4 and X1). The LINAC is either operated with a 100 keV unpolarised thermionic electron source or with a polarised electron source [12]. The latter consists of a *strained layer* $GaAs_{0.95}P_{0.5}$-crystal photo-cathode which is irradiated by 830 nm laser light from a Titanium-Sapphire laser. The laser light is circularly polarised through a Pockel cell. Via the photo-electric effect linearly polarised electrons are emitted from the crystal. A maximum polarisation of 70 to 80% can be obtained with this material. The slow initial electrons are accel-

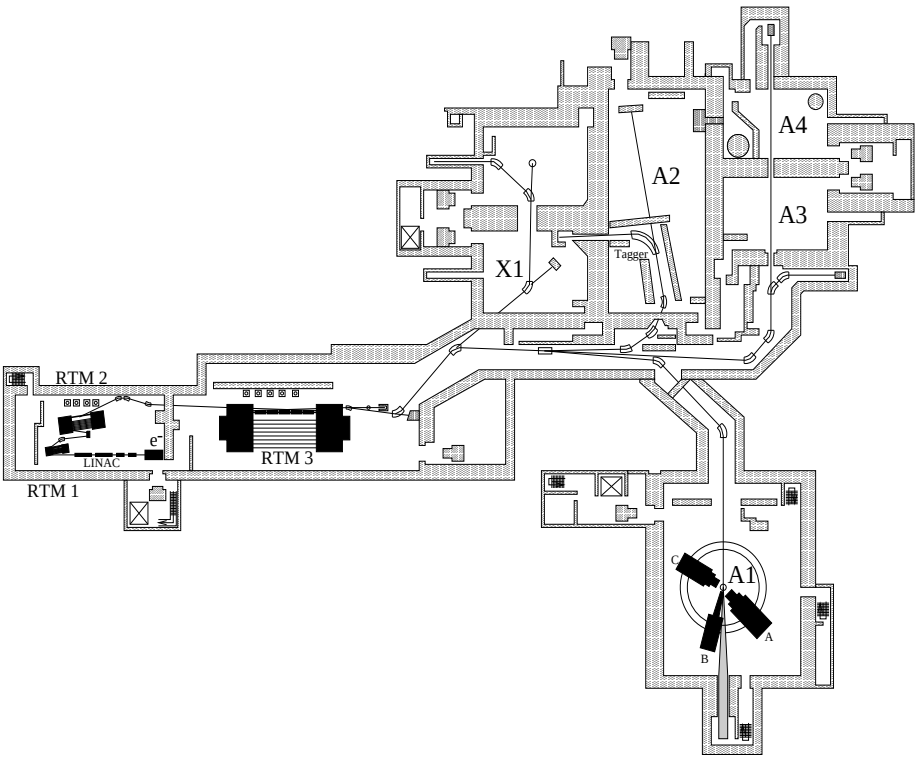

Figure 2.1: Plan of the MAMI facility. The main accelerator parts, the injector LINAC and the three RTMs are indicated as well as several experimental halls. Scale 1:1000.

erated in the LINAC to 3.5 MeV and injected into the cascade of RTMs. The scheme in Figure 2.2 illustrates the principle of an RTM. Each RTM consists of one LINAC section and two magnetic dipoles at the sides of a race-track-like beam path. After the primary injection the particles follow the race-track, they are accelerated each time they pass through the LINAC and deflected at each turn by the dipoles along a radius dependent on their energy. After a specific number of recirculations the beam is extracted. The three MAMI-B RTMs are indicated on the plan. In RTM1 the energy of the electrons is increased from 3.5 MeV to 14.4 MeV in 18 recirculations, RTM2 has 51 recirculations to bring the energy to 180 MeV and finally RTM3 increases the energy further to 855 MeV in 90 recirculations. The energy gain per recirculation evidently depends on the specifications of each individual RTM. By extracting the beam from RTM3 before the end of the full race-track, intermediate energies can be obtained. They are given by $E_0 = 180 + 2n(7.5)$ MeV with $n = 1, \ldots, 45$. The specifications of the complete accelerator apparatus are well optimised. MAMI delivers a continuous beam with a duty factor of 100%. The machine has a high stability and currents of up to 100 μA can be reached. These features, along with the possibility to produce polarised electrons, are major ad-

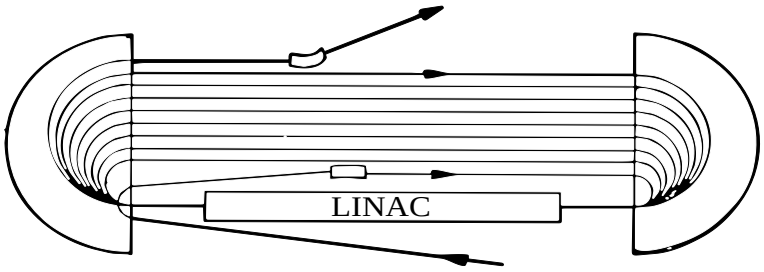

Figure 2.2: Schematic diagram of a Race-Track Microtron at MAMI.

vantages for the successful completion of the GDH experiment.

Both during the unpolarised test measurement and the actual GDH experiment two energy settings have been used, *viz* 525 MeV and 855 MeV. In the former case the unpolarised 100 keV source was used and in the latter case the machine was operated with the polarised electron source with a mean longitudinal polarisation of 75%. The polarisation direction of the electrons was switched with a frequency of 1 Hz. This was done to eliminate systematical errors that may arise from the fluctuation of the polarisation with time. By constantly switching the polarisation direction, these fluctuations are equally distributed over the two directions. As will be discussed in the next section the alternated polarisation direction is also transferred to the photon beam. Since the analysis involves the separation and normalisation of events with parallel beam and target polarisation directions and those with anti-parallel relative orientation, it is essential to know the precise luminosity of each relative orientation. Therefore the flux of the incoming beam for each electron polarisation direction must be determined. The flux corresponding to both polarisation directions was monitored separately by two groups of *tagger channels* (see Section 2.2.1 for a detailed description of the tagging spectrometer), each counting the number of electrons from one specific polarisation direction. An example of the number of events obtained in this way is given in Figure 2.3(a) and the ratio of the normalised rates of the two groups in Figure 2.3(b) as a function of time during one hour. On average the two relative polarisation configurations are equally present. This feature is exploited in the analysis of the data.

2.2 The photon beam in the A2 hall

2.2.1 The Glasgow-Mainz bremsstrahlung photon tagging spectrometer

The GDH experiment was performed in the A2 hall at MAMI. The hall is indicated in the plan in Figure 2.1 and Figure 2.4 gives an overview of the main components of the experimental setup. Real photons are obtained from the electron beam through bremsstrahlung in a radiator. For the experiment it is a prerequisite to know the energy of the photons that induce the stud-

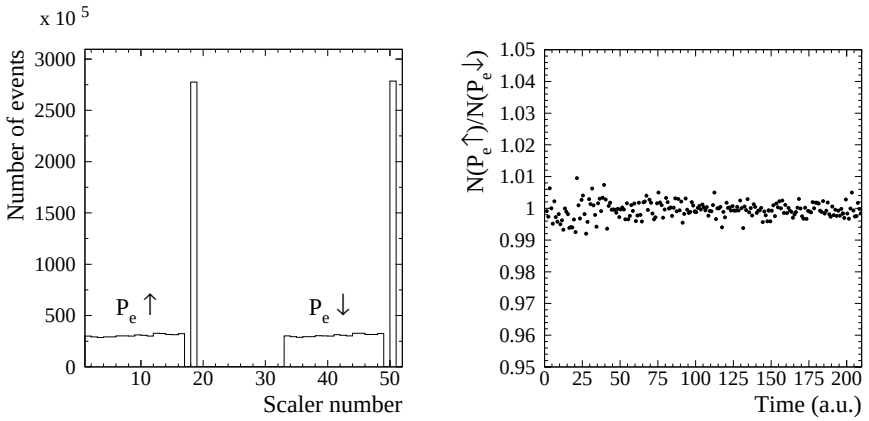

Figure 2.3: Histograms illustrating the relative fluxes of the two electron beam polarisation directions. (a) Number of events in a group of tagger scalers for each polarisation direction. (b) Ratio of the normalised rates for each polarisation direction as a function of time during one hour.

ied reactions. Therefore the photons are tagged by means of the *Glasgow-Mainz bremsstrahlung photon tagging spectrometer* [6, 60]. The technique for bremsstrahlung tagging is well established and its most important features are the high photon flux and the good energy resolution (up to 10^8 s^{-1} and ± 2 MeV in the Mainz case) that can be obtained. Alternatives for high energy photon tagging include *coherent bremsstrahlung* [85], *laser Compton backscattering* [13] and the *in-flight annihilation of positrons* [8]. The latter two however, usually do not reach such high fluxes.

The principle of the Glasgow-Mainz tagger is illustrated with Figure 2.5. Via the bremsstrahlung process, an electron hitting a radiator can cause the emission of a photon. Typical radiator materials are nickel and aluminum. During the GDH experiment a Vacoflux radiator was employed (see next section on the polarimetry). The produced photon beam is collimated towards the target and the detectors. When the incident electron has an energy E_0 and generates a bremsstrahlung photon with energy E_γ, the energy of the scattered electron is simply $E_{e'} = E_0 - E_\gamma$. The energy of the photon is thus determined by E_0 —the known beam energy— and $E_{e'}$. One measures the energy of the scattered electron $E_{e'}$ with a spectrometer and correlates it in time with the reaction products of the bremsstrahlung photon. In this way one controls the energy of the photon inducing the reaction.

The spectrometer consists of a large dipole magnet and an array of 353 *focal plane detectors*. The latter are scintillation detectors of which the position and orientation are determined by the focal points and the exit angles of the electrons deflected by the magnet. Since the deflection radius of the electron de-

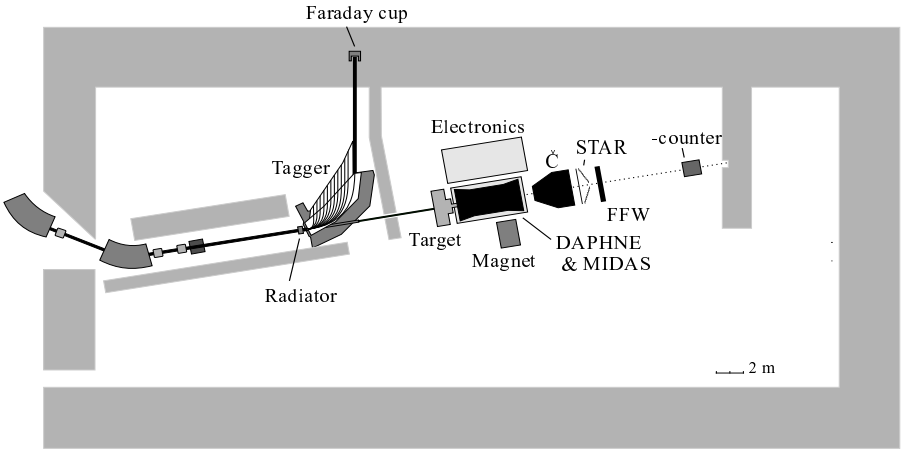

Figure 2.4: Plan of the A2 hall at MAMI.

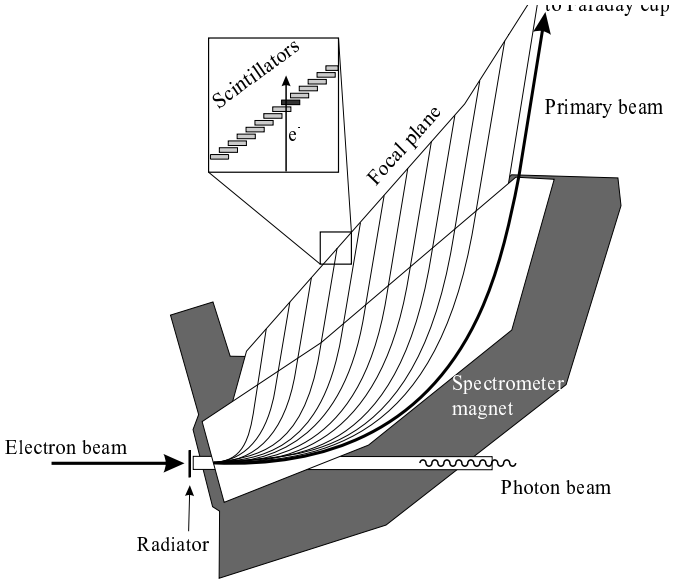

Figure 2.5: Schematic diagram of the Glasgow-Mainz tagger.

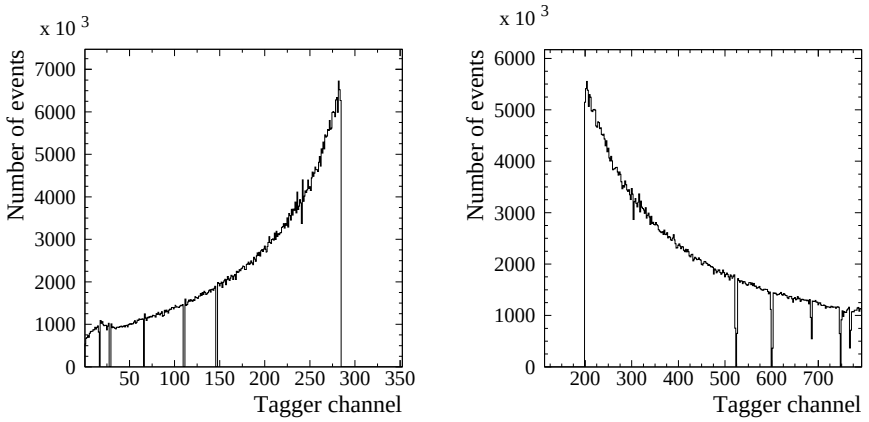

Figure 2.6: Tagger bremsstrahlung spectrum as a function of tagger channel (a), and as a function of photon energy (b).

pends on its energy, a signal in a specific detector —with finite dimensions— corresponds with a specific bin of electron energy $E_{e'}$ (mean value of the bin) and corresponding bremsstrahlung mean photon energy E_γ. Electrons that did not produce a bremsstrahlung photon are dumped into the Faraday cup and do not reach the focal plane. The Faraday cup is calibrated to monitor the electron beam current. Figure 2.5 zooms in on part of the detector array. The overlap between neighbouring detectors is used to generate coincidences between them in order to minimise random background from neutrons, photons or multiply scattered electrons from the primary beam. The tagger is calibrated to exactly correlate each detector-couple with an energy bin. There are thus 352 energy-channels with which an energy resolution of about 2 MeV is obtained. Depending on the experimental needs one can select a specific range of tagger channels. A typical configuration for an 855 MeV primary beam is to tag photons with energies between 200 and 790 MeV with channel numbers 1 (low electron energy and high photon energy) to 284 (high electron energy and low photon energy). For the GDH experiment the tagger was operated with a photon intensity of 10^7 s^{-1}.

The resulting photon energy spectrum evidently is a bremsstrahlung spectrum, which is governed by a $1/E_\gamma$ behaviour. The exact form of a bremsstrahlung spectrum can be found in [112]. As an example Figure 2.6 shows a tagger channel (electron energy) spectrum together with its corresponding photon energy spectrum. The zeros in the spectra are due to defective tagger channels.

2.2.2 Measurement of the number of tagged photons

For the normalisation of the data when calculating cross section values, a precise knowledge of the number of tagged photons that reach the target is required. This number is different from the amount of electrons that produced a photon and that are detected by any of the focal plane detectors. The photon beam is collimated immediately behind the radiator in order to obtain a well-defined beam spot and because of the angular spread of the bremsstrahlung photons, part of the photons are cut away. Moreover some of the electrons that reach the focal plane are not secondary bremsstrahlung electrons but stem from *Møller scattering* in the radiator. Another source of interfering electrons in the tagger is the background coming e.g. from the primary beam. The latter two effects are smaller than the first one and they can be treated by introducing a correction for the Møller electrons and by time correlation (random subtraction), respectively.

The ratio between the number of photons reaching the target $N_\gamma(E_\gamma)$ and the number of electrons detected in the tagger $N_\mathrm{e}(E_\gamma)$ is called the *tagging efficiency* $\epsilon_\mathrm{tagg}(E_\gamma)$. Each of these quantities is considered as a function of photon energy, that is, per tagged photon energy bin. The tagging efficiency reads:

$$\epsilon_\mathrm{tagg}(E_\gamma) = \frac{N_\gamma(E_\gamma)}{N_\mathrm{e}(E_\gamma)}. \tag{2.1}$$

The tagging efficiency evidently depends on the bremsstrahlung radiator material. It is further mainly influenced by the collimation of the photon beam and this effect strongly depends on the focussing of the primary electron beam on the radiator, which may not be constant over a longer period of time. It is therefore necessary to monitor ϵ_tagg continuously during the measurement and/or to measure precisely the number of tagged photons for each data taking run in order to have a reliable normalisation of the data.

The number of electrons N_e is readily obtained from the tagger detector scalers. The measurement of N_γ is less straightforward. A lead-glass photon detector (γ-counter) is positioned at the end of the experiment's beam line. It has a cubic shape ($25 \times 25 \times 25$ cm^3) and a close to 100% efficiency for the detection of photons. The drawback of this counter is that it can take a maximum photon intensity of 10^5 s^{-1} while the experiment is run at an intensity of several orders of magnitude higher. Hence it cannot be used for monitoring during data taking. To overcome this problem the *pair detector* is installed in front of the γ-counter. It is designed to have a low photon detection efficiency such that it can stand higher intensities. The idea is to calibrate its efficiency with the γ-counter during a low-intensity run. Once its efficiency is known, one can monitor the tagging efficiency during high-intensity data taking with the pair detector.

As illustrated in Figure 2.7 the pair detector consists of three thin plastic scintillator detectors (P1–3) and a copper converter foil. A photon that hits the copper foil can produce an electron through Compton scattering off an

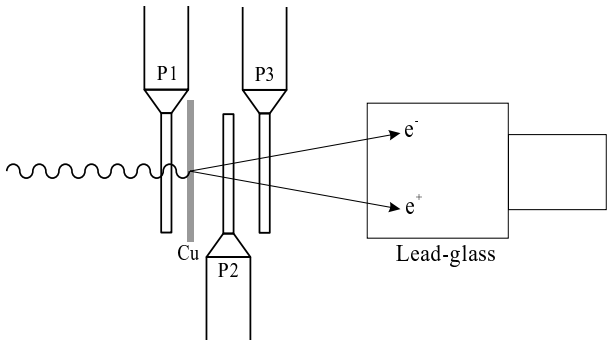

Figure 2.7: The pair detector and the lead-glass γ-counter.

atomic electron or an electron-positron pair through pair production in the field of a nucleus. These produced electrons can be detected by a coincidence between the detectors P2 and P3. The detector P1 in front of the copper foil is placed in anti-coincidence with P2 and P3 in order to veto unwanted events from electrons entering the pair detector. During a low-intensity run the γ-counter is placed in the beam and the ratio of the number of events acquired in the pair detector (N_{pair}) and in the lead-glass detector ($N_{\text{Pb-glass}}$) gives the pair detector efficiency ϵ_{pair}. This efficiency is mainly determined by the converter efficiency for photons in the copper foil and since in the considered energy region the pair production cross section is three orders of magnitude larger than the Compton scattering cross section, its energy behaviour exhibits a pair production behaviour. We define an *effective converter thickness* d_{eff} by:

$$\epsilon_{\text{pair}}(E_\gamma) = \frac{N_{\text{pair}}(E_\gamma)}{N_{\text{Pb-glass}}(E_\gamma)} = d_{\text{eff}}\sigma_{e^+e^-}^{(1\text{cm Cu})}(E_\gamma),$$

where $\sigma_{e^+e^-}^{(1\text{cm Cu})}(E_\gamma)$ gives the known energy dependence of pair production in a copper layer of 1 cm. The effective thickness d_{eff} is used as a fit parameter when fitting the ratio $\frac{N_{\text{pair}}}{N_{\text{Pb-glass}}}$ as a function of E_γ. Once d_{eff} is known, ϵ_{pair} is also determined and the number of tagged photons can be calculated from:

$$N_\gamma(E_\gamma) = \frac{N_{\text{pair}}(E_\gamma)}{\epsilon_{\text{pair}}(E_\gamma)},$$

without the need for the lead-glass counts $N_{\text{Pb-glass}}$. As such, for each run at high intensity the number of photons and the tagging efficiency can be obtained precisely from the pair detector information. At regular times during the experiment the intensity is decreased for a calibration measurement with the lead-glass detector. This is done to check the stability of both the pair detector efficiency and the tagging efficiency.

Typical mean tagging efficiencies during the GDH experiment are 15% for a primary beam of 855 MeV and 7.5% at 525 MeV with the Vacoflux tagger

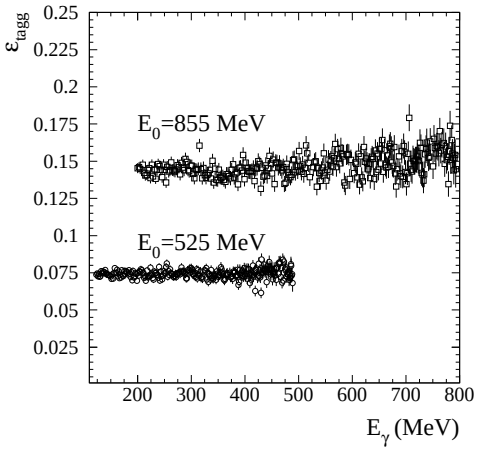

Figure 2.8: Measured tagging efficiency as a function of photon energy for a 525 MeV and 855 MeV primary electron beam energy, calculated per tagger scaler.

radiator. As one observes from Figure 2.8 the tagging efficiency is slightly energy dependent. The dependence on the primary beam energy is evident since the opening angle θ_{o} for bremsstrahlung is energy dependent. It is defined as the angle that encloses 50% of the emitted photons and is given by:

$$\theta_{\mathrm{o}} = \frac{m_{\mathrm{e}}}{E_0}$$

with m_{e} the electron mass. The lower the energy of the primary electrons, the wider the spread of the bremsstrahlung photons and thus the lower the fraction of photons that survive the collimation.

2.2.3 Measurement of the photon polarisation with the Møller polarimeter

The degree of polarisation of the photon beam is another important ingredient for the analysis of the data in the GDH experiment. Since it is different from 100%, not all detected events arise from polarised photons and a precise knowledge of the real polarisation degree allows to correct for this.

The longitudinal polarisation of the primary electrons is transferred to the photon beam in the bremsstrahlung process. According to [103, Eq. (8.11)] the circular polarisation degree P_γ of the photons as a function of photon energy E_γ can be written in terms of the degree of electron polarisation P_{e} and the primary electron energy E_0:

$$P_\gamma = P_{\mathrm{e}} \frac{4E_\gamma E_0 - E_\gamma^2}{4E_0^2 - 4E_\gamma E_0 + 3E_\gamma^2}. \tag{2.2}$$

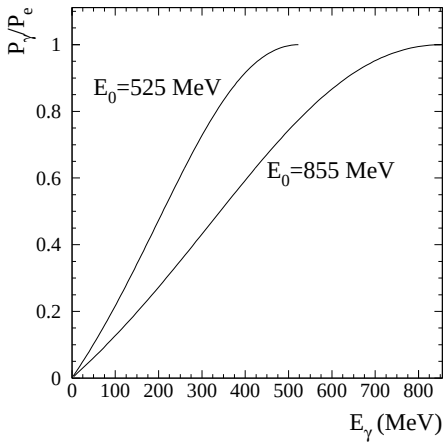

Figure 2.9: Polarisation transferred to the photon in the bremsstrahlung process: the ratio P_γ/P_e as a function of photon energy for two values of the primary electron energy E_0.

At $E_\gamma = E_0$ one has $P_\gamma = P_\mathrm{e}$, the electron polarisation is transferred completely to the photon. The lower the energy of the bremsstrahlung photon, the more the photon polarisation deviates from P_e. Figure 2.9 illustrates the energy behaviour of the polarisation transfer. With the aid of Equation (2.2) the photon polarisation can immediately be calculated once the electron polarisation is known.

The polarisation of the primary electron beam is measured with a *Møller polarimeter*. As mentioned above it is possible that a primary electron produces an electron pair through Møller scattering off the atomic electrons in the tagger radiator. These Møller electrons are also bent by the tagger magnet and can reach the focal plane detectors. This is unwanted background for the tagging of the bremsstrahlung photons but at the same time it allows to measure the electron polarisation simultaneously using the tagger.

Møller scattering is an established and widely used tool to measure electron polarisation. The cross section for Møller scattering of longitudinally polarised electrons off a magnetised ferromagnetic foil is polarisation dependent. The polarised cross section can be factorised as follows:

$$\left(\frac{\mathrm{d}\sigma}{\mathrm{d}E_\mathrm{e}}\right)^{\mathrm{pol}} = \left(\frac{\mathrm{d}\sigma}{\mathrm{d}E_\mathrm{e}}\right)^{\mathrm{unpol}} \left(1 + \sum_{j=\mathrm{x,y,z}} \sum_{k=\mathrm{x,y,z}} a_{jk} P_\mathrm{t}^j P_\mathrm{e}^k\right). \tag{2.3}$$

In this equation $\left(\frac{\mathrm{d}\sigma}{\mathrm{d}E_\mathrm{e}}\right)^{\mathrm{unpol}}$ is the unpolarised Møller cross section, P_t^j and P_e^k are the Cartesian components of the polarisation of the magnetised target foil and the electron beam polarisation respectively and a_{jk} is called the *analysing*

power, see e.g. [118]. The latter parameters a_{jk} can be calculated from QED [102].

One defines *the Møller asymmetry* $A^{\text{Møller}}$ by the following combination of the cross section for the case of a parallel magnetised foil and beam polarisation $\left(\frac{\mathrm{d}\sigma}{\mathrm{d}E_\mathrm{e}}\right)^{\uparrow\uparrow}$ and the one for the anti-parallel case $\left(\frac{\mathrm{d}\sigma}{\mathrm{d}E_\mathrm{e}}\right)^{\uparrow\downarrow}$:

$$A^{\text{Møller}} = \frac{\left(\frac{\mathrm{d}\sigma}{\mathrm{d}E_\mathrm{e}}\right)^{\uparrow\uparrow} - \left(\frac{\mathrm{d}\sigma}{\mathrm{d}E_\mathrm{e}}\right)^{\uparrow\downarrow}}{\left(\frac{\mathrm{d}\sigma}{\mathrm{d}E_\mathrm{e}}\right)^{\uparrow\uparrow} + \left(\frac{\mathrm{d}\sigma}{\mathrm{d}E_\mathrm{e}}\right)^{\uparrow\downarrow}}. \tag{2.4}$$

The larger part of the parameters a_{jk} are small and the asymmetry can be approximated here by:

$$A^{\text{Møller}} \approx a_{zz} P_\mathrm{t} P_\mathrm{e} \cos\alpha, \tag{2.5}$$

with P_t and P_e simply the degree of polarisation of the magnetised foil and the electron beam, respectively and α the angle between both spin directions. The analysing power a_{zz} is equal to $-7/9$.

On the other hand, the Møller asymmetry can be measured experimentally by accumulating events for the two relative orientations of the magnetised target foil and the electron beam, $N^{\uparrow\uparrow}$ and $N^{\uparrow\downarrow}$ separately:

$$A^{\text{Møller}} = \frac{N^{\uparrow\uparrow} - N^{\uparrow\downarrow}}{N^{\uparrow\uparrow} + N^{\uparrow\downarrow}}. \tag{2.6}$$

Since α is known from the orientation of the foil relative to the beam line and P_t is a well determined parameter of the experimental setup, the combination of (2.5) and (2.6) gives access to the electron beam polarisation P_e.

In practice, during the GDH experiment a Vacoflux foil was used as tagger radiator. The used Vacoflux is a FeCo-alloy that can be magnetised to $P_\mathrm{t} = (8.1 \pm 0.2)\%$. It simultaneously serves as a bremsstrahlung and a polarised Møller radiator. It is very thin to allow a high polarisation. However, this implies low bremsstrahlung yields and therefore the foil is rotated over $\alpha = 25^\circ$. Figure 2.10 shows the tagger scheme as in Figure 2.5 from the point of view of the Møller polarimeter. Two sets of tagger detectors were chosen to detect electron pairs in coincidence. A good Møller event is a coincidence of two focal plane detectors with the sum of the corresponding electron energies equal to the primary beam energy E_0. The two main sources of background are secondary bremsstrahlung electrons and electrons from pair electro-production. The former, which are not correlated in time, are suppressed by time correlation. The electrons from pair electro-production are suppressed by demanding coincidences between single tagger channels. With this measurement the asymmetry (2.6) is obtained and the electron beam polarisation is, with (2.5):

$$P_\mathrm{e} = \frac{A^{\text{Møller}}}{a_{zz} P_\mathrm{t} \cos\alpha}. \tag{2.7}$$

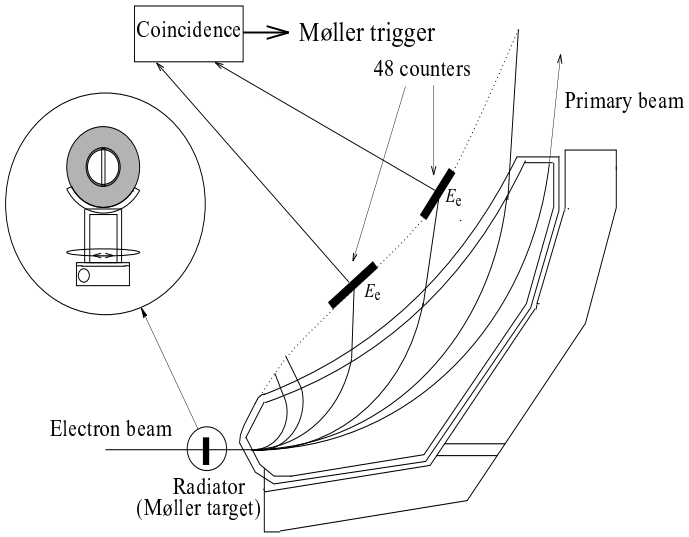

Figure 2.10: The Møller polarimeter.

The electron polarisation degree is typically around 75%. Due to the small values of the asymmetry $A^{\text{Møller}}$ (2.5), a large number of events is required to obtain a reasonable statistical uncertainty. In practice an uncertainty of 2% is obtained from a measurement of about 4 hours. Figure 2.11 illustrates the behaviour of P_e as a function of time. The observed stability justifies the use of the result within smaller periods of time.

2.3 The proton target

2.3.1 The liquid-hydrogen target

The unpolarised hydrogen target used in the test experiment preceding the actual GDH experiment was built in the beginning of the nineties. It was used in the former DAPHNE experiment at MAMI in 1992 for the measurement of photoabsorption and photoproduction cross sections on hydrogen, deuterium, ^{3}He and ^{4}He targets (see e.g. [95]).

The mylar target cell is 25 cm long and has a radius of 2.15 cm. A *Gifford-McMahon refrigerator* reduces the temperature of the cooling gas, ^{4}He, to 17 K. This is sufficient to liquefy hydrogen and deuterium. Coupling a *Joule-Thomson valve* to this primary system, a temperature of 2.5 K can be reached which is suited for the ^{3}He and ^{4}He targets. The pressure and the temperature in the refrigerator are monitored during the experiment. The density of the target material was found to be stable within 0.5 %.

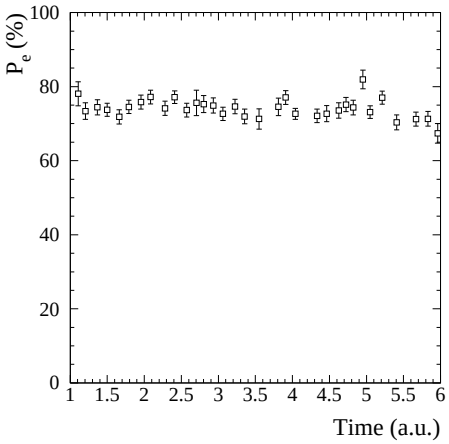

Figure 2.11: Electron polarisation measured with the Møller polarimeter, as a function of time over a total period of 150 hours. Each data point corresponds to a measurement of about 4 hours.

2.3.2 The frozen-spin butanol target

The polarised proton target used in the GDH experiment is the *frozen-spin butanol target* developed by the Bonn, Bochum and Nagoya groups [20, 44]. One of its main features is that it allows the escape of particles in an angular range of almost 4π. Via *Dynamic Nuclear Polarisation* (DNP) the protons in the butanol material can be polarised up to $P_{\mathrm{T}} = 80\%$.

The *Brillouin function* gives the longitudinal polarisation degree of particles with spin J, g-factor g and magnetic moment μ in an applied magnetic field B and at a temperature T:

$$P_J = \frac{2J+1}{2J}\coth\left(\frac{2J+1}{2J}\frac{g\mu BJ}{kT}\right) - \frac{1}{2J}\coth\left(\frac{g\mu BJ}{kT}\right). \qquad (2.8)$$

Due to their low magnetic moment it is not easy to polarise nucleons, it would require a magnetic field larger than 10 T and a temperature lower than 20 mK. The principle of Dynamic Nuclear Polarisation allows to weaken these conditions. In this technique the nucleon target material is doped with paramagnetic impurities. The latter's free electrons can be polarised to nearly 100% in a magnetic field of 2.5 T at a temperature of 300 mK. By irradiating the material with microwaves having a frequency close to the electron Larmor frequency, Zeeman transitions are induced and the electron polarisation is transferred to the nucleon spins.

Once the nucleons are polarised, the material has a long relaxation time at temperatures below 70 mK. This property allows to apply *the frozen-spin*

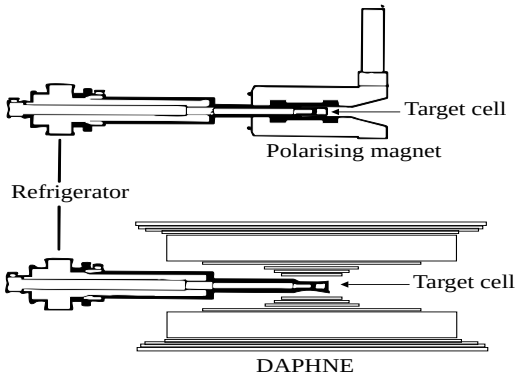

Figure 2.12: Target-detector configuration in the polarisation mode (upper) and in the frozen-spin mode (lower).

technique. The material is cooled down to 50 mK with a ^{3}He/^{4}He dilution refrigerator. An internal super-conducting holding coil provides a holding magnetic field of 0.4 T. In this way a relaxation time of more than 200 h can be obtained for a butanol target. During this time data can be taken without the presence of the high 2.5 T magnetic field and the large installation of such a magnet. The Bonn-Bochum-Nagoya target is the first one that uses the internal holding coil principle in a horizontal refrigerator. This has the important advantage over vertical configurations that all components of the target setup are situated at backward angles, allowing a near 4π escape of the produced particles. A vertical refrigerator inevitably cuts out a large part of an important angular range. The holding coil is also very thin (less than 1 mm) so that it does not hinder the outgoing particles much. Finally the holding coil is built as a solenoid such that its magnetic field has sufficient homogeneity for a *Nuclear Magnetic Resonance* (NMR) measurement. The nucleon polarisation can thus be continuously monitored during the experiment.

Figure 2.12 illustrates how the target system is practically employed. During the first stage, i.e. the polarisation of the target material at 2.5 T, the horizontal target insert is placed in the large polarising magnet (*polarising mode*). Once the optimal polarisation is reached, the insert is placed in the interior of the central detector system. The target material is cooled down to 50 mK and the holding coil is switched on (*frozen-spin mode*), in this configuration the experiment can be run. The movement of the entire target setup and the detectors is made possible by a rail system on which all parts are mounted.

A pure hydrogen/proton target cannot be polarised due to the fact that hydrogen reaches a para-state when it is cooled down. As mentioned before the target material in this case is butanol, C_4H_9OH. The material is doped with the paramagnetic porphyrexide for the Dynamic Nuclear Polarisation. An important property of butanol is its high maximal polarisation for the hydrogen protons (larger than 80%). It also has a short build-up time and long

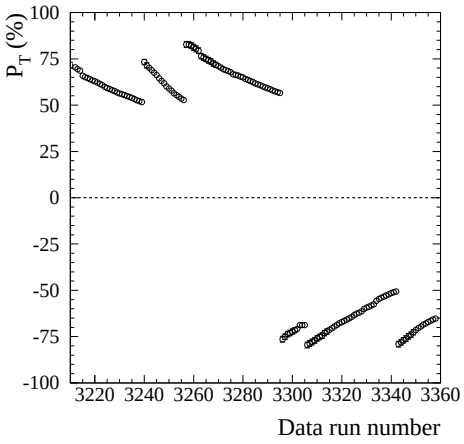

Figure 2.13: Target polarisation for a series of data runs over a total period of 150 hours.

relaxation time. The dilution factor, which is the fraction of polarisable protons in the material, is 0.135. This is not an excellent value but the other good properties of butanol make up for this. Butanol has been tested to have a good radiation resistance which is quite valuable since it spends a lot of time in the photon beam. For the experiment it is essential to have a high proton density and the non-proton ingredients of the material should be unpolarised, as it is for the carbon and the oxygen in butanol. The density of the butanol material is about 0.94 g/cm^3. It is packed into spherical beads which are placed in a cylindrical container which is 2 cm long and has a diameter of 2 cm. The effective filling factor of target beads in this container is 63%.

Figure 2.13 shows the evolution of the target polarisation as a function of time. During the GDH experiment the relaxation time was not always used to the limit; at regular intervals which also depended on the specific situation of the experiment, the material was repolarised to its maximum. From time to time the polarisation direction was switched in order to suppress systematical effects.

Deuterated butanol can also be used as a target material and it is one of the candidates for the measurement of the GDH sum rule on the neutron. Test measurements with this target were performed in Autumn 1998.

2.4 The GDH detector setup

The precise measurement of the total and partial photoabsorption cross sections on the nucleon as envisaged in the GDH experiment imposes some important requirements for the detector system. A near-4π angular acceptance

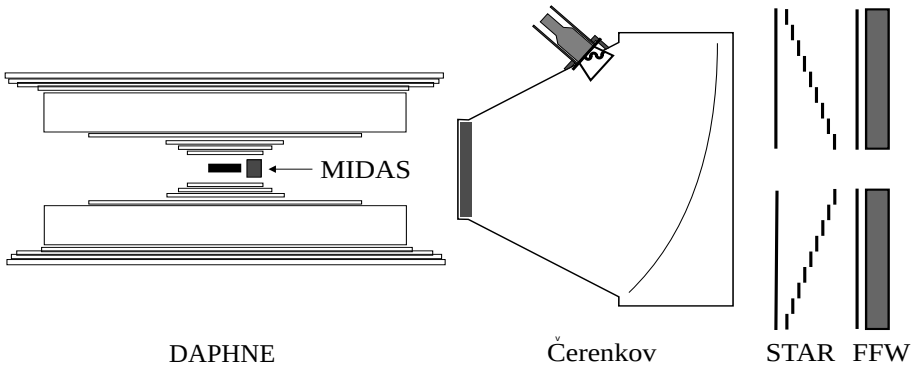

Figure 2.14: The GDH detector setup at MAMI.

and a large momentum acceptance are the primary demands. The larger the acceptance of the detector system, the smaller the contribution of the required extrapolation and the smaller the systematical errors induced thereby. The separation of the single and double pion channels requires the identification of charged and uncharged nucleons and pions, with reasonable efficiency.

The detector setup used at MAMI largely meets these requirements. Figure 2.14 shows a schematic view of the detector arrangement. The central detector is the DAPHNE detector. It covers the main part of the angular acceptance, namely for polar angles $21^\circ < \theta < 159^\circ$. Inside of DAPHNE, the silicon micro-strip detector MIDAS is located, which has an angular acceptance of $7^\circ < \theta < 16^\circ$. Further downstream the combination of the scintillator detector STAR and the lead-scintillator sandwich detector FFW is designed to cover the very forward angles, i.e. $2^\circ < \theta < 5^\circ$. The N_2-aerogel Čerenkov is a veto detector employed to suppress the large amount of electromagnetic background that accompanies the photon beam in the forward direction.

In the following sections each component of the detector array is discussed. The emphasis here is on those parts and properties that are used explicitly in the analysis presented in this thesis. For those features which are less important to the specific analysis here, we refer to other sources. Studies of the detector that are part of the work of this thesis are discussed in more detail in Chapter 3.

2.4.1 The DAPHNE detector

2.4.1.1 Introduction

The *Détecteur à grande Acceptance pour la PHysique photoNucléaire Experimentale*, or DAPHNE for short, was built in the beginning of the 90's by the Saclay and Pavia groups at the *Commissariat à l'Energie Atomique* in Saclay, France [10]. It was designed to measure total photoabsorption and single and double pion photoproduction cross sections of light nuclei, e.g. hydrogen, deuterium and

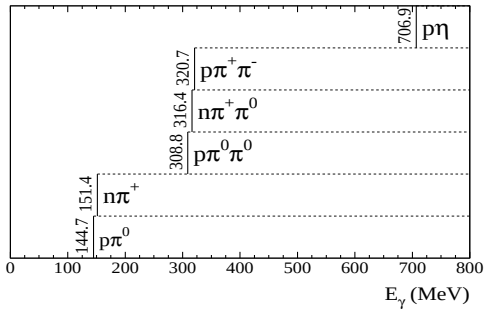

Figure 2.15: Reaction threshold energies of open π and η photoproduction reactions on the proton in the MAMI energy region.

^{3}He, in the intermediate energy range. More specifically it is well suited at the energies available at MAMI, $m_\pi \leq E_\gamma \leq 800$ MeV. In this energy range only a few meson production reaction channels are open. On the proton these are γp $\rightarrow$ pπ^0, nπ^+, p$\pi^+\pi^-$, n$\pi^+\pi^0$, p$\pi^0\pi^0$ and pη.

In the MAMI energy range, the threshold behaviour of each of these reactions can be studied. Moreover, except for the η production, the largest part of the cross section is found in this energy region. Figure 2.15 illustrates the photon energy thresholds for the proton reactions.

The detector's main strong points are its wide angular acceptance of 94% of 4π in total, the large acceptance in momentum and the capability to identify protons and charged pions with a high efficiency (> 80 %) and neutrons and neutral pions with a more moderate but acceptable efficiency. It provides also a precise vertex reconstruction and, in the case of protons and non-relativistic charged pions, the determination of their kinetic energy. This allows a reliable kinematical reconstruction of the reactions. Both the measurements of the total and of the partial cross section benefit from these properties as they reduce the systematical errors due to extrapolation and the uncertainty of particle identification. Low statistical errors can also be obtained in reasonable periods of time.

Successful results obtained with DAPHNE have been published over the past ten years [7, 10, 11, 14, 24, 22, 25, 36, 76, 96, 97, 121]. We further refer to these with the common label 'DAPHNE-92'.

Figure 2.16 gives a schematic view of the DAPHNE detector. It consists of three cylindrical multi-wire proportional chambers (MWPC's), surrounded by a range-telescope detector of six segmented scintillator layers, the latter three of which are completed with four 'dead' converter layers. In Section 2.4.1.2 it is shown how the wire chambers are used to track the charged particles. The identification of the charged and neutral particles by means of the scintillator layer detector is treated in Sections 2.4.1.3 and 2.4.1.4, Section 2.4.1.5 discusses

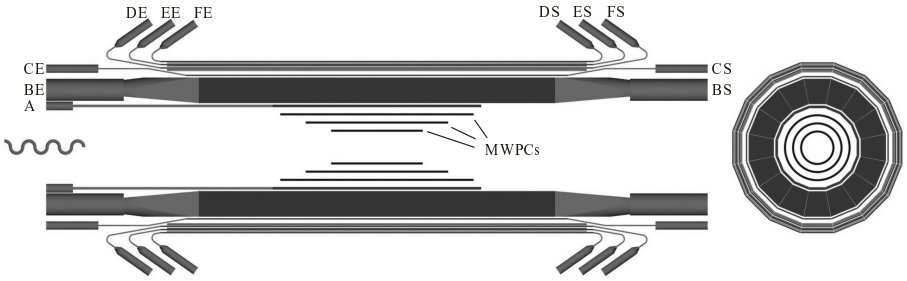

Figure 2.16: Side and front view of DAPHNE.

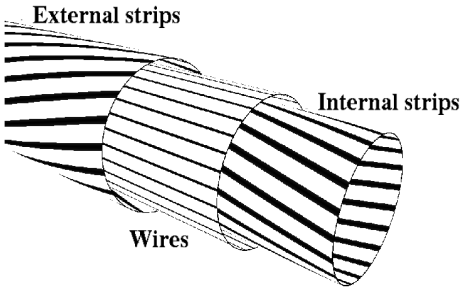

Figure 2.17: Wires and internal and external strips of a MWPC in DAPHNE.

the geometrical corrections which need to be taken into account.

2.4.1.2 Vertex reconstruction

The coaxial cylindrical multi-wire proportional chambers are the central part of DAPHNE. Each of the three chambers has two cylindrical Rohacell walls (1 mm thick) which are covered with 25 μm Kapton film. Aluminum strips are wound helicoidally on the interior surfaces of both the walls, the so-called internal (inner wall) and external (outer wall) strips. They serve as the cathode. The anode consists of parallel tungsten wires (20 μm diameter, spaced by 2 mm) which are placed in between the two strip-walls. Figure 2.17 illustrates how the strips and wires are arranged. The internal and external strips are wound in opposite directions, holding an angle with respect to the wires of $+45^\circ$ and -45°, respectively. The precise design parameters of the three MWPC's are given in Table 2.1. The chambers are filled with a gas mixture of argon (74.5%), ethane (25%) and freon (0.5%). This combination was found to yield a good resolution for the chambers. The anode-cathode gap is 4 mm wide.

A charged particle travelling through the chamber ionises the gas. The negative charge is collected by one ore more wires and the positive charge at the internal and external strips. From the centre of gravity of the charge dis-

MWPC	1	2	3
Length (mm)	360	560	760
Internal radius (mm)	60	92	124
External radius (mm)	68	100	132
Number of wires	192	288	384
Number of internal strips	60	92	124
Number of external strips	68	100	132

Table 2.1: Parameters of the MWPC's.

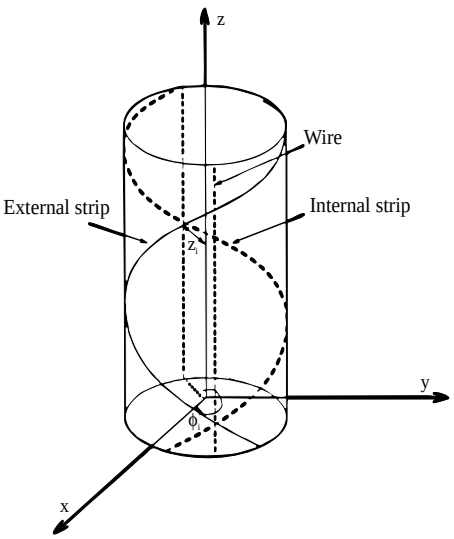

Figure 2.18: The azimuthal angle ϕ_i and the longitudinal coordinate z_i of the particle's impact point on a MWPC are obtained from the combined information of the internal and external strips and the wires.

tribution on the strips of each chamber the azimuthal angle ϕ_i ($i = 1, 2, 3$) and the longitudinal coordinate z_i of the impact point are evaluated. Figure 2.18 illustrates how ϕ_i and z_i are defined. Since the internal and external strips can overlap twice, there may be two possibilities for the ϕ_i angle. The information from the hit wire(s) is then used to resolve this uncertainty. Once ϕ_i and z_i are known from each chamber, a straight line can be fitted to these coordinates and the polar angle θ and the azimuthal angle ϕ of the track are obtained. For details on the track reconstruction we refer to [21]. In principle, two reconstructed points are sufficient to fit a track. However, in practice some of the wires/strips may be defective and then the extra information is important for keeping the global reconstruction efficiency high.

The vertex reconstruction for two or more charged tracks is done by taking the intersect of each pair of tracks. The mean of these positions gives the final

	Hydrogen	Deuterium	Butanol-I	Butanol-II
proton	100%	100%	100%	100%
single π	97.98±0.02%	97.87±0.01%	94.0±0.05%	96.2±0.06%
1 π in p$\pi^+\pi^-$	91.9±0.3%	91.8±0.2%	78.5±1.5%	82.5±1.5 %
2 π in p$\pi^+\pi^-$	91.6±0.3%	91.1±0.2%	76.0±2.0%	80.0±1.5%

Table 2.2: Global MWPC detection and reconstruction efficiencies for protons, single pions and pions in the $\gamma p \rightarrow p\pi^+\pi^-$ reaction [82].

vertex. In the case of one single charged track, the vertex position is defined as that point on the track which has the smallest perpendicular distance to the z-axis (i.e. the beam axis). By taking into account the maximum beam dimension, about 0.6 cm in our case, and the lowest emission angle 21°, one can obtain an idea of the largest error that is made on e.g. the reconstructed z. A particle emitted from $(x, y, z) = (0, 0.6, 0)$ at 21° will have a reconstructed $z = \frac{-0.6 \text{ cm}}{\tan 21^\circ} = -1.5$ cm in stead of $z = 0$. Hence, the largest error on z is taken to be about 1.5 cm.

Cosmic-ray data have been used to determine the track reconstruction resolution of the wire chambers [10, 95, 98]. The polar angle resolution is angle dependent and varies between 0.6° at $\theta = 90^\circ$ and 0.9° at $\theta = 30^\circ$. Due to the discrete spacing of the wires, the azimuthal angular resolution is 2°. Finally, the z-vertex resolution, which is also angle dependent, is about 0.3 mm at $\theta = 90^\circ$ and 1.5 mm at $\theta = 30^\circ$.

By analysing specific single and double pion channels, the detection and reconstruction efficiency for protons and charged pions of the MWPC's system can be obtained. This procedure is discussed in detail in [82]. The results are summarised in Table 2.2. The efficiencies depend on the used target material since the target setup influences the material the particles cross before reaching the wire chambers. This evidently effects the energy and the range of the particles in the detector, and thus also their detection efficiency. The proton is detected with a near-100% efficiency. The pure single pion efficiency differs from the efficiency for detecting one pion in the $\gamma p \rightarrow p\pi^+\pi^-$ reaction. This is due to the larger uncertainty to identify the specific pion track if the wire chambers also contain information on two other particles. One finds in the table two different sets of values for the butanol target. This is due to the fact that part of the butanol data for the GDH experiment were taken with a different MWPC gas mixture which had a degrading influence on the efficiency. These are labeled with butanol-I, while the data taken with the correct gas mixture are refered to as butanol-II.

2.4.1.3 Charged particle detection

Six layers of scintillator detectors surround the central wire chambers. Each layer has sixteen sectors as can be seen from the front view of DAPHNE in Figure 2.16. The layers are labeled from A to F starting from the cen-

Layer	Material	Width (mm)	Length (mm)	Radius (mm)
A	Pilot U	10	865	161
B	NE102A	100	1420	222.5
C	NE102A	5	1475	280.6
	Fe	5	-	-
	Pb	4	-	-
D	NE102A	5	1700	309.75
	Pb	5	-	-
E	NE102A	5	1708	322.75
	Al	5	-	-
F	NE102A	5	1720	334.75

Table 2.3: Specifications of the DAPHNE scintillator and converter layers.

ter. Each A-layer scintillator is equipped with one photomultiplier at the upstream side. The scintillators of the other layers have a photomultiplier at both ends. They are labeled with e.g. for the B-layer 'BE' (E for *entrée*) and 'BS' (S for *sortie*) for upstream and downstream, respectively. Four photon converter layers are placed in between the outer four scintillator layers. Apart from minor mechanical spacings between them, the sectors hold the full 360° around the beam axis. Table 2.3 lists the properties of each layer: the scintillation/converter material, length and radius (i.e. the distance from the beam axis to the middle of the layer). Depending on their energy, direction of motion and type the charged particles in DAPHNE reach different scintillator layers. So-called stop-A, B, C, D, E particles deposit their final energy in the respective layer. Particles that are stopped inside the F-layer or that leave the detector before losing all their energy are called stop-F particles.

The scintillator detectors can be used in two different ways for the identification of charged particles. Depending on the specific analysis, either one of them can be preferable. The first method is the $\Delta E - E$ *and geometrical range method* and the second is the *range-fit method*. Both are fundamentally based on the particle-specific range/energy loss in the scintillator layers. The electronic pulse height signals (ADC signals) are energy-calibrated such that one has the corresponding deposited energy in MeV at one's disposal. This calibration is done by studying two-body reactions of which the kinematics can be fully determined independent of the scintillator signals [79]. The mean energy resolution is of the order of 10% for the thick B-layer and about 15% for the other, thinner, layers.

The $\Delta E - E$ and geometrical range method In a 'classical' $\Delta E - E$ particle identification method one places a thin detector in front of a thick detector in which the particle is stopped. In the former it deposits part of its energy (ΔE) before the major part of the energy (E) is accumulated by the thick de-

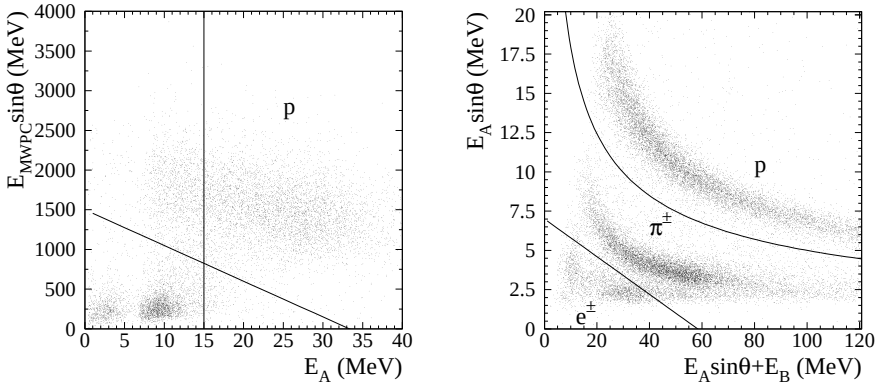

(a) Stop-A (b) Stop-B

Figure 2.19: Illustration of the $\Delta E - E$ charged particle identification method for stop-A and stop-B particles. The selection criteria for protons and charged pions are illustrated by the curves as defined in the text.

tector. The relative energy deposits at a given energy are particle dependent and therefore the $\Delta E - E$ information allows to separate different particle types.

Only for stop-B events one has a typical $\Delta E - E$ situation, with the A-layer as the thin ΔE detector and B as the stopping detector. For the other cases the situation slightly deviates from this, but a particle identification based on similar principles can still be done.

Stop-A particles Particles with a rather low energy can be stopped inside the thin A-layer. Apart from the amount of energy deposited in A, some information is also available on the energy deposited in the wire chambers. The charge deposited on the strips depends on the amount of energy that the particle lost in traversing the chambers. Combination of the A-layer and MWPC information allows to separate protons from electrons and pions in a $\Delta E - E$-like way.

In Figure 2.19(a) the energy deposited in the MWPC's (E_{MWPC}), corrected for the distance travelled inside the material by a factor $\sin\theta$, is plotted versus the energy deposited in the A-layer (E_{A}). Protons, which deposit a large amount of energy in A and in the chambers, are found in an ellipse-shaped zone at the upper-right. The other well-populated zones correspond to electrons and pions which are not well separated due to the lack of good energy resolution of the wire chambers. Hence, for stop-A particles protons can be identified and separated from electron background and pions. No pion identification is done for stop-A particles.

The cuts used to select the protons are drawn in the plot. They are defined

as:

$$E_{\mathrm{A}} > 15\ \mathrm{MeV} \tag{2.9}$$

$$E_{\mathrm{MWPC}} \sin\theta > a_{\mathrm{A}} E_{\mathrm{A}} + b_{\mathrm{A}}. \tag{2.10}$$

The 15 MeV is a fixed cut: the A-layer has a photomultiplier only at one end (see Figure 2.16) and for deposited energies below 15 MeV the scintillator light produced at the other end does not reach the photomultiplier and the threshold for detecting a proton becomes position dependent. Therefore a fixed threshold is set. The values for a_{A} and b_{A} slightly depend on the target setup since the latter influences the energy losses in front of the wire chambers. One has for hydrogen and butanol:

$$\text{Hydrogen}: \quad a_{\mathrm{A}} = -45, \quad b_{\mathrm{A}} = 1500\ \mathrm{MeV}, \tag{2.11}$$

$$\text{Butanol}: \quad a_{\mathrm{A}} = -40, \quad b_{\mathrm{A}} = 1020\ \mathrm{MeV}. \tag{2.12}$$

Stop-B particles For stop-B particles the energy deposited in the thin A-layer (E_{A}) and in the thick B-layer (E_{B}) can be used for a classical $\Delta E - E$ particle identification. The energy deposited in A, corrected for the distance travelled inside the material ($E_{\mathrm{A}} \sin\theta$), is plotted versus the sum of E_{B} and $E_{\mathrm{A}} \sin\theta$ in Figure 2.19(b).

Due to the different relative amount of energy deposited by stopped protons, pions and electrons, three clear bands are visible. Protons can be separated cleanly. There is a region where the electron and pion zones overlap. Due to hadronic interactions, pions may transfer part of their energy to protons or neutrons in the scintillator material. The pion is stopped in the B-layer but the secondary nucleons may take the transferred energy to another sector. These events give a stop-B signal and the value of $E_{\mathrm{A}} \sin\theta$ is as expected but E_{B} is lower, which explains the extra tail into the electron zone.

To select protons one demands:

$$E_{\mathrm{A}} \sin\theta \geq a_{\mathrm{B}} (E_{\mathrm{A}} \sin\theta + E_{\mathrm{B}})^{-1/2} + b_{\mathrm{B}}, \tag{2.13}$$

with $a_{\mathrm{B}} = 60\ \mathrm{MeV}^{3/2}$ and $b_{\mathrm{B}} = -1$ MeV for both the hydrogen and the butanol target.

The electron cut is defined as:

$$E_{\mathrm{A}} \sin\theta \leq c_{\mathrm{B}} (E_{\mathrm{A}} \sin\theta + E_{\mathrm{B}}) + d_{\mathrm{B}}, \tag{2.14}$$

with $c_{\mathrm{B}} = -0.12\ \mathrm{MeV}^{3/2}$ and $d_{\mathrm{B}} = 7$ MeV for both the hydrogen and the butanol target. Hereby all electron background can be cut away. Due to the hadronic interactions effect some pions are also removed. One needs then to correct for this loss by a simulation procedure (see Section 3.6).

Stop-C, stop-D, stop-E and stop-F particles Charged particles that are stopped beyond the B-layer can be identified by comparing the energy they

lost in B to the geometrical path of the particle through the detector expressed in equivalent scintillator thicknesses R. When plotted versus each other, protons, pions and electrons are found in separate regions. This is illustrated in Figure 2.20 where the proton and electron cuts are also shown.

For protons one imposes the condition:

$$E_{\mathrm{B}} > a_{\mathrm{i}} R + b_{\mathrm{i}} \qquad i = \mathrm{C}, \mathrm{D}, \mathrm{E}, \mathrm{F}, \tag{2.15}$$

with, for both hydrogen and butanol:

$$a_{\mathrm{C}} = 0.186\ \mathrm{MeV/mm}, \quad b_{\mathrm{C}} = 32.7\ \mathrm{MeV}, \tag{2.16}$$
$$a_{\mathrm{D}} = 0.152\ \mathrm{MeV/mm}, \quad b_{\mathrm{D}} = 21.6\ \mathrm{MeV}, \tag{2.17}$$
$$a_{\mathrm{E}} = 0.130\ \mathrm{MeV/mm}, \quad b_{\mathrm{E}} = 14.0\ \mathrm{MeV}, \tag{2.18}$$
$$a_{\mathrm{F}} = 0.132\ \mathrm{MeV/mm}, \quad b_{\mathrm{F}} = 5.0\ \mathrm{MeV}. \tag{2.19}$$

Electrons can be cut away by demanding:

$$E_{\mathrm{B}} < c_{\mathrm{i}} R + d_{\mathrm{i}} \qquad i = \mathrm{C}, \mathrm{D}, \mathrm{E}, \mathrm{F}, \tag{2.20}$$

with, both for hydrogen and butanol:

$$c_{\mathrm{C}} = 0.205\ \mathrm{MeV/mm}, \quad d_{\mathrm{C}} = 4.21\ \mathrm{MeV}, \tag{2.21}$$
$$c_{\mathrm{D}} = 0.123\ \mathrm{MeV/mm}, \quad d_{\mathrm{D}} = 0,\ \mathrm{MeV} \tag{2.22}$$
$$c_{\mathrm{E}} = 0.080\ \mathrm{MeV/mm}, \quad d_{\mathrm{E}} = 0\ \mathrm{MeV}, \tag{2.23}$$
$$c_{\mathrm{F}} = 0.086\ \mathrm{MeV/mm}, \quad d_{\mathrm{F}} = -4.91\ \mathrm{MeV}. \tag{2.24}$$

As one can see from the figure, most of the particles that reach the E- and F-layer are pions. In the reactions studied here, pions are the most energetic reaction products and many of them are minimum ionising and leave the detector without being stopped by the scintillators.

The range-fit method The range-fit method is an extension of the $\Delta E - E$ technique for two detectors to several subsequent scintillator layers. The information of all layers traversed by a particle is used. It allows a clean particle identification and yields the initial kinetic energy. The application of this technique has been well studied and refined during the analysis of DAPHNE data over the past ten years. For details, see [24, 98].

The integrated Bethe-Bloch formula relates the energy loss of a certain type of particle to its path through a particular material. This path is called the *range* of the particle in this material. Since all detector materials and their dimensions are known, the Bethe-Bloch relation can be used to calculate the energy deposited in each layer $\left(\Delta E^{\mathrm{theor}}_{i_{\mathrm{layer}}}\right)$ theoretically, starting from an initial kinetic energy E_0.

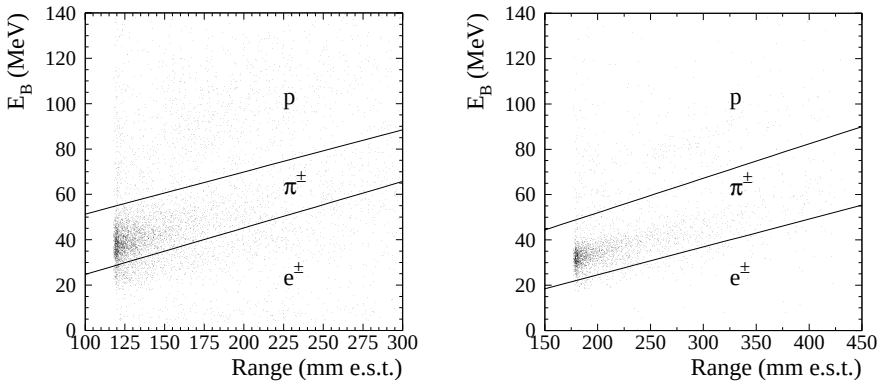

(a) Stop-C

(b) Stop-D

(c) Stop-E

(d) Stop-F

Figure 2.20: Illustration of the charged particle identification by means of the geometrical range method for stop-C, D, E and F particles. The straight lines delimiting the charged pion zones are as defined in the text. The geometrical range is expressed in millimeter equivalent scintillator thickness.

With the experimental energy losses in each detector layer $\left(\Delta E^{\text{exp}}_{i_{\text{layer}}}\right)$ the unknown initial energy E_0 can be obtained by minimising

$$\chi^2 = \frac{1}{N-1} \sum_{l=1}^{N} \frac{\left|\Delta E_l^{\text{theor}} - \Delta E_l^{\text{exp}}\right|^2}{\sigma_l^2} \tag{2.25}$$

with respect to E_0. In this expression l runs over all hit detector layers, N is the layer in which the particle is stopped and σ_l is the energy resolution of layer l. Using a least-square fit, the E_0 corresponding to the minimal χ^2 is obtained.

This procedure can be repeated under the assumption of different particle types in the Bethe-Bloch function. A χ^2 is then obtained for pions, protons, deuterons, ... The lowest χ^2 corresponds with the best fit; consequently, a comparison of the set of obtained values provides a good particle discrimination.

For a least-square fit of (2.25) to be feasible, at least two measured energies are needed. Therefore the range-fit method cannot be applied to identify stop-A particles. However, when the proton selection is performed with the $\Delta E - E$-like method as described above, the Bethe-Bloch relations and the experimental energy deposit in A can be used to simply calculate the particle's initial kinetic energy.

Stop-F particles that leave the detector are high-energetic and, within the scintillator resolution, such pions and protons have the same energy losses and no particle separation is possible. Moreover, for particles that left the detector, the total energy information is not contained in the measured energy deposits. This takes place for proton momenta larger than 600 MeV/c and pion momenta above 200 MeV/c. For these particles the technique as such is not useful. However, at the energy ranges and reactions studied by DAPHNE few protons leave the detector. The problem is more significant for pions. In these cases another method has to be used for particle identification or extra information has to be extracted from a simulation. For protons that actually did stop in the F-layer, the range-fit method can still be applied by putting an upper threshold on the obtained energy of the particle.

Protons that just enter B but do not have much excess energy have a low identification efficiency in the range-fit method. These protons can be well defined in the $E_{\text{A}} \sin\theta$ versus $E_{\text{A}} \sin\theta + E_{\text{B}}$ plot, as the energy they deposit in B is very low. Therefore in this case we do not use the range method but define a *stop-B proton corner* in which all events are accepted as protons. It is given by

$$a_{\text{B-corner}} \leq E_{\text{A}} \sin\theta \leq b_{\text{B-corner}} \tag{2.26}$$

$$E_{\text{A}} \sin\theta + E_{\text{B}} \leq c_{\text{B-corner}}, \tag{2.27}$$

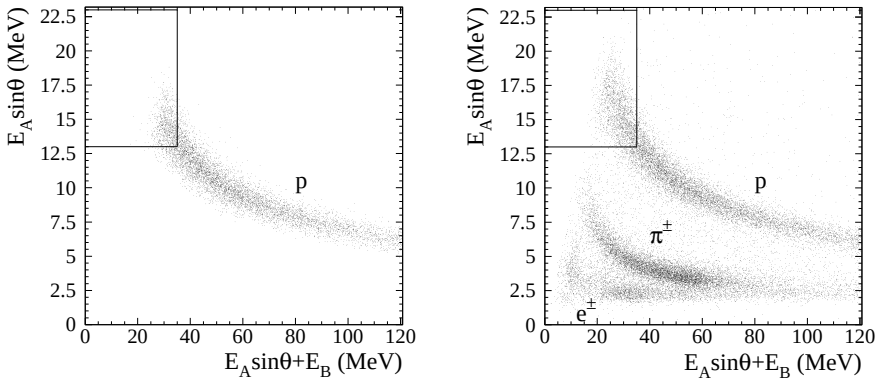

Figure 2.21: Identification of protons with a low energy deposit in B. (a) The $\Delta E - E$ plot for protons identified with the range-fit method. (b) The full $\Delta E - E$ plot. The indicated *stop-B proton corner* is used for a backup identification for protons not identified with the range-fit method due to its low efficiency in this region.

with for the different target setups:

$$\text{Hydrogen}: \quad a_{\text{B-corner}} = 13\ \text{MeV}, \quad b_{\text{B-corner}} = 23\ \text{MeV}, \quad c_{\text{B-corner}} = 35\ \text{MeV}, \tag{2.28}$$

$$\text{Butanol}: \quad a_{\text{B-corner}} = 13\ \text{MeV}, \quad b_{\text{B-corner}} = 24\ \text{MeV}, \quad c_{\text{B-corner}} = 38\ \text{MeV}. \tag{2.29}$$

This procedure is illustrated in Figure 2.21.

In summary: protons stopped in layer B, C, D, E or F and pions stopped in B, C, D or E are well identified with the range-fit method and their kinetic energy can be determined. The energy of stop-A protons can also be calculated.

The efficiency with which protons and pions can be identified with the range-fit method is angle and momentum dependent. It is of the order of 70–90%. In Figure 2.22 the efficiency is plotted as a function of momentum and angle for both protons and pions.

A mean energy resolution of about 5% is obtained.

In the case of proton identification, pion contamination is less than 1% but a conservative overall systematical error of 2% is adapted for the range-fit identification in this case.

2.4.1.4 Neutral particle detection

Neutrons and neutral pions are the two types of neutral particles that are studied with DAPHNE. The thick B-layer serves as a neutron detector. Efficiencies of about 20–30% can be obtained. By calibrating the time difference between

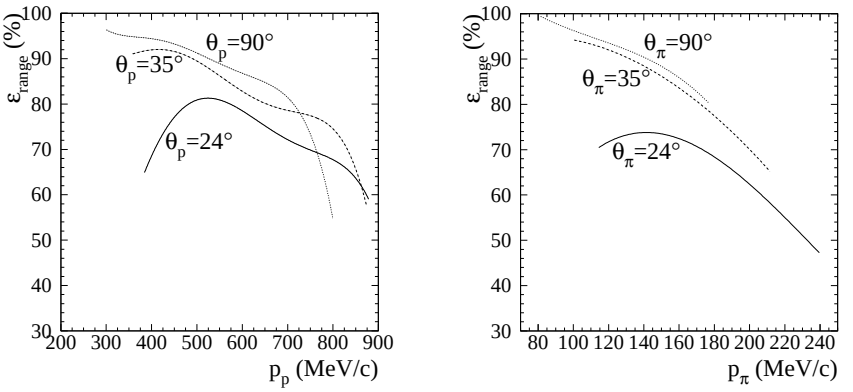

(a) (b)

Figure 2.22: Range-fit identification efficiency for protons (a) and charged pions (b) as a function of particle momentum for different emission angles.

the signals of the two photomultipliers at opposite ends of the scintillator, the outgoing polar angle of the neutron can be determined with a resolution of $4.5°$.

The detection and identification of a π^0 can be performed by detecting its decay photons. These can be converted in the lead, aluminum or iron converter layers in between scintillator layers C, D, E and F. The showers thus produced allow the detection of these uncharged events. The D, E and F-layer are trapezium-shaped, with the small base facing the center of the detector. This design provides π^0 detection efficiencies with a very small angular dependence.

Both the neutron and the π^0 identification and detection efficiency have been studied in detail and are used in the analysis presented in this PhD work, they are discussed further in Chapter 3.

2.4.1.5 Geometrical corrections

Azimuthal correction The sixteen sectors of each scintillator layer surround the beam axis. Although each sector is shaped to fit to its neighbours and thus to form a cylinder, it is mechanically not possible to mount the sectors perfectly. As illustrated in Figure 2.23 there are holes in the cylinder. When a particle is emitted from the target with an azimuthal angle ϕ such that it enters such a hole, it will not be detected. If it does not enter the hole, but reaches the detector close to it, the probability that it does not properly deposit its energy in the detector is quite large. Therefore a fixed safe azimuthal region $\left[\phi^{\min}_{i_{\text{sector}}}, \phi^{\max}_{i_{\text{sector}}}\right]$ is set by software to the azimuthal angles obtained by the wire chambers. Events that are lost in this way can be recovered by applying a global

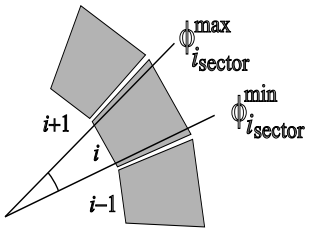

Figure 2.23: Illustration of the mechanical holes in the azimuthal acceptance of DAPHNE.

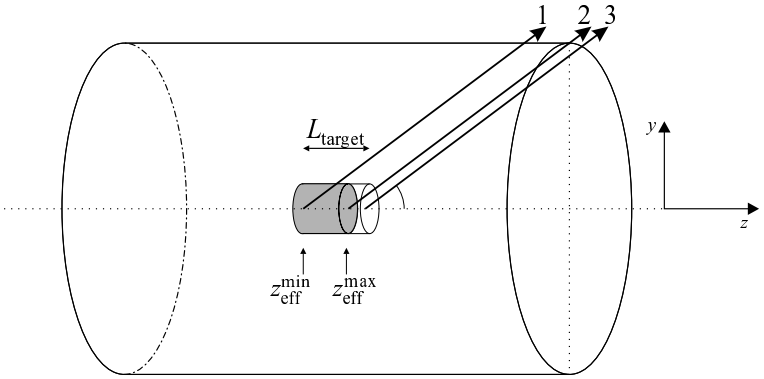

Figure 2.24: Effective target seen by DAPHNE.

correction factor, since the measured cross sections are not ϕ dependent. This purely geometrical correction can be calculated exactly. In the case of one single track, the azimuthal acceptance is 84% of 2π. For two or three uncorrelated tracks this would be $(84\%)^2 = 71\%$ and $(84\%)^3 = 59\%$ respectively. Since in the studied reactions with two or more detected particles, the tracks are correlated, the correction values slightly deviate from this. The exact ones are obtained by simulation.

Effective target length correction The target used in the experiment is not a point-like target but it has a certain thickness d_{target} in the z-direction (beam axis). Moreover the length of the detector components of DAPHNE is not infinite. These two aspects imply that, for a specific emission angle, the possibility for a track to be observed depends on the vertex position from which it originates. Figure 2.24 illustrates this effect. A *control cylinder* is drawn: it represents the active part of DAPHNE and so its acceptance. The cylinder is centred around the beam axis, has a radius of 40 mm and is 212 mm long.

As an example three single tracks are shown. All three have the same emission angle θ and originate from a different position in the target on the z-axis. Track 1 is clearly inside the acceptance. Track 2 intersects the control cylinder at the edge and is still detected but Track 3 is outside of the acceptance

as it does not intersect the cylinder. In this way one can see that only a part of the full target length is effectively 'seen' by the detector. This *effective target length*, defined by $\left[z_{\text{eff}}^{\min}(\theta),\, z_{\text{eff}}^{\max}(\theta)\right]$ in the figure, can simply be calculated geometrically for each θ.

For DAPHNE events for which two or more tracks are emitted from the target the situation is somewhat more complicated since off-beam-axis effects and effects of the azimuthal emission angle ϕ need to be taken into account. However it remains a purely geometrical calculation that can be performed exactly to give an effective target range $\left[z_{\text{eff},i}^{\min}(\theta_i,\phi_i),\, z_{\text{eff},i}^{\max}(\theta_i,\phi_i)\right]$, for each track i. The overall limits $\left[z_{\text{eff}}^{\min}(\theta,\phi),\, z_{\text{eff}}^{\max}(\theta,\phi)\right]$ for the event are taken to be the largest of all $z_{\text{eff},i}^{\min}(\theta_i,\phi_i)$ and the smallest of all $z_{\text{eff},i}^{\max}(\theta_i,\phi_i)$ respectively.

To correct for these effects each event is weighted by:

$$w_{\text{eff}}(\theta,\phi) = \frac{d_{\text{target}}}{z_{\text{eff}}^{\max}(\theta,\phi) - z_{\text{eff}}^{\min}(\theta,\phi)}, \tag{2.30}$$

such that all events are normalised to the same true target length.

2.4.2 The MIDAS detector

MIDAS, the *MIcrostrip Detector Array System* was designed to enlarge the angular acceptance of the GDH detector setup in the forward direction [3]. The DAPHNE detector is mounted on a mechanical frame which masks particles emitted with a polar angle between 5° and 21°. This restriction is almost completely overcome by the compactness of MIDAS such that it can be placed inside this frame. As it is inside of the frame, the acceptance of MIDAS is not affected by the particle masking and it covers the region $7^\circ < \theta < 16^\circ$. At this position inside DAPHNE it is not feasible to go to lower angles due to the beam halo; only further downstream, this problem becomes smaller (see Section 2.4.4 on the STAR and the FFW detector). The three main features of the MIDAS detector are the ability for detecting protons and charged pions with a small electromagnetic background contamination, track reconstruction for charged particles and particle identification for protons and pions.

A schematic view of MIDAS is given in Figure 2.25. There are two main parts. The first part is the tracking detector and consists of two annular double-sided semiconductor silicon detectors (V_1 and V_2). The n-sides are radially segmented in 16 sectors while the p-sides are divided into 48 concentric rings. The second part is an annular silicon-lead sandwich (Q_1, Pb, Q_2, Pb, Q_3) that is used for the particle identification and energy measurement. The three single-sided silicon detectors have the p-sides segmented in four quadrants.

A coincidence between Q_1 and Q_2 provides a good trigger for lower energy protons whereas a Q_1-Q_2-Q_3 coincidence serves as a pion and high energy proton trigger. The kinetic energy threshold for protons in MIDAS is 60 MeV and for pions this is 50 MeV. Most of the electromagnetic background is suppressed through absorption in the lead layers. This is done with an efficiency of 99%. The background that is not stopped in this way mainly

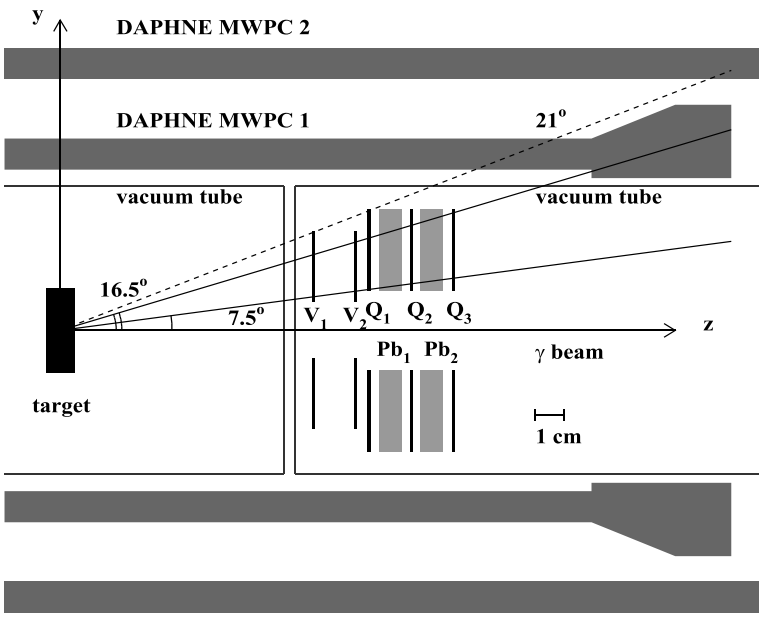

Figure 2.25: Side view of the MIDAS detector.

originates from pair production. In most cases only one of the two produced electrons is within the MIDAS acceptance. The other one is usually detected by the veto-Čerenkov detector such that also these events can be suppressed.

The trajectory of a charged track in MIDAS can be reconstructed from the knowledge of its impact points on V_1 and on V_2. The impact point of a particle on each of these detectors is obtained from the intersection of the hit rings and sectors. The overall polar and azimuthal angular resolutions are 1.4° and 12° respectively.

For the identification of pions and protons the range-fit method, described above for DAPHNE, is adapted to the MIDAS geometry. Protons are identified with a pion contamination smaller than 3%. The proton kinetic energy can be obtained with a resolution of about 6 MeV at 105 MeV.

2.4.3 The Čerenkov detector

The electromagnetic background contribution to the hadronic processes under study in the GDH experiment is forwardly peaked. As a consequence any detector meant to detect particles at forward angles is subject to a lot of background. To deal with this the threshold-Čerenkov detector was designed and built by our Gent group. Above Čerenkov threshold, it has an efficiency of 99.99% for the detection of electrons and positrons. When placed in anti-coincidence with the triggers of the other detectors it removes a large amount of background. The design and the properties of the Čerenkov detector are

extensively described in [82].

When the velocity of a charged particle travelling through a material exceeds the velocity of light in that material, Čerenkov light is emitted. The direction under which this light is emitted depends on the particle's velocity and on the refractive index $n_{\text{r.i.}}$ of the material. The latter determines the speed of light in the material and hence also the minimum velocity at which the particle should travel for the Čerenkov effect to occur. When translating this velocity to the energy of the particle, the Čerenkov threshold energy for a particle with rest mass m_0 is given by:

$$E_{\text{Č-threshold}} = m_0 c^2 \sqrt{\frac{n_{\text{r.i.}}^2}{n_{\text{r.i.}}^2 - 1}} \tag{2.31}$$

It is clear that lighter particles have a lower threshold for Čerenkov radiation.

The choice of the radiator material used in the Čerenkov detector is dictated by the fact that electrons should be detected but hadronic particles should not. The lightest hadronic particle one is dealing with in the GDH experiment at MAMI is the pion. With a maximum photon beam of 800 MeV, the produced pions will have a maximum energy of about 700 MeV. The demand on the Čerenkov radiator is thus to have a threshold for pions larger than 700 MeV such that only electrons are detected. As amply discussed in [82] the final choice was to use a 5 cm thick *aerogel* radiator of ($45 \times 45 \times 5$ cm^3). Aerogel has a Č-threshold of 3 MeV for electrons and 810 MeV for pions. The detector volume is regularly flushed with N_2 gas and kept under a continuous nitrogen flow during measurements in order to avoid impurities (oxygen, water) in the detector interior. The nitrogen also acts as an extra radiator, with a Č-threshold of 21 MeV for electrons and 5.7 GeV for pions.

Figure 2.26 gives a schematic side view of the Čerenkov detector. The radiator is mounted at the front of the detector. The inner volume is filled with N_2 gas. A large ellipsoidally shaped mirror focusses the produced Čerenkov light onto the photomultiplier tube at the top. A reflective cone, or *funnel* is attached in front of the photomultiplier to increase the focussing at its entrance surface.

In this way the Čerenkov detector reaches the required efficiency of 99.99% for the detection of electrons and positrons. This number is not unnecessarily large as it is the minimum value necessary to reduce the electromagnetic background level to 10% of the number of hadronic events, which is acceptable.

2.4.4 The STAR and the FFW detector

The combination of the *Scintillator from Tübingen for Angular Reconstruction*, or STAR detector for short, and the *Far Forward Wall*, or FFW, is placed at the end of the GDH detector setup. They have been designed to cover the very forward $2^\circ < \theta < 5^\circ$ angular region [48, 111].

The STAR detector consists of a large square scintillator sheet with a photomultiplier tube at each corner. It serves as a trigger plate for charged particles.

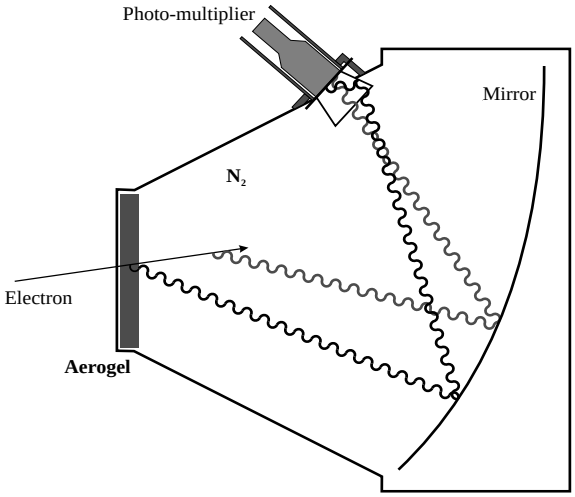

Figure 2.26: Schematic side view of the Čerenkov detector.

It is followed by an array of nine segmented concentric scintillator rings from which information on the polar angle of the charged particle can be obtained.

A similar trigger plate as for STAR is implemented in the FFW detector. It is followed by a scintillator-lead sandwich which acts as a shower detector for photons stemming from π^0 decay.

Unfortunately, during the GDH experiment at MAMI, the STAR and the FFW were not correctly functioning. As a consequence the data taken with these detectors have not been used in the analysis. The encountered problems are discussed in detail in [82].

2.5 The data acquisition

The signals recorded by the different detectors during the experiment need to be registered. A prerequisite for the used data acquisition system is that data can be obtained and stored at a high speed. To this end the data acquisition programme ACQU was designed specifically for the GDH experiment [4]. The raw signals from the detector electronics are acquired by a VME computer and transferred to a fast Linux PC where the data can be checked online. The data are finally saved on Exabyte data tape.

To allow a high acquisition speed it is also important to restrict the amount of background events as much as possible by electronics, that is before storing any data. This can be done by applying appropriate triggers for event definition to the various detectors. Each detector trigger is placed in coincidence with the tagger such that the corresponding photon energy is known for each detected event.

DAPHNE has two main types of triggers: one for charged particles and

one for neutral particles. Any charged DAPHNE trigger requires a signal in the thin A-layer. Additional threshold conditions on the sum of A- and B-layer and on C-layer signals are used to suppress a large part of the electron background. For a neutral trigger one demands that there was no signal at all in the wire chambers nor in the A-layer.

As mentioned before, a MIDAS trigger is either a Q_1-Q_2 or a Q_1-Q_2-Q_3 coincidence to select low energy protons, and pions and high energy protons respectively, removing a large amount of electron background.

The Čerenkov detector signal is placed in anti-coincidence with all detector triggers to suppress electromagnetic background in the forward direction.

During data-taking, a mean overall live time of about 84% was obtained.

3

Calibration analysis of $\gamma p \rightarrow p\pi^+\pi^-$ and $\gamma p \rightarrow n\pi^+\pi^0$

3.1 Introduction

In 1997, in the preparation phase of the GDH experiment at MAMI, a test measurement with unpolarised beam and liquid-hydrogen target was performed. Its purpose was the calibration of the complete detector setup.

The DAPHNE detector had been unused for several years. The performance of some of its components had deteriorated with age. One example is the attenuation length of the scintillator material, i.e. the path length of the produced light after which its intensity has dropped to $1/e$ of its initial value. This attenuation length had decreased over the years. Additionally some of the wires and strips of the wire chambers had become defective, some cable connections were destroyed, ... A full calibration of DAPHNE, including each of these features, was therefore required before carrying out the GDH experiment. The forward detectors were new and also had to be tested thoroughly.

From this unpolarised measurement the total photoabsorption cross section and the single and double pion photoproduction cross sections can be obtained. The majority of these are known from previous DAPHNE measurements and other experiments. They can thus serve as a reference to test the detector and the analysis. For this analysis, the existing programme *daphne* has been adapted to take into account the full new setup. The objective of the calibration analysis is threefold:

- ➢ To verify our control over the new detector setup and to check the analysis programme and procedures by comparing the results with existing data.
- ➢ To improve the particle identification methods and the detection efficiencies in order to minimise both the statistical and systematical errors.
- ➢ To obtain a reliable analysis procedure that is immediately portable to the doubly polarised data.

In this thesis, two double pion photoproduction channels are studied in detail: γp $\rightarrow$ p$\pi^+\pi^-$ and γp $\rightarrow$ n$\pi^+\pi^0$. Results for these channels from the DAPHNE-92 measurement were published in 1995 [22]. The larger part of the events selected for the discussed reaction channels are detected by DAPHNE. For the first time events from MIDAS are added to improve the acceptance in the forward direction. Due to the technical problems with the STAR detector and the FFW detector (cfr. Section 2.4.4, p. 52), it was not possible to include events detected by these forward detectors.

The total integrated cross section for a specific photo-induced reaction σ_{R} is written as:

$$\sigma_{\mathrm{R}}(E_\gamma) = \frac{N_{\mathrm{R}}(E_\gamma)}{\mathcal{L}(E_\gamma)}, \tag{3.1}$$

with $N_{\mathrm{R}}(E_\gamma)$ the number of reaction events corresponding with a photon energy E_γ and $\mathcal{L}(E_\gamma)$ the *integrated luminosity* of the reaction.

After introducing some notations and common conditions in Section 3.2, the calculation of the integrated luminosity is discussed in Section 3.3. A treatment of random events is required (Section 3.4) as well as a precise knowledge of the statistical and systematical uncertainty of the results (Section 3.5). The detection and identification efficiencies are obtained by means of a GEANT simulation (Section 3.6). The reaction specific selection mechanisms and results are presented in Sections 3.7 and 3.8 for the γp $\rightarrow$ p$\pi^+\pi^-$ and γp $\rightarrow$ n$\pi^+\pi^0$ channels, respectively.

3.2 Notations and common conditions

An event in DAPHNE is mainly characterised by two counters. The first one is the number of charged tracks reconstructed by the wire chambers and is denoted as n_{MWPC}. Each event set is globally corrected for the corresponding wire chamber inefficiency. The second counter gives the number of good charged scintillator tracks n_{scint}. A good charged scintillator track has a hit in the A-layer —a thin layer giving a charged trigger— and can be coupled with a wire chamber track in front of the hit scintillator sector ($n_{\mathrm{scint}} \leq n_{\mathrm{MWPC}}$).

The number of neutral tracks is denoted as n_{neutral}. A general neutral track is a scintillator track with no hit in the A-layer and no wire chamber track in front of the hit sector.

For events detected in MIDAS, the counter n_{MIDAS} describes the number of well reconstructed tracks in MIDAS. There is a global correction factor of $1/0.65$ that accounts for the reconstruction inefficiency and geometrical imperfections.

There is a number of common conditions applied to each detected track, regardless of the reaction-specific selection method.

In order to cleanly define the angular acceptance, the condition

$$23^\circ < \theta_i < 158^\circ$$

is imposed on the **polar angle** of each wire chamber trajectory i with $i = 1, \ldots, n_{\text{MWPC}}$. The limits slightly differ from the geometrical DAPHNE limits to eliminate tracks that hit the MIDAS detector.

The emission angle θ_{MIDAS} for MIDAS tracks is delimited by:

$$5^\circ < \theta_{\text{MIDAS}} < 15^\circ.$$

As explained in Section 2.4.1.5 (p. 48) the DAPHNE **azimuthal angle** ϕ_i ($i = 1, \ldots, n_{\text{MWPC}}$) is also limited by software, in order to avoid events entering a mechanical hole between scintillator sectors. Depending on the number of demanded scintillator tracks, a global correction factor is applied to each data set to correct for these losses.

A final common condition for charged tracks is related to the effective target length correction (see also Section 2.4.1.5, p. 48). This correction is exactly calculated for events originating from the target and entering the defined **control cylinder** (centred around the beam axis, radius 40 mm and length 212 mm). For this correction to be applied correctly the events are limited by software to this control cylinder. The weight defined in Equation (2.30) (p. 50, with d_{target} as defined below, appropriately introduces the correction.

3.3 Calculation of the integrated luminosity

The integrated luminosity in an experiment is determined by the used equipment and is needed to normalise the number of reaction events, i.e. the conversion to a cross section via (3.1). It is defined as:

$$\mathcal{L}(E_\gamma) = N_\gamma(E_\gamma) n_{\text{target}} d_{\text{target}},$$

with $N_\gamma(E_\gamma)$ the number of incoming photons with energy E_γ, n_{target} the number of target nucleons per unit volume and d_{target} the target thickness.

The number of photons N_γ impinging on the target is obtained from the pair detector information as described in Section 2.2.2 (p. 27). With the aid of the calibrated pair detector efficiency, the number of tagged photons, corresponding with each tagger channel, and thus with each photon energy E_γ, is calculated.

The amount of target protons per unit volume can be written as $n_{\text{target}} = \frac{\rho N_{\text{A}}}{A} Z$ with ρ the material density, N_{A} Avogadro's number and A and Z the atomic mass and the atomic number of the material respectively. For the liquid-H_2 target as used in the unpolarised measurement, $\rho = 0.0708$ g/cm^3, $A = 1.00794$ g/mol, $Z = 1$ and thus $n_{\text{target}} = 4.23\ 10^{22}$ cm^{-3}.

The target thickness d_{target} is determined by the actual size of the target cell along the beam axis. The physical limits in the z direction of the liquid-H_2 target are [-153 mm, 43 mm]. However, software limits are set in the

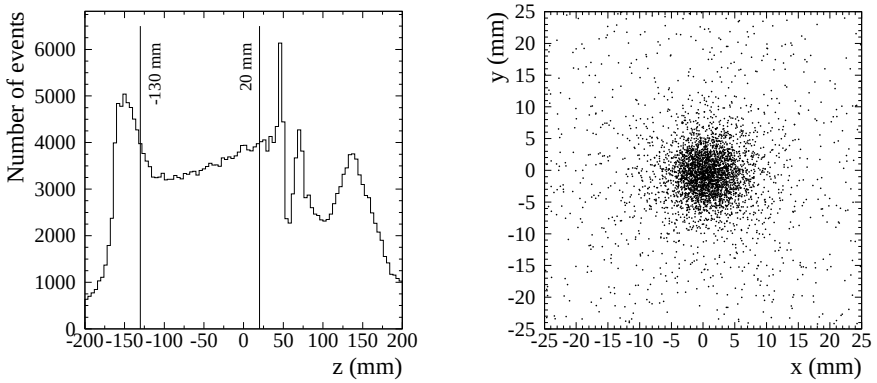

(a) (b)

Figure 3.1: (a) Reconstructed z vertex position. The vertical lines represent condition (3.2), (b) Reconstructed x-y plane.

analysis to avoid events coming from the walls of the cell such that no *empty target subtraction* needs to be performed. This is done by placing a condition on the vertex reconstructed by the wire chambers. Since the largest error on the reconstructed z for charged particles in the wire chambers is about 1.5 cm (see Section 2.4.1.2, p. 38), a safety zone of this order of magnitude needs to be taken into account to ensure that no background events originating from the wall material are accepted. Therefore the condition:

$$-130 \text{ mm} \leq z \leq 20 \text{ mm} \tag{3.2}$$

is set for the reconstructed z vertex position of each selected event. One has then for the thickness $d_{\text{target}} = 15$ cm.

The histogram in Figure 3.1(a) shows the event yield at different reconstructed vertices along the beam axis. Outside the range given by (3.2) there are peaks corresponding to the target walls and the frame of the MIDAS detector further downstream. As an illustration the reconstructed x-y plane is shown in Figure 3.1(b). Due to the low beam dispersion the diameter of the beam spot is much smaller than the 43 mm diameter of the target.

3.4 Random subtraction

Each detector trigger is placed in coincidence with the tagger to relate the event with the energy of the photon that induced the reaction. TDC-modules (Time to Digital Converter) register the relative time difference between a detector event and a tagger event. A typical TDC-spectrum for a coincidence between one tagger channel and the detector trigger is shown in Figure 3.2. By placing a time window the *prompt peak*, which contains the well correlated

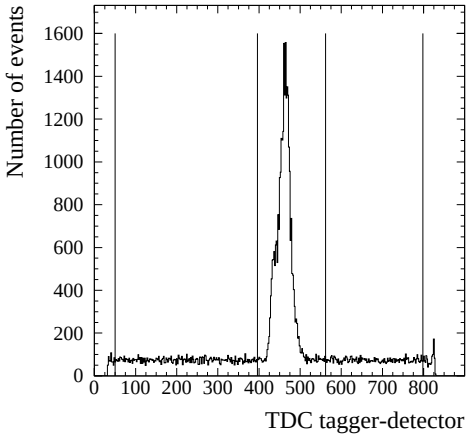

Figure 3.2: TDC-spectrum for the coincidence of one tagger channel and the detector trigger. The lines indicate the time window used in the random subtraction procedure.

events, is selected together with some random background. Random events with a TDC value outside the time window are normalised to the width of the time window and subtracted.

For each detector event, multiple hits in the tagger are possible. There are two types of such events:

- A single electron that produced a bremsstrahlung photon enters the tagger and by multiple scattering or Møller scattering, more than one focal plane detector is hit.
- One or more random electrons and possibly a 'good' electron enter the tagger within a time interval.

The first type is straightforwardly recognised by the fact that the hit tagger channels are adjacent. When taking each of these hits into account as different hadronic events —and also count each of them in the number of incoming photons— the normalisation would be correct. However, the energy behaviour of the cross section would slightly deviate from the true one. Moreover, the statistical error would be overestimated. Therefore only the 'first' —corresponding with the lowest photon energy— of the adjacent channels is taken and a correction is applied to the number of incoming photons to account for the events excluded in the analysis. This correction is obtained by dividing for each tagger channel the number of tagger counts after suppressing the adjacent hits by the number of counts without suppressing adjacent channels.

The second type of multiple hits are the 'true' random events and are treated by the random subtraction as described above, in case they are not

Tagger channel	E_γ (MeV)	E_γ bin (MeV)
1	792.689	1.131
2	791.534	1.179
3	790.331	1.227
4	789.080	1.275
5	787.781	1.323
6	786.433	1.373
7	785.034	1.424
8	783.585	1.475
9	782.085	1.523
10	780.538	1.571

Table 3.1: The first ten tagger channels with corresponding photon energies and photon energy bin widths, for a setting with an 855 MeV primary electron beam.

adjacent. The probability for true random coincidences to hit adjacent tagger channels, which need to be treated as the first type of multiple hits, is negligible.

3.5 Presentation of the data and precision calculation

3.5.1 Converting tagger channels to photon energies

In order to present the data as a function of photon energy it is necessary to convert the tagger channel numbers to photon energies. The tagger channels are calibrated in energy; with each channel, a specific photon energy bin of a specific width is associated. Table 3.1 lists the first ten tagger channels with their corresponding photon energies and bin widths for an 855 MeV primary beam setting. The energy bin width is not constant and as a consequence one cannot convert a tagger channel spectrum to a photon energy spectrum with equally sized bins via a simple one-to-one relation. Possibilities to cope with this include the randomisation the one-to-one photon energy into the photon energy bin and grouping several bins into one large photon energy bin. In this work another method is used, named the *bin-overlap method*. It is illustrated in Figure 3.3. The idea is to redistribute each event corresponding with a tagger channel, over those photon energy bins with which the tagger channel bin overlaps. Each event has a weight f_i ($i = 1, \ldots, n$) in the corresponding photon energy bins, with n the number of photon energy bins with which one tagger channel bin overlaps. The weights are obtained by dividing the width of the overlap region by the width of the full tagger channel bin. It evidently holds that:

$$\sum_{i=1}^{n} f_i = 1,$$

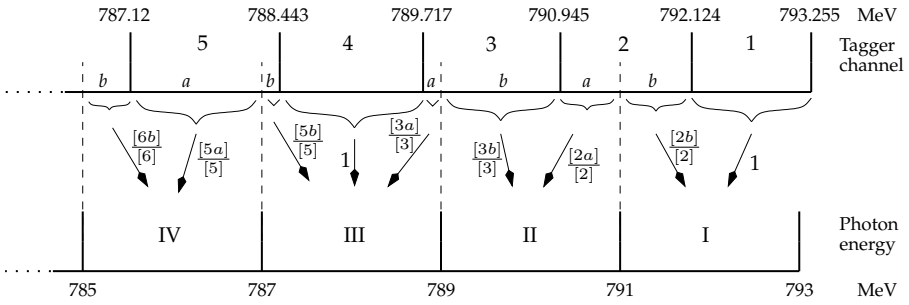

Figure 3.3: Illustration of the *bin-overlap method*. The upper scale shows the tagger channel bins whereas the lower scale shows the chosen equally sized photon energy bins. The arrows carry the weights given to the event in the photon energy bins. The quantities in square brackets represent the width of the labeled regions (see text).

for each tagger channel. All data presented here are treated with the bin-overlap method.

3.5.2 Statistical precision

For each presented data point, the number of acquired events is large enough to allow a Gaussian precision calculation. For a measured number of events N, the error is taken as:

$$\sigma_N = \sqrt{N}.$$

This poses no problem to the events stored with the bin-overlap method since the full weight of one event is simply distributed over different bins, with appropriate weights.

Weights that are assigned on an event-to-event basis and global correction factors such as the effective target length correction, the corrections for detection inefficiencies etc., need to be taken into account differently, since they do not enhance the statistics but merely influence the absolute value of the result. If these weights are globally represented by f, one has for the error on the final result $x = fN$:

$$\sigma_x = f\sqrt{N}.$$

3.5.3 Systematical errors

The systematical errors on the data are inherent to the experimental apparatus. An error that is common to each analysis is the error on the measurement of the integrated luminosity. It slightly depends on the photon energy but is overall taken to be 2% as a safe upper limit.

To the particle identification obtained with the range-fit or geometrical range method, a systematical error on the result of maximum 2% is assigned.

Other systematical errors related to reaction identification, simulated efficiencies and background are specific to the different studied reaction channels and, if required, they will be commented upon for each result separately.

As a rule, only statistical errors will be shown when cross sections are presented while the systematical errors are mentioned in the text.

3.6 GEANT simulation

Although quite large, the detection efficiencies and the acceptance of the detectors in the GDH experiment are not 100%. With the aid of a GEANT ('GEometry ANd Tracking') simulation the number of lost events can be estimated [26].

The geometry of the components of each detector and of the target is included in the simulation programme. An interface that translates the simulated detector response to the corresponding variables in the *daphne* analysis programme allows to simply port the event analysis between the two programmes.

The default GEANT routines that generate hadronic interactions (nucleon-nucleus, nucleon-nucleon, pion-nucleon, ...) are well suited for high energy multi-hadron showers. However, below energies of a few GeV they are not sufficiently accurate. As the physics investigated with DAPHNE is exactly in this low and intermediate energy range, a modification of the standard GEANT hadronic interaction generation was mandatory [106]. This was done by integrating the *HADRIN* and *NUCRIN* routines in GEANT. These routines simulate the inelastic hadron-nucleon and the inelastic hadron-nucleus interactions at energies below 5 GeV respectively [61, 62, 63].

Several event generators are implemented for single and double pion photoproduction. Both for the $\gamma p \rightarrow n\pi^+$ and $\gamma p \rightarrow p\pi^0$ reaction channels, angular distributions from the Landolt-Börnstein parametrisation [55], the HDT model [64] and the SAID calculation [9] are incorporated. The double pion channels are generated uniformly over phase space, using the *GENBOD* routine from the CERN library [30].

As an illustration Figure 3.4 shows the example of a $\Delta E - E$ plot for stop-B protons and pions as generated by the simulation. This plot can be compared with the experimental one (Figure 2.19(b), p. 42). The cuts used for particle identification are also drawn. In this way one can simulate the identification methods and determine the efficiency with which this identification is done.

3.7 $\gamma p \rightarrow p\pi^+\pi^-$

The $\gamma p \rightarrow p\pi^+\pi^-$ channel has three charged particles in the final state. DAPHNE has a high detection and identification efficiency for non-neutral particles which makes it ideally suited for the study of this channel. The only drawback is the limited acceptance of the detector in the forward direction, which

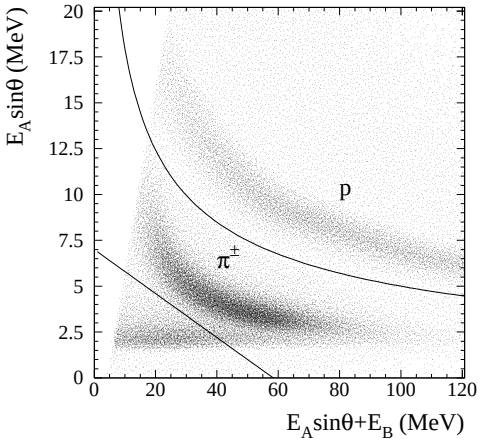

Figure 3.4: Simulated $\Delta E - E$ plot for stop-B protons and pions.

encompasses a non-negligible fraction of the cross section. These losses are simulated with GEANT to reconstruct the full 4π cross section.

The total cross section for this pion photoproduction channel from the DAPHNE-92 measurement has been published in 1995 [22]. As outlined in the introduction of this chapter, the aim here is to cross-check this result with the present analysis procedure and to improve where possible the global efficiency and uncertainty on the results for this channel. The analysis is also developed in such a way that it is immediately applicable to the butanol data.

Kinematically, there are three types of $p\pi^+\pi^-$ events from the point of view of DAPHNE. They are classified in terms of the number of charged particles inside the acceptance, ranging from one to three. We define 'inside the acceptance' for the charged particles here as 'polar angle between 23° and 158° and a reconstructed wire chamber track'. A simple simulation helps to obtain a quantitative idea of the relative contributions of the *three-charged*, *two-charged* and *one-charged* yields to the full 4π cross section. With the *GENBOD* routine from the CERN libraries, $p\pi^+\pi^-$ events for a range of incident photon energies are generated. With a check on the particle emission angles ($23^\circ < \theta < 158^\circ$), the accepted fraction for each type of event is obtained. The result is plotted in Figure 3.5. The three- and two-charged yields are the largest contributors, whereas the one-charged events gain importance near the threshold. As the simulation is performed with a phase space generator, this result evidently remains an approximation. It allows however to estimate the relative importance of the event types.

The analysis procedure is as follows. In a first step the partial cross sections for each type of event is determined: the 'three-charged', 'two-charged' and 'one-charged' cross section. For the three cases, a specific selection mech-

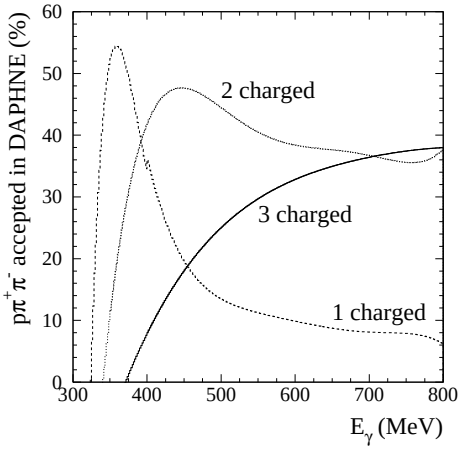

Figure 3.5: $\gamma p \rightarrow p\pi^+\pi^-$: Simulated fraction of events that are accepted by DAPHNE as three-charged, two-charged and one-charged events.

anism is developed. This yields the event sets $N_{3ch}^{p\pi^+\pi^-}$, $N_{2ch}^{p\pi^+\pi^-}$ and $N_{1ch}^{p\pi^+\pi^-}$, respectively. Each selection mechanism has its global (i.e. not event-per-event) identification efficiency. For each event type, the selected event set is corrected for this efficiency. Also the corrections for the wire chamber efficiency, the mechanical holes in azimuthal angle and the effective target length are applied. In this way, the three cross sections are obtained: $\sigma_{3ch}^{p\pi^+\pi^-}$, $\sigma_{2ch}^{p\pi^+\pi^-}$ and $\sigma_{1ch}^{p\pi^+\pi^-}$. In the following Sections 3.7.1, 3.7.2 and 3.7.3, these partial cross sections are treated.

The next step in the analysis procedure is to reconstruct the full $p\pi^+\pi^-$ cross section by extrapolating the measured yield inside the DAPHNE acceptance to 4π. To this end an extrapolation function, or acceptance function ϵ_{expol} is determined by simulation. This function brings into account those events that were not inside the DAPHNE acceptance. Then one obtains the total cross section $\sigma_{4\pi}^{p\pi^+\pi^-}$ starting from the sum of the measured cross sections as follows:

$$\sigma_{4\pi}^{p\pi^+\pi^-} = \frac{\sigma_{3ch}^{p\pi^+\pi^-} + \sigma_{2ch}^{p\pi^+\pi^-} + \sigma_{1ch}^{p\pi^+\pi^-}}{\epsilon_{expol}}.$$

This acceptance function and the extrapolation to the full cross section is discussed in Section 3.7.4

3.7.1 $\gamma p \rightarrow p\pi^+\pi^-$: three charged particles in DAPHNE acceptance

3.7.1.1 Event selection procedure

Four out of six 'active' pion photoproduction channels in the photon energy range up to 800 MeV can have three charged particles in the final state. Apart from the studied $p\pi^+\pi^-$ channels these are $p\pi^0$, $p\pi^0\pi^0$ and $n\pi^+\pi^0$. The π^0 namely has a 1.2% branching ratio for the decay into $e^+e^-\gamma$ instead of into two photons. Moreover a π^0 decay photon may produce an e^+e^- pair before entering DAPHNE ($\pm 1.5\%$ probability). This small percentage yields a non-negligible background to the mentioned channels. Therefore the demand for three charged tracks inside DAPHNE is not sufficient to identify a $p\pi^+\pi^-$ event. Therefore, the selection procedure is extended as follows:

- $n_{\text{MWPC}} = 3$: three charged tracks reconstructed in the wire chambers,
- $n_{\text{scint}} \geq 1$: at least one scintillator track,
- one proton is identified,
- $m_X > 280$ MeV: the missing mass is above limit for double pion production.

Evidently, each of these conditions has to be fulfilled. The weak restriction for n_{scint} is sufficient since at most one particle is identified. For non-identified particles it is of no importance whether they cleanly entered the scintillators or not. The importance of this weak condition is that the necessary azimuthal correction factor is only $1/0.84 = 1.19$. This is considerably smaller than the $1/0.59 = 1.7$ to be used in the case that three scintillator tracks would be demanded. Statistics is largely improved by this feature.

The proton is identified with the range-fit method. The range-fit method also provides the initial kinetic energy of the proton. This information is combined with the known incoming photon energy and the polar angle of the proton supplied by the wire chambers to yield the mass of the non-detected system X, i.e. the *missing mass* m_X. A typical two-dimensional plot of this missing mass versus photon energy and its one-dimensional projection are shown in Figure 3.6. The single pion zone ($p\pi^0$) with m_X around the π^0 mass is well separated from the double pion zone with a missing mass higher than twice the pion mass. The width of the single pion peak is mainly due to the range-fit resolution. The double pion zone is quite broad owing to the increasing relative kinetic energy of the two pions with rising photon energy.

By setting the condition $m_X > 280$ MeV the single pion contribution from $p\pi^0$ is suppressed. Figure 3.7 illustrates this. The uncorrected yield of events that satisfy all the above conditions except for the missing mass requirement is shown in Figure 3.7(a). The single pion contribution is obvious in the Δ region (below the double pion threshold). After application of the missing mass cut, the yield in Figure 3.7(b) is obtained. This result is clearly freed from single pion background.

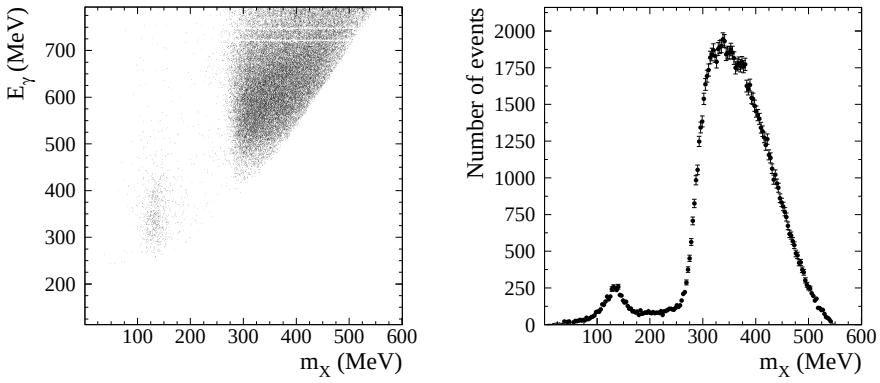

(a) (b)

Figure 3.6: $\gamma p \rightarrow p\pi^+\pi^-$ three-charged: (a) Missing mass versus incoming photon energy, (b) Missing mass spectrum for a detected proton.

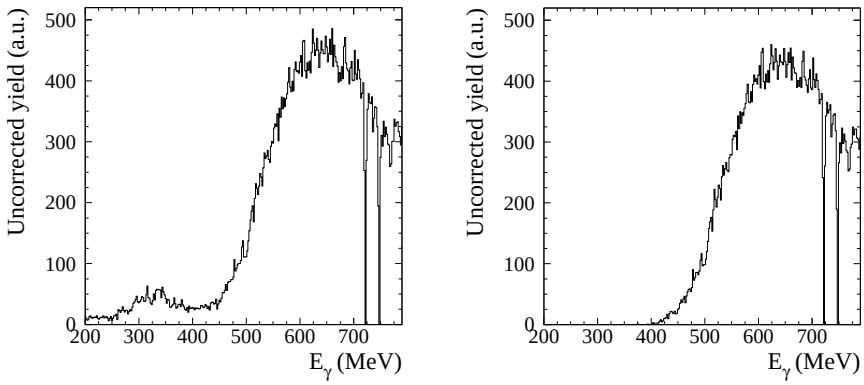

(a) (b)

Figure 3.7: $\gamma p \rightarrow p\pi^+\pi^-$ three-charged: (a) Uncorrected yield before the missing mass cut, (b) Uncorrected yield after the missing mass cut.

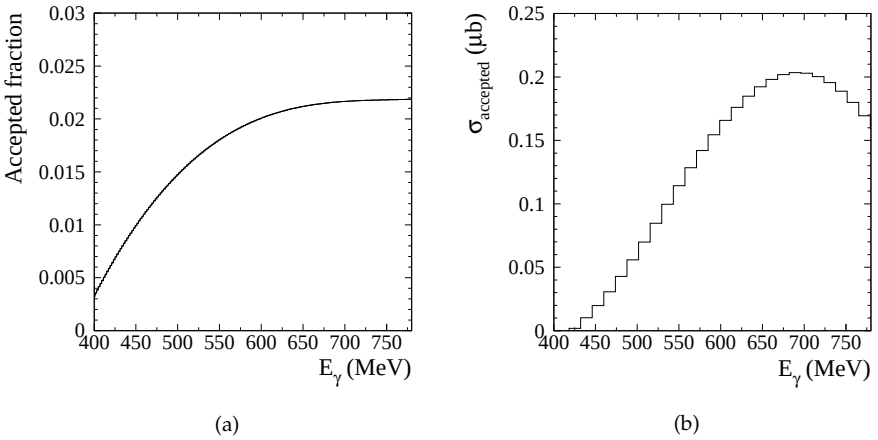

Figure 3.8: $\gamma p \rightarrow p\pi^+\pi^-$ three-charged: (a) Simulated fraction of $p\pi^0\pi^0$ events that are accepted by the $p\pi^+\pi^-$ selection conditions, (b) Simulated background contribution of the $p\pi^0\pi^0$ cross section to $p\pi^+\pi^-$.

The threshold value of 280 MeV is chosen rather high to minimise the background contribution. The good events that are lost in this way are retrieved by simulation. The effect is of the order of 2%.

Events from $n\pi^+\pi^0$ are almost completely suppressed by the identification of the proton. The small fraction of events with a pion misidentified as a proton by the range-fit method does not survive the missing mass cut.

At this point the only background that remains stems from the $p\pi^0\pi^0$ channel which may also satisfy all the above conditions since the proton is accompanied by two pions. Its effect is simulated with GEANT by generating $p\pi^0\pi^0$ events and applying the selection conditions to them. Figure 3.8(a) shows the resulting percentage of the $p\pi^0\pi^0$ cross section that is mistaken as originating from $p\pi^+\pi^-$. Figure 3.8(b) is obtained by multiplying this fraction with the total $p\pi^0\pi^0$ cross section [22, 119]. The plot illustrates that the maximum background contribution is about 0.2 μb which is less than 1% of the three-charged $p\pi^+\pi^-$ cross section. These numbers are small enough so that this background can be neglected.

3.7.1.2 Cross section

The analysis as described above is repeated for $p\pi^+\pi^-$ events generated in the GEANT simulation. The ratio of accepted events over generated ones provides the global efficiency of the analysis method and can be used to correct for the good events that are lost. Figure 3.9(a) shows the simulated efficiency curve. It comprises losses due to the following effects:

- Range-fit identification efficiency and momentum threshold for the pro-

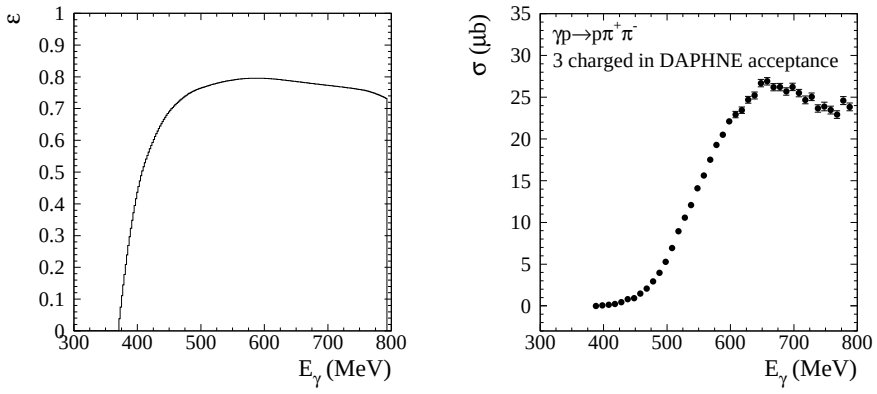

(a) (b)

Figure 3.9: $\gamma\mathrm{p} \rightarrow \mathrm{p}\pi^+\pi^-$ three-charged: (a) Simulated identification efficiency, (b) Cross section.

ton,

- ➢ Stop-A identification efficiency and momentum threshold for the proton,
- ➢ The missing mass cut.

It does not contain the loss of particles before reaching the wire chambers; this effect will be taken into account when extrapolating to the full 4π cross section.

At threshold there is a sharp rise in the efficiency with photon energy. At these energies most protons are stopped in the A-layer and need to deposit at least 15 MeV to be identified. Above 600 MeV the efficiency slightly decreases. This is mainly due to the fact that protons start to have enough energy to leave the detector in which case they can not be identified.

The cross section for $\gamma\mathrm{p} \rightarrow \mathrm{p}\pi^+\pi^-$ with the three final state particles in the DAPHNE acceptance is shown in Figure 3.9(b). It exhibits a broad peak at about 650 MeV. Statistical errors are drawn. The systematical error is about 3%, which is a combination of the range-fit identification uncertainty and the systematical error on the luminosity.

Combining all available kinematical information —the incoming photon energy, the azimuthal and polar emission angles of all three produced particles and the kinetic energy of the proton— the invariant mass of the two pions or of the proton and one of the pions can be calculated. This allows to obtain the invariant mass distributions $\mathrm{d}\sigma/\mathrm{d}W_{\pi^+\pi^-}$ and $\mathrm{d}\sigma/\mathrm{d}W_{\pi^\pm\mathrm{p}}$. Since no distinction between the π^+ and the π^- is possible, the latter will be a superposition of $\mathrm{d}\sigma/\mathrm{d}W_{\pi^+\mathrm{p}}$ and $\mathrm{d}\sigma/\mathrm{d}W_{\pi^-\mathrm{p}}$. The pion-pion and the pion-proton invariant mass spectra at different photon energies are shown in Figure 3.10

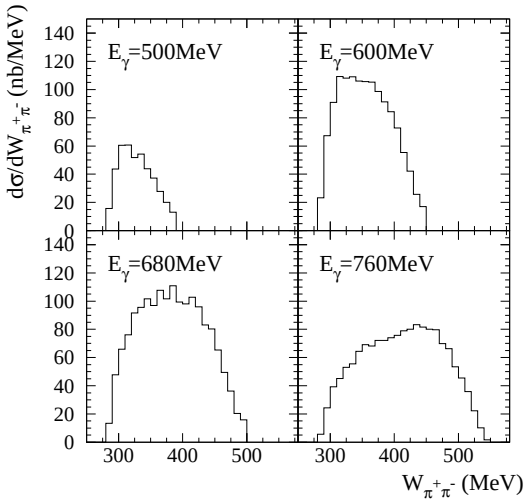

Figure 3.10: $\gamma p \rightarrow p\pi^+\pi^-$ three-charged: Pion-pion invariant mass spectra at $E_\gamma = 500$, 600, 680 and 760 MeV.

and Figure 3.11, respectively. The former principally exhibit a phase space behaviour, which points to the uncorrelated emission of the two pions. At sufficiently high photon energy, the pion-proton invariant mass distribution has a broad peak around 1232 MeV, the Δ mass. In Chapter 7 it is shown that the $p\pi^+\pi^-$ reaction is governed by the $\gamma p \rightarrow \pi^-\Delta^{++} \rightarrow \pi^-\pi^+p$ mechanism, which explains the peak at 1232 MeV in the π^+p distribution. The less dominant mechanism $\gamma p \rightarrow \pi^+\Delta^0 \rightarrow \pi^+\pi^-p$ gives rise to a peak at the Δ mass in the π^-p distribution. Due to the fact that we have access only to the superposition of the two distributions, these effects are slightly masked.

3.7.2 $\gamma p \rightarrow p\pi^+\pi^-$: two charged particles in DAPHNE acceptance

When DAPHNE detects a pair of charged particles from the proton target, it can be either one of the following types:

$$(p, \pi^\pm), \quad (\pi^\pm, \pi^\mp), \quad (p, e^\pm), \quad (\pi^\pm, e^\pm), \quad (e^\pm, e^\mp).$$

The first two stem from $\gamma p \rightarrow p\pi^+\pi^-$, the other kinds of events are background from $p\pi^0$, $n\pi^+$, $p\pi^0\pi^0$ or $n\pi^+\pi^0$. For processes in which a π^0 is involved, the origin of the extra charged particles is again the decay of the π^0 into an $e^+e^-\gamma$ state or pair production by one of its decay photons before reaching the wire chambers. The $n\pi^+$ reaction gives rise to a non-negligible amount of events with two charged chamber tracks due to hadronic interactions of the pions in the target.

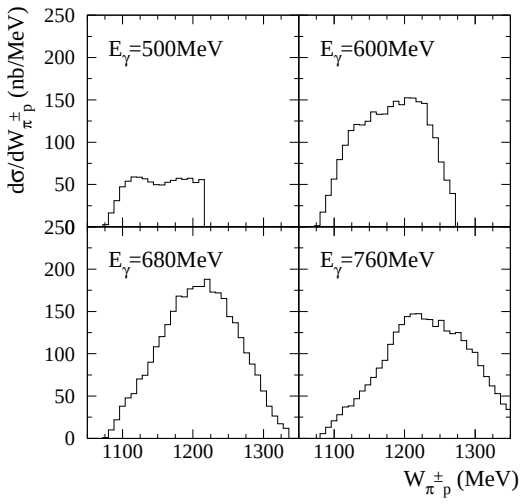

Figure 3.11: $\gamma p \rightarrow p\pi^+\pi^-$ three-charged: Pion-nucleon invariant mass spectra at $E_\gamma = 500$, 600, 680 and 760 MeV.

Two procedures have been developed for this channel. The first one has a *direct selection* method, an event set with a low background level is explicitly selected. In the second method an *indirect selection* is performed. In this case the collection of good $p\pi^+\pi^-$ events is obtained by subtracting identified $p\pi^0$ background —which is the single important one in this method— from the set of all two-charged events.

The importance of studying these two methods is that it allows an internal cross-check of the obtained data and so provides a means to determine the systematical error on the result. As discussed in Chapter 4 this cross-check is even more crucial when analysing the butanol data, where the direct method has a larger uncertainty concerning background subtraction while the second method is less attractive from the statistical point of view.

In the following sections the two selection procedures are subsequently presented before comparing both resulting cross sections.

3.7.2.1 Event selection procedure: direct selection

The following selection procedure yields a clean $p\pi^+\pi^-$ event set with a very low background level:

- $n_{\text{MWPC}} = 2$: two charged tracks reconstructed in the wire chambers,
- $n_{\text{scint}} = 2$: two scintillator tracks,

- ❑ if one proton is identified:
  - → $m_X > 280$ MeV: the missing mass is above the limit for double pion production,

  if no proton is identified:
  - → at least one charged pion is identified,
  - → no electron is identified,
  - → there is no stop-A particle.

Again, all conditions need to be fulfilled. The requirement to have two scintillator tracks suppresses an important amount of events from $n\pi^+$. In the case of hadronic interaction of the pion with a nucleon in the target, there is a high probability that the produced particle reaches the wire chambers, —as does the pion— but is not high enough in energy to attain the scintillator layers. Such an event is characterised by $n_{\text{MWPC}} = 2$, $n_{\text{scint}} = 1$ and can thus be rejected by demanding two scintillator tracks. This implies that the necessary azimuthal correction is rather large, namely $1/0.71 = 1.41$.

In the case that a proton is identified, the procedure is completely analogous to the three-charged case. The missing mass m_X is calculated and events corresponding to a double pion process can thus be selected.

If no proton is identified, the next step is to check whether a charged pion is seen and no electron is present. The range-fit method is applied to identify Stop-B, C, D and E pions. The identification for stop-F pions is done with the geometrical range method. Stop-A particles —if not identified as a proton— are either pions or electrons but the separation of these is not reliable enough for this purpose. Therefore, in order to avoid $(\pi^\pm, e^\pm)$ particle pairs, the condition is set that no electron and no stop-A particle is detected. Electrons are identified with the $\Delta E - E$ (stop-B) and geometrical range method (Stop-C, D, E, F).

By simulating the different possible background channels and the listed selection conditions, the fraction of mistakenly identified events can again be obtained. Multiplying this fraction with the total cross section of the respective reaction channels gives the contribution in microbarn of the background channels to the $p\pi^+\pi^-$ channel. The cross sections used for this purpose are taken from SAID [9] for the $n\pi^+$ and $p\pi^0$ channels and from the analysis in this thesis for the $n\pi^+\pi^0$ channel. The results are plotted in Figure 3.12(a). The $n\pi^+$ and the $n\pi^+\pi^0$ channel contributions are significantly larger than the one from $p\pi^0$. The $p\pi^0\pi^0$ contribution is negligible and is not shown. The larger hadronic interaction cross section for pions explains the larger probability for the first two reactions to produce a two-charged event. These background contributions can be subtracted at the cross section level, before correcting the data for the global identification inefficiency of the selection method. This is done in Figure 3.12(b), the small amount of background visible in the Δ region is adequately subtracted.

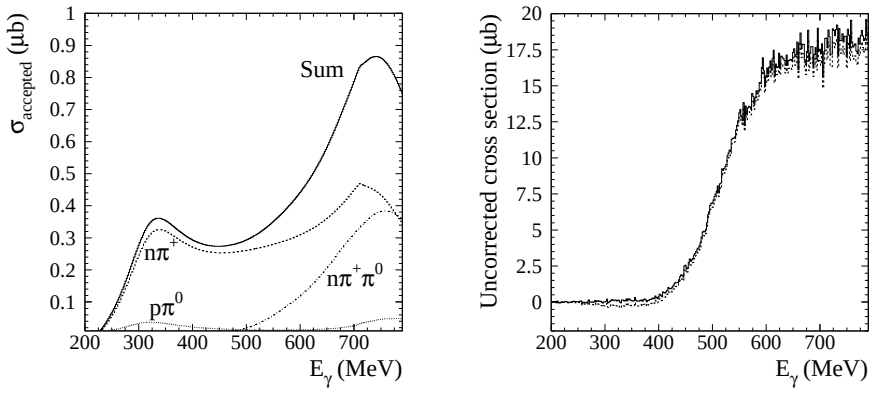

(a) (b)

Figure 3.12: $\gamma p \rightarrow p\pi^+\pi^-$ two-charged, direct selection: (a) Simulated background contribution of $\gamma p \rightarrow p\pi^0$, $n\pi^+$, and $n\pi^+\pi^0$, (b) Uncorrected cross section before and after the background subtraction.

3.7.2.2 Event selection procedure: indirect selection

When using the indirect selection method, two sets of events are selected. The first set contains all two-charged events N_{2ch}. At this level the largest amount of background comes from $p\pi^0$. The second set contains all two-charged events that are identified as a $p\pi^0$ event, $N_{2ch}^{1p,m_X<280\ MeV}$, and is subtracted from the first one. The contribution from other possible background channels, which are relatively less important here, is neglected in this method.

The selection procedure is as follows, the first three conditions are common for both sets, the conditions per set are listed in two separate columns:

- ❑ $n_{MWPC} = 2$: two charged tracks reconstructed in the wire chambers,
- ❑ $n_{scint} = 2$: two scintillator tracks,
- ❑ if no proton is identified there is no stop-A particle present,

N_{2ch}	$N_{2ch}^{1p,m_X<280MeV}$
❑ no electron is identified.	❑ no electron is identified, ❑ one proton is identified, ❑ $m_X < 280$ MeV.

As before, the conditions, per set in this case, must all be fulfilled. The first two conditions have the same motivation as in the direct method. Avoiding events with stop-A particles in the case no proton is detected is done to suppress stop-A electrons which cannot be separated from pions and would not be subtracted in the case no proton is identified. The demand to have no

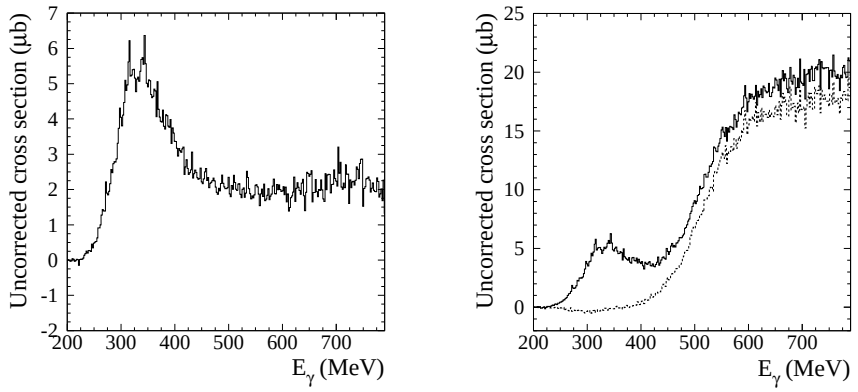

Figure 3.13: $\gamma p \rightarrow p\pi^+\pi^-$ two-charged, indirect selection: (a) Simulated background contribution of $\gamma p \rightarrow p\pi^0$, (b) Uncorrected cross section before and after the background subtraction.

detected electron (i.e. stop-B or further) is also meant to avoid any source of unwanted background. For the $p\pi^0$ event set a proton is identified with the range-fit method and a cut on the calculated mass allows to select single pion events.

The number of $p\pi^+\pi^-$ events is taken to be:

$$N_{\text{2ch}}^{p\pi^+\pi^-} = N_{\text{2ch}} - N_{\text{2ch}}^{\text{1p},m_X<280\text{ MeV}} \left(\epsilon_{\text{p},m_X}^{p\pi^0}\right)^{-1},$$

with $\epsilon_{\text{p},m_X}^{p\pi^0}$ the efficiency to identify a $p\pi^0$ event by detecting a proton and applying the missing mass cut $m_X < 280$ MeV. This efficiency is obtained by simulation.

Figure 3.13(a) shows the second term of this expression, converted to microbarn. Figure 3.13(b) illustrates how subtracting the second term from the first one, in microbarn but uncorrected for any inefficiency specific for the selection mechanism, yields a result freed of single pion contribution.

3.7.2.3 Cross section

The simulated global detection efficiencies for events selected with the above procedures are plotted in Figure 3.14.

The direct selection efficiency contains the following effects:

- Range-fit identification efficiency and momentum threshold for the pions and for the proton,
- Stop-A identification efficiency and momentum threshold for the proton,

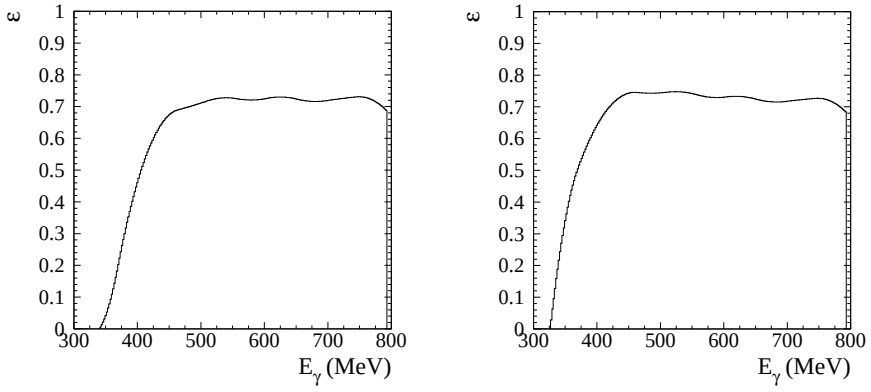

Figure 3.14: γp $\rightarrow$ p$\pi^+\pi^-$ two-charged: (a) Simulated identification efficiency for the direct selection method, (b) Simulated identification efficiency for the indirect selection method.

➢ The missing mass cut in the case of proton detection.

The efficiency for the indirect selection method simply incorporates the losses due to the demand to have a proton identified if there is one or more stop-A particle.

As in the three-charged case, losses that occur before the wire chambers are taken into account only when extrapolating to the full 4π cross section.

In both the direct and the indirect approach, there is a less obvious efficiency decrease above 600 MeV as compared to the efficiency for the three-charged case (Figure 3.9(a)). Events lost due to the fact that protons start to leave DAPHNE at these energies are recovered in the direct method by the pion detection. In the indirect method these protons are simply not lost.

The resulting cross sections for both methods are presented in Figure 3.15. The threshold photon energy for two-charged detection is slightly lower than in the three-charged case, in accordance with Figure 3.5. Apart from this the two-charged cross section is very similar to the three-charged one. The relative agreement between the two selection methods is satisfactory and supports the reliability of the different approaches. The small discrepancies between them are an indication of the systematical errors of both methods. In this way the systematical error is estimated to be about 3%. This is the maximum value of the relative difference as a function of photon energy. It is a combination of the errors inherent to the particle identification —an upper systematical error limit of 2%— and the simulated background subtraction. The latter can thus be estimated to be also of the order of 2%.

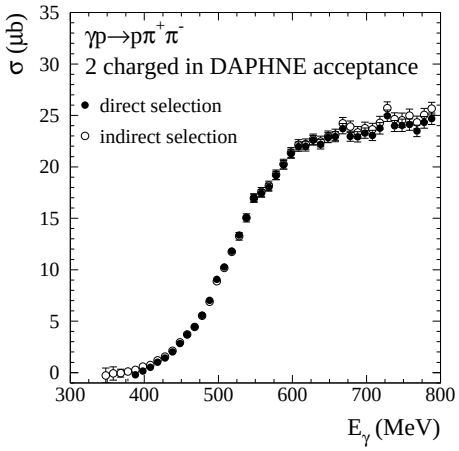

Figure 3.15: $\gamma p \rightarrow p\pi^+\pi^-$ two-charged: Cross section obtained with the direct and the indirect selection method.

3.7.3 $\gamma p \rightarrow p\pi^+\pi^-$: one charged particle in DAPHNE acceptance

All pion photoproduction channels on the proton in the Mainz energy range have at least one charged particle in the final state. As a consequence a one-charged trigger is very inappropriate to select $p\pi^+\pi^-$ events. However, with the aid of the MIDAS detector, part of these events can be accessed. At present, the basic MIDAS study, concerning e.g. the track reconstruction, the particle identification and the effective target correction by the Pavia group is still ongoing [104, 23]. As a consequence the analysis here is also still preliminary. It illustrates nevertheless the possibilities of using the MIDAS detector to increase the angular acceptance of the setup.

From Figure 3.5 it is clear that events with one charged particle in DAPHNE are mostly found below 450 MeV. This is very close to threshold, where the cross section is quite low, and so the one-charged events represent a relatively small contribution to the total $p\pi^+\pi^-$ cross section. Figure 3.16(a) shows that fraction of the one-charged events when the proton or one of the pions, respectively enters the DAPHNE acceptance. The fraction of these last events which have at least one of the other particles inside the MIDAS acceptance is given in Figure 3.16(b). This means that of all one-charged $p\pi^+\pi^-$ events which coincide with an event in MIDAS, about 40% have a pion in DAPHNE and in about 20% of the cases the particle detected in DAPHNE is the proton.

3.7.3.1 Event selection procedure

A first observation when testing DAPHNE-MIDAS coincidences is that for events with a proton in DAPHNE, the majority of the events is concentrated

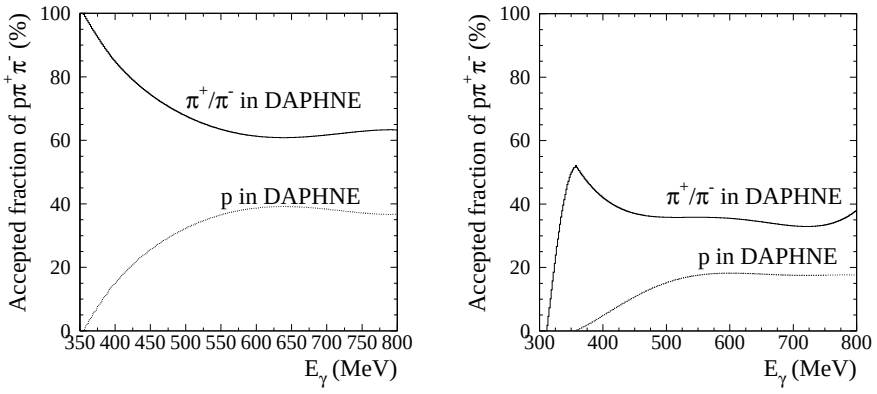

Figure 3.16: γp $\rightarrow$ p$\pi^+\pi^-$ one-charged: (a) Simulated fraction of events that have a pion/proton inside DAPHNE acceptance, (b) Simulated fraction of events that have a pion/proton inside DAPHNE acceptance and at least one of the other particles inside MIDAS acceptance.

below 350 MeV photon energy. This energy is below the threshold for having a proton in DAPHNE and a pion in MIDAS for the p$\pi^+\pi^-$ channel (see Figure 3.16(b)). This means that most of these events come from the pπ^0 channel, where the π^0 results into an e^+e^- pair of which one electron is seen by MIDAS. The fact that the pπ^0 cross section is much higher than the p$\pi^+\pi^-$ one, combined with the respective kinematical conditions, is responsible for the predomination of pπ^0 under these specific conditions, even with a $\pi^0 \rightarrow e^+e^-$ effect of only about 2.5%. In order to avoid this large amount of background, it was opted here to incorporate only one-charged events with a pion identified in DAPHNE.

The selection procedure is thus established as follows:

- ❏ $n_{\text{MWPC}} = 1$: one charged track reconstructed in the wire chambers,
- ❏ $n_{\text{scint}} = 1$: one scintillator track,
- ❏ one pion is identified,
- ❏ $n_{\text{MIDAS}} = 1$: one well reconstructed MIDAS track,
- ❏ MIDAS track reached at least Q_1,
- ❏ if MIDAS track stopped in Q_1 :
  - $\rightarrow$ $E_{Q_1} > 0.7$ MeV.

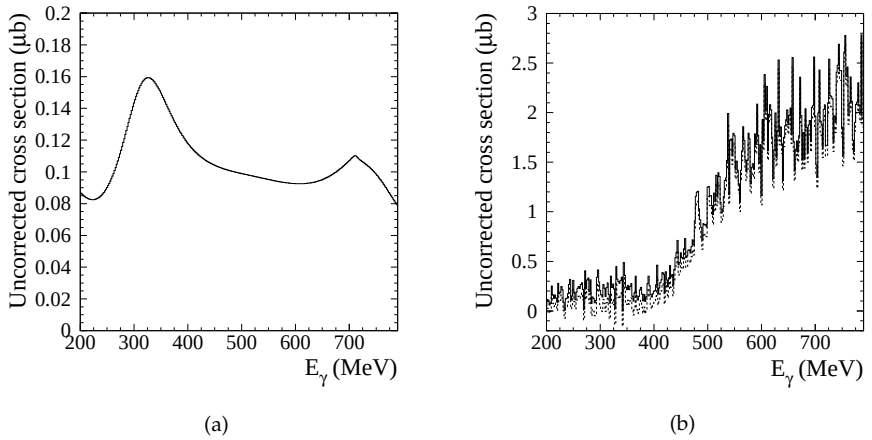

Figure 3.17: $\gamma p \rightarrow p\pi^+\pi^-$ one-charged: (a) Simulated background contribution of $\gamma p \rightarrow n\pi^+$, (b) Uncorrected cross section before and after the background subtraction.

All listed conditions must be fulfilled. The demand for one scintillator track in DAPHNE is a prerequisite since the one detected charged particle needs to be identified. Therefore an azimuthal correction of $1/0.84$ needs to be brought into account.

The pion is identified with range-fit when stopped in B, C, D or E and with the geometrical range method if it is stopped in F or leaves the detector.

The condition for the MIDAS track to reach at least the first silicon detector Q_1 contains also a TDC condition. Combined with a lower energy deposit threshold if the track stopped in this detector, this suppresses most electromagnetic background. It also serves to diminish background generated by the $n\pi^+$ channel, where the pion is in DAPHNE and hadronic interactions of the neutron in the forward direction produce a MIDAS hit. The remaining background from this channel is again simulated with the GEANT programme and subtracted at the uncorrected cross section level. This procedure is illustrated in Figure 3.17.

3.7.3.2 Cross section

Figure 3.18(a) shows the result of the simulation for the global detection efficiency in the one-charged case. It is about 30% and it comprises the following effects:

- Range-fit identification efficiency and momentum threshold for the pion in DAPHNE,
- Probability to have a MIDAS-DAPHNE coincidence when one charged particle is seen in DAPHNE,

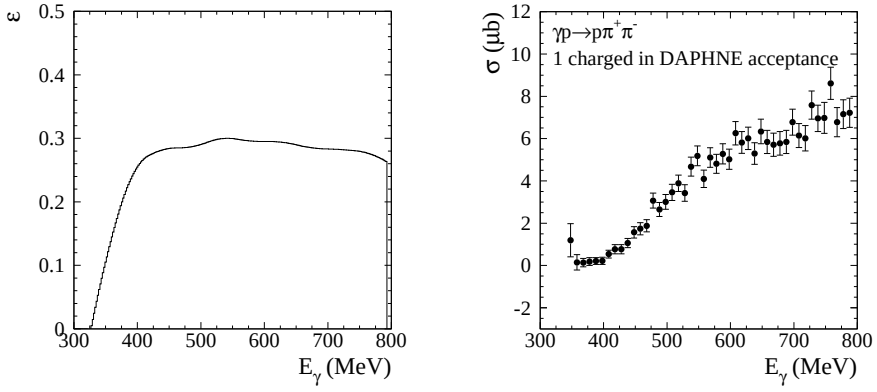

(a) (b)

Figure 3.18: $\gamma p \rightarrow p\pi^+\pi^-$ one-charged: (a) Simulated identification efficiency, (b) Cross section.

➢ MIDAS detection efficiency for a particle to reach at least Q_1 and deposit a minimum energy when stopped in Q_1.

Again, any loss in DAPHNE before the wire chambers is not taken into account at this level. The efficiency is quite low, mainly due to kinematical restraints on the MIDAS-DAPHNE coincidences (cfr. Figure 3.16).

The total one-charged cross section is shown in Figure 3.18(b). In comparison with the two-charged and the three-charged cross section, it is much lower. Combining effects due to the error on the luminosity, the range-fit identification and the simulated background subtraction, a systematical error of 4% is attached to these data. It is important to stress here that the result contains some uncertainties due to the preliminary status of the standard MIDAS analysis, such as the global track reconstruction efficiencies and effects due to geometrical imperfections. Therefore the systematical error is increased to 6%.

3.7.4 $\gamma p \rightarrow p\pi^+\pi^-$: extrapolation to 4π

The measured $p\pi^+\pi^-$ data are summed up and, using the GEANT simulation programme, extrapolated from the DAPHNE acceptance to 4π. As mentioned above, a phase space generator is used in the simulation to this end. The simulated extrapolation function, or acceptance function ϵ_{expol}, contains effects due to the polar angular acceptance (23°–158°) and due to the loss of particles before they reach the wire chambers. The latter loss arises from interactions in the target, its windows or any other material in front of the wire chambers or simply a too low momentum of the emitted particle. The simulated lower momentum thresholds of the respective cases are:

➢ Three-charged case: $n_{\text{MWPC}} = 3$ and $n_{\text{scint}} \geq 1$

$$p_{\text{p}}^{\text{min,3ch}} = 250 + 0.08(\theta_{\text{p}} - 45^\circ)^2 \text{ MeV/c},$$
$$p_{\pi^\pm}^{\text{min,3ch}} = 55 + 0.005(\theta_{\pi^\pm} - 90^\circ)^2 \text{ MeV/c}.$$

➢ Two-charged case: $n_{\text{MWPC}} = 2$ and $n_{\text{scint}} = 2$

$$p_{\text{p}}^{\text{min,2ch}} = 187 - 2.2\theta_{\text{p}} + 0.055\theta_{\text{p}}^2 \text{ MeV/c},$$
$$p_{\pi^\pm}^{\text{min,2ch}} = 20 + 0.003(\theta_{\pi^\pm} - 90^\circ)^2 \text{ MeV/c}.$$

➢ One-charged case: $n_{\text{MWPC}} = 1$ and $n_{\text{scint}} = 1$

$$p_{\text{p}}^{\text{min,1ch}} = 225 - 6.5\theta_{\text{p}} + 0.11\theta_{\text{p}}^2 \text{ MeV/c},$$
$$p_{\pi^\pm}^{\text{min,1ch}} = 8 + 0.002(\theta_{\pi^\pm} - 90^\circ)^2 \text{ MeV/c}.$$

The acceptance function represents the fraction of events accepted for analysis as one of the considered event types. Two choices can be made for the extrapolation depending on whether one incorporates the less reliable one-charged cross section or not. When taking into account the measured three-, two- and one-charged cross sections, the acceptance function ϵ_{expol} corresponds to the fraction of all events that are accepted as three-, two- or one-charged. One can then write for the extrapolated cross section, as above:

$$\sigma_{4\pi}^{\text{p}\pi^+\pi^-} = \frac{\sigma_{\text{3ch}}^{\text{p}\pi^+\pi^-} + \sigma_{\text{2ch}}^{\text{p}\pi^+\pi^-} + \sigma_{\text{1ch}}^{\text{p}\pi^+\pi^-}}{\epsilon_{\text{expol}}}.$$

Alternatively, one can omit the measured one-charged cross section, and rely only on the two- and three-charged cross sections. For this case one has a different acceptance function, ϵ'_{expol}, which is the fraction of all events that are accepted as three-, two-charged. In this case the 4π cross section is:

$$\sigma_{4\pi}^{\text{p}\pi^+\pi^-} = \frac{\sigma_{\text{3ch}}^{\text{p}\pi^+\pi^-} + \sigma_{\text{2ch}}^{\text{p}\pi^+\pi^-}}{\epsilon'_{\text{expol}}}.$$

Figure 3.19 shows the acceptance functions for the two choices.

With these functions the 4π cross section can be deduced in both cases. All obtained cross sections are gathered in Figure 3.20. It was chosen here to incorporate for the two-charged case the cross section obtained with the direct selection method. The 4π cross section obtained with all three types of events should be considered less reliable owing to the mentioned uncertainties in the MIDAS analysis. Therefore the total $\gamma p \rightarrow p\pi^+\pi^-$ cross section obtained from the sum of three- and two-charged events is presented as the final result. Nevertheless, the very reasonable agreement between both results indicates that only small problems are left to be solved in the MIDAS treatment.

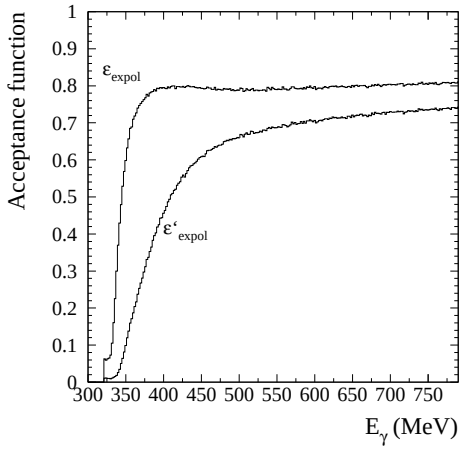

Figure 3.19: $\gamma p \rightarrow p\pi^+\pi^-$: Acceptance function for three-charged plus two-charged combination (ϵ'_{expol}) and for three-charged plus two-charged plus one-charged combination (ϵ_{expol}).

After a strong rise above threshold, the total $p\pi^+\pi^-$ cross section exhibits a broad peak around 600–650 MeV. Within the measured energy range, it only starts falling off.

The systematical error on the 4π cross section, obtained with the three- and two-charged combination, is estimated as follows. For the three-charged case, the source of systematical error is the range-fit identification. This error is taken to be 2% as an upper value, as mentioned above. In the two-charged case we have estimated the systematical error from the comparison between the two selection methods to be 3%. The error on the extrapolation to 4π is estimated to be about 2%. Combining these with the error on the integrated luminosity of 2% by quadratically adding them, we find that the systematical error on the cross section is at most 5%.

3.7.5 $\gamma p \rightarrow p\pi^+\pi^-$: comparison with DAPHNE-92 data

While analysing the GDH calibration data and comparing them with the published DAPHNE-92 data, a problem was found in the latter. An imprecise efficiency correction led to an overestimation of the total cross section. In order to confirm this and to ensure our understanding of the origin of the problem, an attempt was made to reproduce as closely as possible the DAPHNE-92 result with the present measurement and analysis programme. In Figure 3.21 the new data of this work are plotted together with the DAPHNE-92 result and the 'reproduction' of the latter. Above 650 MeV, where the discrepancy with the present data is most severe, the DAPHNE-92 data are well reproduced.

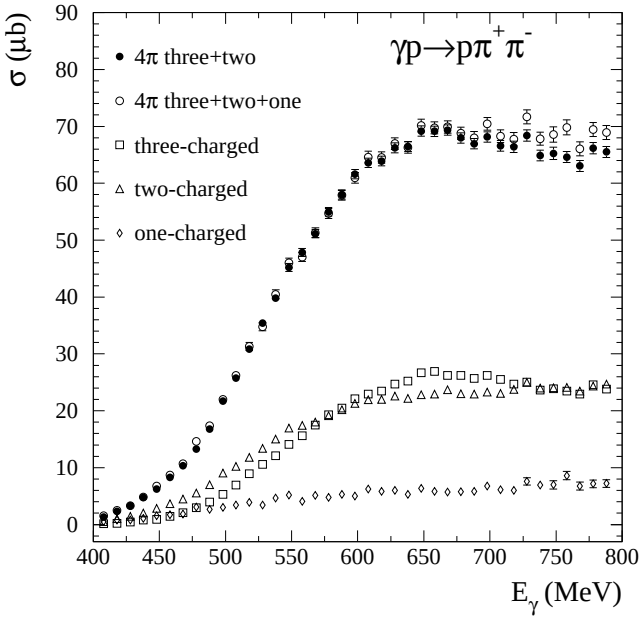

Figure 3.20: $\gamma p \rightarrow p\pi^+\pi^-$: Overview of the obtained partial and total cross sections.

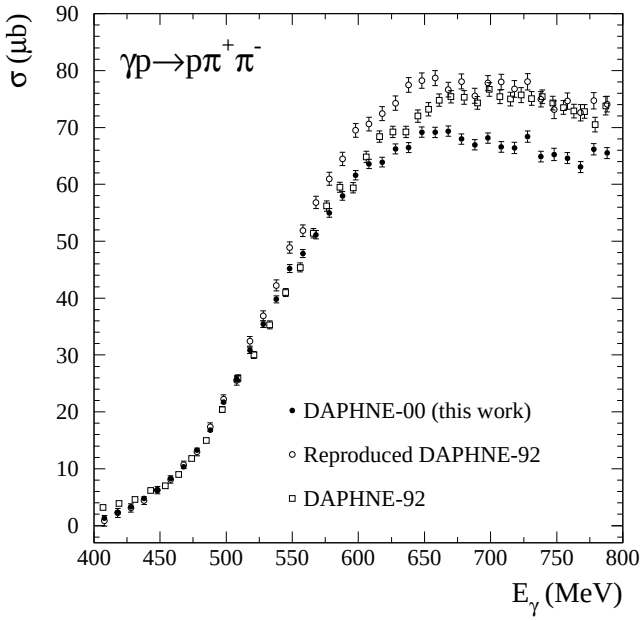

Figure 3.21: γp $\rightarrow$ p$\pi^+\pi^-$: Comparison of the present result with the DAPHNE-92 data points.

Below these photon energies, some effect remains. This is supposedly due to the different approximation that was used to obtain the extrapolation function; phase space in the present data and the Laget model calculation in the DAPHNE-92 data [99].

3.8 $\gamma p \rightarrow n\pi^+\pi^0$

With two neutral particles in the final state, the $\gamma p \rightarrow n\pi^+\pi^0$ channel is a bigger challenge for the DAPHNE analysis than e.g. the above $\gamma p \rightarrow p\pi^+\pi^-$. There is a unique possibility to separate it from the other reaction channels, namely the coincident detection of a π^+ and a π^0. A careful study of the π^0 identification method allows to obtain a reasonable detection efficiency for the neutral pion. Combined with the high detection efficiency for charged pions this results in an accurate cross section, with low statistical and systematical errors.

Again the aim is the cross-check of the DAPHNE-92 result [22], with a refined and improved π^0 detection efficiency. The full analysis is immediately usable for the analysis of the doubly polarised butanol data.

In the next section the π^0 detection is studied in detail. In the sections thereafter the $n\pi^+\pi^0$ event selection procedure and the cross section within the DAPHNE acceptance are presented. In this case 'inside the acceptance' is defined as 'the π^+ has a polar angle between 23° and 158° and this track has been reconstructed in the wire chambers'. A tedious simulation of the acceptance allows to extrapolate these data to the 4π cross section as described in the last section.

3.8.1 π^0 identification

The π^0 is identified in DAPHNE by means of the detection of one or two of its decay photons. The mean life time of the π^0 is $8.4\ 10^{-17}$ s [105] and thus the decay occurs before the π^0 reaches the detector. A photon is selected by requiring the combined fulfilment of the following conditions:

- ❏ one neutral scintillator track D-E, E-F or D-E-F (no A, B or C-layer hit in this sector),
- ❏ no wire chamber track in front of this hit scintillator sector,
- ❏ no charged scintillator track adjacent to this one,
- ❏ at least 400 keV is deposited in each hit layer if only one neutral track is present.

The choice for the hit layers D, E and F is evident since these layers are preceded by photon-converter layers, a combination especially designed for the detection of photons. At least two layers are demanded in coincidence to avoid spurious signals. The absence of a wire chamber track is of course a

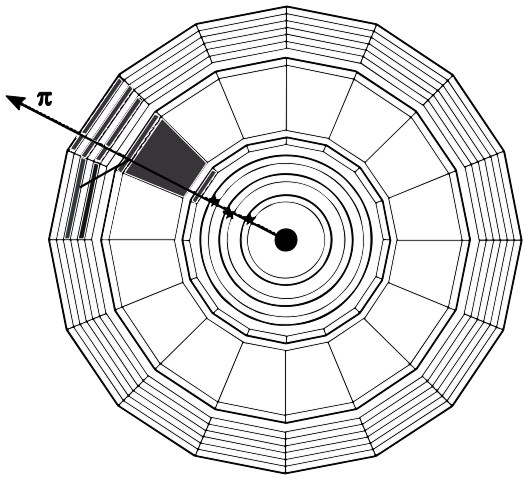

Figure 3.22: Example of a charged pion track that gives rise to an adjacent uncharged track, in this case a D-E hit.

prerequisite for a neutral signal. In principle, also a single B-layer hit is a possible photon signal. This extra possibility would increase the detection efficiency. However, a B-layer hit is the most typical neutron signal in DAPHNE and consequently a lot of neutron background would be present in the selected photon set. Therefore, in order to obtain a cleaner photon signal, it was chosen not to include these. This significantly reduces the systematical error.

The omission of tracks adjacent to a charged track serves to avoid the quite common situation illustrated in Figure 3.22. A charged pion track in sector i induces e.g. a D-E hit in sector i+1 through multiple scattering. Such a combination would mistakenly be identified as a charged pion-photon couple.

The lower threshold of 400 keV in the case of one single neutral track serves to enhance the purity of the photon track, which is even more crucial when only one of the two decay photons is detected.

The number of identified photons is denoted as n_γ. Two methods to identify a π^0 are considered. In the first case $n_\gamma = 2$ is required to identify the π^0 and both decay photons are detected. The second possibility is to require $n_\gamma \geq 1$. We further refer to these two options as $\pi^0(2\gamma)$ and $\pi^0(\geq 1\gamma)$ respectively. In both cases the efficiency with which a π^0 is identified in the $n\pi^+\pi^0$ reaction needs to be well known. It is obtained by generating $n\pi^+\pi^0$ events in the GEANT simulation programme. Defining $N^{n\pi^+\pi^0}(E_\gamma)$ as the total number of $n\pi^+\pi^0$ events, and $N^{n\pi^+\pi^0}_{\pi^0}(E_\gamma)$ as the number of these events for which a π^0 is identified, $\epsilon^{n\pi^+\pi^0}_{\pi^0}(E_\gamma)$ reads:

$$\epsilon^{n\pi^+\pi^0}_{\pi^0}(E_\gamma) = \frac{N^{n\pi^+\pi^0}_{\pi^0}(E_\gamma)}{N^{n\pi^+\pi^0}(E_\gamma)}. \tag{3.3}$$

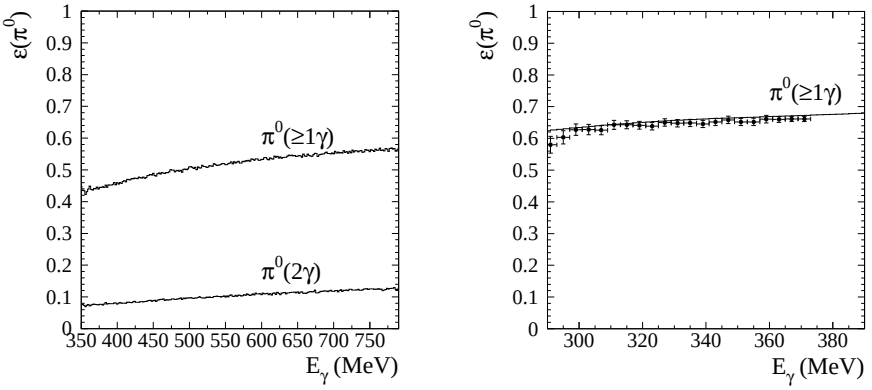

Figure 3.23: (a) Simulated π^0 efficiency in $n\pi^+\pi^0$ as a function of photon energy obtained with the $n_\gamma = 2$ and the $n_\gamma \geq 1$ identification, (b) Simulated and experimental π^0 efficiency in $p\pi^0$ as a function of photon energy obtained with the $n_\gamma \geq 1$ identification.

The cross section along the beam axis of the scintillator bars in the D, E and F-layer has a trapezoidal shape, with the small base towards the beam axis. As a consequence the polar angle dependence of the efficiency is negligible. Moreover, since the decay photons can be found inside DAPHNE for all initial π^0 emission angles and momenta, there is no acceptance limit for the π^0 detection.

The most straightforward possibility to identify a π^0 is to demand $n_\gamma = 2$. This yields a very clean identification and the probability to misidentify another type of particle as a π^0 is negligible. The major drawback of this choice is the relatively low resulting π^0 detection efficiency $\epsilon^{n\pi^+\pi^0}_{\pi^0(2\gamma)}$. The result of the simulation is shown in Figure 3.23(a). A mean value of about 10 % is found which is quite pernicious from the statistics point of view.

In order to improve this situation, the possibility to identify a π^0 with the weaker condition $n_\gamma \geq 1$ is investigated. One out of two decay photons is then sufficient which means an important gain in efficiency. The simulated efficiency $\epsilon^{n\pi^+\pi^0}_{\pi^0(\geq 1\gamma)}$ is also plotted in Figure 3.23(a). Since it is a factor of five higher than the efficiency in the $n_\gamma = 2$ case, it is certainly preferable in terms of statistics. However, the relaxed condition $n_\gamma \geq 1$ evidently implies some unwanted background events, mainly produced neutrons. A neutron has a non-negligible probability to induce a signal that satisfies the above conditions for the identification of a photon and may thus be misidentified as a π^0. The simulation of this effect allows then to subtract the background, as discussed in the next section.

The reliability of the simulated efficiency is verified by comparing it with the experimentally obtained one. Unfortunately the experimental efficiency $\epsilon_{\pi^0}^{\mathrm{n}\pi^+\pi^0}$ is not directly accessible from the $\mathrm{n}\pi^+\pi^0$ data. This would require the possibility to uniquely identify $\mathrm{n}\pi^+\pi^0$ events with a neutron-π^+ coincidence. The fraction of such events with a π^0 detected would immediately yield the π^0 efficiency. However, background from the $\mathrm{n}\pi^+$ channels is unavoidable when detecting a neutron and a π^+ in coincidence, which influences the π^0 efficiency.

Therefore the simulated π^0 efficiency is verified using the $\mathrm{p}\pi^0$ reaction. Due to a different number of final state particles and different kinematical conditions, the magnitude of the π^0 efficiency in this channel slightly differs from the one in $\mathrm{n}\pi^+\pi^0$. However, if this $\epsilon_{\pi^0}^{\mathrm{p}\pi^0}$ is well simulated, we trust that this is also true for $\epsilon_{\pi^0}^{\mathrm{n}\pi^+\pi^0}$.

Below 400 MeV photon energy, it is quite straightforward to obtain the experimental π^0 efficiency in the $\mathrm{p}\pi^0$ reaction. In this energy range, below the DAPHNE double pion detection threshold, each proton should be accompanied by a π^0. The fraction of proton events with a coincident π^0 signal immediately yields $\epsilon_{\pi^0}^{\mathrm{p}\pi^0}$. In Figure 3.23(b) the so obtained experimental efficiency, in the $\pi^0(\geq 1\gamma)$ case, is compared with the corresponding simulated efficiency, obtained from a simulation of the $\mathrm{p}\pi^0$ channel. The agreement in the energy range where one has access to the experimental efficiency is very good. This justifies the assumption to rely on the simulated π^0 efficiency also at higher energies and for different reaction channels.

3.8.2 $\gamma\mathbf{p} \rightarrow \mathbf{n}\pi^+\pi^0$ with $\pi^+\pi^0$ in DAPHNE acceptance

3.8.2.1 Event selection procedure

An event from $\gamma\mathrm{p} \rightarrow \mathrm{n}\pi^+\pi^0$ is selected using the following procedure:

- $n_{\mathrm{MWPC}} = 1$: one charged track reconstructed in the wire chambers,
- $n_{\mathrm{scint}} = 1$: one scintillator track,
- one charged pion is identified,
- one π^0 is identified.

Each of these conditions has to be fulfilled. The demand for one single scintillator track implies the minimal azimuthal correction of $1/0.84 = 1.19$.

The charged pion is identified with the range-fit method when stopped in the B, C, D or E-layer and with the geometrical range method when stopped in the F-layer.

The $n_\gamma \geq 1$ option for the π^0 identification is used in the final analysis of the data. As a cross-check for this result, the analysis with the $n_\gamma = 2$ requirement is done in parallel. Since this latter method has much less background

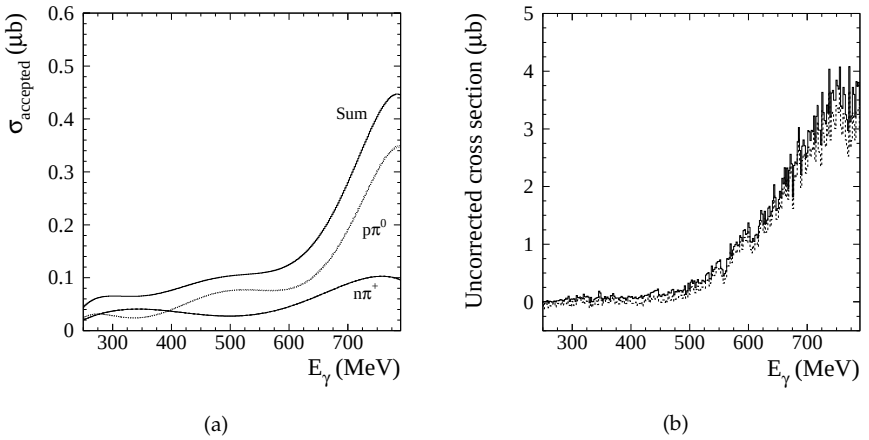

Figure 3.24: $\gamma p \rightarrow n\pi^+\pi^0$ for $\pi^0(2\gamma)$: (a) Simulated background contribution from $n\pi^+$ and $p\pi^0$, (b) Uncorrected cross section before and after background subtraction.

to deal with, it can serve as a control reference for the background subtraction needed when using the former.

By simulation one finds that both the $p\pi^0$ and $n\pi^+$ channels contribute to the background. The effect of the former reaction is the smallest as it merely corresponds to the small fraction of protons that are misidentified as a pion by the range-fit method. The contribution of the $n\pi^+$ channel is the largest, especially in the $\pi^0(\geq 1\gamma)$ case, where the probability to identify mistakenly a neutron as a π^0, is larger. The background contributions are obtained with the aid of the simulation. The fractions of the $p\pi^0$ and $n\pi^+$ generated events that satisfy the $n\pi^+\pi^0$ selection conditions are multiplied with the respective cross sections, taken again from SAID [9].

Figure 3.24(a) and Figure 3.25(a) illustrate these contributions for both π^0 detection methods, respectively. The sum of both background contributions, which is also plotted in these figures, is then subtracted from the above raw yields and the result is shown in Figure 3.24(b) and Figure 3.25(b). In both the $\pi^0(\geq 1\gamma)$ and $\pi^0(2\gamma)$ case the yield in the Δ region vanishes, which proves that the background is well subtracted. The only further background that could be present would be $p\pi^0\pi^0$ events, which could be mistakenly accepted on the same grounds as the $p\pi^0$ events. However, the low probability for this, combined with the relatively small cross section of this reaction channel, justifies neglecting this effect.

3.8.2.2 Cross section

Once the background is properly subtracted the global detection efficiency can be applied in order to correct for the inefficiency in the π^+ and π^0 detection.

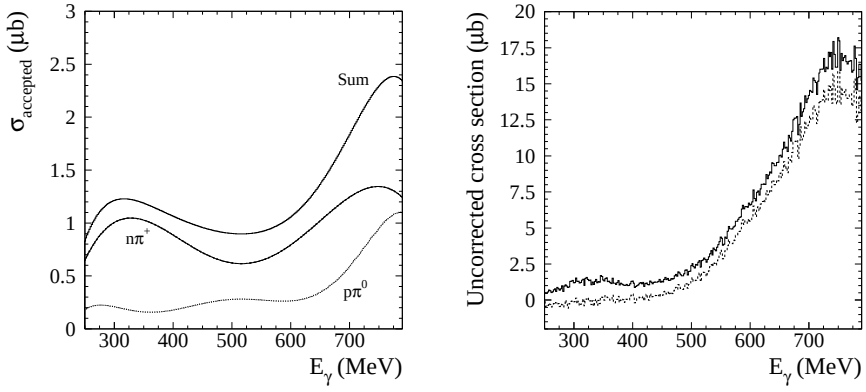

Figure 3.25: $\gamma p \rightarrow n\pi^+\pi^0$ for $\pi^0(\geq 1\gamma)$: (a) Simulated background contribution from $n\pi^+$ and $p\pi^0$, (b) Uncorrected cross section before and after background subtraction.

The global efficiency for both the $\pi^0(\geq 1\gamma)$ and $\pi^0(2\gamma)$ option is illustrated in Figure 3.26(a). It takes into account the following effects:

- Loss of π^+ before reaching DAPHNE and producing one MWPC track and one charged scintillator track,
- Range-fit efficiency and momentum threshold for π^+,
- π^0 detection efficiency.

Figure 3.26(b) shows the final result for the $n\pi^+\pi^0$ cross section with the π^+ and the π^0 inside the DAPHNE acceptance. The good agreement between the data obtained with the two different π^0 identification methods justifies the use of the more relaxed $\pi^0(\geq 1\gamma)$ which is advantageous with respect to the statistical error. The observed discrepancies can be interpreted as systematical imprecision on the π^0 identification which is estimated here to be at most 4%.

3.8.3 $\gamma p \rightarrow n\pi^+\pi^0$: extrapolation to 4π

The simulation programme is also used to calculate the acceptance for the above analysis procedure. The acceptance function as a function of incoming photon energy is plotted in Figure 3.27. It accounts for the loss of $n\pi^+\pi^0$ events not accepted due to the fact that the π^+ is not inside the DAPHNE polar acceptance. At this stage no momentum threshold effect is needed anymore since it is taken into account in the cross section inside the acceptance. This situation is slightly different from what was done in the $p\pi^+\pi^-$ channel, where the momentum threshold depends on the type of accepted events.

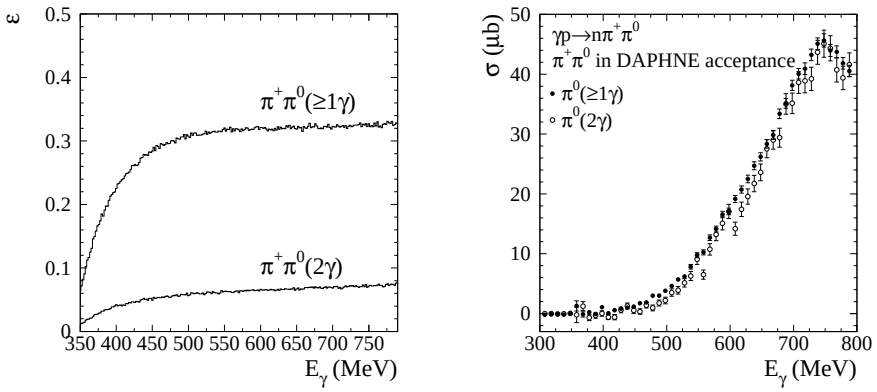

(a) (b)

Figure 3.26: $n\pi^+\pi^0$ with $\pi^+\pi^0$ in DAPHNE acceptance: (a) Simulated detection efficiency for the $\pi^0(2\gamma)$ and the $\pi^0(\geq 1\gamma)$ method, (b) Cross section for $\pi^0(2\gamma)$ and $\pi^0(\geq 1\gamma)$.

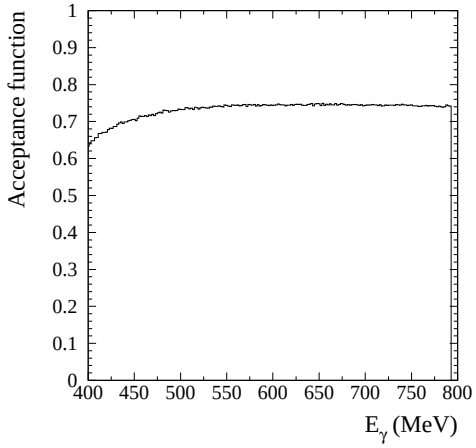

Figure 3.27: $n\pi^+\pi^0$: Acceptance function.

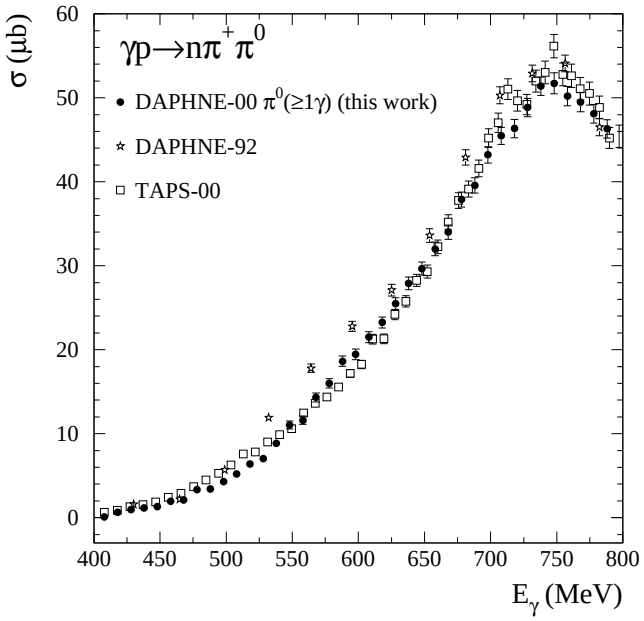

Figure 3.28: $n\pi^+\pi^0$: 4π cross section (DAPHNE-00) compared with DAPHNE-92 and TAPS data.

The acceptance function allows to simply extrapolate the data from within the DAPHNE acceptance to the full 4π space. Figure 3.28 shows the result for the total $n\pi^+\pi^0$ cross section. Above threshold a slow rise is observed and a strong peak at about 750 MeV is present.

For the systematical error, we add the following errors quadratically: 2% on the integrated luminosity, 2% on the π^+ identification, 4% on the π^0 identification and 2% on the extrapolation. In this way the systematical error is estimated to be 5%.

The DAPHNE-92 data for this channel are also plotted in Figure 3.28. They have a similar efficiency correction problem as discussed above for the $p\pi^+\pi^-$ channel. The effect on the cross section is less severe but is responsible for the observed discrepancies with the DAPHNE data presented here. The results are also compared with recent data from the TAPS collaboration [81] with which they show an excellent agreement. This agreement is an indication to assume that the estimated systematical error is an upper limit.

4

Analysis of $\vec{\gamma}\vec{\mathrm{p}} \longrightarrow \mathrm{p}\pi^+\pi^-$ and $\vec{\gamma}\vec{\mathrm{p}} \longrightarrow \mathrm{n}\pi^+\pi^0$

4.1 Introduction

In this chapter the doubly polarised data for the double pion photoproduction channels $\mathrm{p}\pi^+\pi^-$ and $\mathrm{n}\pi^+\pi^0$ on the proton are presented. These results belong to the primary goals of this PhD work. They are the first of their kind as the helicity dependence of these reactions has not been measured before.

The observables of interest are the absorption cross sections for the two relative beam-target (photon-proton) polarisation orientations. The cross section corresponding to the anti-parallel orientation, i.e. the spin-1/2 state, is denoted $\sigma_{1/2}$, the cross section in the case of parallel orientation, the spin-3/2 state, is written as $\sigma_{3/2}$.

An important issue in the analysis of the butanol data is the fact that the target is not a pure proton target. The polarised butanol (C_4H_9OH) target contains, besides hydrogen, also carbon and oxygen. These elements give rise to unwanted background contributions since one is only interested in photoproduction reactions on the proton. Subtraction of this large amount of background would require a tedious measurement of the carbon and oxygen contribution to the cross sections. Without this option being impossible, it is opted here to take advantage of the fact that neither the carbon, nor the oxygen in the butanol target are polarised. This means that their contribution to $\sigma_{1/2}$ and $\sigma_{3/2}$ is equal such that it vanishes when subtracting the two cross sections and studying the cross section difference $\Delta\sigma^{\mathrm{pol}} = \sigma_{3/2} - \sigma_{1/2}$.

The main advantage of studying the cross section difference lies of course in the fact that no carbon or oxygen background needs to be subtracted, which would give rise to an extra source of systematical uncertainty. For the contribution to the GDH sum rule and the forward spin polarisability the difference is all that is needed since it occurs as such in the integrand. The influence of different nucleon resonances can also be well examined by means of the cross section difference, its sign and magnitude can point to the dominance

of a particular resonance. Moreover, when combining the cross section difference with the unpolarised total cross section, the separate $\sigma_{1/2}$ and $\sigma_{3/2}$ can be accessed:

$$\begin{aligned} \sigma^{\text{unpol}} &= \tfrac{\sigma_{1/2}+\sigma_{3/2}}{2} & & \sigma_{1/2} = \sigma^{\text{unpol}} - \tfrac{\Delta\sigma^{\text{pol}}}{2} \\ & & \Rightarrow & \\ \Delta\sigma^{\text{pol}} &= \sigma_{3/2} - \sigma_{1/2} & & \sigma_{3/2} = \sigma^{\text{unpol}} + \tfrac{\Delta\sigma^{\text{pol}}}{2} \end{aligned}$$

The principal disadvantage of considering only $\sigma_{3/2} - \sigma_{1/2}$, besides the lack of direct access to $\sigma_{1/2}$ and $\sigma_{3/2}$ separately, is the unavoidable increase of the propagated statistical error on the cross section difference.

Another interesting observable that can be obtained by combining σ^{unpol} and $\Delta\sigma^{\text{pol}}$ is the helicity asymmetry E:

$$E = \frac{\sigma_{3/2} - \sigma_{1/2}}{\sigma_{3/2} + \sigma_{1/2}}.$$

It describes the relative strength of the helicity dependence for the studied process.

The calibration analysis discussed in the previous chapter is designed to be immediately applicable to the doubly polarised butanol data. This means that it does not rely on any target-specific conditions. Moreover the analysis has been optimised to reduce statistical and systematical errors. Exactly the same procedures are applied to obtain events in the $1/2$ and $3/2$ helicity state, respectively. These events are then normalised and the one is subtracted from the other to obtain $\sigma_{3/2} - \sigma_{1/2}$.

A few parameters, especially the target dimensions, its composition and its density, differ from the hydrogen case. Moreover the beam and target polarisation introduce some extra systematical errors. Each difference with respect to the calibration analysis is detailed in the next section. In Section 4.3 and Section 4.4 the obtained results for the cross section difference in the $\vec{\gamma}\vec{\mathrm{p}} \to \mathrm{p}\pi^+\pi^-$ and $\vec{\gamma}\vec{\mathrm{p}} \to \mathrm{n}\pi^+\pi^0$ channels are presented and discussed. Finally the contribution of the measured data to the GDH sum rule and to the forward spin polarisability are presented in Section 4.5.

4.2 Modifications with respect to the calibration analysis

Common conditions All conditions concerning polar and azimuthal angle limits mentioned in Section 3.2 on p. 56 remain unchanged in the butanol analysis. The target length in the effective target length correction (2.30) (p. 50) is equal to the true butanol target length $d_{\text{target}} = 1.88$ cm.

Luminosity Recall the definition for the integrated luminosity:

$$\mathcal{L}(E_\gamma) = N_\gamma(E_\gamma) n_{\text{target}} d_{\text{target}},$$

with $N_\gamma(E_\gamma)$ the number of incoming photons with energy E_γ, n_{target} the number of target nucleons per unit volume and d_{target} the target thickness. To calculate the number of target protons per unit volume, not only the density of the butanol target, $\rho = 0.94 g/\text{cm}^3$, needs to be taken into account, but also the filling factor of the butanol beads, which is 63%, and the dilution factor of 0.135. Thusly one finds $n_{\text{target}} = 4.8\ 10^{22}\ \text{cm}^{-3}$.

For the imposed target length a different philosophy from the hydrogen case is adopted. The reason for this is that the target is quite short, its physical limits being [−23.4 mm,−4.6 mm]. Taking into account the maximum error on the reconstructed z vertex of 1.5 cm, a lot of good events would be cut by setting a software condition corresponding to these limits. However, since they are unpolarised, the influence of the target walls disappears in $\sigma_{3/2} - \sigma_{1/2}$ such that it is no problem to widen the software limits to:

$$-40\ \text{mm} \leq z \leq 20\ \text{mm},$$

preventing the loss of good events emitted from the target but with a reconstructed vertex outside the true target limits. Evidently, for the normalisation of the data, the true target thickness $d_{\text{target}} = 1.88$ cm needs to be used in the luminosity calculation.

Systematical errors Apart from the 2% systematical error arising from the measurement of the number of incoming photons, a few additional sources of systematical error are introduced in the doubly polarised measurement: the error on the photon polarisation is 3%, while the systematical error attached to the polarisation of the target material is about 1.6%.

In any polarisation experiment it is of primary importance to be aware of any false asymmetry arising from the apparatus, and not from the studied target. This can be checked e.g. with a measurement during which the target is unpolarised and the beam is polarised. A short run period like this was performed during the GDH experiment. The primary electron beam energy was 525 MeV. The result of a basic analysis, accepting all hadronic events well correlated with the tagger is shown in Figure 4.1. Represented is the asymmetry in number of events $E_N = \frac{N_{3/2} - N_{1/2}}{N_{3/2} + N_{1/2}}$ as a function of photon energy. $N_{3/2}$ ($N_{1/2}$) corresponds in this case with a photon polarisation of $+1$ (-1). A weighted mean of 0.0007 ± 0.0010 is found. Since the sum of $N_{3/2}$ and $N_{1/2}$ does contain the carbon and oxygen background, whereas the difference does not, this asymmetry is underestimated if one wants to compare it with the true proton asymmetries. From the results in [82] one can conclude that it is underestimated by a factor of five. In this way a value of about 0.35% is estimated for the effect of apparatus asymmetry, which is small enough to neglect the effect.

A check of the unpolarised background subtraction in the study of the cross section difference $\sigma_{3/2} - \sigma_{1/2}$ is done in the analysis of the $p\pi^+\pi^-$ channel (see next section). This test reveals that the chosen approach is satisfactory.

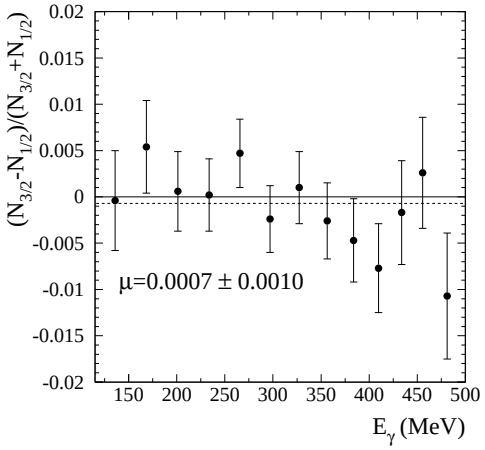

Figure 4.1: Measured apparatus asymmetry in number of events as a function of photon energy in the Δ region.

The systematical error for particle identification remains of the same order of magnitude as in the hydrogen analysis (about 2%). Systematical errors due to the required cross section extrapolation will increase for the butanol data since there may be a larger uncertainty on the helicity dependent behaviour of the investigated processes outside the detector acceptance.

GEANT simulation The only difference in the simulation programme is that butanol is taken as a target material and, more importantly, the reaction generators differ. For the single pion production channels, the helicity cross sections $\sigma_{1/2}$ and $\sigma_{3/2}$ from SAID are generated. This allows to simulate polarised background contributions to $\sigma_{1/2} - \sigma_{3/2}$ where necessary. At present no polarised double pion cross sections are incorporated, as for these simulations we rely on the unpolarised generators.

4.3 $\vec{\gamma}\vec{\mathrm{p}} \rightarrow \mathrm{p}\pi^+\pi^-$

As the analysis procedure used to obtain the polarised $\mathrm{p}\pi^+\pi^-$ data is identical to the one used in the calibration analysis, the details are not repeated here and we merely comment where necessary on the peculiarities of the analysis of the butanol data.

In Figures 4.3, 4.4 and 4.5 the results for the three types of events —three-charged, two-charged and one-charged— are gathered in order to be able to compare their relative contribution. In each figure this is done for a different observable, namely the cross section difference, the helicity asymmetry and

the separated cross sections $\sigma_{1/2}$ and $\sigma_{3/2}$, respectively. The measured data are then combined and extrapolated to 4π via the same procedure as in the unpolarised cross section analysis.

4.3.1 $\vec{\gamma}\vec{\mathrm{p}} \rightarrow \mathrm{p}\pi^+\pi^-$: three charged particles in DAPHNE acceptance

In the three-charged case, the missing mass spectrum used to cut away single pion photoproduction events, can be used as a check for the background subtraction in $\Delta\sigma^{\mathrm{pol}}$. Figures 4.2(a) and 4.2(b) show the separate missing mass spectra for events in the $3/2$ and the $1/2$ state. In these spectra no clear separation between single and double pion production is observed. This effect stems from the protons in the carbon and oxygen nuclei in the butanol target. Due to interactions with these non-free proton target particles, a different kinematical range is accessed. When subtracting the $1/2$ events from the $3/2$ events (Figure 4.2(c)), a spectrum very similar to the one obtained from the pure proton —also drawn in the picture to guide the eye— is obtained. A good separation between single and double pion events is thus again found. This illustrates how the unpolarised background from the target is well eliminated in $\Delta\sigma^{\mathrm{pol}}$. The fact that the difference spectrum is not identical to the one on hydrogen can be explained by the fact that the former contains a helicity dependence which evidently is not present in the latter.

The cross section difference for the three-charged case is presented in Figure 4.3(a). The difference $\sigma_{3/2} - \sigma_{1/2}$ is positive, the $3/2$ state is thus the dominating one. A peak is observed at 600–650 MeV; this position is comparable to the peak position in the unpolarised cross section. For the calculation of the helicity asymmetry and the helicity cross sections, the cross section difference is combined with the unpolarised three-charged cross section σ^{unpol}. However, as discussed below, the momentum thresholds for the proton and the pions are slightly different for butanol and hydrogen. Therefore, before combining $\sigma_{3/2} - \sigma_{1/2}$ with the unpolarised cross section, a correction is applied to the latter to take this effect into account. The helicity asymmetry is shown in Figure 4.4(a). The asymmetry is quite large. A maximum value of about 60% is observed below 650 MeV. Above this energy, the asymmetry decreases. This corresponds to the fact that the cross section difference $\sigma_{3/2} - \sigma_{1/2}$ strongly decreases above 650 MeV whereas the unpolarised cross section, decreases more slowly. In Figure 4.5(a) the separated helicity cross sections are presented. These again nicely illustrate how the $3/2$ state predominates. Moreover the $\sigma_{3/2}$ exhibits a clear resonant structure, whereas $\sigma_{1/2}$ has a more background-like behaviour.

4.3.2 $\vec{\gamma}\vec{\mathrm{p}} \rightarrow \mathrm{p}\pi^+\pi^-$: two charged particles in DAPHNE acceptance

4.3.2.1 Direct selection

The most crucial ingredient in the analysis of the two-charged case by direct selection is the correct simulation of the background contributions from $\vec{\gamma}\vec{\mathrm{p}} \rightarrow$

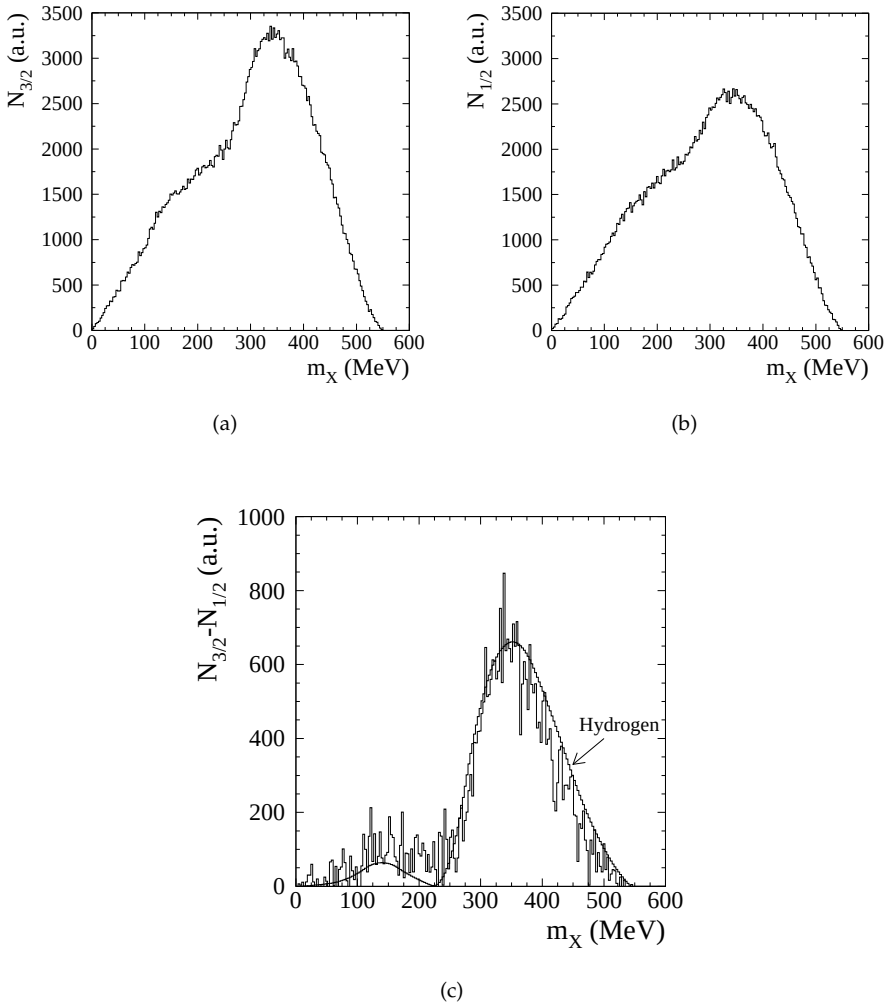

Figure 4.2: $\vec{\gamma}\mathrm{p} \rightarrow \mathrm{p}\pi^+\pi^-$ three-charged: (a) Missing mass spectrum in the 3/2 state, (b) Missing mass spectrum in the 1/2 state, (c) Difference missing mass spectrum illustrating the suppression of unpolarised background. The full line corresponds to the analogous missing mass spectrum on the free proton.

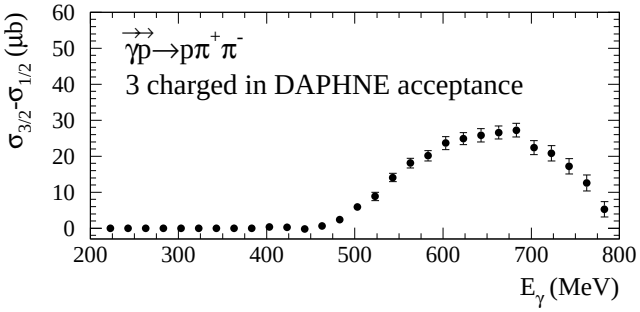

(a)

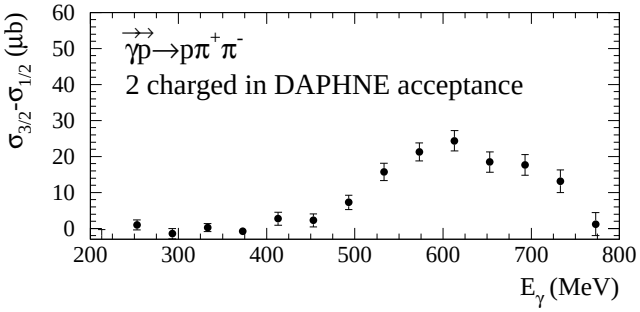

(b)

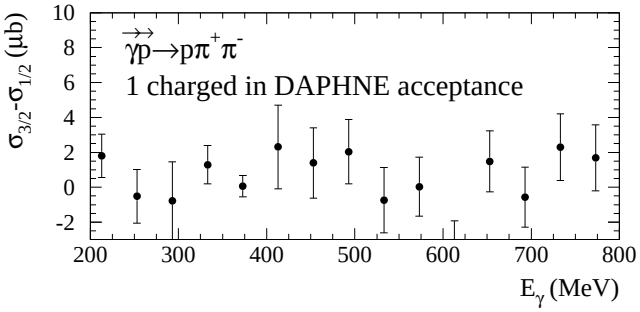

(c)

Figure 4.3: $\vec{\gamma}\vec{\mathrm{p}} \rightarrow \mathrm{p}\pi^+\pi^-$: Cross section difference $\sigma_{3/2} - \sigma_{1/2}$ as a function of photon energy in the three-charged case (a), two-charged case (b) and one-charged case (c).

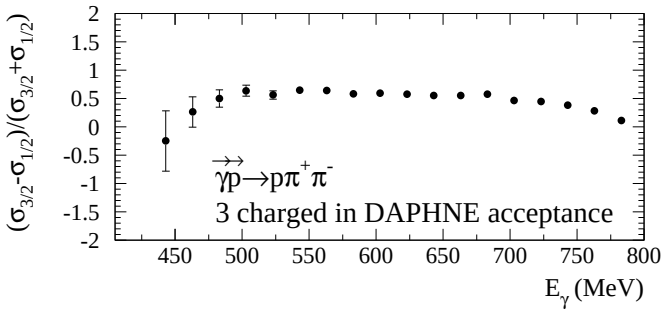

(a)

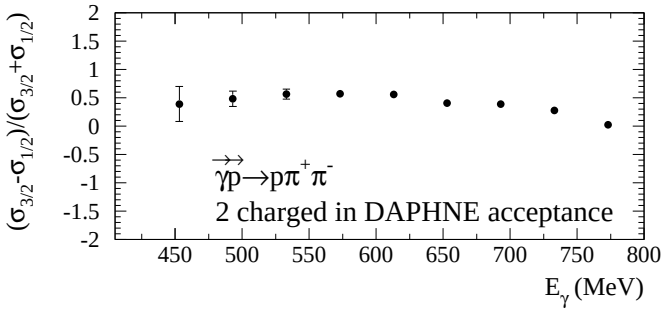

(b)

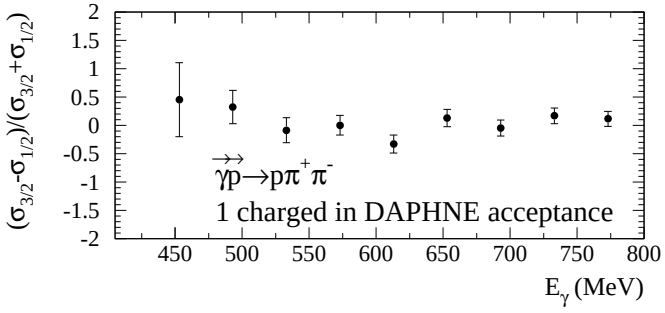

(c)

Figure 4.4: $\vec{\gamma}\vec{\mathrm{p}} \rightarrow \mathrm{p}\pi^+\pi^-$: Helicity asymmetry as a function of photon energy in the three-charged case (a), two-charged case (b) and one-charged case (c).

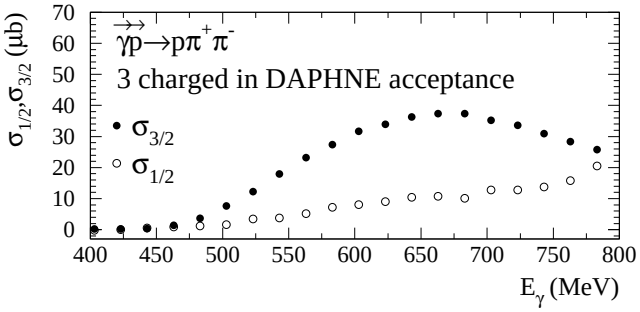

(a)

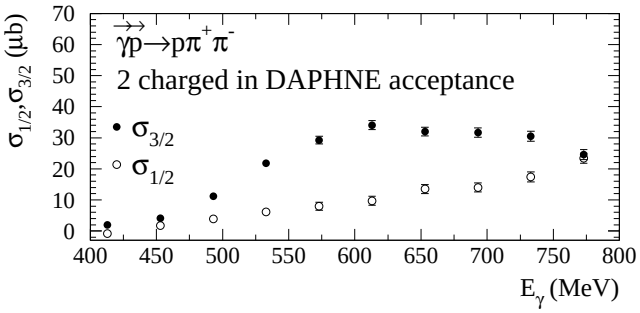

(b)

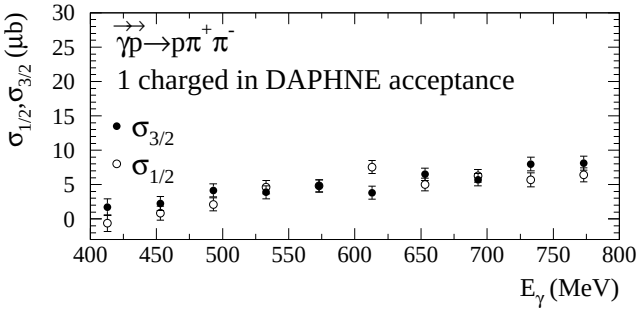

(c)

Figure 4.5: $\vec{\gamma}\vec{\mathrm{p}} \rightarrow \mathrm{p}\pi^+\pi^-$: Cross sections $\sigma_{3/2}$ and $\sigma_{1/2}$ as a function of photon energy in the three-charged case (a), two-charged case (b) and one-charged case (c).

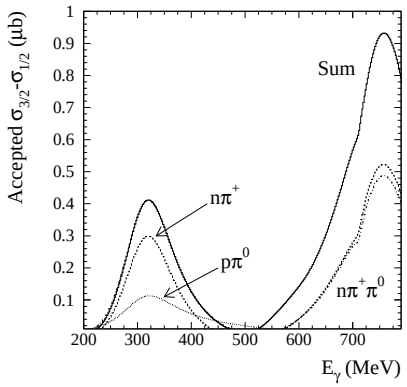

Figure 4.6: $\vec{\gamma}\vec{\mathrm{p}} \to \mathrm{p}\pi^+\pi^-$ two-charged, direct selection: Simulated background contribution from $\vec{\gamma}\vec{\mathrm{p}} \to \mathrm{p}\pi^0$, $\mathrm{n}\pi^+$ and $\mathrm{n}\pi^+\pi^0$.

$\mathrm{p}\pi^0$, $\mathrm{n}\pi^+$ and $\mathrm{n}\pi^+\pi^0$. In order to be able to subtract this background, one needs to know, for each background reaction channel i, the simulated fraction of $\sigma_{1/2,i}$ and $\sigma_{3/2,i}$ that is accepted by the selection. Denoting these fractions as $\epsilon_{1/2,i}$ and $\epsilon_{3/2,i}$ respectively, the background contribution to be subtracted from the measured uncorrected cross section difference is:

$$\sum_i \epsilon_{3/2,i}\sigma_{3/2,i} - \epsilon_{1/2,i}\sigma_{1/2,i},$$

with $\sigma_{1/2,i}$ and $\sigma_{3/2,i}$ the total helicity cross sections for the different background reactions. For the two single pion channels this procedure can be followed since the separate generation of $\sigma_{1/2,i}$ and $\sigma_{3/2,i}$ is provided in the simulation and the helicity cross sections can be taken from SAID. For the $\mathrm{n}\pi^+\pi^0$ channel there is no helicity dependent event generation available at present. Therefore, in this case the accepted fraction is simulated by generating the unpolarised $\mathrm{n}\pi^+\pi^0$ cross section. It is then multiplied with the measured cross section difference (discussed in Section 4.4). Figure 4.6 shows the simulated background for the three channels. One finds that the magnitude of the background does not exceed the statistical error of the measured cross section difference, the influence of the background subtraction is therefore of minor importance.

4.3.2.2 Indirect selection

Recall the formula for two-charged $\mathrm{p}\pi^+\pi^-$ events in the indirect selection method:

$$N_{\mathrm{2ch}}^{\mathrm{p}\pi^+\pi^-} = N_{\mathrm{2ch}} - N_{\mathrm{2ch}}^{\mathrm{1p},m_X<280\ \mathrm{MeV}} \left(\epsilon_{\mathrm{p},m_X}^{\mathrm{p}\pi^0}\right)^{-1}.$$

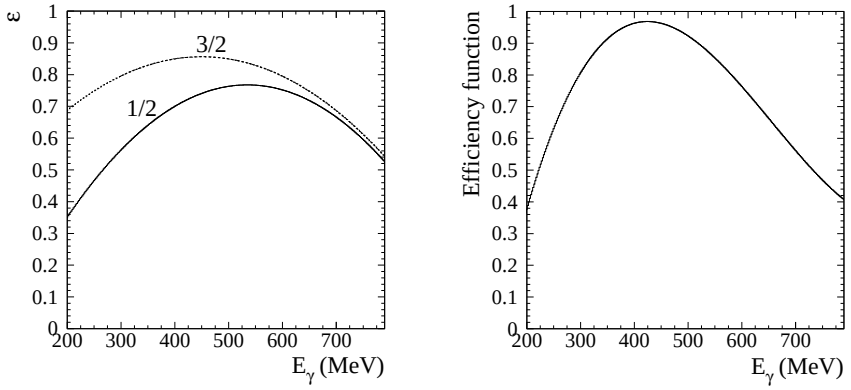

(a) (b)

Figure 4.7: $\vec{\gamma}\vec{\mathrm{p}} \rightarrow \mathrm{p}\pi^+\pi^-$ two-charged, indirect selection: (a) Simulated efficiencies $\epsilon^{\mathrm{p}\pi^0}_{1/2,\mathrm{p},m_\mathrm{X}}$ and $\epsilon^{\mathrm{p}\pi^0}_{3/2,\mathrm{p},m_\mathrm{X}}$, (b) Effective efficiency function $\epsilon^{\mathrm{p}\pi^0}_{(3/2-1/2),\mathrm{p},m_\mathrm{X}}$.

In the analysis of the butanol data, one needs to subtract $N^{\mathrm{p}\pi^+\pi^-}_{\mathrm{2ch}}(1/2)$ from $N^{\mathrm{p}\pi^+\pi^-}_{\mathrm{2ch}}(3/2)$:

$$N^{\mathrm{p}\pi^+\pi^-}_{\mathrm{2ch}}(1/2) = N_{\mathrm{2ch}}(1/2) - N^{\mathrm{1p},m_\mathrm{X}<280\ \mathrm{MeV}}_{\mathrm{2ch}}(1/2)\left(\epsilon^{\mathrm{p}\pi^0}_{3/2,\mathrm{p},m_\mathrm{X}}\right)^{-1}, \qquad (4.1)$$

$$N^{\mathrm{p}\pi^+\pi^-}_{\mathrm{2ch}}(3/2) = N_{\mathrm{2ch}}(3/2) - N^{\mathrm{1p},m_\mathrm{X}<280\ \mathrm{MeV}}_{\mathrm{2ch}}(3/2)\left(\epsilon^{\mathrm{p}\pi^0}_{1/2,\mathrm{p},m_\mathrm{X}}\right)^{-1}. \qquad (4.2)$$

The simulated efficiencies $\epsilon^{\mathrm{p}\pi^0}_{1/2,\mathrm{p},m_\mathrm{X}}$ and $\epsilon^{\mathrm{p}\pi^0}_{3/2,\mathrm{p},m_\mathrm{X}}$ to identify a $\mathrm{p}\pi^0$ event are obtained by simulating $\mathrm{p}\pi^0$ events in the $1/2$ and $3/2$ state respectively. They are not found to be equal as can be seen in Figure 4.7(a). This difference is understood since the $1/2$ and $3/2$ angular and momentum distributions differ from each other and therefore also the energy dependence of the identification efficiencies differs.

The number of events in the second terms of (4.1) and (4.2) contains — apart from the wanted $\mathrm{p}\pi^0$ events— unpolarised background events stemming from the oxygen and carbon nuclei, which are identical in both the $1/2$ and $3/2$ state. However, when weighted with different efficiency corrections, they are no longer equal and thus will not be subtracted correctly in the difference $3/2 - 1/2$.

In order to cope with this, an *effective efficiency function* $\epsilon^{\mathrm{p}\pi^0}_{(3/2-1/2),\mathrm{p},m_\mathrm{X}}$ is defined, for which it holds that:

$$\frac{\epsilon^{\mathrm{p}\pi^0}_{3/2,\mathrm{p},m_\mathrm{X}}\sigma^{\mathrm{p}\pi^0}_{3/2}}{\epsilon^{\mathrm{p}\pi^0}_{3/2,\mathrm{p},m_\mathrm{X}}} - \frac{\epsilon^{\mathrm{p}\pi^0}_{1/2,\mathrm{p},m_\mathrm{X}}\sigma^{\mathrm{p}\pi^0}_{1/2}}{\epsilon^{\mathrm{p}\pi^0}_{1/2,\mathrm{p},m_\mathrm{X}}} = \frac{\epsilon^{\mathrm{p}\pi^0}_{3/2,\mathrm{p},m_\mathrm{X}}\sigma^{\mathrm{p}\pi^0}_{3/2} - \epsilon^{\mathrm{p}\pi^0}_{1/2,\mathrm{p},m_\mathrm{X}}\sigma^{\mathrm{p}\pi^0}_{1/2}}{\epsilon^{\mathrm{p}\pi^0}_{(3/2-1/2),\mathrm{p},m_\mathrm{X}}}.$$

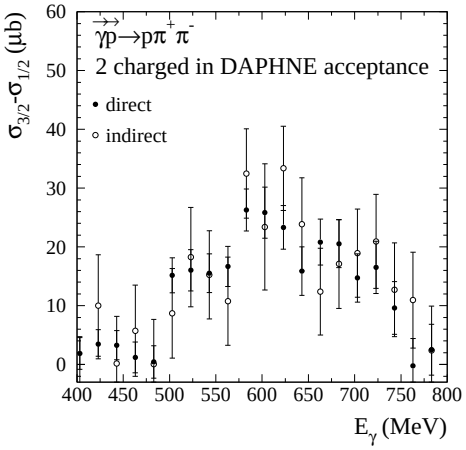

Figure 4.8: $\vec{\gamma}\vec{\mathrm{p}} \rightarrow \mathrm{p}\pi^+\pi^-$ two-charged: Comparison between the direct and the indirect selection method.

Using again the SAID $\mathrm{p}\pi^0$ helicity cross sections this equation can be solved for the effective efficiency function and the result is shown in Figure 4.7(b).

The final number of events is then:

$$N_{\mathrm{2ch}}^{\mathrm{p}\pi^+\pi^-}(3/2) - N_{\mathrm{2ch}}^{\mathrm{p}\pi^+\pi^-}(1/2) = N_{\mathrm{2ch}}(3/2) - N_{\mathrm{2ch}}(1/2) - \left(N_{\mathrm{2ch}}^{\mathrm{1p},m_X<280\ \mathrm{MeV}}(3/2) - N_{\mathrm{2ch}}^{\mathrm{1p},m_X<280\ \mathrm{MeV}}(1/2)\right)\left(\epsilon_{(3/2-1/2),\mathrm{p},m_X}^{\mathrm{p}\pi^0}\right)^{-1}.$$

The resulting cross section differences obtained with the direct and indirect selection method can be compared. This is done in Figure 4.8. The agreement is good but it is clear that the direct method is preferable from the statistical point of view. The indirect method suffers from the fact that two large and almost equal numbers, —$N_{\mathrm{2ch}}^{\mathrm{1p},m_X<280\ \mathrm{MeV}}(3/2)$ and $N_{\mathrm{2ch}}^{\mathrm{1p},m_X<280\ \mathrm{MeV}}(1/2)$— need to be subtracted, which introduces large errors. By default, the data presented further for the two-charged case are taken from the direct selection method.

Figure 4.3(b) gives again the cross section difference. The absolute value and shape compares quite well with what is found in the three-charged case. This situation reminds one of the unpolarised cross sections, where the three and two-charged cases also yield similar contributions. The asymmetry is again quite large, as observed in Figure 4.4(b). The helicity cross sections in Figure 4.5(b) illustrate once more the predominance of the $3/2$ state over the $1/2$ state.

4.3.3 $\vec{\gamma}\vec{\mathrm{p}} \to \mathrm{p}\pi^+\pi^-$: one charged particle in DAPHNE acceptance

The analysis of the butanol data in the one-charged case is again identical to the hydrogen analysis. The same caution as for the unpolarised results is required due to the preliminary status of the MIDAS analysis. The obtained cross section difference $\sigma_{3/2} - \sigma_{1/2}$ is presented in Figure 4.3(c). Figures 4.4(c) and 4.5(c) give the helicity asymmetry and separated cross sections found by combining the cross section difference with the measured unpolarised cross section. Due to the uncertainties in the MIDAS analysis and the low statistics obtained for this type of events, these results are not sufficiently reliable. They are therefore not used when summing up the partial channels and extrapolating to 4π.

4.3.4 $\vec{\gamma}\vec{\mathrm{p}} \to \mathrm{p}\pi^+\pi^-$: extrapolation to 4π

A priori it is not evident that the extrapolation used for the unpolarised total cross section can be analogously applied to the cross section difference $\sigma_{3/2} - \sigma_{1/2}$. The sign of the difference might change outside the acceptance which would make the straightforward extrapolation incorrect. At this point a model is required to predict the helicity dependence outside the acceptance. When discussing the results of the RPR model in Chapter 7 we will come back to this issue.

In order to obtain a first idea of the extrapolated result, we assume at the moment that the cross section difference does not change outside the acceptance. We have observed that the relative strength of the cross section difference for the three types of $\mathrm{p}\pi^+\pi^-$ events corresponds to the relative strength of the total unpolarised cross section. This supports the use of the unpolarised acceptance function for the extrapolation to 4π. The unpolarised acceptance function is the simulated acceptance function obtained by generating unpolarised $\gamma\mathrm{p} \to \mathrm{p}\pi^+\pi^-$ events uniformly over phase space. In full analogy with the unpolarised case, this extrapolation accounts for those events missed because they are outside the polar angle acceptance (23°–158°) or because their momentum is below threshold. With the simulation the momentum thresholds for each type of events can be determined:

➢ Three-charged case: $n_{\mathrm{MWPC}} = 3$ and $n_{\mathrm{scint}} \geq 1$

$$p_{\mathrm{p}}^{\mathrm{min,3ch}} = 300 + 0.08(\theta_{\mathrm{p}} - 45^\circ)^2 \text{ MeV/c},$$
$$p_{\pi^\pm}^{\mathrm{min,3ch}} = 67 + 0.005(\theta_{\pi^\pm} - 90^\circ)^2 \text{ MeV/c}.$$

➢ Two-charged case: $n_{\mathrm{MWPC}} = 2$ and $n_{\mathrm{scint}} = 2$

$$p_{\mathrm{p}}^{\mathrm{min,2ch}} = 187 - 2.2\theta_{\mathrm{p}} + 0.055\theta_{\mathrm{p}}^2 \text{ MeV/c},$$
$$p_{\pi^\pm}^{\mathrm{min,2ch}} = 20 + 0.003(\theta_{\pi^\pm} - 90^\circ)^2 \text{ MeV/c}.$$

➢ One-charged case: $n_{\mathrm{MWPC}} = 1$ and $n_{\mathrm{scint}} = 1$

$$p_{\mathrm{p}}^{\mathrm{min,1ch}} = 225 - 6.5\theta_{\mathrm{p}} + 0.11\theta_{\mathrm{p}}^2 \ \mathrm{MeV/c},$$
$$p_{\pi^\pm}^{\mathrm{min,1ch}} = 8 + 0.002(\theta_{\pi^\pm} - 90^\circ)^2 \ \mathrm{MeV/c}.$$

Comparing these values to what was found in the case of the hydrogen target (see p. 79), one observes that only for the three-charged events the thresholds are different in the butanol case. They are about 10% higher. This increase can be understood since the charged particles loose more energy when traveling through the denser butanol target than through the hydrogen target. The fact that only the three-charged events suffer from this effect can be explained by the fact that in the other cases, events where a particle does not reach the detector, can be recovered by the detection of one or more of the other particles.

In Figure 4.9 the extrapolated result for the total cross section difference, the helicity asymmetry and the separated helicity cross sections are gathered. Only the combined three- and two-charged partial results are used to carry out the extrapolation.

The systematical errors on the measured cross section difference are the same as for the unpolarised cross section. However, as the uncertainty for the extrapolation is larger in the polarised case, we increase this systematical error from 2% to 3%. As mentioned, extra errors are present due to the beam and target polarisation. Summed quadratically, we find a systematical error of 6%.

In summary, we find for the $\vec{\gamma}\vec{\mathrm{p}} \to \mathrm{p}\pi^+\pi^-$ reaction a large and positive helicity asymmetry. The $\sigma_{3/2}$ cross section is dominating and has a strong resonance behaviour with a peak around 600–650 MeV. The $\sigma_{1/2}$ cross section is significantly smaller and does not exhibit a resonance structure. The dominance of the 3/2 intermediate state can be explained by the interference of the following two processes: $\gamma\mathrm{p} \to \pi^-\Delta^{++} \to \pi^-\pi^+\mathrm{p}$ and $\gamma\mathrm{p} \to \mathrm{D}_{13} \to \pi^-\Delta^{++} \to \pi^-\pi^+\mathrm{p}$. As amply discussed when presenting the results of the double pion photoproduction model in Chapter 7, these are the main processes contributing to the reaction. Both have a spin-3/2 intermediate state and thus enhance $\sigma_{3/2}$ over $\sigma_{1/2}$.

4.4 $\vec{\gamma}\vec{\mathrm{p}} \to \mathrm{n}\pi^+\pi^0$

4.4.1 $\vec{\gamma}\vec{\mathrm{p}} \to \mathrm{n}\pi^+\pi^0$ with $\pi^+\pi^0$ in DAPHNE acceptance

As mentioned above, also the analysis for the $\mathrm{n}\pi^+\pi^0$ channel has been designed to be directly applicable to the butanol data. The main ingredient in this analysis is the neutral pion detection efficiency. In the case of the butanol target this efficiency is found to be equal to the one found for the hydrogen target. The simulation of the background contributions from $\vec{\gamma}\vec{\mathrm{p}} \to \mathrm{n}\pi^+$ and $\vec{\gamma}\vec{\mathrm{p}} \to \mathrm{p}\pi^0$ is separately performed for the 1/2 and the 3/2 state in order to obtain their contribution to $\sigma_{3/2} - \sigma_{1/2}$. Figure 4.10 illustrates the simulated

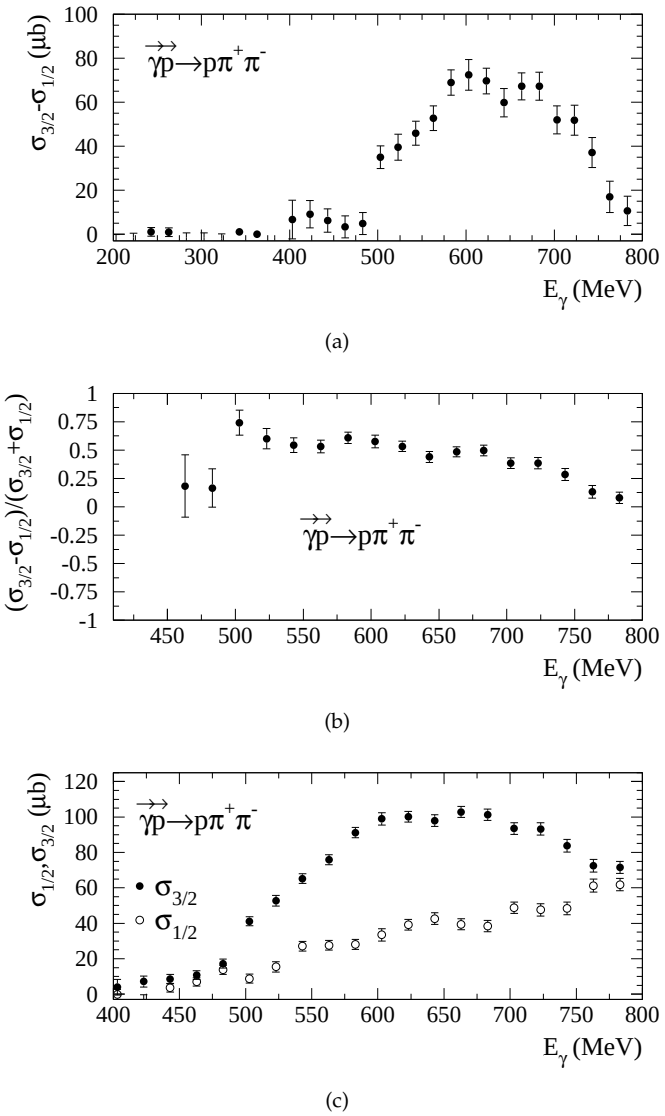

Figure 4.9: $\vec{\gamma}\vec{\mathrm{p}} \rightarrow \mathrm{p}\pi^+\pi^-$: (a) Cross section difference $\sigma_{3/2} - \sigma_{1/2}$ as a function of photon energy, (b) Helicity asymmetry as a function of photon energy, (c) Cross sections $\sigma_{3/2}$ and $\sigma_{1/2}$ as a function of photon energy.

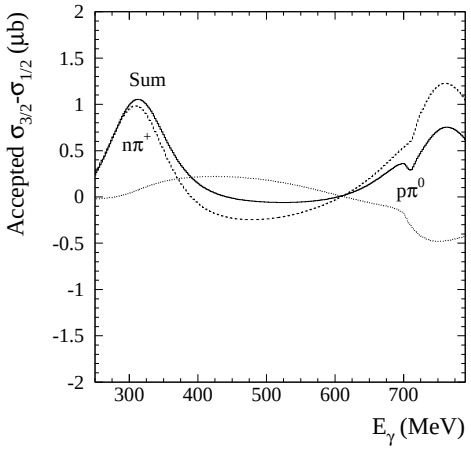

Figure 4.10: $\vec{\gamma}\vec{\mathrm{p}} \rightarrow \mathrm{n}\pi^+\pi^0$ for $\pi^0(\geq 1\gamma)$: Simulated background contribution from $\mathrm{n}\pi^+$ and $\mathrm{p}\pi^0$.

background in the case of $\pi^0(\geq 1\gamma)$. The magnitude of this background is smaller than the statistical error we find for the final result and therefore the background subtraction has a minor influence. The situation for $\pi^0(2\gamma)$ is analogous, save for the fact that the background level is even lower.

The resulting cross section difference $\sigma_{3/2} - \sigma_{1/2}$ in both π^0 detection options is compared in Figure 4.11. As for the unpolarised cross section, the agreement between the two methods is quite good such that one can rely on the more extensive background subtraction in the $\pi^0(\geq 1\gamma)$ case. This is again preferable in terms of statistics. By default the results obtained with this method are shown further on.

Figure 4.12 shows, apart from the cross section difference, also the helicity asymmetry and the separated cross sections $\sigma_{3/2}$ and $\sigma_{1/2}$. A strong positive cross section difference is found, indicating that the 3/2 intermediate state is clearly favoured in this reaction. The relative strength of the helicity dependence as observed in the asymmetry is of the order of 50%. The $\sigma_{3/2}$ cross section has a very strong resonance peak around 750 MeV while $\sigma_{1/2}$ is flatter.

4.4.2 $\vec{\gamma}\vec{\mathrm{p}} \rightarrow \mathrm{n}\pi^+\pi^0$: extrapolation to 4π

The same arguments as given for the extrapolation of the $\vec{\gamma}\vec{\mathrm{p}} \rightarrow \mathrm{p}\pi^+\pi^-$ reaction hold here: information from a model calculation is needed to perform the extrapolation correctly. This subject is revisited in Chapter 7. At the moment we confine the extrapolation to the naive method as used in the unpolarised case. Figure 4.13 presents the so obtained results. The D_{13} resonance is assumed to be responsible for the strong signal in the 3/2 cross section $\sigma_{3/2}$.

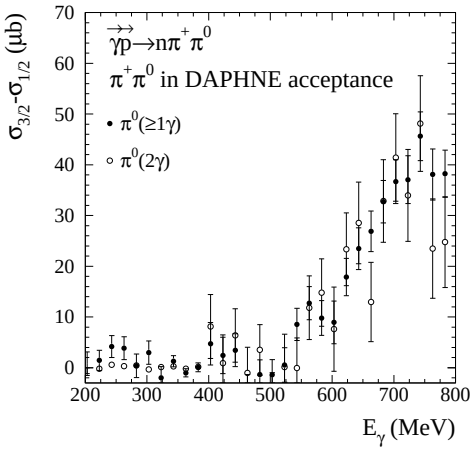

Figure 4.11: $\vec{\gamma}\vec{\mathrm{p}} \to \mathrm{n}\pi^+\pi^0$ with $\pi^+\pi^0$ in DAPHNE acceptance: Comparison between $\pi^0(2\gamma)$ and $\pi^0(\geq 1\gamma)$.

Also this interpretation is extensively treated in Chapter 7.

The systematical error on the measured cross section difference is increased with respect to the unpolarised cross section due to the larger uncertainty in the extrapolation and the beam and target polarisation. We estimate the total systematical error to be 6%.

4.5 Contribution of $\mathrm{p}\pi^+\pi^-$ and $\mathrm{n}\pi^+\pi^0$ to the GDH sum rule on the proton and the proton forward spin polarisability

Having measured the cross section difference $\sigma_{3/2} - \sigma_{1/2}$, we are able to calculate the contribution of the studied reaction channels to the total GDH integral I_{GDH}:

$$I_{\mathrm{GDH}} = \int_{\nu_0}^{\infty} \frac{\sigma_{1/2} - \sigma_{3/2}}{\nu} \mathrm{d}\nu, \tag{4.3}$$

and the forward spin polarisability γ_0:

$$\gamma_0 = \frac{1}{4\pi^2} \int_{\nu_0}^{\infty} \frac{\sigma_{1/2} - \sigma_{3/2}}{\nu^3} \mathrm{d}\nu. \tag{4.4}$$

Evidently, the maximum value of the photon energy ν to which the measured integrand can be integrated is restricted to 800 MeV. Replacing the infinity sign by $E_{\gamma,\mathrm{max}}$, both integrals can be evaluated as a function of this upper integration limit. The so obtained results for I_{GDH} and γ_0 are shown in Figure 4.14 and Figure 4.15 for the $\mathrm{p}\pi^+\pi^-$ and the $\mathrm{n}\pi^+\pi^0$ channel, respectively.

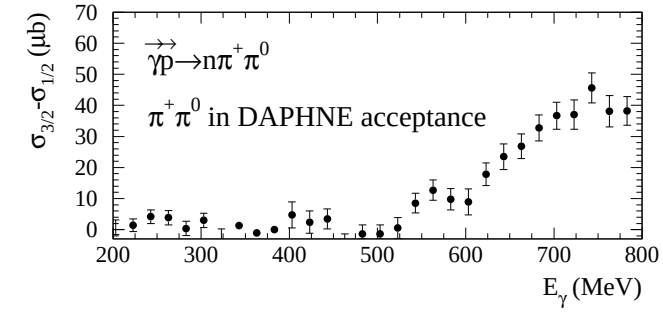

(a)

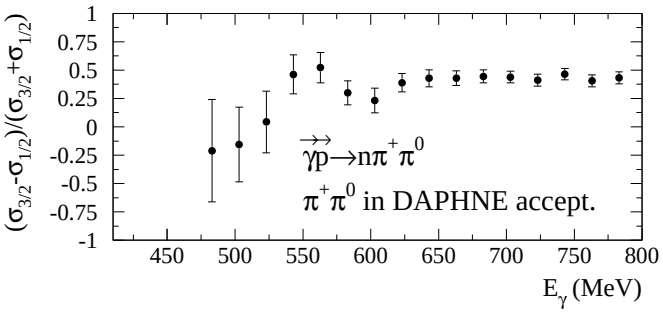

(b)

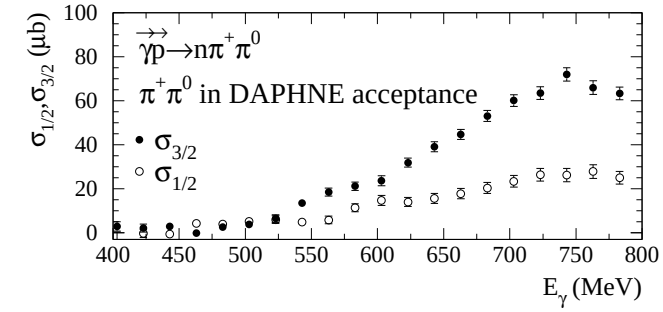

(c)

Figure 4.12: $\vec{\gamma}\vec{\mathrm{p}} \rightarrow \mathrm{n}\pi^+\pi^0$ with $\pi^+\pi^0$ inside DAPHNE acceptance: (a) Cross section difference $\sigma_{3/2} - \sigma_{1/2}$ as a function of photon energy, (b) Helicity asymmetry as a function of photon energy, (c) Cross sections $\sigma_{3/2}$ and $\sigma_{1/2}$ as a function of photon energy.

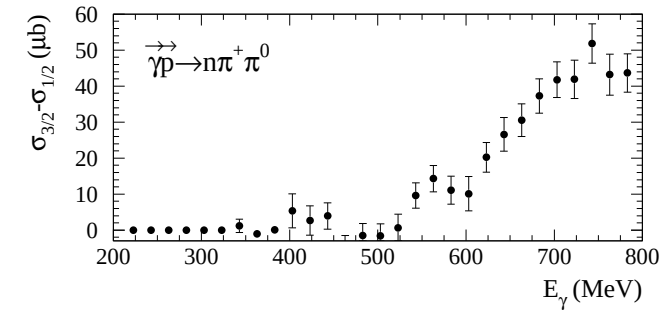

(a)

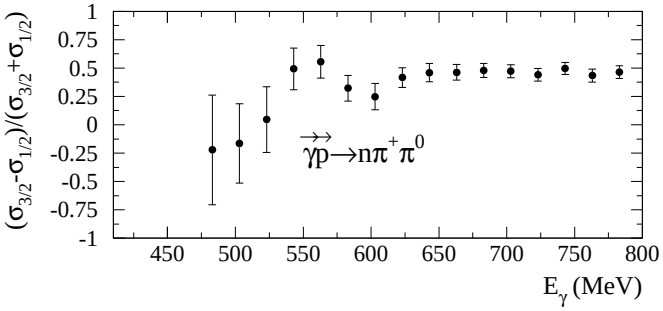

(b)

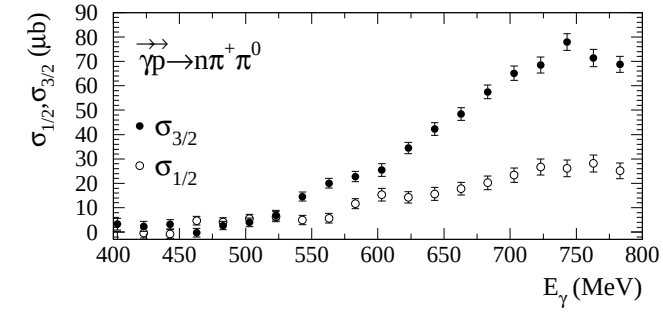

(c)

Figure 4.13: $\vec{\gamma}\vec{p} \rightarrow n\pi^+\pi^0$: (a) Cross section difference $\sigma_{3/2} - \sigma_{1/2}$ as a function of photon energy, (b) Helicity asymmetry as a function of photon energy, (c) Cross sections $\sigma_{3/2}$ and $\sigma_{1/2}$ as a function of photon energy.

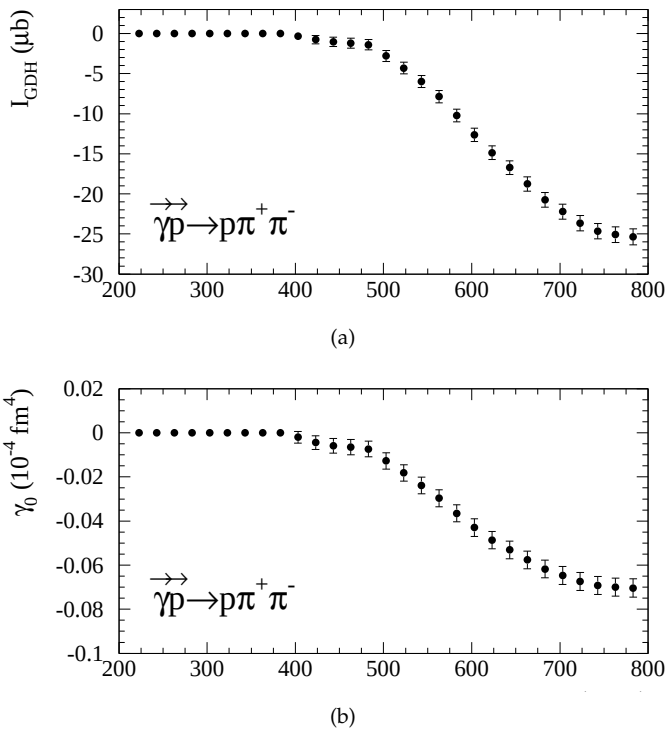

Figure 4.14: $\vec{\gamma}\vec{\mathrm{p}} \rightarrow \mathrm{p}\pi^+\pi^-$: (a) Contribution to the GDH integral I_{GDH} as a function of the upper integration limit, (b) Contribution to the forward spin polarisability γ_0 as a function of the upper integration limit.

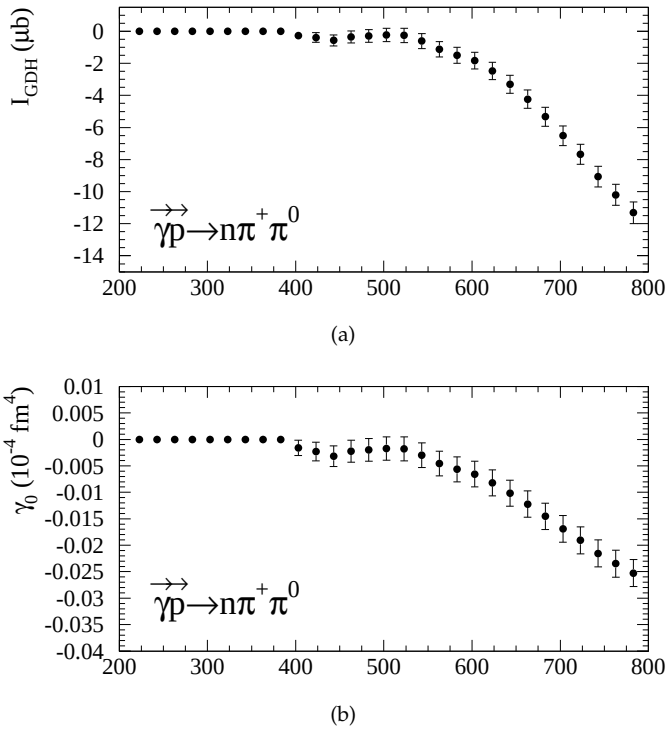

Figure 4.15: $\vec{\gamma}\vec{\mathrm{p}} \rightarrow \mathrm{n}\pi^+\pi^0$: (a) Contribution to the GDH integral I_{GDH} as a function of the upper integration limit, (b) Contribution to the forward spin polarisability γ_0 as a function of the upper integration limit.

The GDH sum rule predicts -204 μb as a value for the total I_{GDH}. The measured contributions, integrated up to 800 MeV, are $-(25.4 \pm 1 \pm 1.5)$ μb (statistical and systematical error, respectively) from $\mathrm{p}\pi^+\pi^-$ and $-(11.3 \pm 0.7 \pm 0.7)$ μb from $\mathrm{n}\pi^+\pi^0$. This means that both channels together contribute about 18% to the GDH sum rule. As a consequence we can conclude from this measurement that these double pion channels significantly contribute to the GDH sum rule.

The value for γ_0 found in [54] by combining the measured contribution of the total absorption cross section difference in the energy range between 200 and 800 MeV with predictions for the contributions of the lower and higher energy ranges is $-(0.87 \pm 9 \pm 19)\ 10^{-4}$ fm^4. The contributions from the $\mathrm{p}\pi^+\pi^-$ and the $\mathrm{n}\pi^+\pi^0$ channel up to 800 MeV amount to $-(0.070 \pm 0.004 \pm 0.004)\ 10^{-4}$ fm^4 and $-(0.025 \pm 0.003 \pm 0.002)\ 10^{-4}$ fm^4, respectively. Summed, the studied channels contribute 11% to the forward spin polarisability, which is again a sizeable fraction.

5

Regge theory

The RPR model for double pion photoproduction presented in the next chapter contains Regge trajectory exchange. As a prologue, a brief introduction to Regge theory is given in this chapter. In Section 5.1 the basic principles of Regge theory are illustrated phenomenologically. The formal derivation of the Regge scattering amplitude is detailed in Section 5.2. Finally Section 5.3 presents a closer look at Regge trajectories.

5.1 Introduction and phenomenology

In 1959 Regge introduced the idea of complex angular momenta in non-relativistic potential scattering [108, 109]. He showed that it is useful to analytically continue the scattering amplitude into the complex angular momentum plane. The singularities in the scattering amplitudes coincide in many cases with the poles in this complex plane, known as *Regge poles*. Details on the basic principles and applications of *Regge theory* can be found in [35]. In the beginning of the 60's the Regge concept was adopted in high energy particle physics in order to be able to cope theoretically with the exchange of high spin particles [17, 31, 32, 33, 50]. It has also been shown to be successful in the phenomenology of high energy exchange mechanisms e.g. quite recently in [15, 37, 58].

In order to introduce the main features of Regge theory, consider a general two-body reaction

$$\mathrm{a} + \mathrm{b} \rightarrow \mathrm{c} + \mathrm{d}. \tag{5.1}$$

It is usual to define the *Mandelstam variables* s, t and u as the relativistic invariants

$$\begin{aligned} s &= (p_\mathrm{a} + p_\mathrm{b})^2, \\ t &= (p_\mathrm{a} - p_\mathrm{c})^2, \\ u &= (p_\mathrm{a} - p_\mathrm{d})^2, \end{aligned}$$

with p_a, p_b, p_c, p_d the respective four-vector momenta of the involved particles. The Mandelstam variables obey

$$s + t + u = m_\mathrm{a}^2 + m_\mathrm{b}^2 + m_\mathrm{c}^2 + m_\mathrm{d}^2$$

where m_a, m_b, m_c and m_d are the respective masses of the particles. The existence of such a relation is natural since a two-body reaction has only two independent variables. Define θ_s as the scattering angle between the direction of motion of the particles a and c in the rest-frame defined by $\vec{p}_\mathrm{a} + \vec{p}_\mathrm{b} = \vec{0}$, which is the s-channel center-of-mass system. Analogously define θ_t as the scattering angle in the t-channel center-of-mass system ($\vec{p}_\mathrm{a} + \vec{p}_\mathrm{c} = \vec{0}$). One has the following general relations for t and u, where the label 's' is used for s-channel center-of-mass quantities:

$$t = m_\mathrm{a}^2 + m_\mathrm{c}^2 - 2\left(E_\mathrm{a}^s E_\mathrm{c}^s - |\vec{p}_\mathrm{a}^{\,s}|\,|\vec{p}_\mathrm{c}^{\,s}|\cos\theta_s\right)$$
$$u = m_\mathrm{a}^2 + m_\mathrm{d}^2 - 2\left(E_\mathrm{a}^s E_\mathrm{d}^s + |\vec{p}_\mathrm{a}^{\,s}|\,|\vec{p}_\mathrm{d}^{\,s}|\cos\theta_s\right)$$

In the *equal-mass hypothesis* where $m_\mathrm{a} = m_\mathrm{b} = m_\mathrm{c} = m_\mathrm{d} = m$ this can simply be written as:

$$t = -\frac{s - 4m^2}{2}\left(1 - \cos\theta_s\right)$$
$$u = -\frac{s - 4m^2}{2}\left(1 + \cos\theta_s\right).$$

A typical two-body angular distribution $\frac{\mathrm{d}\sigma}{\mathrm{d}t}$ exhibits at high s a strong forward peaking. A forward peak corresponds with $\cos\theta_s \to 1$ and small $|t|$. As an example, Figure 5.1 shows the differential cross section $\frac{\mathrm{d}\sigma}{\mathrm{d}t}$ as a function of t for the two-body process $\gamma p \to \pi^+\mathrm{n}$, for different incoming photon energies [58]. A similar behaviour is generally observed for backward angles, i.e. $\cos\theta_s \to -1$ and small $|u|$.

The peak-features appear to depend on the quantum numbers exchanged in the scattering process and can thus be explained in terms of exchange mechanisms. Phenomenologically one finds that a good understanding of these features cannot be obtained by assuming a simple pole exchange. However, the exchange of a *family* of particles which have the same internal quantum numbers like charge, baryon number, strangeness, ... but carry different spin can give a satisfactory result and this is what can be obtained in Regge theory. The families of particles are called *Regge trajectories*. In the following section, a formal description of the discussed phenomenology is given.

5.2 Formal derivation of the Regge scattering amplitude

In order to gain a better insight in the basic Regge ideas, consider the behaviour of the *scattering amplitude* $A(s,t)$ for a process as in (5.1), specifically for the exchange of high spin particles at high energies.

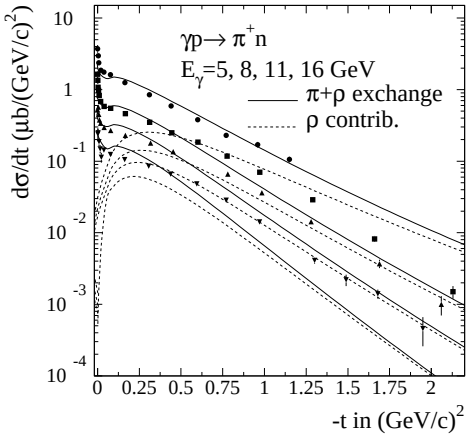

Figure 5.1: High energy angular distribution $\frac{d\sigma}{dt}$ for $\gamma p \to \pi^+ n$ at photon energies $E_\gamma = 5$, 8, 11 and 16 GeV. The upper curves and data correspond with $E_\gamma = 5$ GeV, the lower ones are at $E_\gamma = 16$ GeV. The curves represent a calculation including π and ρ Regge trajectory exchanges from [58]. The data are from [19].

The reaction a + b $\to$ c + d can be identified as the s-channel process. Through crossing symmetry it shares its scattering amplitude with a + $\bar{\text{c}}$ $\to$ $\bar{\text{b}}$ + d (t-channel) and a + $\bar{\text{d}}$ $\to$ $\bar{\text{b}}$ + c (u-channel). The three kinds of scattering processes are illustrated in Figure 5.2. The s, t and u-channels are described with the same scattering amplitude, albeit in different kinematical regions of the involved variables. As will become clear from the following formal discussion, it is the physically acceptable analytical continuation of $A(s,t)$ between these regions that will benefit from Regge's postulate concerning complex angular momenta.

Further on in this discussion, we will assume for simplicity of the presenta-

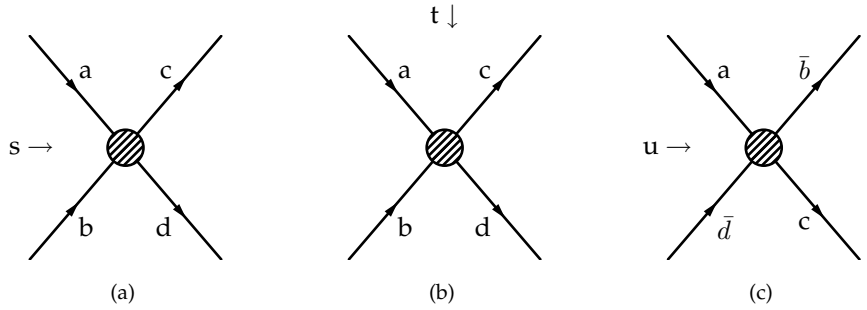

Figure 5.2: The a + b $\to$ c + d scattering process in the s, t and u-channel.

tion, that the four particles involved in the scattering process have equal mass (equal-mass hypothesis) and do not carry internal spin. These simplifying assumptions do not alter the conclusions and the generalisation is straightforward.

Because of the conservation of angular momentum one is classically led to work with *partial-wave amplitudes* , defining a separate scattering amplitude for each possible angular momentum state. Since the initial state is in general a sum over several eigenstates of angular momentum, the total scattering amplitude is a sum over all partial-wave amplitudes. The total angular momentum j carried by two spin-less particles is given by their relative orbital momentum l. The angular dependence of such a state can be described with a Legendre function of the first kind. In the s-channel the scattering amplitude $A(s,t)$ can be written as the partial-wave series:

$$A(s,t) = \sum_{l=0}^{\infty} (2l+1) A_l(s) P_l(\cos\theta_s), \tag{5.2}$$

where $A_l(s)$ is defined as:

$$A_l(s) = \frac{1}{2} \int_{-1}^{+1} A\left(s, t\left(\cos\theta_s\right)\right) P_l(\cos\theta_s) \mathrm{d}\cos\theta_s \tag{5.3}$$

and $\cos\theta_s$ can be written as:

$$\cos\theta_s = 1 + \frac{2t}{s-4m^2} = -\left(1 + \frac{2u}{s-4m^2}\right). \tag{5.4}$$

Analogously one has for the t-channel:

$$A(s,t) = \sum_{l=0}^{\infty} (2l+1) A_l(t) P_l(\cos\theta_t), \tag{5.5}$$

$$A_l(t) = \frac{1}{2} \int_{-1}^{+1} A\left(s\left(\cos\theta_t\right), t\right) P_l(\cos\theta_t) \mathrm{d}\cos\theta_t, \tag{5.6}$$

$$\cos\theta_t = 1 + \frac{2s}{t-4m^2} = -\left(1 + \frac{2u}{t-4m^2}\right). \tag{5.7}$$

The physical regions for the s and t-channel are delimited by:

s-channel	t-channel
$s \geq 4m^2$	$t \geq 4m^2$
$-1 \leq \cos\theta_s \leq +1$	$-1 \leq \cos\theta_t \leq +1$
$\Updownarrow$	$\Updownarrow$
$4m^2 - s \leq t \leq 0$	$4m^2 - t \leq s \leq 0$
$4m^2 - s \leq u \leq 0$	$4m^2 - t \leq u \leq 0.$

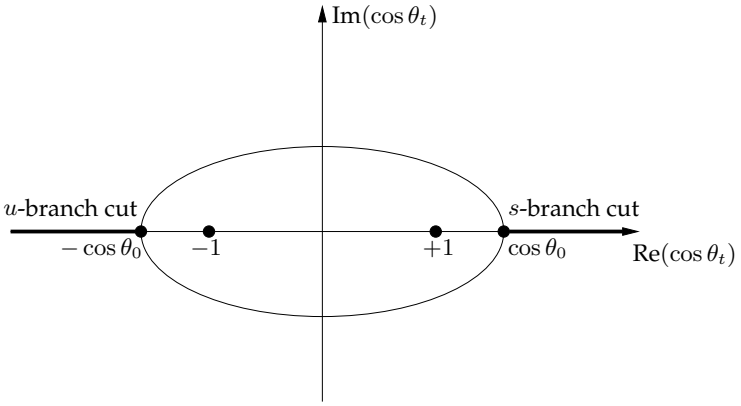

Figure 5.3: The Lehmann-Martin ellipse in the complex $\cos\theta_t$ plane. The s and u-branch cuts are indicated on the real axis by a thick line.

Similar expressions hold for the u-channel.

The partial-wave series (5.2), resp. (5.5) are known to converge for $s \geq 4m^2$, resp. $t \geq 4m^2$ and within the *Lehmann-Martin ellipse* [83, 93, 94]. The Lehmann-Martin ellipse is defined in the complex $\cos\theta_s$ ($\cos\theta_t$) plane, has foci at $+1$ and -1 and large axis $\cos\theta_0$:

$$\cos\theta_0 := 1 + \frac{8m^2}{s - 4m^2} \qquad (s\text{-channel}),$$
$$\cos\theta_0 := 1 + \frac{8m^2}{t - 4m^2} \qquad (t\text{-channel}).$$

In Figure 5.3 the ellipse in the t-channel case is plotted. In accordance with (5.7) the axis $\cos\theta_0$ stems from the s and u-channel branch points of $A(s,t)$, which occur at $s(u) = 4m^2$ for fixed t ($t > 0$):

$$\cos\theta_t(s = 4m^2) = 1 + \frac{8m^2}{t - 4m^2} = \cos\theta_0,$$
$$\cos\theta_t(u = 4m^2) = -\left(1 + \frac{8m^2}{t - 4m^2}\right) = -\cos\theta_0.$$

Corresponding branch cuts are defined along the real axis: one has the *s-branch cut* for $\cos\theta_t \geq \cos\theta_0$ and the *u-branch cut* for $\cos\theta_t \leq -\cos\theta_0$. These cuts represent the s and u-channel singularities at fixed t in the t-channel.

Figure 5.4 depicts the Mandelstam plane for the discussed scattering process under the equal-mass hypothesis. The hatched regions are the respective physical environments for the s, t and u-channel. The two-particle branch points at $s = 4m^2$, $t = 4m^2$ and $u = 4m^2$ with corresponding branch cuts are drawn. Also shown are the poles at $s = m^2$, $t = m^2$ and $u = m^2$ which correspond e.g. with resonant exchanges in each channel.

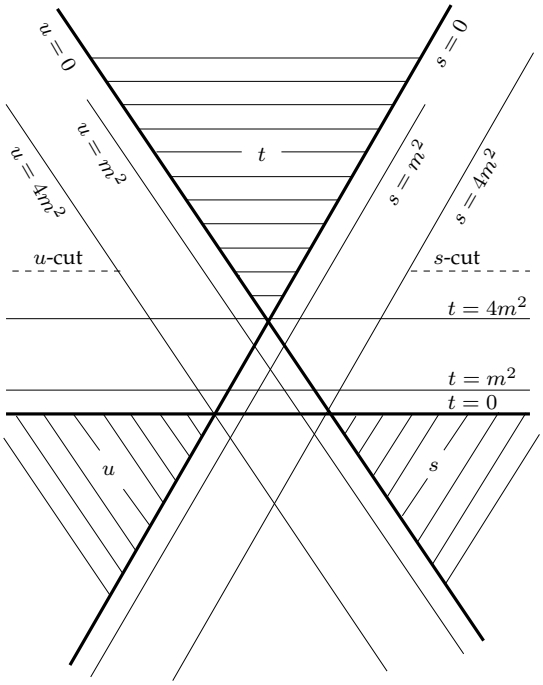

Figure 5.4: Mandelstam plane for the equal-mass scattering process as discussed in the text. The poles at m^2 and the branch points at $4m^2$ are shown.

In order to investigate the phenomenology discussed in Section 5.1, consider the scattering amplitude in the t-channel. The t-channel pole is e.g. an exchanged particle with spin l and mass m_l. Consider $\frac{\mathrm{d}\sigma}{\mathrm{d}t}$ in the region where s is large and $|t|$ is small, with $s \gg |t|$ and $t < 0$, a region called the *Regge limit*. The angular distribution can be expressed as a function of the invariant amplitude $A(s,t)$ as:

$$\frac{\mathrm{d}\sigma}{\mathrm{d}t} = \frac{|A(s,t)|^2}{16\pi s^2} \tag{5.8}$$

where one can write for the exchange of a particle with spin l and mass m_l:

$$A(s,t) \sim \mathcal{V}_{\text{ac}}(t)\mathcal{V}_{\text{bd}}(t)\frac{P_l(\cos\theta_t)}{t - m_l^2}. \tag{5.9}$$

Here $\mathcal{V}_{\text{ac}}(t)$ and $\mathcal{V}_{\text{bd}}(t)$ are the (ac) and (bd) vertex functions respectively. The *optical theorem*, which is imposed by unitarity, gives for the total cross section, where $t = 0$:

$$\sigma_{\text{tot}} = \frac{\text{Im}A(s, t = 0)}{s}. \tag{5.10}$$

The Legendre functions have the following asymptotic behaviour:

$$P_l(z) \xrightarrow{z\to\infty} \frac{1}{\sqrt{\pi}}\frac{\Gamma(l + 1/2)}{\Gamma(l + 1)}(2z)^l, \tag{5.11}$$

under the condition that $l \geq -1/2$, with Γ the gamma function. In combination with (5.7) one finds in the Regge limit:

$$P_l(\cos\theta_t) \xrightarrow{s\to\infty, s\gg|t|} \frac{1}{\sqrt{\pi}}\frac{\Gamma(l + 1/2)}{\Gamma(l + 1)}(2\cos\theta_t)^l \sim s^l. \tag{5.12}$$

for $l \geq -1/2$. This implies for (5.8), (5.9) and (5.10):

$$A(s,t) \sim s^l \tag{5.13}$$

$$\frac{\mathrm{d}\sigma}{\mathrm{d}t} \sim s^{2l-2} \qquad s \gg |t| \quad (t < 0) \tag{5.14}$$

$$\sigma_{\text{tot}} \sim s^{l-1}. \tag{5.15}$$

As soon as the spin $l > 1$ this behaviour is in contradiction with the trend of experimental data as well as with the *Froissart bound*. Froissart, and later also Martin, showed that unitarity limits the asymptotic increase of σ_{tot} to [51, 92]:

$$\sigma_{\text{tot}} \leq \mathcal{C}\ln^2 s \qquad \text{The Froissart bound},$$

where $\mathcal{C}$ is a constant.

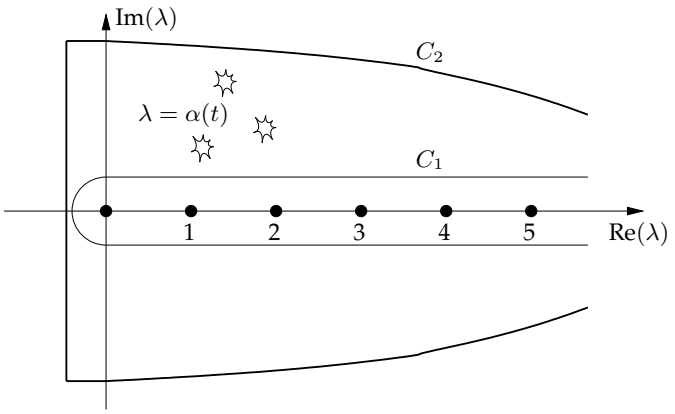

Figure 5.5: The complex angular momentum plane. Regge poles $\alpha(t)$ are represented by small 'explosions'.

The origin of this problem is that in traversing the kinematical region towards the Regge limit, one leaves the convergence region of the t-channel partial-wave expansion and ends up outside of the Lehmann-Martin ellipse. This difficulty can be solved by summing the t-channel partial-wave series before continuing into the Regge limit. As is shown below, this corresponds to moving from a single particle exchange to the exchange of a family of particles (Regge trajectory). The purpose is to find an expression for $A(s,t)$ that allows a good analytical continuation outside the Lehmann-Martin ellipse.

It is a well-tried technique to transform a series expansion into a contour integral in the complex plane of the summation variable. For the partial-wave expansion of $A(s,t)$ the complex version of the angular momentum l is denoted λ. The *Residue theorem* allows to write (5.5) as the contour integral:

$$A(s,t) = -\frac{1}{2i}\oint_{\mathrm{C}_1} \frac{(2\lambda+1)A_\lambda(t)P_\lambda(-\cos\theta_t)}{\sin(\pi\lambda)}\mathrm{d}\lambda. \tag{5.16}$$

This expression is known as the *Sommerfeld-Watson representation*. We have defined $P_\lambda(z) := P_l(z)$ and $A_\lambda(z) := A_l(z)$ for $\lambda = l$ a positive integer. The contour C_1 is defined as shown in Figure 5.5, it encircles the positive real λ-axis. The factor $\frac{1}{\sin(\pi\lambda)}$ provokes poles at $\lambda = 0, 1, 2, 3, \ldots$ with

$$\sin(\pi\lambda) \xrightarrow{\lambda\to l} (-1)^\lambda(\lambda - l)\pi$$

for l a positive integer. A necessary condition for (5.16) to be valid is the *postulate of maximal analyticity of the second kind* (after [35]), which states that $A_l(t)$ has only isolated singularities in l. The validity of the application of Regge theory to particle physics stands with this assumption. Although not proven in general, it appears to be in agreement with experimental data and it has been shown to hold for several strong interaction models.

The advantage of the Sommerfeld-Watson representation (5.16) is that the contour C_1 can be deformed to infinity in order to perform the sought analytical continuation. The expression can then be continued into the Regge limit. To this end, the convergence of $A_l(t)$ for $l \to \infty$ needs to be verified. Bringing the singularities of the s and u-branch cuts of $A(s,t)$ into account, one can write down the *Froissart-Gribov projection*:

$$A_l(t) = \frac{1}{2\pi} \int_{\cos\theta_0}^{\infty} \left[D_s(\cos\theta_t, t) + (-)^l D_u(-\cos\theta_t, t) \right] Q_l(\cos\theta_t) \mathrm{d}\cos\theta_t,$$

which is completely equivalent to (5.6) including now the s and u-channel singularities. The discontinuity functions D_s and D_u along the s and u-branch are defined as:

$$D_s(s,t) = \frac{1}{2i} \left[A(s + i\epsilon, t, u) - A(s - i\epsilon, t, u) \right]$$
$$D_u(u,t) = \frac{1}{2i} \left[A(s, t, u + i\epsilon) - A(s, t, u - i\epsilon) \right].$$

The Legendre function of the second kind $Q_l(z)$ has the limit

$$Q_l(z) \xrightarrow{l\to\infty}\sim l^{-1/2} e^{-(l+1/2) log(z+\sqrt{z^2-1})}.$$

This ensures the convergence of $A_l(t)$ for $l \to \infty$, provided the non-converging factor $(-)^l$ is dealt with properly. To this end one defines two amplitudes, one for even l and one for odd l:

$$A_l^{\zeta}(t) = \frac{1}{2\pi} \int_{\cos\theta_0}^{\infty} \left[D_s(\cos\theta_t, t) + \zeta D_u(-\cos\theta_t, t) \right] Q_l(\cos\theta_t) \mathrm{d}\cos\theta_t,$$

where the *signature* $\zeta = \pm 1$ has been introduced. The *even-signature* amplitude $A_l^{+1}(t)$ and the *odd-signature* amplitude $A_l^{-1}(t)$ both converge in the $l \to \infty$ limit. Therefore the analytical continuation will be feasible if the even and odd angular momenta cases are separated. This separation can be associated with the different symmetry properties under $s \leftrightarrow u$ crossing (interchange of the two final state particles) for an even and odd angular momentum final state.

Having confirmed the necessary convergence properties of $A_l(t)$, the contour C_1 can be deformed to C_2 as plotted in Figure 5.5 and C_2 can safely be extended to infinity. Regge theory postulates that the only singularities of $A_\lambda(t)$ in the complex λ plane are poles, at $\lambda = \alpha(t)$, which are shown as little 'explosions' in Figure 5.5. They are called Regge poles, $\alpha(t)$ is the Regge trajectory. One can then write for $A^{\zeta}(s,t)$:

$$A^{\zeta}(s,t) = -\frac{1}{2i} \int_{-k-i\infty}^{-k+i\infty} (2\lambda+1) \frac{A_\lambda^{\zeta}(t)}{\sin(\pi\lambda)} P_\lambda(-\cos\theta_t) \mathrm{d}\lambda$$
$$- \frac{2\pi i}{2i} (2\alpha^{\zeta}(t) + 1) \frac{\beta^{\zeta}(t)}{\sin(\pi\alpha^{\zeta}(t))} P_{\alpha^{\zeta}(t)}(\cos\theta_t)$$
$$+ \text{other poles}, \quad (5.17)$$

where $\beta(t)$ is the residue of the Regge pole and k is a strictly positive constant.

In the Regge regime where $s \gg |t|$ and $t < 0$, the first term appears as a background term since, ($k \leq 1/2$, cfr. (5.12)),

$$P_{-k}(-\cos\theta_t) \xrightarrow{\cos\theta_t\to\infty, s\to\infty} \sim s^{-k} \to 0$$

as one can choose $k = 1/2$. Following the asymptotic limit of the Legendre function as given in (5.11), the second term is governed by the behaviour:

$$P_{\alpha^\zeta(t)}(\cos\theta_t) \xrightarrow{\cos\theta_t\to\infty, s\to\infty} \frac{1}{\sqrt{\pi}} \frac{\Gamma(\alpha^\zeta(t)+1/2)}{\Gamma(\alpha^\zeta(t)+1)} (2\cos\theta_t)^{\alpha^\zeta(t)} \sim s^{\alpha^\zeta(t)}, \quad (5.18)$$

for $\alpha^\zeta(t) \geq -1/2$. This results in:

$$A^\zeta(s,t) \sim (2\alpha^\zeta(t)+1) \frac{\beta^\zeta(t)}{\sin(\pi\alpha^\zeta(t))} \frac{1}{\Gamma(\alpha^\zeta(t)+1)} s^{\alpha^\zeta(t)}.$$

Except for $\frac{1}{\Gamma(\alpha^\zeta(t)+1)}$, all factors from the limit of the Legendre function (5.18), have been absorbed in $\beta^\zeta(t)$). The remaining factor $\frac{1}{\Gamma(\alpha^\zeta(t)+1)}$ rules out any non-physical pole coming from $\sin(\pi\alpha(t))$ at negative values of $\alpha(t)$ for $t < 0$. Suppressing further the labels ζ we introduce the factor $\frac{\zeta + e^{-i\pi\alpha(t)}}{2}$ with which the signature is specified. Its form in the Regge amplitude will ensure that a specific trajectory, with even/odd signature, will deliver a t-channel pole only when $\alpha(t)$ reaches an even/odd integer. It is also usual to introduce s_0 which is a typical mass scale usually taken to be 1 GeV^2. In QCD, s_0 corresponds to the string tension between a quark and an antiquark. Finally, absorbing $(1 + 2\alpha(t))$ into the residue $\beta(t)$ and introducing the constant C the Regge amplitude is obtained:

$$A_{\text{Regge}}(s,t) = C \frac{\beta(t)}{\Gamma(1+\alpha(t))\sin(\pi\alpha(t))} \frac{\zeta + e^{-i\pi\alpha(t)}}{2} \left(\frac{s}{s_0}\right)^{\alpha(t)}. \quad (5.19)$$

The importance of this result is that, in analogy with (5.13)-(5.15):

$$A_{\text{Regge}}(s,t) \sim s^{\alpha(t)} \quad (5.20)$$

$$\frac{\mathrm{d}\sigma}{\mathrm{d}t} \sim s^{2\alpha(t)-2} \qquad s \gg |t| \quad (t<0) \quad (5.21)$$

$$\sigma_{\text{tot}} \sim s^{\alpha(0)-1}. \quad (5.22)$$

This means that, as long as $\alpha(t) \leq 1$ for $t < 0$, the Froissart bound is not violated in the Regge limit and A_{Regge} gives a unitary description of the scattering process. One should bear in mind that the Regge amplitude as derived is valid as long as $\alpha(t) \geq -1/2$ for $t < 0$.

5.3 General Regge trajectories

When the Regge trajectory $\alpha(t)$ reaches different integers for $t > 0$, one encounters a family of exchanged particles, identical in charge, baryon number, strangeness, ... but carrying different spin. The first materialisation for $t > 0$ is a bound state and is followed by subsequent resonant states, with increasing spin and mass. Phenomenologically it was found that all Regge trajectories can be described well by a straight line:

$$\alpha(t) = \alpha(0) + \alpha' t = \alpha_0 + \alpha'(t - m_{\alpha_0}^2). \tag{5.23}$$

Here, α' is the slope of the Regge trajectory which appears to be universal and is of the order of 0.8 GeV^2, α_0 is the spin and $m_{\alpha_0}^2$ the squared mass of the first materialisation of the trajectory.

We have derived the Regge amplitude (5.19) under the assumption of spinless particles. This led to the exchange of a trajectory whose first materialisation has spin $\alpha_0 = 0$. The expression can straightforwardly be generalised to positive integer or half-integer values of α_0. In order to achieve this, one can rely on the fact that the limit of $A_{\text{Regge}}(s,t)$ in the vicinity of simple t-channel pole exchange, should coincide with the Feynman-pole expression for the amplitude. At the pole one has $t \to m_{\alpha_0}^2$ such that, with (5.23):

$$\alpha(t) = \alpha_0 + \alpha'(t - m_{\alpha_0}^2) \xrightarrow{t \to m_{\alpha_0}^2} \alpha_0$$

and

$$\sin(\pi\alpha(t)) \xrightarrow{t \to m_{\alpha_0}^2} \pi\alpha'(t - m_{\alpha_0}^2).$$

For $\alpha_0 = 0$, this gives for $A_{\text{Regge}}(s,t)$ in (5.19):

$$A_{\text{Regge}}(s,t) \xrightarrow{t \to m_{\alpha_0}^2} \frac{\beta(t)}{t - m_{\alpha_0}^2} \tag{5.24}$$

if one chooses the normalisation constant $C = \pi\alpha'$ and takes $\zeta = +1$. The residue $\beta(t)$ coincides with the vertex functions of the considered scattering process. This means that near the particle pole, the Regge amplitude is reduced to the classical Feynman expression for the exchange of a single particle. Taking this as a criterion for the extension of the Regge expression to trajectories with $\alpha_0 > 0$, it suffices to replace $\alpha(t)$ by $\alpha(t) - \alpha_0$ in the factors $(s/s_0)^{\alpha(t)}$ and $\Gamma(1 + \alpha(t))$.

Regge trajectories are usually presented in *Chew-Frautschi plots* where the different materialisations at $t > 0$ are shown as a function of their mass squared, corresponding with the t-channel invariant momentum transfer t [32]. Figure 5.6 and Figure 5.7 show some examples for mesonic and baryonic trajectories, respectively. A trajectory is usually named after its first materialisation, hence e.g. the pion-trajectory or the rho-trajectory. From (5.19) it is clear that

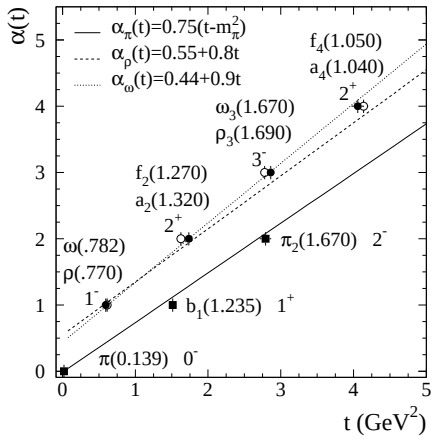

Figure 5.6: Mesonic Regge trajectories for the π, the ρ and the ω.

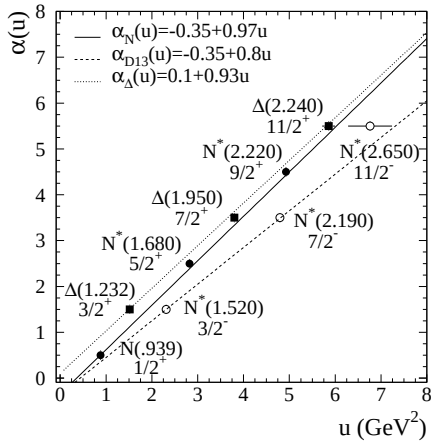

Figure 5.7: Baryonic Regge trajectories for the nucleon, the D_{13} and the Δ.

the highest lying contributing trajectory dominates the cross section. On the Chew-Frautschi plots the straight lines that approximate the trajectories have a slope α' that is universal for all particle types.

In accordance with the discussion on the signature of the Regge amplitude where one has separate descriptions for even and odd spins, a Regge trajectory groups either even or odd-spin particles. It is possible that two trajectories are *degenerate*. The corresponding scattering amplitude is then obtained by combining the *non-degenerate* trajectories with opposite signature $\zeta = \pm 1$ by adding or subtracting them, which results in different phases:

$$\frac{1 + e^{-i\pi\alpha(t)}}{2} \mp \frac{1 - e^{-i\pi\alpha(t)}}{2} = \begin{cases} e^{-i\pi\alpha(t)} & \text{rotating phase,} \\ 1 & \text{constant phase.} \end{cases}$$

A priori there is no rule that determines the degree of degeneracy for specific trajectories. Phenomenologically one finds that the exchange of a non-degenerate trajectory gives rise to minima in the angular distribution and one can thus rely on the presence or absence of this feature to decide on the used degeneracy.

6

The RPR model for double pion photoproduction

6.1 Introduction

In this chapter, a model for double pion photoproduction is presented. It is a Regge Plus Resonances model, or RPR model for short. The RPR model has two main ingredients: Regge trajectory exchange in the t-channel is combined with resonant s-channel scattering. One could embark in a purely s-channel description for double pion production. At lower energies the partial-wave expansion of the scattering amplitude (5.2) (p. 116) is dominated by resonance pole contributions which, through interference, can give a fair description of the cross sections in the resonance region. However, as s increases, the number of resonances in the partial-wave amplitudes increases and individual contributions are no longer easily disentangled. Moreover, as discussed in Chapter 5, unitarity is no longer satisfied if one moves too far away from the s-channel physical region. The partial-wave expansion diverges at the closest t-singularity, namely at the verge of the Lehmann-Martin ellipse. It was shown that this can be overcome in Regge theory with the Sommerfeld-Watson representation (5.16) (p. 120) for the t-channel exchange of Regge trajectories. In QCD language, meson Regge trajectory exchange corresponds to the t-channel exchange of a quark-antiquark pair with a given set of internal quantum numbers and which are connected through a gluonic flux tube (string). As discussed in Chapter 5, the states on a Regge trajectory with a given set of internal quantum numbers correspond to different angular momenta. As such, t-channel Regge trajectory exchange corresponds to the exchange of a given meson (e.g. a ρ meson) and its orbital excitations (a_2, ρ_3, a_4, ρ_5, ...).

Regge theory thus provides a unitary description for high s. While in such a way it works very well to describe the high energy behaviour it does not yield any explicit resonant structure. It yields an average over all resonances, evoking the duality between resonance and Regge descriptions (meson Regge

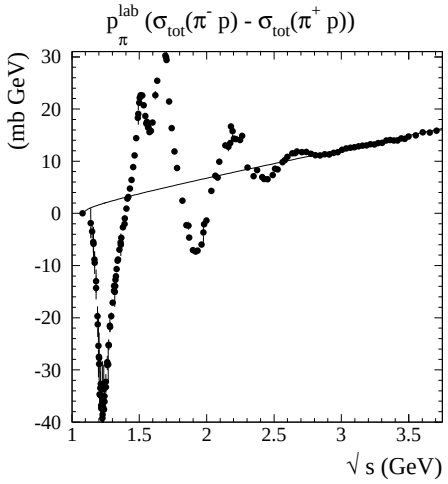

Figure 6.1: Illustration of global and local duality. The experimental data represent the difference of the total cross sections for π^-p and π^+p, multiplied with the pion momentum in the laboratory frame, as a function of the center of mass energy $\sqrt{s}$ [105]. The curve describes the forward scattering amplitude for $\pi^-\mathrm{p} \to \pi^0\mathrm{n}$ as a function of the center of mass energy.

trajectories are dual to quark-antiquark exchange and the Pomeron trajectory is dual to two-gluon exchange).

We illustrate the duality between resonances and Regge trajectory exchange for the difference of the total cross sections for π^-p and π^+p. Figure 6.1 shows the difference of the experimental data for these cross sections as a function of the center of mass energy $\sqrt{s}$ [105]. Following the optical theorem, this total cross section difference multiplied with the pion momentum in the laboratory frame, is given by the forward scattering amplitude for the charge exchange reaction $\pi^-\mathrm{p} \to \pi^0\mathrm{n}$. This reaction has been measured over a large energy range and its forward differential cross section was found to be dominated by the exchange of the ρ Regge trajectory. This leads to a forward scattering amplitude proportional to $s^{0.5}$. As a consequence the total cross sections drop as $s^{0.5-1} = s^{-0.5}$, respecting unitarity in contrast with a ρ pole exchange. This ρ trajectory exchange yields the full curve in Figure 6.1. One observes that, in the resonance region, the difference of the experimental data for the total cross section for π^-p —which contains both N* and Δ resonances— and for π^+p —which contains only Δ resonances— oscillates around the ρ Regge trajectory exchange curve. This illustrates what one calls *global duality*. At higher energies, $\sqrt{s} \geq 3$ GeV, the resonance 'oscillations' disappear and go over in the smooth energy behaviour of the Regge trajectory exchange. At these higher energies, summing all resonances is equivalent to the ρ Regge trajectory exchange in the t-channel. In this case, one speaks of

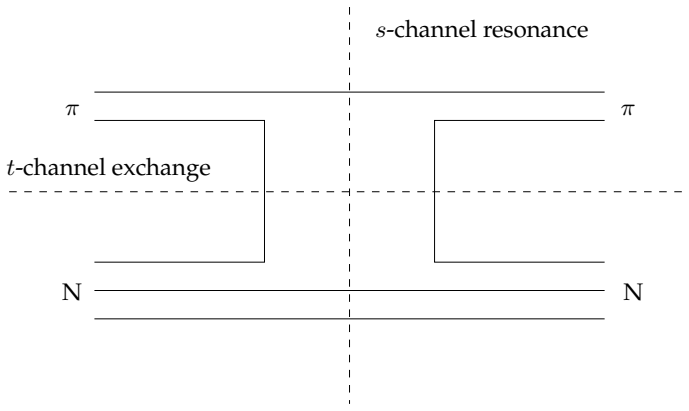

Figure 6.2: Quark line diagram for πN scattering illustrating duality.

local duality. It is clear that at higher energies, the Regge trajectory exchange approach is a more efficient —albeit equivalent— way to account for the sum over all resonances. At center of mass energies $\sqrt{s}$ below about 3 GeV, separate resonance excitations become prominent and the Regge amplitude can only be seen as a global average over these resonances.

The aim of the RPR model presented here is to combine the two approaches —Regge and resonance description— into one description covering a large energy range starting from threshold. Practically the Regge description is extrapolated to lower energies where it serves as the background contribution to which the resonant s-channel poles are added coherently. Due to duality, one is then confronted with the following question: to what extent are the s-channel resonances included into the summed t-channel Regge trajectory exchange. One can illustrate the idea of duality diagrammatically when drawing a quark line diagram for e.g. πN scattering as in Figure 6.2. One can interpret the process through meson exchange in the t-channel or alternatively through s-channel baryonic exchanges. Duality implies that there would be some double counting when simply adding the two approaches. To deal with this, one can expand the Regge amplitude in partial-waves and subtract from it the Regge partial-wave that corresponds to the s-channel resonance before adding the true s-channel channel partial wave.

For the extrapolation of the Regge amplitude to lower energies there is no firmly established rule. A possibility is to use the non-asymptotic form of the Regge amplitude by replacing $s^{\alpha(t)}$ by $\left(\frac{s-u}{2}\right)^{\alpha(t)}$. The crossing-symmetric variable $\frac{s-u}{2}$ has the correct high-s limit since $\frac{s-u}{2} \xrightarrow{s\to\infty} s$.

After the introduction of a few conventions and quantities in Section 6.2, the RPR formalism is presented in Section 6.3. Regge trajectory exchange in the t-channel is calculated by starting from a classical Feynman approach which is used to define the vertex functions. The matrix element is then *reggeised* by replacing the Feynman propagator by the appropriate Regge propaga-

tor. The advantage of this method over e.g. Regge fits is that no new parameters need to be introduced. Only the usually well-fixed vertex coupling constants are required along with well-checked properties of Regge trajectories. A Breit-Wigner formalism is employed for the description of the s-channel resonances.

6.2 Kinematics and observables

Notational conventions As a unit convention $\hbar = c = 1$ is used and the electric charge $e = \sqrt{\frac{4\pi}{137}}$. A general contravariant four-vector in the Bjorken en Drell notation is defined as:

$$p^\mu(p^0, p^1, p^2, p^3).$$

With the metric tensor $g_{\mu\nu}$

$$g_{\mu\nu} = \begin{pmatrix} 1 & 0 & 0 & 0 \\ 0 & -1 & 0 & 0 \\ 0 & 0 & -1 & 0 \\ 0 & 0 & 0 & -1 \end{pmatrix},$$

the covariant four-vector is written as:

$$p_\mu(p^0, -p^1, -p^2, -p^3) = g_{\mu\nu}p^\mu$$

We use also the notation:

$$\not{p} = \gamma^\mu p_\mu,$$

with γ^μ the Dirac matrices.

Kinematics A double pion photoproduction process is a general three-body reaction as depicted in Figure 6.3. The involved particles are characterized by their four-vector momentum, spin and isospin projection:

incoming photon	$\gamma(k^\mu, \lambda)$	with	$k^\mu = (E_\gamma, \vec{k})$	$\lambda = \pm 1,$
incoming nucleon	$\mathrm{N_i}(p_\mathrm{i}^\mu, s_\mathrm{i})$	with	$p_\mathrm{i}^\mu = (E_\mathrm{i}, \vec{p}_\mathrm{i})$	$s_\mathrm{i} = \pm 1/2,$
outgoing nucleon	$\mathrm{N_f}(p_\mathrm{f}^\mu, s_\mathrm{f})$	with	$p_\mathrm{f}^\mu = (E_\mathrm{f}, \vec{p}_\mathrm{f})$	$s_\mathrm{f} = \pm 1/2,$
outgoing pion 1	$\pi(p_{\pi_1}^\mu)$	with	$p_{\pi_1}^\mu = (E_{\pi_1}, \vec{p}_{\pi_1}),$	
outgoing pion 2	$\pi(p_{\pi_2}^\mu)$	with	$p_{\pi_2}^\mu = (E_{\pi_2}, \vec{p}_{\pi_2}).$	

The numbering of the two pions has no physical meaning and is merely used for easy reference. The mechanisms included in the RPR model involve intermediate states containing the Δ resonance or the ρ meson:

intermediate Δ	$\Delta(p_\Delta^\mu, s_\Delta)$	with	$p_\Delta^\mu = (E_\Delta, \vec{p}_\Delta)$	$s_\Delta = \pm 1/2,\ \pm 3/2,$
intermediate ρ	$\rho(p_\rho^\mu, \lambda_\rho)$	with	$p_\rho^\mu = (E_\rho, \vec{p_\rho})$	$\lambda_\rho = 0,\ \pm 1.$

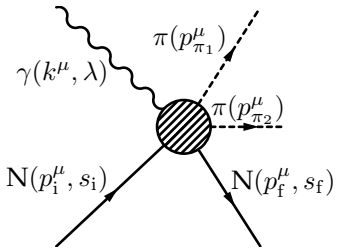

Figure 6.3: A general three-body double pion photoproduction process.

The four-vector index μ is suppressed throughout if no confusion is possible, writing p instead of p^μ. The isospin projections of the nucleon isospin-1/2 state are the proton ($i=+1/2$) and the neutron ($i=-1/2$). In the case of the Δ one has the Δ^- ($i=-3/2$), Δ^0 ($i=-1/2$), Δ^+ ($i=+1/2$) and Δ^{++} ($i=+3/2$). The π and the ρ meson have the respective charge states $\left(\pi^-,\,\pi^0,\,\pi^+\right)$ and $\left(\rho^-,\,\rho^0,\,\rho^+\right)$.

The helicity dependent nucleon Dirac spinor is defined as

$$\mathrm{u}(\vec{p},s)=\sqrt{E_\mathrm{N}+m_\mathrm{N}}\begin{pmatrix}\chi(s)\\ \frac{\vec{\sigma}\cdot\vec{p}}{E_\mathrm{N}+m_\mathrm{N}}\chi(s)\end{pmatrix}, \tag{6.1}$$

with E_N and m_N the nucleon energy and the nucleon mass, $\vec{\sigma}$ the Pauli matrices and

$$\chi\left(\tfrac{1}{2}\right)=\begin{pmatrix}1\\0\end{pmatrix}\quad\text{and}\quad\chi\left(-\tfrac{1}{2}\right)=\begin{pmatrix}0\\1\end{pmatrix}.$$

The Δ resonance is described by the relativistic *Rarita-Schwinger spinor*

$$\Delta^\mu(\vec{p}_\Delta,s_\Delta)=\sum_{\lambda=0,\pm1}\sum_{s=\pm1/2}\langle 1/2\quad s\quad 1\quad \lambda\mid 3/2\quad s_\Delta\rangle\,\epsilon^\mu(\vec{p}_\Delta,\lambda)\mathrm{u}(\vec{p}_\Delta,s).$$

In this expression $\mathrm{u}(\vec{p}_\Delta,s)$ is the Dirac spinor as in (6.1) with mass m_Δ. The general spin-1 polarisation four-vector $\epsilon^\mu(\vec{p}_\Delta,\lambda)$ is defined as:

$$\epsilon^\mu(\vec{p}_\Delta,\lambda)=\left(\frac{\vec{p}_\lambda}{m_\Delta},\vec{\epsilon}_\lambda+\frac{1}{m_\Delta}\frac{\vec{p}_\lambda}{E_\Delta+m_\Delta}\vec{p}\right)$$

where $\vec{\epsilon}_\lambda$ is the spherical unit vector:

$$\vec{\epsilon}_{\lambda=0}=(0,0,1),$$
$$\vec{\epsilon}_{\lambda=\pm1}=\mp\frac{1}{\sqrt{2}}(1,\pm i,0).$$

The spherical components p_λ of a vector $\vec{p}$ are defined through $p_\lambda = \vec{p}\cdot\vec{\epsilon}_\lambda$.

The polarisation four-vector of the real photon travelling in the z-direction is given by

$$\epsilon^\mu_\gamma(k,\lambda=\pm1) = \mp\frac{1}{\sqrt{2}}(0,1,\pm i,0). \tag{6.2}$$

If no confusion can arise we simply use ϵ_μ to denote the real photon polarisation vector. The general ρ polarisation vector can be written as:

$$\epsilon^\mu_\rho(k,\lambda=\pm1) = \mp\frac{1}{\sqrt{2}}(0,\cos\theta,\pm i,-\sin\theta), \tag{6.3}$$

$$\epsilon^\mu_\rho(k,\lambda=0) = \frac{1}{m_\rho}(|\vec{p}_\rho|, E_\rho\sin\theta, 0, E_\rho\cos\theta). \tag{6.4}$$

where m_ρ is the mass of the ρ meson and θ is the angle of its direction of motion with respect to the reference z-axis.

It is convenient to define the four-vector of the combined system of two out of three outgoing particles in the double pion process. There are two physically relevant possibilities:

$$p_{\pi_2\mathrm{N}} := p_{\pi_2} + p_\mathrm{N}, \qquad W^2_{\pi_2\mathrm{N}} = p^2_{\pi_2\mathrm{N}}$$
$$p_{\pi_1\pi_2} := p_{\pi_1} + p_{\pi_2}, \quad W_{\pi_1\pi_2} = p^2_{\pi_1\pi_2}$$

with $W_{\pi_2\mathrm{N}}$ and $W_{\pi_1\pi_2}$ the invariant masses of the respective π_2N and $\pi_1\pi_2$ systems. The use of such variables is well suited to treat the correlated emission of the π_2 and the nucleon through the Δ ($\gamma N \to \pi_1\Delta \to \pi_1\pi_2$N) processes or the two pions resulting from the decay of the ρ meson ($\gamma N \to \rho\mathrm{N} \to \pi_1\pi_2$N).

In accordance with the definition of the Mandelstam variables s, t and u in Chapter 5 for a general two-body reaction, one can write:

$$s = (k+p_\mathrm{i})^2,$$
$$t = (k-p_{\pi_1})^2,$$
$$u = (k-p_{\pi_2\mathrm{N}})^2.$$

The quantity $\sqrt{s}$ represents the center-of-mass (CM) energy of the system, where the CM-reference system is fixed by $\vec{k}+\vec{p_\mathrm{i}} = \vec{0}$. Each further subscript 'CM' refers to quantities in this reference system, subscripts 'LAB' refer to quantities in the laboratory frame. The reference system for which $\vec{p_\mathrm{f}}+\vec{p}_{\pi_2} = \vec{0}$ is the center-of-mass system of the outgoing nucleon and π_2. It will be referred to by 'CMπ_2N'. Similarly 'CM$\pi_1\pi_2$' refers to the frame where $\vec{p}_{\pi_1}+\vec{p}_{\pi_2} = \vec{0}$.

The following useful kinematical relations hold:

$$s = 2m_\mathrm{N}E^\mathrm{LAB}_\gamma + m^2_\mathrm{N},$$
$$t = m^2_\pi - 2E^\mathrm{CM}_\gamma\left(E^\mathrm{CM}_{\pi_1} - \left|\vec{p}^{\,\mathrm{CM}}_{\pi_1}\right|\cos\theta^\mathrm{CM}_{\pi_1}\right),$$
$$u = W^2_{\pi_2\mathrm{N}} - 2E^\mathrm{CM}_\gamma\left(E^\mathrm{CM}_{\pi_2\mathrm{N}} - \left|\vec{p}^{\,\mathrm{CM}}_{\pi_2\mathrm{N}}\right|\cos\theta^\mathrm{CM}_{\pi_2\mathrm{N}}\right)$$

where, for $E_\gamma^{\rm CM}$ and $E_\gamma^{\rm LAB}$:

$$E_\gamma^{\rm CM} = \frac{s - m_{\rm N}^2}{2\sqrt{s}} = \frac{m_{\rm N} E_\gamma^{\rm LAB}}{\sqrt{s}}.$$

For the CM-pion momentum one has:

$$\left|\vec{p}_{\pi_1}^{\,\rm CM}\right| = \frac{1}{2\sqrt{s}}\sqrt{s^2 - 2s\left(W_{\pi_2{\rm N}}^2 + m_\pi^2\right) + \left(W_{\pi_2{\rm N}}^2 - m_\pi^2\right)^2}.$$

The above relations are completely analogous for the $\pi_1\pi_2$ system. In particular, we introduce the t-channel momentum transfer $t_{\pi_1\pi_2}$ of the $\gamma{\rm N} \to (\pi_1\pi_2){\rm N}$ process via:

$$t_{\pi_1\pi_2} = (k - p_{\pi_1} - p_{\pi_2})^2.$$

Observables The four-fold differential cross section for the three-body process can be expressed in terms of the three-body matrix element $\mathcal{M}_{\rm fi}^{(3b)}$, as a function of the '$\pi_2$N' variables:

$$\frac{{\rm d}\sigma}{{\rm d}t{\rm d}W_{\pi_2 N}{\rm d}\Omega_{\pi_2}^{{\rm CM}\pi_2{\rm N}}} = \frac{1}{(16\pi^2)^2}\frac{\left|\vec{p}_{\pi_2}^{\,{\rm CM}\pi_2{\rm N}}\right|}{\left(s - m_{\rm N}^2\right)^2}\frac{1}{4}\sum_\lambda\sum_{s_{\rm i}}\sum_{s_{\rm f}}\left|\mathcal{M}_{\rm fi}^{(3b)}\left(\gamma{\rm N} \to \pi_1\pi_2{\rm N}\right)\right|^2. \quad (6.5)$$

This form is well suited when studying a mechanism where the nucleon and one of the pions are produced correlatedly, in which case the invariant mass distribution $\frac{{\rm d}\sigma}{{\rm d}W_{\pi_2 N}}$ is a natural observable.

Alternatively one can express the matrix element and the cross section in terms of the $\pi_1\pi_2$ system as follows:

$$\frac{{\rm d}\sigma}{{\rm d}t_{\pi_1\pi_2}{\rm d}W_{\pi_1\pi_2}{\rm d}\Omega_{\pi_1}^{{\rm CM}\pi_1\pi_2}} = \frac{1}{(16\pi^2)^2}\frac{\left|\vec{p}_{\pi_1}^{\,{\rm CM}\pi_1\pi_2}\right|}{\left(s - m_{\rm N}^2\right)^2}\frac{1}{4}\sum_\lambda\sum_{s_{\rm i}}\sum_{s_{\rm f}}\left|\mathcal{M}_{\rm fi}^{(3b)}\left(\gamma{\rm N} \to \pi_1\pi_2{\rm N}\right)\right|^2. \quad (6.6)$$

This would then be a more natural way to describe a process in which the two pions are strongly correlated (e.g. $\gamma{\rm N} \to \rho{\rm N} \to \pi_1\pi_2{\rm N}$). Evidently (6.5) and (6.6) are equivalent and both can be used when coherently adding different types of mechanisms and comparing with available data for mass distributions, angular distributions and total cross sections.

In what follows, we calculate the matrix element $\mathcal{M}_{\rm fi}$ for different double pion photoproduction mechanisms. This matrix element can be expressed in terms of the four-vector hadronic current J^μ which describes the dynamics of the pion production process. The hadronic current J^μ is defined through:

$$\mathcal{M}_{\rm fi} = -i\epsilon_\mu J^\mu. \quad (6.7)$$

6.3 Formalism

6.3.1 General method

In a classical Feynman formalism one defines the scattering matrix element $\mathcal{M}_{\text{fi}}$ as:

$$\mathcal{M}_{\text{fi}}^{\text{Feynman}} = V_1 \mathcal{P}_{\text{Feynman}} V_2. \tag{6.8}$$

The vertex functions, or *Feynman rules*, V_1 and V_2 can be obtained from the appropriate interaction Lagrangian, derived from the free Lagrangian through minimal substitution. The Feynman rules used here are derived from well established expressions for the Lagrangians, applied by different authors, e.g. [38, 52, 58, 59, 80, 84, 101, 117].

The general expression for the Feynman pole propagator of a particle with four-vector momentum p, mass m and wave function Ψ is:

$$\mathcal{P}_{\text{Feynman}} = i \frac{\sum\limits_{\text{spins}} |\Psi><\Psi|}{p^2 - m^2}. \tag{6.9}$$

In the RPR model the t-channel exchange mechanisms are not described by Feynman pole exchange but through Regge trajectory exchange. The motivation for this is obvious from the discussion in Chapter 5; it is a prerequisite in order to ensure unitarity, as the t-channel partial wave expansion does not converge when going to negative t and higher s. The Regge limit, however, is an asymptotic ($s \gg -t$) statement about the amplitude. Reviews and references on the application of the Regge concept can be found in [75, 114, 115]. Often one uses fits of the particular helicity amplitudes to construct the vertex functions (residues) needed in the Regge model. A disadvantage of these approaches is that free parameters need to be introduced. In order to avoid this we adopt a different prescription.

The main idea is that the Regge amplitude reduces to the Feynman amplitude as one approaches the first materialisation of the trajectory, i.e. for $t \to m_{\alpha_0}^2$. The expression for the Regge amplitude as derived in Chapter 5 is

$$A_{\text{Regge}}(s,t) = \pi\alpha' \frac{\beta(t)}{\Gamma(1+\alpha(t))\sin(\pi\alpha(t))} \frac{\zeta + e^{-i\pi\alpha(t)}}{2} \left(\frac{s}{s_0}\right)^{\alpha(t)}. \tag{6.10}$$

At the particle pole $t \to m_{\alpha_0}^2$ we found exactly the Feynman amplitude for a t-channel pole exchange (5.24):

$$A_{\text{Regge}}(s,t) \xrightarrow{t \to m_{\alpha_0}^2} \frac{\beta(t)}{t - m_{\alpha_0}^2}. \tag{6.11}$$

Here, $\frac{1}{t-m_{\alpha_0}^2}$ coincides with the Feynman propagator (6.9) for a simple pole exchange, the Regge pole residue $\beta(t)$ corresponds to the vertex functions V_1

and V_2. For $\beta(t) \neq 0$ one can define the Regge propagator $\mathcal{P}_{\text{Regge}}(s,t)$ through:

$$A_{\text{Regge}}(s,t) = \beta(t)\mathcal{P}_{\text{Regge}}(s,t),$$

with

$$\mathcal{P}_{\text{Regge}}(s,t) = \pi\alpha' \frac{1}{\Gamma(1+\alpha(t))\sin(\pi\alpha(t))} \frac{\zeta + e^{-i\pi\alpha(t)}}{2} \left(\frac{s}{s_0}\right)^{\alpha(t)}. \qquad (6.12)$$

As such, the *regge-isation* can be performed by simply replacing the Feynman propagator by the Regge propagator in the classical Feynman matrix element (6.8). At the position of the pole one finds again the Feynman pole exchange. The further one goes from the pole, the stronger the Regge trajectory exchange effects become. This procedure was applied successfully in [58, 59] and is similar to what was used by Levy et al. in 1973 [84]. The primary advantage is that the vertex structure of the Feynman graphs can be conserved and that the corresponding coupling constants are in many cases very well known, e.g. from extended (partial-wave) analysis of electromagnetic and hadronic scattering data.

Another important ingredient of the RPR model is the demand of *gauge invariance*. In any electromagnetic theory one has an extra degree of freedom for the photon field which can be pinned down by choosing an *electromagnetic gauge*. Evidently any model should be independent of the chosen gauge. This gauge invariance condition can be expressed by $k_\mu J^\mu = 0$ where k_μ is the photon four-vector momentum and J^μ the current to which the photon couples. It can equivalently be interpreted as charge conservation. Strictly speaking, we use J^μ for the matrix elements of the current operator in what follows.

In (6.7) we have defined the hadronic current J^μ. It contains the dynamical information of the reaction. In what follows, the J^μ expressions for the incorporated t and s-channel processes are presented. The isospin factor is denoted as $\mathcal{I}$ and will be specified for each studied isospin channel separately.

In Section 6.3.2 the following regge-ised t-channel mechanisms are discussed:

$\gamma\mathrm{N} \to \pi\Delta \to \pi\pi\mathrm{N}$	π exchange	(Section 6.3.2.1),
$\gamma\mathrm{N} \to \pi\pi\mathrm{N}$	π exchange	(Section 6.3.2.2),
$\gamma\mathrm{N} \to \pi\Delta \to \pi\pi\mathrm{N}$	ρ exchange	(Section 6.3.2.4),
$\gamma\mathrm{N} \to \rho\mathrm{N} \to \pi\pi\mathrm{N}$	ρ exchange	(Section 6.3.2.3),
$\gamma\mathrm{N} \to \rho\mathrm{N} \to \pi\pi\mathrm{N}$	π exchange	(Section 6.3.2.5),
$\gamma\mathrm{N} \to \rho\mathrm{N} \to \pi\pi\mathrm{N}$	f_1 exchange	(Section 6.3.2.6).

The s-channel resonances that are dealt with in Section 6.3.3 are:

$\gamma\mathrm{N} \to \mathrm{D}_{13} \to \pi\Delta \to \pi\pi\mathrm{N}$	D_{13} resonance	(Section 6.3.3.1),
$\gamma\mathrm{N} \to \mathrm{D}_{13} \to \rho\mathrm{N} \to \pi\pi\mathrm{N}$	D_{13} resonance	(Section 6.3.3.2).

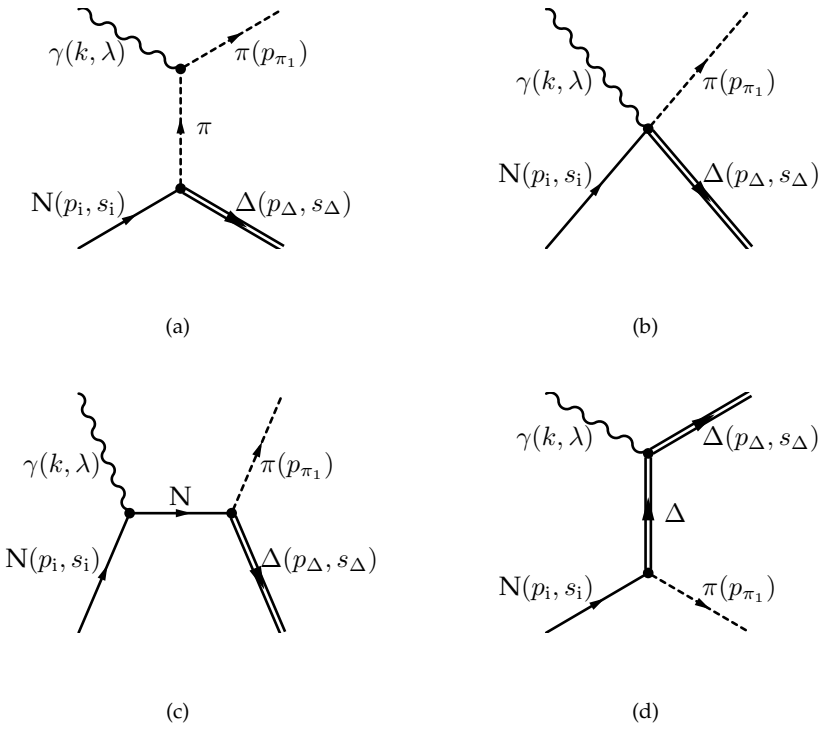

Figure 6.4: $\gamma N \rightarrow \pi\Delta$: Gauge invariant pion exchange. (a) Pion exchange diagram, (b) Kroll-Rudermann contact term, (c) sN term: nucleon exchange in the s-channel, (d) $u\Delta$ term: exchange of the Δ in the u-channel.

6.3.2 Regge trajectory exchange in the t-channel

6.3.2.1 γN $\rightarrow \pi\Delta \rightarrow \pi\pi$N: Gauge invariant π exchange

The Feynman diagram in Figure 6.4(a) illustrates the pion exchange $\gamma\mathrm{N} \rightarrow \pi\Delta$ process. Decay of the $\Delta \rightarrow \pi\mathrm{N}$ yields a double pion final state. In a first step, the two-body process $\gamma\mathrm{N} \rightarrow \pi\Delta$ is treated. The Δ decay is then incorporated in the treatment to extend it to the three-body case.

If one defines a *Born term* as the exchange of a particle which also occurs among the external particles, the diagram in Figure 6.4(a) is a Born term. *Non-Born terms* can generally be written as one single gauge invariant term. It is known that this is not the case for Born terms and one needs to add all possible Born terms in order to reach gauge invariance, i.e. coupling the photon to all charged particles. These extra diagrams, in addition to the t-channel π exchange, are in this case: the *Kroll-Rudermann contact term* (Figure 6.4(b)), the sN term, i.e. nucleon exchange in the s-channel (Figure 6.4(c)), and the $u\Delta$ term, i.e. exchange of the Δ in the u-channel (Figure 6.4(d)). The π exchange

diagram is regge-ised as proposed above. Although the three extra diagrams are not t-channel exchanges, they are inherently connected to the first one and should therefore be treated consistently. To this end we follow an idea by Jones [77] as adopted by Guidal et al. [58, 59], and multiply the extra diagrams with a factor $\mathcal{P}_{\text{Regge}}\left(t - m_\pi^2\right)$. This factor reduces to 1 at the particle pole where one returns to the classical non-Regge expressions for the diagrams.

The hadronic current J_π^μ corresponding to the diagram in Figure 6.4(a) reads:

$$J_\pi^\mu = -i\mathcal{I}\frac{e f_{\pi\mathrm{N}\Delta}}{m_\pi}\left(2p_\pi - k\right)^\mu \mathcal{P}^\pi_{\text{Regge}}\left(k - p_\pi\right)_\alpha \bar{\Delta}^\alpha(p_\Delta, s_\Delta)\mathrm{N}(p_\mathrm{i}, s_\mathrm{i}).$$

The Regge propagator $\mathcal{P}^\pi_{\text{Regge}}(s,t)$ is given by:

$$\mathcal{P}^\pi_{\text{Regge}}(s,t) = \pi\alpha'_\pi \frac{e^{-i\pi\alpha_\pi(t)}}{\Gamma(1+\alpha_\pi(t))\sin(\pi\alpha_\pi(t))}\left(\frac{s}{s_0}\right)^{\alpha_\pi(t)}, \tag{6.13}$$

for a degenerate trajectory with rotating phase. The pion Regge trajectory $\alpha_\pi(t)$ is given by:

$$\alpha_\pi(t) = \alpha'_\pi(t - m_\pi^2) \quad \text{with } \alpha'_\pi = 0.75. \tag{6.14}$$

The value of the strong $\pi\mathrm{N}\Delta$ coupling constant $f_{\pi\mathrm{N}\Delta}$ is obtained from the decay width $\Gamma_{\Delta\to\pi\mathrm{N}}$ at the resonance position (m_Δ=1.232 GeV):

$$\Gamma_{\Delta\to\pi\mathrm{N}}(m_\Delta) = \frac{f^2_{\pi\mathrm{N}\Delta}}{4\pi}\frac{E_\mathrm{N} + m_\mathrm{N}}{m_\Delta}\frac{|\vec{p}_\pi|^3}{3m_\pi^2}, \tag{6.15}$$

where

$$|\vec{p}_\pi| = \frac{1}{2m_\Delta}\sqrt{m_\Delta^4 - 2m_\Delta^2\left(m_\pi^2 + m_\mathrm{N}^2\right) + \left(m_\pi^2 - m_\mathrm{N}^2\right)^2}.$$

With $\Gamma_{\Delta\to\pi\mathrm{N}}(m_\Delta) = 0.120$ GeV as given by [105] this yields $|f_{\pi\mathrm{N}\Delta}| = 2.2151$.

The contact term J_c^μ, the sN term $J_{s\mathrm{N}}^\mu$ and the $u\Delta$ term $J_{u\Delta}^\mu$ are given by:

$$J_c^\mu = -i\mathcal{I}\frac{e f_{\pi\mathrm{N}\Delta}}{m_\pi}\mathcal{P}^\pi_{\text{Regge}}\left(t - m_\pi^2\right)\bar{\Delta}^\alpha(p_\Delta, s_\Delta)g^\mu_\alpha\mathrm{N}(p_\mathrm{i}, s_\mathrm{i}) \tag{6.16}$$

$$J_{s\mathrm{N}}^\mu = -i\mathcal{I}\frac{e f_{\pi\mathrm{N}\Delta}}{m_\pi}\mathcal{P}^\pi_{\text{Regge}}\left(t - m_\pi^2\right)(p_\pi)_\alpha\bar{\Delta}^\alpha(p_\Delta, s_\Delta)\frac{\not{p}_s + m_\mathrm{N}}{s - m_\mathrm{N}^2}\gamma^\mu\mathrm{N}(p_\mathrm{i}, s_\mathrm{i}) \tag{6.17}$$

$$J_{u\Delta}^\mu = i\mathcal{I}\frac{e f_{\pi\mathrm{N}\Delta}}{m_\pi}\mathcal{P}^\pi_{\text{Regge}}\left(t - m_\pi^2\right)(p_\pi)_\alpha\bar{\Delta}^\lambda(p_\Delta, s_\Delta)\Gamma^\mu_{\lambda\beta}$$
$$\left[g^{\beta\alpha} - \frac{\gamma^\beta\gamma^\alpha}{3} - \frac{\gamma^\beta(p_u)^\alpha - \gamma^\alpha(p_u)^\beta}{3m_\Delta} - \frac{2(p_u)^\alpha(p_u)^\beta}{3m_\Delta^2}\right]$$
$$\frac{\not{p}_u + m_\Delta}{u - m_\Delta^2}\mathrm{N}(p_\mathrm{i}, s_\mathrm{i}). \tag{6.18}$$

$\mathcal{I}$	$\gamma p \to \pi^- \Delta^{++}$	$\gamma p \to \pi^+ \Delta^0$	$\gamma p \to \pi^0 \Delta^+$
J^μ_π	$+1$	$-\sqrt{1/3}$	0
J^μ_c	$+1$	$-\sqrt{1/3}$	0
$J^\mu_{s\mathrm{N}}$	$+1$	$+\sqrt{1/3}$	$+\sqrt{2/3}$
$J^\mu_{u\Delta}$	$+2$	0	$+\sqrt{2/3}$

Table 6.1: Isospin factors for the $\gamma p \to \pi\Delta$ channel.

$\mathcal{I}$	$\gamma n \to \pi^+ \Delta^-$	$\gamma n \to \pi^0 \Delta^0$	$\gamma n \to \pi^- \Delta^+$
J^μ_π	-1	0	$-\sqrt{1/3}$
J^μ_c	-1	0	$-\sqrt{1/3}$
$J^\mu_{s\mathrm{N}}$	-	-	-
$J^\mu_{u\Delta}$	-1	0	$-\sqrt{1/3}$

Table 6.2: Isospin factors for the $\gamma n \to \pi\Delta$ channel.

The four-vector momenta p_s and p_u are defined as $p_s = k + p_\mathrm{i}$ ($p_s^2 = s$) and $p_u = p_\Delta - k$ ($p_u^2 = u$). They represent the momentum transfer of the exchanged nucleon and Δ respectively.

Expressions (6.17) and (6.18) contain both the electric and the magnetic terms of the interaction with the nucleon/Δ. However, the electric terms are sufficient to fulfil gauge invariance [28]. Since we have included these diagrams here only to enforce gauge invariance and moreover have been forced to regge-ise them in the t-channel, which is not usual for s- and u-channel processes, we can restrict the currents to these electric terms. One refers to this procedure as *minimal gauge invariance* (mgi). The magnetic terms may be added as separate s- and u-channel processes without regge-isation, they are gauge invariant by themselves. The corresponding currents in the minimal gauge scheme are then:

$$J^\mu_{s\mathrm{N,mgi}} = -i\mathcal{I}\frac{e f_{\pi\mathrm{N}\Delta}}{m_\pi}\mathcal{P}^\pi_{\mathrm{Regge}}\left(t - m_\pi^2\right)(p_\pi)_\alpha \bar{\Delta}^\alpha(p_\Delta, s_\Delta)\frac{(2p_\mathrm{i} + k)^\mu}{s - m_\mathrm{N}^2}\mathrm{N}(p_\mathrm{i}, s_\mathrm{i}) \tag{6.19}$$

$$J^\mu_{u\Delta\mathrm{,mgi}} = -i\mathcal{I}\frac{e f_{\pi\mathrm{N}\Delta}}{m_\pi}\mathcal{P}^\pi_{\mathrm{Regge}}\left(t - m_\pi^2\right)(p_\pi)_\alpha \bar{\Delta}^\alpha(p_\Delta, s_\Delta)\frac{(2p_\mathrm{f} - k)^\mu}{u - m_\Delta^2}\mathrm{N}(p_\mathrm{i}, s_\mathrm{i}). \tag{6.20}$$

The isospin factors $\mathcal{I}$ for the different studied isospin channels in the $\gamma\mathrm{N} \to \pi\Delta$ reaction are collected in Tables 6.1 and 6.2.

With the above hadronic currents, the two-body matrix element $\mathcal{M}^{(2b)}_{\mathrm{fi}}$ for the $\gamma\mathrm{N} \to \pi\Delta$ process can be written as:

$$\mathcal{M}^{(2b)}_{\mathrm{fi}}\left(\gamma\mathrm{N} \to \pi_1\Delta(m_\Delta, s_\Delta)\right) = -i\epsilon_\mu\left(J^\mu_\pi + J^\mu_c + J^\mu_{s\mathrm{N,mgi}} + J^\mu_{u\Delta\mathrm{,mgi}}\right).$$

$\Delta \to \pi\mathrm{N}$	$\mathcal{I}$
$\Delta^{++} \to \pi^+\mathrm{p}$	1
$\Delta^{0} \to \pi^-\mathrm{p}$	$\sqrt{1/3}$
$\Delta^{0} \to \pi^0\mathrm{n}$	$\sqrt{2/3}$
$\Delta^{+} \to \pi^0\mathrm{p}$	$\sqrt{2/3}$
$\Delta^{+} \to \pi^+\mathrm{n}$	$\sqrt{1/3}$
$\Delta^{-} \to \pi^-\mathrm{n}$	1

Table 6.3: Isospin factors for the $\Delta \to \pi\mathrm{N}$ decay.

From this, the three-body matrix element for $\gamma\mathrm{N} \to \pi\Delta \to \pi\pi\mathrm{N}$ is derived. This requires a treatment of the Δ decay into $\pi\mathrm{N}$. The Δ resonance peaks at the Δ mass (m_Δ=1.232 GeV) and has a non-zero width. The Δ produced in the double pion process is not necessarily found at this peak but has an invariant mass $W_{\pi_2\mathrm{N}} = \sqrt{(p_{\pi_2} + p_\mathrm{f})^2} = \sqrt{(k + p_\mathrm{f} - p_{\pi_1})^2}$. Using a Breit-Wigner form the three-body matrix element can be written in terms of the two-body matrix element:

$$\begin{aligned}\mathcal{M}^{(3\mathrm{b})}_{\mathrm{fi}}(\gamma\mathrm{N} \to \pi_1\Delta \to \pi_1\pi_2\mathrm{N}) = \\ \mathcal{I}\frac{f_{\pi\mathrm{N}\Delta}}{m_\pi}\frac{i}{W^2_{\pi_2\mathrm{N}} - m^2_\Delta + iW_{\pi_2\mathrm{N}}\Gamma_{\Delta\to\pi\mathrm{N}}(W_{\pi_2\mathrm{N}})} \\ \sum_{s_\Delta=-3/2}^{+3/2}\bar{\mathrm{N}}(p_\mathrm{f}, s_\mathrm{f})(p_{\pi_2})_\beta\Delta^\beta(p_\Delta, s_\Delta) \\ \mathcal{M}^{(2\mathrm{b})}_{\mathrm{fi}}(\gamma\mathrm{N} \to \pi_1\Delta(W_{\pi_2\mathrm{N}}, s_\Delta)),\end{aligned} \quad (6.21)$$

where the mass of the Δ is systematically taken to be $W_{\pi_2\mathrm{N}}$ in $\mathcal{M}^{(2\mathrm{b})}_{\mathrm{fi}}$. The isospin factors $\mathcal{I}$ for the $\Delta \to \pi\mathrm{N}$ decay are gathered in Table 6.3.

The general energy dependent decay width $\Gamma_{\Delta\to\pi\mathrm{N}}(W_{\pi_2\mathrm{N}})$ is (cfr. (6.15)):

$$\Gamma_{\Delta\to\pi\mathrm{N}}(W_{\pi_2\mathrm{N}}) = \frac{f^2_{\pi\mathrm{N}\Delta}}{4\pi}\frac{E_\mathrm{N} + m_\mathrm{N}}{W_{\pi_2\mathrm{N}}}\frac{\left|\vec{p}^{\,\mathrm{CM}\pi_2\mathrm{N}}_{\pi_2}\right|^3}{3m^2_\pi}. \quad (6.22)$$

Here, the momentum of the pion π_2 in the $\pi_2\mathrm{N}$ rest frame is given by:

$$\left|\vec{p}^{\,\mathrm{CM}\pi_2\mathrm{N}}_{\pi_2}\right| = \frac{1}{2W_{\pi_2\mathrm{N}}}\sqrt{W^4_{\pi_2\mathrm{N}} - 2W^2_{\pi_2\mathrm{N}}(m^2_\pi + m^2_\mathrm{N}) + (m^2_\pi - m^2_\mathrm{N})^2}. \quad (6.23)$$

It holds that $\Gamma_{\Delta\to\pi\mathrm{N}}(W_{\pi_2\mathrm{N}} = m_\Delta) = 0.120$ GeV.

Resonance damping is taken into account by introducing a *barrier penetration factor* after Blatt and Weisskopf [18, 90]. To this end one writes:

$$\Gamma^{\mathrm{RD}}_{\Delta\to\pi\mathrm{N}}(W_{\pi_2\mathrm{N}}) = \Gamma_{\Delta\to\pi\mathrm{N}}(m_\Delta)\frac{\left|\vec{p}^{\,\mathrm{CM}\pi_2\mathrm{N}}_{\pi_2}\right|}{W_{\pi_2\mathrm{N}}}\frac{m_\Delta}{\left|\vec{p}^{\,*\mathrm{CM}\pi_2\mathrm{N}}_{\pi_2}\right|}\frac{B^2_1\left(\left|\vec{p}^{\,\mathrm{CM}\pi_2\mathrm{N}}_{\pi_2}\right|R\right)}{B^2_1\left(\left|\vec{p}^{\,*\mathrm{CM}\pi_2\mathrm{N}}_{\pi_2}\right|R\right)}$$

where R is called the *interaction radius*, $\left|\vec{p}^{\,*\mathrm{CM}\pi_2\mathrm{N}}_{\pi_2}\right|$ is obtained from (6.23) with $W_{\pi_2\mathrm{N}} = m_\Delta$ and $B_1(x)$ is the p-wave ($l = 1$) *Blatt-Weisskopf barrier penetration factor* defined by:

$$B_1(x) = \frac{x}{\sqrt{1+x^2}}.$$

Different values for R have been tested and, in accordance with [91], a reliable value of $R = 0.4$ fm was accepted. The inverse, $R^{-1} \approx 0.5$ GeV can be interpreted as a resonance damping parameter.

6.3.2.2 $\gamma\mathrm{N} \to \pi\pi\mathrm{N}$: Gauge invariant π exchange with nucleon intermediate state

In this section, the non-resonant double pion photoproduction via π exchange with a nucleon in the intermediate state is examined. To this end we start from the diagrams that contribute to the gauge invariant π exchange for single pion photoproduction. A pion is then coupled to the nucleon lines to obtain the diagrams for double pion production. In the following paragraphs, we subsequently treat the $\gamma\mathrm{p} \to \mathrm{p}\pi^+\pi^-$ and $\gamma\mathrm{p} \to \mathrm{n}\pi^+\pi^0$ processes.

$\gamma\mathbf{p} \to \mathbf{p}\pi^+\pi^-$ Figure 6.5 shows the four diagrams for the π exchange with a nucleon in the intermediate state that contribute to the $\gamma\mathrm{p} \to \mathrm{p}\pi^+\pi^-$ process. They are derived from the gauge invariant π^+ (π^-) exchange for the $\gamma\mathrm{p} \to \pi^+\mathrm{n}$ ($\gamma\mathrm{p} \to \pi^-\mathrm{p}$) reactions by coupling the second pion π^- (π^+) to the nucleon line, respectively.

The contributions of the diagrams in Figures 6.5(a) and 6.5(b), which correspond to π^+ exchange, are given by:

$$J^\mu_{\pi^+(a)} + J^\mu_{\pi^+(b)} = e\,2\,g^2_{\pi\mathrm{NN}}\,\mathcal{P}^{\pi^+}_{\mathrm{Regge}}(s,t_{\pi^+})\bar{\mathrm{N}}(p_\mathrm{f},s_\mathrm{f})\,\frac{\not{p}_{\pi^-}}{(p_\mathrm{f}+p_{\pi^-})^2 - M^2_\mathrm{N}}$$
$$\left\{(2p_{\pi^+}-k)^\mu + \frac{t_{\pi^+}-m^2_\pi}{(p_\mathrm{i}+k)^2 - M^2_\mathrm{N}}\left(\not{p}_\mathrm{i} + \not{k} + M_\mathrm{N}\right)\gamma^\mu\right\}\mathrm{N}(p_\mathrm{i},s_\mathrm{i}).$$

Their sum is gauge invariant:

$$k_\mu\left(J^\mu_{\pi^+(a)} + J^\mu_{\pi^+(b)}\right) = 0\,.$$

The πNN coupling constant $g_{\pi\mathrm{NN}}$ is well known and it is obtained here through $g_{\pi\mathrm{NN}} = \frac{2m_\mathrm{N} f_{\pi\mathrm{NN}}}{m_\pi}$ with $f_{\pi\mathrm{NN}} = 1.00265$ as given by [89].

The diagrams in Figures 6.5(c) and 6.5(d) correspond to π^- exchange and

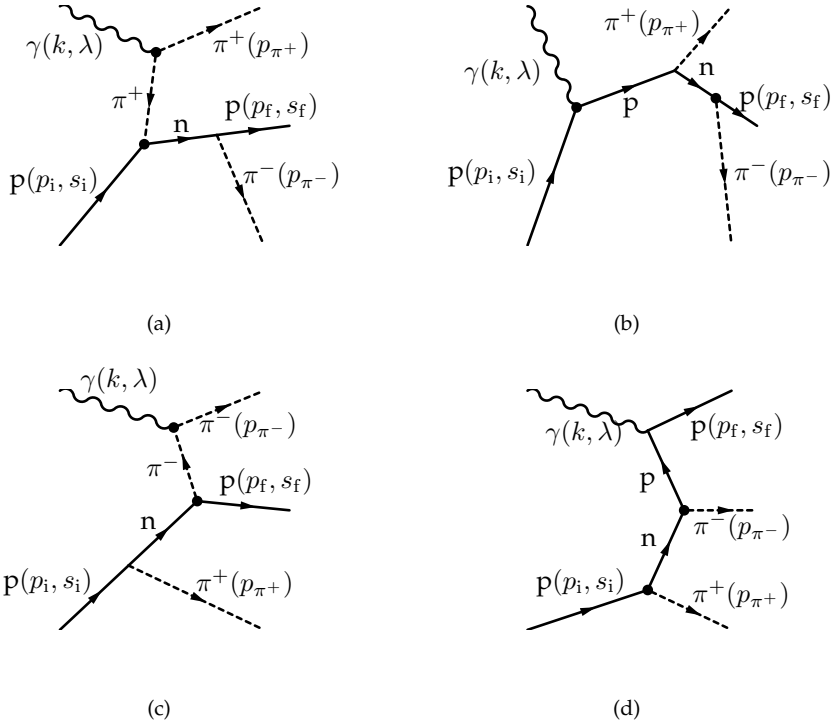

Figure 6.5: $\gamma p \to \mathrm{p}\pi^+\pi^-$: Gauge invariant π exchange with a nucleon intermediate state.

their contributions read:

$$J^{\mu}_{\pi^-(c)} + J^{\mu}_{\pi^-(d)} = e\,2\,g^2_{\pi\mathrm{NN}}\,\mathcal{P}^{\pi^-}_{\mathrm{Regge}}(s,t_{\pi^-})\bar{\mathrm{N}}(p_\mathrm{f},s_\mathrm{f})$$
$$\left\{(2p_{\pi^-}-k)^\mu - \frac{t_{\pi^-}-m_\pi^2}{(p_\mathrm{f}-k)^2-M_\mathrm{N}^2}\,\gamma^\mu\left(\not{p}_\mathrm{f}-\not{k}+M_\mathrm{N}\right)\right\}$$
$$\frac{\not{p}_{\pi^+}}{(p_\mathrm{i}-p_{\pi^+})^2-M_\mathrm{N}^2}\mathrm{N}(p_\mathrm{i},s_\mathrm{i}).$$

The sum of these two diagrams is again gauge invariant:

$$k_\mu\left(J^{\mu}_{\pi^-(c)} + J^{\mu}_{\pi^-(d)}\right) = 0\,.$$

The π^+ exchange in Figures 6.5(a) and 6.5(b) is regge-ised by means of the Regge propagator $\mathcal{P}^{\pi^+}_{\mathrm{Regge}}(s,t_{\pi^+})$. The t-channel momentum transfer t_{π^+} is defined as $t_{\pi^+} = (k-p_{\pi^+})^2$. On the other hand, the π^- exchange in Figures 6.5(c) and 6.5(d) is regge-ised with the Regge propagator $\mathcal{P}^{\pi^-}_{\mathrm{Regge}}(s,t_{\pi^-})$, where $t_{\pi^+} = (k-p_{\pi^-})^2$. We follow the arguments given in [58] for the degeneracy of the trajectories for the $\gamma\mathrm{p}\to\pi^+\mathrm{n}$ and $\gamma\mathrm{n}\to\pi^-\mathrm{p}$ reactions. Due to the negative G-parity of the pion, it couples with a negative relative sign to the $\gamma\pi^+\pi^-$ and $\gamma\pi^-\pi^+$ vertices. The b_1, in contrast, has a positive G-parity such that the couplings to the $\gamma\pi^+\mathrm{b}_1^-$ and $\gamma\pi^-\mathrm{b}_1^+$ vertices have the same relative sign. Following these considerations, a degenerate trajectory with a rotating phase is used for the π^+ exchange whereas a constant phase is employed for the π^- exchange. Explicitly, this means that we use:

$$\mathcal{P}^{\pi}_{\mathrm{Regge}}(s,t_{\pi^+}) = \pi\alpha'_\pi\frac{e^{-i\pi\alpha_\pi(t_{\pi^+})}}{\Gamma(1+\alpha_\pi(t_{\pi^+}))\sin(\pi\alpha_\pi(t_{\pi^+}))}\left(\frac{s}{s_0}\right)^{\alpha_\pi(t_{\pi^+})}$$

and

$$\mathcal{P}^{\pi}_{\mathrm{Regge}}(s,t_{\pi^-}) = \pi\alpha'_\pi\frac{1}{\Gamma(1+\alpha_\pi(t_{\pi^-}))\sin(\pi\alpha_\pi(t_{\pi^-}))}\left(\frac{s}{s_0}\right)^{\alpha_\pi(t_{\pi^+})},$$

with the Regge trajectory as in (6.14).

The single pion production diagrams from which we started are well defined at high energies. The Regge trajectory exchange accounts for the exchange of the pion and its orbital excitations, yielding an amplitude which drops with a power of the energy. By coupling an extra pion to the nucleon line, however, there is a propagation of the nucleon which is off its mass shell. As this propagator is not regge-ised the internal structure of the nucleon is not taken into account. As a first approach, we apply a pion-nucleon form factor to quantitatively incorporate the arising reduction. An invariant form factor of the following shape is used:

$$\mathrm{F}_\mathrm{N}(p^2) = \frac{\Lambda_\mathrm{N}^4}{\Lambda_\mathrm{N}^4+(p^2-m_\mathrm{N}^2)^2}.$$

This form factor only depends on the four-vector momentum squared of the nucleon. It has the property that it reduces to 1 for $p \to m_{\rm N}^2$. As a cutoff value, $\Lambda_{\rm N} = 0.675$ GeV is used. In the case of the π^+ exchange diagrams in Figures 6.5(a) and 6.5(b), one has for the four-vector momentum p:

$$p^2 = (p_{\rm f} + p_{\pi^-})^2,$$

whereas, for the diagrams in Figures 6.5(c) and 6.5(d):

$$p^2 = (p_{\rm i} - p_{\pi^+})^2.$$

Similarly as for the $\pi\Delta$ production via π exchange, one can also restrict oneself to minimal gauge invariance, i.e. only regge-ise the electric terms in the nucleon coupling. We have then, for the π^+ exchange diagrams:

$$J^\mu_{\pi^+(a),\rm mgi} + J^\mu_{\pi^+(b),\rm mgi} = e\,2\,g^2_{\pi\rm NN}\,\mathcal{P}^{\pi^+}_{\rm Regge}(s,t_{\pi^+})\bar{\rm N}(p_{\rm f},s_{\rm f})\,\frac{\not{p}_{\pi^-}}{(p_{\rm f}+p_{\pi^-})^2 - M_{\rm N}^2}$$
$$\left\{(2p_{\pi^+} - k)^\mu + \frac{t_{\pi^+} - m_\pi^2}{(p_{\rm i}+k)^2 - M_{\rm N}^2}\,(2p_{\rm i}+k)^\mu\right\}{\rm N}(p_{\rm i},s_{\rm i}).$$

Analogously for the π^- exchange diagrams:

$$J^\mu_{\pi^-(c),\rm mgi} + J^\mu_{\pi^-(d),\rm mgi} = e\,2\,g^2_{\pi\rm NN}\,\mathcal{P}^{\pi^-}_{\rm Regge}(s,t_{\pi^-})\bar{\rm N}(p_{\rm f},s_{\rm f})$$
$$\left\{(2p_{\pi^-} - k)^\mu - \frac{t_{\pi^-} - m_\pi^2}{(p_{\rm f}-k)^2 - M_{\rm N}^2}\,(2p_{\rm f}-k)^\mu\right\}$$
$$\frac{\not{p}_{\pi^+}}{(p_{\rm i}-p_{\pi^+})^2 - M_{\rm N}^2}{\rm N}(p_{\rm i},s_{\rm i}).$$

$\gamma\mathbf{p} \to \mathbf{n}\pi^+\pi^0$ In the case of the $\gamma{\rm p} \to {\rm n}\pi^+\pi^0$ process the contributing diagrams are derived from the gauge-invariant π^+ exchange in the $\gamma p \to \pi^+ n$ reaction by coupling a π^0 to all nucleon lines. This results in the five diagrams in Figure 6.6.

The contributions of the diagrams of Figures 6.6(a), 6.6(b) and 6.6(c) are given by:

$$J^\mu_{\pi^+(a)} + J^\mu_{\pi^+(b)} + J^\mu_{\pi^+(c)} = -e\sqrt{2}\,g^2_{\pi\rm NN}\,\mathcal{P}^{\pi}_{\rm Regge}(s,t_{\pi^+})\bar{\rm N}(p_{\rm f},s_{\rm f})$$
$$\left\{\left((2p_{\pi^+} - k)^\mu + \frac{t_{\pi^+} - m_\pi^2}{(p_{\rm f}+p_{\pi^+})^2 - M_{\rm N}^2}\;\not{p}_{\pi^+}\gamma^\mu\right)\frac{\not{p}_{\pi^0}}{(p_{\rm i}-p_{\pi^0})^2 - M_{\rm N}^2}\right.$$
$$\left. - \frac{t_{\pi^+} - m_\pi^2}{(p_{\rm f}+p_{\pi^+})^2 - M_{\rm N}^2}\,\frac{1}{(p_{\rm i}+k)^2 - M_{\rm N}^2}\;\not{p}_{\pi^+}\left(\not{p}_{\rm i} + \not{k} + M_{\rm N}\right)\gamma^\mu\right\}{\rm N}(p_{\rm i},s_{\rm i}),$$

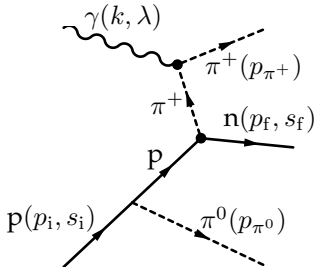

(a)

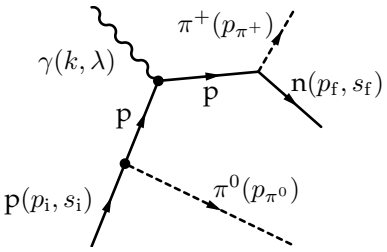

(b)

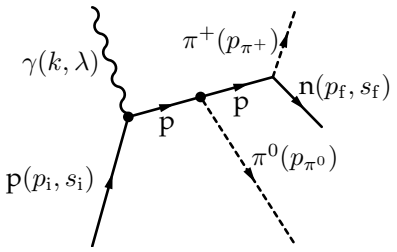

(c)

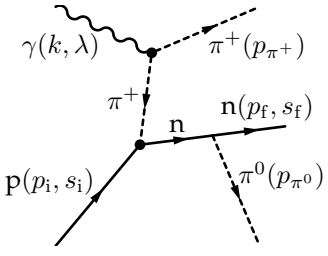

(d)

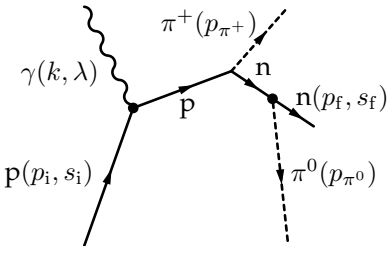

(e)

Figure 6.6: $\gamma p \to \mathrm{n}\pi^+\pi^0$: Gauge invariant π exchange with a nucleon intermediate state.

The sum of these three diagrams is gauge invariant, i.e.

$$k_\mu \left(J^\mu_{\pi^+(a)} \, + \, J^\mu_{\pi^+(b)} \, + \, J^\mu_{\pi^+(c)} \right) \, = \, 0 \, .$$

The contribution of the diagrams Figures 6.6(d) and 6.6(e) is given by:

$$J^\mu_{\pi^+(d)} \, + \, J^\mu_{\pi^+(e)} = -e\sqrt{2}\, g^2_{\pi \mathrm{NN}}\, \mathcal{P}^\pi_{\mathrm{Regge}}(s, t_{\pi^+}) \bar{\mathrm{N}}(p_\mathrm{f}, s_\mathrm{f}) \, \frac{\not{p}_{\pi^0}}{(p_\mathrm{f} + p_{\pi^0})^2 - M^2_\mathrm{N}}$$
$$\left\{ (2p_{\pi^+} - k)^\mu \, + \, \frac{t_{\pi^+} - m^2_\pi}{(p_\mathrm{i} + k)^2 - M^2_\mathrm{N}} \left(\not{p}_\mathrm{i} + \not{k} + M_\mathrm{N} \right) \gamma^\mu \right\} \mathrm{N}(p_\mathrm{i}, s_\mathrm{i}),$$

The sum of these two diagrams is again gauge invariant:

$$k_\mu \left(J^\mu_{\pi^+(c)} \, + \, J^\mu_{\pi^+(d)} \right) \, = \, 0 \, .$$

6.3.2.3 γN $\to$ ρN $\to$ $\pi\pi$N: Gauge invariant ρ exchange

In this section the production of two pions via the exchange of a ρ meson is considered. The so-called *ρ Born graphs* are quite isospin dependent since the coupling of the photon is charge dependent. Figures 6.7 and 6.8 depict the gauge invariant ensemble of diagrams for $\gamma\mathrm{p} \to \mathrm{p}\pi^+\pi^-$ and $\gamma\mathrm{p} \to \mathrm{n}\pi^+\pi^0$, respectively. The former involves the exchange of a ρ^0 and the latter the exchange of a ρ^+. In each case there is a contact diagram and a diagram for each possible coupling of the photon to the pions and the ρ. We define:

$$p_\rho = p_\mathrm{i} - p_\mathrm{f} \tag{6.24}$$
$$p'_\rho = p_{\pi_1} + p_{\pi_2}. \tag{6.25}$$

$\gamma\mathbf{p} \to \mathbf{p}\pi^+\pi^-$ With the labeling as in Figure 6.7, the respective contributions to $\gamma\mathrm{p} \to \mathrm{p}\pi^+\pi^-$ are:

$$J^\mu_{\rho^0(a)} = e g_{\rho \mathrm{NN}} g_{\rho\pi\pi} \frac{(2p_{\pi^+} - k)^\mu}{2k \cdot p_{\pi^+}} \mathcal{P}^\rho_{\mathrm{Regge}}(s, p^2_\rho)(p_{\pi^+} - p_{\pi^-} - k)_\alpha$$
$$\bar{\mathrm{N}}(p_\mathrm{f}, s_\mathrm{f}) \left(\gamma^\alpha - i\kappa_\rho \sigma^{\alpha\beta} \frac{(p_\rho)_\beta}{2m_\mathrm{N}} \right) \mathrm{N}(p_\mathrm{i}, s_\mathrm{i}),$$

$$J^\mu_{\rho^0(b)} = e g_{\rho \mathrm{NN}} g_{\rho\pi\pi} \frac{(2p_{\pi^-} - k)^\mu}{2k \cdot p_{\pi^-}} \mathcal{P}^\rho_{\mathrm{Regge}}(s, p^2_\rho)(-p_{\pi^+} + p_{\pi^-} - k)_\alpha$$
$$\bar{\mathrm{N}}(p_\mathrm{f}, s_\mathrm{f}) \left(\gamma^\alpha - i\kappa_\rho \sigma^{\alpha\beta} \frac{(p_\rho)_\beta}{2m_\mathrm{N}} \right) \mathrm{N}(p_\mathrm{i}, s_\mathrm{i}),$$

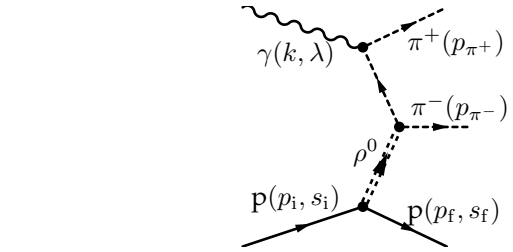

(a)

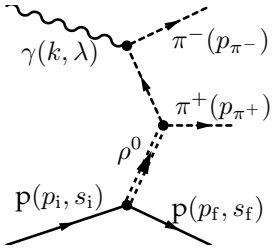

(b)

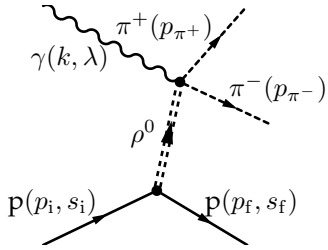

(c)

Figure 6.7: $\gamma p \to \mathrm{p}\pi^+\pi^-$: Gauge invariant ρ exchange.

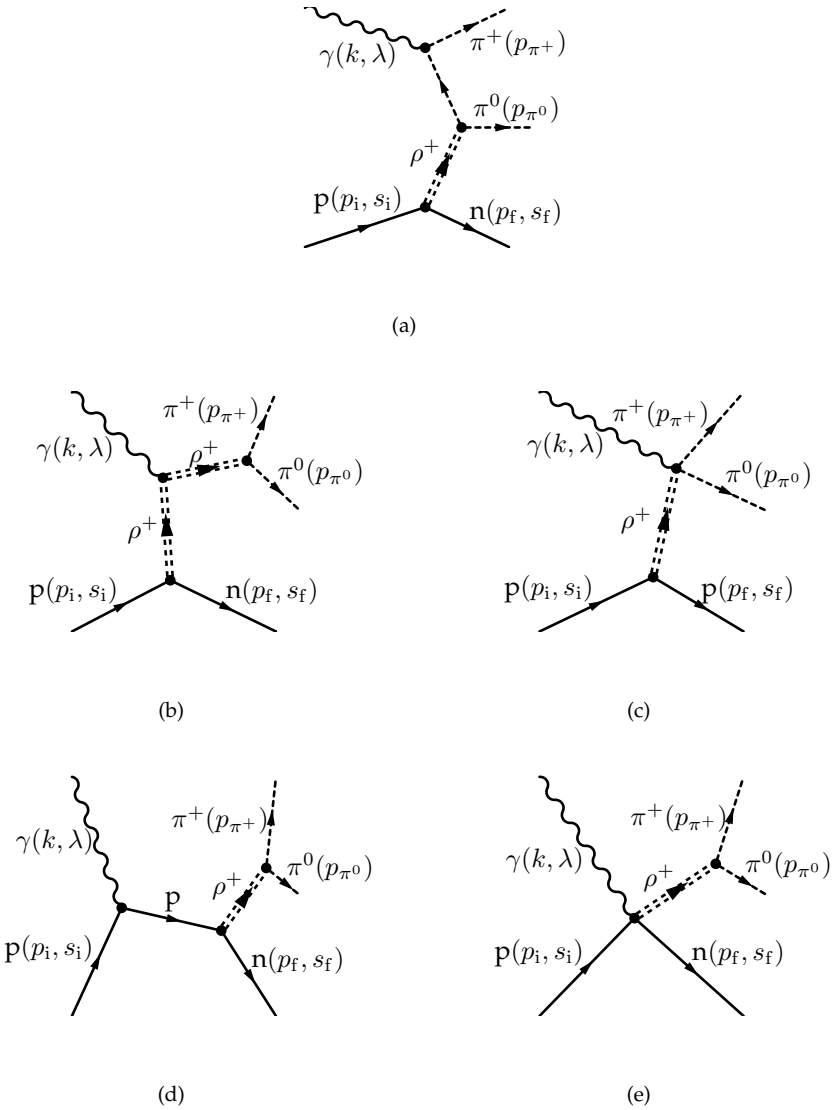

Figure 6.8: $\gamma p \to \mathrm{n}\pi^+\pi^0$: Gauge invariant ρ exchange.

$$J^{\mu}_{\rho^0(c)} \;=\; 2eg_{\rho\mathrm{NN}}g_{\rho\pi\pi}\mathcal{P}^{\rho}_{\mathrm{Regge}}(s,p_\rho^2)\bar{\mathrm{N}}(p_\mathrm{f},s_\mathrm{f})\left(\gamma^{\mu} \;-\; i\kappa_\rho\sigma^{\mu\beta}\frac{(p_\rho)_\beta}{2m_\mathrm{N}}\right)\mathrm{N}(p_\mathrm{i},s_\mathrm{i}).$$

The invariant mass of the exchanged ρ meson p_ρ^2 naturally serves as the t in the Regge trajectory with the propagator:

$$\mathcal{P}^{\rho}_{\mathrm{Regge}}(s,t) = \pi\alpha'_\rho\frac{e^{-i\pi\alpha_\rho(t)}}{\Gamma(\alpha_\rho(t))\sin(\pi\alpha_\rho(t))}\left(\frac{s}{s_0}\right)^{\alpha_\rho(t)-1}, \tag{6.26}$$

for a degenerate trajectory with rotating phase. The ρ trajectory is parametrized as:

$$\alpha_\rho(t) = \alpha_\rho(0) + \alpha'_\rho t \quad \text{with } \alpha_\rho(0) = 0.55 \text{ and } \alpha'_\rho = 0.8.$$

$\boldsymbol{\gamma\mathrm{p}\to\mathrm{n}\pi^+\pi^0}$ When using pole exchanges, the five contributions to $\gamma\mathrm{p}\to\mathrm{n}\pi^+\pi^0$ are described by:

$$J^{\mu}_{\rho^+(a)} = -e\sqrt{2}g_{\rho\mathrm{NN}}g_{\rho\pi\pi}\frac{(2p_{\pi^+}-k)^\mu}{2k\cdot p_{\pi^+}}\frac{1}{p_\rho^2-m_\rho^2+im_\rho\Gamma_{\rho\to\pi\pi}}(p_{\pi^+}-p_{\pi^0}-k)_\alpha$$
$$\bar{\mathrm{N}}(p_\mathrm{f},s_\mathrm{f})\left(\gamma^{\alpha} - i\kappa_\rho\sigma^{\alpha\beta}\frac{(p_\rho)_\beta}{2m_\mathrm{N}}\right)\mathrm{N}(p_\mathrm{i},s_\mathrm{i}),$$

$$J^{\mu}_{\rho^+(b)} = -e\sqrt{2}g_{\rho\mathrm{NN}}g_{\rho\pi\pi}\frac{1}{p_\rho^2-m_\rho^2+im_\rho\Gamma_{\rho\to\pi\pi}}\frac{1}{p_\rho'^2-m_\rho^2+im_\rho\Gamma_{\rho\to\pi\pi}}$$
$$(p_{\pi^+}-p_{\pi^0})_\alpha\Big(-g^{\alpha\beta}(p_\rho+p'_\rho)^\mu + g^{\alpha\mu}(p'_\rho)^\beta + g^{\beta\mu}(p_\rho)^\alpha\Big)$$
$$\bar{\mathrm{N}}(p_\mathrm{f},s_\mathrm{f})\left(\gamma_{\beta} - i\kappa_\rho\sigma_{\beta\lambda}\frac{(p_\rho)^\lambda}{2m_\mathrm{N}}\right)\mathrm{N}(p_\mathrm{i},s_\mathrm{i}),$$

$$J^{\mu}_{\rho^+(c)} = -e\sqrt{2}g_{\rho\mathrm{NN}}g_{\rho\pi\pi}\frac{1}{p_\rho^2-m_\rho^2+im_\rho\Gamma_{\rho\to\pi\pi}}$$
$$\bar{\mathrm{N}}(p_\mathrm{f},s_\mathrm{f})\left(\gamma^{\mu} - i\kappa_\rho\sigma^{\mu\beta}\frac{(p_\rho)_\beta}{2m_\mathrm{N}}\right)\mathrm{N}(p_\mathrm{i},s_\mathrm{i}).$$

$$J^{\mu}_{\rho^+(d)} = e\sqrt{2}g_{\rho\mathrm{NN}}g_{\rho\pi\pi}\frac{1}{p_\rho'^2-m_\rho^2+im_\rho\Gamma_{\rho\to\pi\pi}}\frac{(p_{\pi^+}-p_{\pi^0})_\alpha}{2k\cdot p_\mathrm{i}}$$
$$\bar{\mathrm{N}}(p_\mathrm{f},s_\mathrm{f})\left(\gamma^{\alpha} - i\kappa_\rho\sigma^{\alpha\beta}\frac{(p'_\rho)_\beta}{2m_\mathrm{N}}\right)(\not{k}\gamma^\mu + 2p_\mathrm{i}^\mu)\mathrm{N}(p_\mathrm{i},s_\mathrm{i}),$$

$$J^{\mu}_{\rho^+(e)} = -e\sqrt{2}g_{\rho\mathrm{NN}}g_{\rho\pi\pi}\frac{1}{p_\rho'^2-m_\rho^2+im_\rho\Gamma_{\rho\to\pi\pi}}(p_{\pi^+}-p_{\pi^0})_\alpha$$
$$\bar{\mathrm{N}}(p_\mathrm{f},s_\mathrm{f})\left(-\frac{i\kappa_\rho\sigma^{\beta\mu}}{2m_\mathrm{N}}\right)\mathrm{N}(p_\mathrm{i},s_\mathrm{i}).$$

The regge-isation of the ρ^+ exchange is performed globally:

$$(p_\rho^2 - m_\rho^2)\mathcal{P}^\rho_{\text{Regge}}(s, p_\rho^2)\left(J^\mu_{\rho^+(a)} + J^\mu_{\rho^+(b)} + J^\mu_{\rho^+(c)} + J^\mu_{\rho^+(d)} + J^\mu_{\rho^+(e)}\right), \quad (6.27)$$

with the Regge propagator as above.

The electromagnetic coupling constant $g_{\rho\pi\gamma}$ can be obtained from the decay width of the ρ into $\pi\gamma$:

$$\Gamma_{\rho\to\pi\gamma} = \frac{\alpha}{24}\left(\frac{g_{\rho\pi\gamma}}{m_\pi}\right)^2\left(1 - \left(\frac{m_\pi}{m_\rho}\right)^2\right)^3 m_\rho^3.$$

For the charged pion decay $\Gamma_{\rho^\pm\to\pi^\pm\gamma} = 0.0678$ MeV [105] and so $g_{\rho^\pm\pi^\pm\gamma} = 0.103$. The decay width for the ρ^0 is $\Gamma_{\rho^0\to\pi^0\gamma} = 0.102$ MeV [105] which yields $g_{\rho^0\pi^0\gamma} = 0.122$.

The strong coupling constant $g_{\rho\pi\pi}$ is extracted from the hadronic decay $\rho \to \pi\pi$:

$$\Gamma_{\rho\to\pi\pi} = \frac{2}{3}\frac{g^2_{\rho\pi\pi}}{4\pi}\frac{1}{m_\rho^2}\left(\left(\frac{m_\rho}{2}\right)^2 - m_\pi^2\right)^{3/2}.$$

Taking the value $\Gamma_{\rho\to\pi\pi} = 150.7$ MeV from [105] we find $g_{\rho\pi\pi} = 6.038$. For κ_ρ we adopt the value given by [89]: $\kappa_\rho = 6.1$. These values for the hadronic coupling constants correspond to a *strong* ρ, favoured over a *weak* ρ in accordance with [58].

The diagrams discussed in the following sections are not derived from Born terms and can thus be written as a single invariant term. We consider the production of a $\pi\Delta$ intermediate state through ρ trajectory exchange and ρN production through the exchange of a π and f_1 meson trajectory exchange. Quantitatively we found that these three diagrams only yield a small contribution to the here studied cross sections at lower energies.

6.3.2.4 γN $\to \pi\Delta \to \pi\pi$N: ρ exchange

The ρ exchange diagram depicted in Figure 6.9(a) is gauge invariant by itself. It is regge-ised through the ρ Regge propagator $\mathcal{P}^\rho_{\text{Regge}}$. Its hadronic current is given by:

$$J^\mu_{(\rho)\pi\Delta} = -i\mathcal{I}\frac{e g_{\rho\pi\gamma}}{m_\pi}\frac{m_\rho}{f_\rho}G_{\text{M}}\mathcal{P}^\rho_{\text{Regge}}(s, p_\rho^2)\epsilon^{\nu\mu\kappa\beta}k_\nu(k - p_\pi)_\kappa \bar{\Delta}_\alpha(p_\Delta, s_\Delta)\Gamma^{\alpha\beta}_{\text{M}}(k - p_\pi)\text{N}(p_\text{i}, s_\text{i}),$$

with the Regge propagator $\mathcal{P}^\rho_{\text{Regge}}(s, t)$ as in (6.26). Analogously as for the non-resonant $\pi\Delta$ production by π exchange, this current gives the two-body

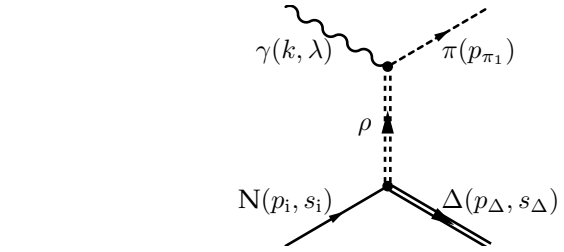

(a)

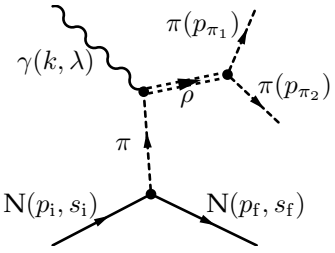

(b)

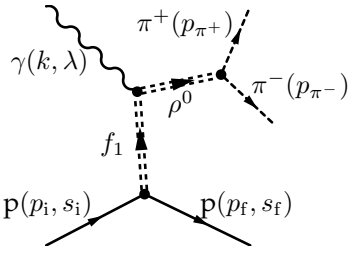

(c)

Figure 6.9: (a) $\gamma\mathrm{N} \to \pi\Delta \to \pi\pi\mathrm{N}$: ρ exchange diagram, (b) $\gamma\mathrm{N} \to \rho\mathrm{N} \to \pi\pi\mathrm{N}$: π exchange diagram, (c) $\gamma\mathrm{N} \to \rho\mathrm{N} \to \pi\pi\mathrm{N}$: f_1 exchange diagram.

matrix element $\mathcal{M}_{\text{fi}}^{(2b)}(\gamma N \to \pi_1 \Delta(m_\Delta, s_\Delta))$ from which the three-body matrix element $\mathcal{M}_{\text{fi}}^{(3b)}(\gamma N \to \pi_1 \Delta \to \pi_1 \pi_2 N)$ can be deduced. The ρ-γ transition constant f_ρ is obtained in the vector dominance model (VDM) and has a value of 0.153 GeV. The magnetic coupling to the Δ is determined by $G_M = 2.8$. The vertex $\Gamma_M^{\alpha\beta}$ is as defined in [117]. In the case of $\gamma p \to \pi^- \Delta^{++}$ the isospin factor $\mathcal{I}$ is equal to 1.

6.3.2.5 $\gamma N \to \rho N \to \pi\pi N$: π exchange

The intermediate ρN state can be reached through the exchange of a π trajectory. The strong decay of the ρ in two pions is described by a Breit-Wigner form. Figure 6.9(b) represents the corresponding diagram. The three-body hadronic current reads:

$$J^\mu_{(\pi)\rho N} = \mathcal{I} \frac{ie g_{\rho\pi\gamma} g_{\rho\pi\pi} g_{\pi NN}}{m_\pi} \frac{1}{W^2_{\pi_1\pi_2} - m^2_\rho + i W_{\pi_1\pi_2} \Gamma_\rho(W_{\pi_1\pi_2})} \epsilon^{\lambda\mu\alpha\beta} k_\lambda (p'_\rho)_\alpha (p_{\pi_2} - p_{\pi_1})_\beta \mathcal{P}^\pi_{\text{Regge}}(s, p^2_\rho) \bar{N}(p_f, s_f) \gamma_5 N(p_i, s_i).$$

The four-vectors p_ρ and p'_ρ are defined as in (6.24) and (6.25). The pion Regge propagator is given in (6.13). For the pion-nucleon coupling constant $g_{\pi NN} = \frac{2 m_N f_{\pi NN}}{m_\pi}$ we use $f_{\pi NN} = 1.00265$ as given by [89]. For the $\gamma p \to p\pi^+\pi^-$ reaction, the isospin factor is $\mathcal{I} = 1$. For $\gamma p \to n\pi^+\pi^0$ this is $\mathcal{I} = \sqrt{2}$.

6.3.2.6 $\gamma N \to \rho N \to \pi\pi N$: f_1 exchange

Led by the fact that the $f_1 \rho^0 \gamma$ coupling is relatively strong, we also investigate ρN production via the exchange of the axial f_1 meson for the $\gamma p \to \rho^0 p \to \pi^+\pi^- p$ channel (Figure 6.9(c)). Define the four-vector momentum of the exchanged f_1 as:

$$p_{f_1} = p_f - p_i. \tag{6.28}$$

The regge-ised f_1 exchange is described by the three-body current:

$$J^\mu_{(f_1)\rho^0 p} = -e \tilde{g}_{f_1\rho^0\gamma} g_{f_1 NN} g_{\rho\pi\pi} \frac{-g_{\alpha\alpha'} + \frac{(p'_\rho)_\alpha (p'_\rho)_{\alpha'}}{W^2_{\pi_1\pi_2}}}{W^2_{\pi_1\pi_2} - m^2_\rho + i W_{\pi_1\pi_2} \Gamma_\rho(W_{\pi_1\pi_2})} \epsilon^{\mu\nu\alpha\beta} k_\nu (p_{\pi^+} - p_{\pi^-})^{\alpha'} \mathcal{P}^{f_1}_{\text{Regge}}(s, p^2_{f_1}) \left(-g_{\beta\beta'} + \frac{(p'_{f_1})_\beta (p'_{f_1})_{\beta'}}{m^2_{f_1}} \right) \bar{N}(p_f, s_f) \gamma^{\beta'} \gamma_5 N(p_i, s_i),$$

where we have retained the definition of p'_ρ in (6.25). The $f_1 NN$ coupling is obtained using axial vector dominance (ADM) as $g_{f_1 NN} = 2.5$. The electromagnetic coupling constant is obtained from the decay width for $f_1 \to \rho^0 \gamma$:

$$\Gamma_{f_1 \to \rho^0 \gamma} = \frac{e^2}{96\pi} \tilde{g}^2_{f_1\rho^0\gamma} \frac{(m^2_{f_1} + m^2_\rho)(m^2_{f_1} - m^2_\rho)^3}{m^5_{f_1} m^2_\rho}.$$

With $\Gamma_{f_1\to\rho^0\gamma} = 1.296$ MeV [105] one has $\left|\tilde{g}_{f_1\rho^0\gamma}\right| = 1.84$.

6.3.3 s-channel resonances

The non-resonant mechanisms in double pion photoproduction considered in the previous section, account for the smooth energy behaviour of the background of the double pion photoproduction cross sections. In this section, explicit s-channel resonance contributions are examined, in particular through the excitation of the $\mathrm{D}_{13}(1520)$ resonance.

A general s-channel resonance mechanism in double pion photoproduction is described in first instance by the excitation of the nucleon to a resonant state, which then decays into a final double pion state. Two examples are:

$$\gamma\mathrm{N} \to \mathrm{D}_{13} \to \pi\Delta \to \pi\pi\mathrm{N},$$
$$\gamma\mathrm{N} \to \mathrm{D}_{13} \to \rho\mathrm{N} \to \pi\pi\mathrm{N}.$$

The D_{13} is the first prominent resonance that shows up in double pion photoproduction. Before addressing the calculation of the matrix elements of the specific contributions, the main properties of this resonance are studied: its coupling at the $\gamma\mathrm{ND}_{13}$ vertex and its decay widths from which the hadronic coupling constants can be deduced. We also study the energy —or invariant mass— dependence of the decay width. The coupling constants G_1 and G_2 used to describe the $\gamma\mathrm{ND}_{13}$ vertex can be calculated from the following relations with the helicity dependent photon decay amplitudes $A^{\mathrm{N}}_{1/2}(\mathrm{D}_{13})$ and $A^{\mathrm{N}}_{3/2}(\mathrm{D}_{13})$:

$$A^{\mathrm{N}}_{1/2}(\mathrm{D}_{13}) = \frac{e}{4\sqrt{3}m_{\mathrm{N}}}\sqrt{\frac{2m_{\mathrm{D}_{13}}|\vec{k}|}{m_{\mathrm{N}}}}\frac{m_{\mathrm{N}}}{m_{\mathrm{D}_{13}}}\left(G^{\mathrm{N}}_1 - G^{\mathrm{N}}_2\frac{m_{\mathrm{D}_{13}}}{m_{\mathrm{N}}}\frac{m_{\mathrm{D}_{13}}+m_{\mathrm{N}}}{4m_{\mathrm{N}}}\right)$$
$$A^{\mathrm{N}}_{3/2}(\mathrm{D}_{13}) = \frac{e}{4m_{\mathrm{N}}}\sqrt{\frac{2m_{\mathrm{D}_{13}}|\vec{k}|}{m_{\mathrm{N}}}}\left(G^{\mathrm{N}}_1 - G^{\mathrm{N}}_2\frac{m_{\mathrm{D}_{13}}+m_{\mathrm{N}}}{4m_{\mathrm{N}}}\right).$$

Adopting the recommended values from [105] one finds for the coupling with the proton:

$$\begin{aligned} A^{\mathrm{p}}_{1/2}(\mathrm{D}_{13}) &= -20.10^{-3}\ \mathrm{GeV}^{-1/2} \\ A^{\mathrm{p}}_{3/2}(\mathrm{D}_{13}) &= 167.10^{-3}\ \mathrm{GeV}^{-1/2} \end{aligned} \quad \Rightarrow \quad \begin{aligned} G^{\mathrm{p}}_1 &= 5.33 \\ G^{\mathrm{p}}_2 &= 5.58 \end{aligned} \tag{6.29}$$

and with the neutron:

$$\begin{aligned} A^{\mathrm{n}}_{1/2}(\mathrm{D}_{13}) &= -59.10^{-3}\ \mathrm{GeV}^{-1/2} \\ A^{\mathrm{n}}_{3/2}(\mathrm{D}_{13}) &= -139.10^{-3}\ \mathrm{GeV}^{-1/2} \end{aligned} \quad \Rightarrow \quad \begin{aligned} G^{\mathrm{n}}_1 &= -0.968 \\ G^{\mathrm{n}}_2 &= 0.656. \end{aligned}$$

The full Breit-Wigner width of the D_{13} ($m_{\mathrm{D}_{13}} = 1.520$ GeV) is $\Gamma_{\mathrm{D}_{13},\mathrm{total}} \approx 120$ MeV. The main decay modes are πN, $\pi\Delta$ via s-wave decay, $\pi\Delta$ via d-wave decay and ρN via s-wave decay. The energy dependence of the D_{13}

decay width is given by:

$$\Gamma_{\mathrm{D}_{13},\mathrm{total}}(W_{\mathrm{D}_{13}}) = \Gamma_{\mathrm{D}_{13}\to\pi\mathrm{N}}(W_{\mathrm{D}_{13}}) + \Gamma_{\mathrm{D}_{13}\to(\rho\mathrm{N})_\mathrm{s}}(W_{\mathrm{D}_{13}}) + \Gamma_{\mathrm{D}_{13}\to(\pi\Delta)_\mathrm{s}}(W_{\mathrm{D}_{13}}) + \Gamma_{\mathrm{D}_{13}\to(\pi\Delta)_\mathrm{d}}(W_{\mathrm{D}_{13}}).$$

At the resonance position one has $\Gamma_{\mathrm{D}_{13},\mathrm{total}}(W_{\mathrm{D}_{13}} = m_{\mathrm{D}_{13}}) \approx 120$ MeV, and with the branching ratios given by [91] and [105]:

$$\Gamma_{\mathrm{D}_{13}\to\pi\mathrm{N}}(W_{\mathrm{D}_{13}} = m_{\mathrm{D}_{13}}) \approx 73\,\mathrm{MeV} \quad (\pm 60\%) \tag{6.30}$$
$$\Gamma_{\mathrm{D}_{13}\to(\rho\mathrm{N})_\mathrm{s}}(W_{\mathrm{D}_{13}} = m_{\mathrm{D}_{13}}) \approx 26\,\mathrm{MeV} \quad (\pm 21\%) \tag{6.31}$$
$$\Gamma_{\mathrm{D}_{13}\to(\pi\Delta)_\mathrm{s}}(W_{\mathrm{D}_{13}} = m_{\mathrm{D}_{13}}) \approx 7\,\mathrm{MeV} \quad (\pm 5\%) \tag{6.32}$$
$$\Gamma_{\mathrm{D}_{13}\to(\pi\Delta)_\mathrm{d}}(W_{\mathrm{D}_{13}} = m_{\mathrm{D}_{13}}) \approx 18\,\mathrm{MeV} \quad (\pm 15\%). \tag{6.33}$$

The energy dependence of the $\mathrm{D}_{13} \to \pi\mathrm{N}$ decay width is given by:

$$\Gamma_{\mathrm{D}_{13}\to\pi\mathrm{N}}(W_{\mathrm{D}_{13}}) = \frac{(f_{\pi\mathrm{N}\mathrm{D}_{13}})^2}{4\pi} \frac{\left|\vec{p}_\pi^{\,\mathrm{CM}\pi\mathrm{N}}\right|^5}{W_{\mathrm{D}_{13}}(E_\mathrm{N}+m_\mathrm{N})m_\pi^2},$$

with the pion momentum in the πN rest frame:

$$\left|\vec{p}_\pi^{\,\mathrm{CM}\pi\mathrm{N}}\right| = \frac{1}{2W_{\mathrm{D}_{13}}}\sqrt{W_{\mathrm{D}_{13}}^4 - 2W_{\mathrm{D}_{13}}^2\left(m_\pi^2+m_\mathrm{N}^2\right) + \left(m_\pi^2-m_\mathrm{N}^2\right)^2}. \tag{6.34}$$

For the decay of the D_{13} into $\pi\Delta$, the s- and d-wave widths read:

$$\Gamma_{\mathrm{D}_{13}\to(\pi\Delta)_\mathrm{s}}(W_{\mathrm{D}_{13}}) = \frac{(f^\mathrm{s}_{\pi\Delta\mathrm{D}_{13}})^2}{\pi} \frac{\left|\vec{p}_\pi^{\,\mathrm{CM}\pi\Delta}\right| m_\Delta}{W_{\mathrm{D}_{13}}}$$
$$\Gamma_{\mathrm{D}_{13}\to(\pi\Delta)_\mathrm{d}}(W_{\mathrm{D}_{13}}) = \frac{(f^\mathrm{d}_{\pi\Delta\mathrm{D}_{13}})^2}{\pi} \frac{\left|\vec{p}_\pi^{\,\mathrm{CM}\pi\Delta}\right|^5 m_\Delta}{W_{\mathrm{D}_{13}}m_\pi^4},$$

with the pion momentum in the $\pi\Delta$ rest frame:

$$\left|\vec{p}_\pi^{\,\mathrm{CM}\pi\Delta}\right| = \frac{1}{2W_{\mathrm{D}_{13}}}\sqrt{W_{\mathrm{D}_{13}}^4 - 2W_{\mathrm{D}_{13}}^2\left(m_\pi^2+m_\Delta^2\right) + \left(m_\pi^2-m_\Delta^2\right)^2}. \tag{6.35}$$

Finally, the width corresponding to $\mathrm{D}_{13} \to \rho\mathrm{N}$ is:

$$\Gamma_{\mathrm{D}_{13}\to(\rho\mathrm{N})_\mathrm{s}}(W_{\mathrm{D}_{13}}) = \frac{3(f^\mathrm{s}_{\rho\mathrm{N}\mathrm{D}_{13}})^2}{4\pi} \frac{(E_\mathrm{N}+m_\mathrm{N})\left|\vec{p}_\rho^{\,\mathrm{CM}\rho\mathrm{N}}\right|}{W_{\mathrm{D}_{13}}} \left(1 + \frac{\left|\vec{p}_\rho^{\,\mathrm{CM}\rho\mathrm{N}}\right|^2}{3m_{\pi\pi}^2}\right).$$

The ρ is not necessarily produced on-shell and has a mass $m_{\pi\pi}$ varying between $2m_\pi$ and the maximum available energy $W_{\mathrm{D}_{13}} - m_\mathrm{N}$. This mass distribution gives the following distribution for the momentum:

$$\left|\vec{p}_\rho^{\,\mathrm{CM}\rho\mathrm{N}}\right| = \int_{2m_\pi}^{W_{\mathrm{D}_{13}}-m_\mathrm{N}} \frac{\left|\vec{p}_{\pi\pi}^{\,\mathrm{CM}\rho\mathrm{N}}\right|}{2\pi} \frac{\Gamma_{\rho\to\pi\pi}}{(m_{\pi\pi}-m_\rho)^2 + \left(\frac{\Gamma_{\rho\to\pi\pi}}{2}\right)^2} \mathrm{d}m_{\pi\pi},$$

with $\Gamma_{\rho\to\pi\pi} = 150.7$ MeV [105] and

$$\left|\vec{p}^{\,\mathrm{CM}\rho\mathrm{N}}_{\pi\pi}\right| = \frac{1}{2W_{\mathrm{D}_{13}}}\sqrt{W^4_{\mathrm{D}_{13}} - 2W^2_{\mathrm{D}_{13}}\left(m^2_{\pi\pi} + m^2_{\mathrm{N}}\right) + \left(m^2_{\pi\pi} - m^2_{\mathrm{N}}\right)^2}.$$

The above expressions for the decay widths can be used to determine the absolute value of the coupling constants $f_{\pi\mathrm{N}\mathrm{D}_{13}}$, $f^{\mathrm{s}}_{\pi\Delta\mathrm{D}_{13}}$, $f^{\mathrm{d}}_{\pi\Delta\mathrm{D}_{13}}$ and $f^{\mathrm{s}}_{\rho\mathrm{N}\mathrm{D}_{13}}$. At the D_{13} resonance position $W_{\mathrm{D}_{13}} = m_{\mathrm{D}_{13}}$ all ingredients can exactly be calculated and given (6.30)–(6.33), one can solve for the coupling constants. In this way one obtains:

$$\begin{aligned}
|f_{\pi\mathrm{N}\mathrm{D}_{13}}| &= 1.580\\
|f^{\mathrm{s}}_{\pi\Delta\mathrm{D}_{13}}| &= 0.345\\
|f^{\mathrm{d}}_{\pi\Delta\mathrm{D}_{13}}| &= 0.207\\
|f^{\mathrm{s}}_{\rho\mathrm{N}\mathrm{D}_{13}}| &= 2.257.
\end{aligned}$$

Similarly as for the Δ decay we describe resonance damping for the d-wave decay $\mathrm{D}_{13} \to \pi\mathrm{N}$ and $\mathrm{D}_{13} \to (\pi\Delta)_{\mathrm{d}}$ with the d-wave Blatt-Weisskopf barrier penetration factor $B_2(x)$:

$$B_2(x) = \frac{x^2}{\sqrt{9 + 3x^2 + x^4}}.$$

The corresponding decay widths are then written:

$$\begin{aligned}
\Gamma^{\mathrm{RD}}_{\mathrm{D}_{13}\to\pi\mathrm{N}}(W_{\mathrm{D}_{13}}) &= \Gamma_{\mathrm{D}_{13}\to\pi\mathrm{N}}(m_{\mathrm{D}_{13}})\frac{\left|\vec{p}^{\,\mathrm{CM}\pi\mathrm{N}}_{\pi}\right|}{W_{\mathrm{D}_{13}}}\frac{m_{\mathrm{D}_{13}}}{\left|\vec{p}^{\,*\mathrm{CM}\pi\mathrm{N}}_{\pi}\right|}\frac{B_2^2\left(\left|\vec{p}^{\,\mathrm{CM}\pi\mathrm{N}}_{\pi}\right|R\right)}{B_2^2\left(\left|\vec{p}^{\,*\mathrm{CM}\pi\mathrm{N}}_{\pi}\right|R\right)},\\
\Gamma^{\mathrm{RD}}_{\mathrm{D}_{13}\to(\pi\Delta)_{\mathrm{d}}}(W_{\mathrm{D}_{13}}) &= \Gamma_{\mathrm{D}_{13}\to(\pi\Delta)_{\mathrm{d}}}(m_{\mathrm{D}_{13}})\frac{\left|\vec{p}^{\,\mathrm{CM}\pi\Delta}_{\pi}\right|}{W_{\mathrm{D}_{13}}}\frac{m_{\mathrm{D}_{13}}}{\left|\vec{p}^{\,*\mathrm{CM}\pi\Delta}_{\pi}\right|}\frac{B_2^2\left(\left|\vec{p}^{\,\mathrm{CM}\pi\Delta}_{\pi}\right|R\right)}{B_2^2\left(\left|\vec{p}^{\,*\mathrm{CM}\pi\Delta}_{\pi}\right|R\right)},
\end{aligned}$$

where $\left|\vec{p}^{\,*\mathrm{CM}\pi\mathrm{N}}_{\pi}\right|$ and $\left|\vec{p}^{\,*\mathrm{CM}\pi\Delta}_{\pi}\right|$ represent (6.34) and (6.35) at $W_{\mathrm{D}_{13}} = m_{\mathrm{D}_{13}}$ respectively. The interaction radius R is taken to be $R = 0.4$ fm.

6.3.3.1 $\gamma\mathrm{N} \to \mathrm{D}_{13} \to \pi\Delta \to \pi\pi\mathrm{N}$: D_{13} resonance in the s-channel

The hadronic current that corresponds to the resonant $\pi\Delta$ production diagram illustrated in Figure 6.10(a) is written as the sum of the s- and d-wave contri-

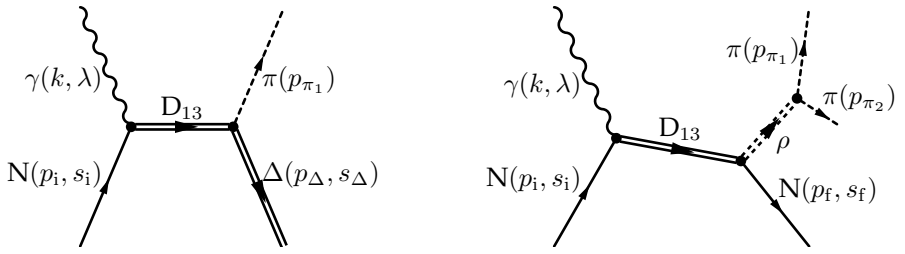

(a) (b)

Figure 6.10: (a) $\gamma\mathrm{N} \to \mathrm{D}_{13} \to \pi\Delta$, (b) $\gamma\mathrm{N} \to \mathrm{D}_{13} \to \rho\mathrm{N} \to \pi\pi\mathrm{N}$.

$\mathcal{I}$	$\gamma\mathrm{p} \to \mathrm{D}_{13} \to \pi^-\Delta^{++}$	$\gamma\mathrm{p} \to \mathrm{D}_{13} \to \pi^+\Delta^0$	$\gamma\mathrm{p} \to \mathrm{D}_{13} \to \pi^0\Delta^+$
$J^\mu_{\mathrm{D}_{13}\to\pi\Delta}$	-1	$+\sqrt{1/3}$	$+\sqrt{2/3}$

Table 6.4: Isospin factors for the $\gamma\mathrm{p} \to \mathrm{D}_{13} \to \pi\Delta$ channel.

bution:

$$J^\mu_{\mathrm{D}_{13}\to\pi\Delta} = ie\mathcal{I}\sqrt{E_\Delta + m_\Delta}\sqrt{2\sqrt{s}}\frac{1}{p_s^2 - m^2_{\mathrm{D}_{13}} + i\sqrt{s}\Gamma_{\mathrm{D}_{13},\mathrm{total}}(\sqrt{s})}$$
$$\sum_{s_{\mathrm{D}_{13}}=-3/2}^{+3/2}\left\{ f^\mathrm{s}_{\pi\Delta\mathrm{D}_{13}}\delta_{s_\Delta,s_{\mathrm{D}_{13}}} + f^\mathrm{d}_{\pi\Delta\mathrm{D}_{13}}F^\mathrm{RD}\frac{\left|\vec{p}_\pi^{\,\mathrm{CM}\pi\Delta}\right|^2}{m_\pi^2}\sqrt{4\pi}\right.$$
$$\left.\sum_{\mu=-2}^{+2}\langle 3/2 \quad s_{\mathrm{D}_{13}} \quad 2 \quad \mu | 3/2 \quad s_\Delta\rangle\, Y_{2\mu}(\Omega_\pi)\right\}$$
$$\bar{u}_\beta(p_s,s_{\mathrm{D}_{13}})\left[\frac{G_1^\mathrm{N}}{2m_\mathrm{N}}(k^\beta\gamma^\mu - \not{k}g^{\beta\mu}) - \frac{G_2^\mathrm{N}}{(2m_\mathrm{N})^2}(k^\beta P^\mu - (k\cdot P)g^{\beta\mu}\right]\mathrm{N}(p_\mathrm{i},s_\mathrm{i}).$$

The four-vector p_s is defined as $p_s = k + p_\mathrm{i}$ ($p_s^2 = s$) and $P = \frac{1}{2}(p_\mathrm{i} + p_s)$. Taking resonance damping into account we multiply the d-wave amplitude with a factor F^RD:

$$F^\mathrm{RD} = \sqrt{\frac{9 + 3(x^*)^2 + (x^*)^4}{9 + 3x^2 + x^4}},$$

with $x = R\left|\vec{p}_\pi^{\,\mathrm{CM}\pi\Delta}\right|$ and $x^* = R\left|\vec{p}_\pi^{\,*\mathrm{CM}\pi\Delta}\right|$ as above. The isospin factors for the different isospin channels are listed in Tables 6.4 and 6.5.

As did the non-resonant $\pi\Delta$ currents, $J^\mu_{\mathrm{D}_{13}\to\pi\Delta}$ describes the two-body process $\gamma\mathrm{N} \to \pi\Delta$ with the matrix element:

$$\mathcal{M}^{(2\mathrm{b})}_\mathrm{fi}\left(\gamma\mathrm{N} \to \mathrm{D}_{13} \to \pi_1\Delta(m_\Delta,s_\Delta)\right) = -i\epsilon_\mu J^\mu_{\mathrm{D}_{13}\to\pi\Delta}.$$

$\mathcal{I}$	$\gamma n \to D_{13} \to \pi^+\Delta^-$	$\gamma n \to D_{13} \to \pi^0\Delta^0$	$\gamma n \to D_{13} \to \pi^-\Delta^+$
$J^\mu_{D_{13}\to\pi\Delta}$	$+1$	$+\sqrt{2/3}$	$-\sqrt{1/3}$

Table 6.5: Isospin factors for the $\gamma n \to D_{13} \to \pi\Delta$ channel.

$\gamma N \to D_{13} \to \rho N \to \pi\pi N$	$\mathcal{I}$
$\gamma p \to D_{13} \to \rho^0 p \to \pi^+\pi^- p$	$+1$
$\gamma p \to D_{13} \to \rho^+ n \to \pi^+\pi^0 n$	$-\sqrt{2}$
$\gamma n \to D_{13} \to \rho^- p \to \pi^-\pi^0 p$	$+\sqrt{2}$

Table 6.6: Isospin factors for $\gamma N \to D_{13} \to \rho N \to \pi\pi N$.

The three-body matrix element $\mathcal{M}^{(3b)}_{fi}$ $(\gamma N \to D_{13} \to \pi_1\Delta \to \pi_1\pi_2 N)$ is obtained as in (6.21) by systematically replacing all m_Δ by $W_{\pi_2 N}$ in $\mathcal{M}^{(2b)}_{fi}$. The corresponding Δ decay isospin factors are found in Table 6.3 on p. 139.

6.3.3.2 $\gamma N \to D_{13} \to \rho N \to \pi\pi N$: D_{13} resonance in the s-channel

The Feynman graph in Figure 6.10(b) depicts the resonant ρN production. Its three-body hadronic current reads:

$$J^\mu_{D_{13}\to\rho N} = e\mathcal{I} f^s_{\rho N D_{13}} g_{\rho\pi\pi}\sqrt{E_i + m_N}\sqrt{2\sqrt{s}}\frac{1}{p_s^2 - m^2_{D_{13}} + i\sqrt{s}\Gamma_{D_{13},\text{total}}(\sqrt{s})}$$
$$\frac{1}{W^2_{\pi_1\pi_2} - m^2_\rho + iW_{\pi_1\pi_2}\Gamma_\rho(W_{\pi_1\pi_2})}$$
$$\sum_{s_{D_{13}}=-3/2}^{+3/2}\left\{(-1)^\lambda \langle 1/2 \quad s_i \quad 1 \quad \lambda | 3/2 \quad s_{D_{13}}\rangle (\vec{p}_{\pi^+} - \vec{p}_{\pi^-})_\lambda\right\}$$
$$\bar{u}_\beta(p_s, s_{D_{13}})\left[\frac{G_1^N}{2m_N}(k^\beta\gamma^\mu - \not{k}g^{\beta\mu}) - \frac{G_2^N}{(2m_N)^2}(k^\beta P^\mu - (k\cdot P)g^{\beta\mu}\right] N(p_i, s_i),$$

where $\lambda = s_{D_{13}} - s_i$ and $\vec{p}_\lambda$ denotes the spherical component of the vector $\vec{p}$. The isospin factors for the studied isospin channels are given in Table 6.6.

7

Results and discussion

In this chapter, the combined experimental and theoretical results obtained in this thesis are presented. This reveals further insight into the mechanisms responsible for the observed behaviour of the measured cross sections. Furthermore it provides a test for the accuracy of the RPR model. The detailed results for the $p\pi^+\pi^-$ and the $n\pi^+\pi^0$ reactions on the proton are discussed in Sections 7.1 and 7.2, respectively. Section 7.3 briefly treats the $p\pi^0\pi^0$ channel. In the final Section 7.4 we present the combined findings for the contribution of the double pion photoproduction processes to the GDH sum rule and the forward spin polarisability γ_0. Throughout this chapter, all data are the DAPHNE data presented in Chapters 3 and 4 and all calculations are obtained with the RPR model, unless stated explicitly.

7.1 $\gamma p \rightarrow p\pi^+\pi^-$

We first consider the two-body reaction $\gamma p \rightarrow \pi^-\Delta^{++}$. This is the dominating intermediate state resulting in $p\pi^+\pi^-$. For this reaction, experimental data for the angular distribution $\frac{d\sigma}{dt}$ at high photon energy by Boyarski and others [19] are available. The data for $E_\gamma = 5$, 8, 11 and 16 GeV are shown in Figure 7.1. Within the RPR model, a calculation for non-resonant $\pi\Delta$ production via π exchange was performed and the result is also plotted in the figure. The dominant feature of these high energy angular distributions is well described. It is the inclusion of the exchange of the π Regge trajectory that allows to nicely reproduce the strong forward peak at low $|t|$ and the exponential fall-off of the angular distribution with increasing $|t|$. At intermediate values of $|t|$ $\left(|t| \geq 0.2\ \mathrm{GeV/c^2}\right)$, the data call for an additional mechanism beyond the dominant π Regge trajectory exchange.

The necessity for the Regge approach at higher energies is illustrated in Figure 7.2 for the unpolarised cross section for $\gamma p \rightarrow p\pi^+\pi^-$. The DAPHNE data from this work are plotted together with data from the ABBHHM collaboration [1] for $\gamma p \rightarrow \pi^-\Delta^{++}$. The latter were measured up to 4 GeV photon energy and are thus well suited to verify the high energy behaviour of the RPR

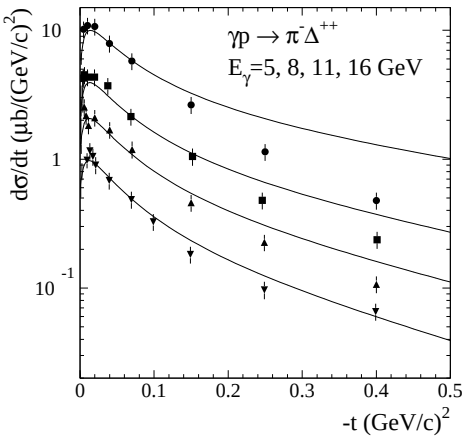

Figure 7.1: High energy angular distribution $\frac{d\sigma}{dt}$ for $\gamma p \to \pi^- \Delta^{++}$ at photon energies $E_\gamma = 5$, 8, 11 and 16 GeV. The upper curves and data correspond to $E_\gamma = 5$ GeV, the lower ones are at $E_\gamma = 16$ GeV. The data are from [19]. The curves represent a calculation for the non-resonant $\pi\Delta$ production via π exchange.

model. All curves are calculations for the non-resonant $\pi^- \Delta^{++}$ production via π exchange. Two of them are Regge calculations; one is calculated with the asymptotic form of the Regge amplitude as a function of s. In the other case the non-asymptotic form with the crossing symmetric variable $\frac{s-u}{2}$ is used. Above 2 GeV these two calculations agree, as expected since $\frac{s-u}{2} \to s$ for high s. Below that energy, the difference between both results can be seen as a theoretical uncertainty in the extrapolation of the Regge description to lower energies. When understanding the different double pion production mechanisms with a sufficient accuracy through the resonance region, one could determine which extrapolation gives the best fit to the data. However, at this point this is not done. Also plotted in Figure 7.2 is a curve where the π exchange is not regge-ised but a Feynman pole exchange is applied. One observes, as expected, that the cross section grows without bound above 1 GeV and is not at all in agreement with the trend of the data. The situation can be slightly improved by incorporating a hadronic form factor at the πNΔ vertex. This partially cuts off the rising cross section. The form factor $\frac{\Lambda^2 - m_\pi^2}{t - m_\pi^2}$ is calculated with a cutoff value $\Lambda = 1.25$ GeV. The origin of the problem of the rising cross sections in pole exchange calculations, is that such calculations do not respect unitarity. It is clearly not sufficient to introduce form factors which reduce the real part of the amplitude but do not give the phase of the amplitude.

These observations acknowledge the importance of the Regge trajectory exchange incorporated in the model. Each calculation that is presented fur-

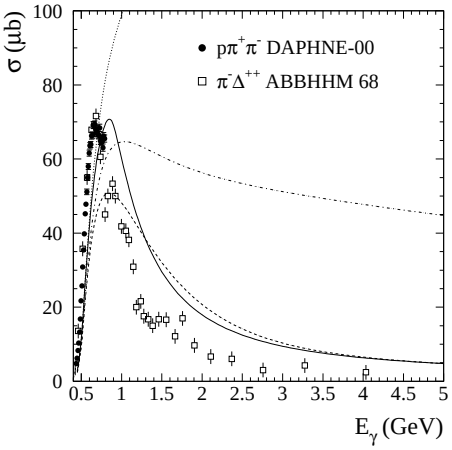

Figure 7.2: $\gamma p \rightarrow \pi^-\Delta^{++} \rightarrow p\pi^+\pi^-$: Total cross section as a function of photon energy. The curves are a calculation for the non-resonant $\pi^-\Delta^{++}$ production via π exchange. Full curve: Regge calculation with $(s-u)/2$ dependence. Dashed curve: Regge calculation with s dependence. Dotted curve: Feynman pole calculation. Dashed-dotted curve: Pole calculation with a hadronic $\pi\Delta$ form factor (see text). The full circles represent the $\gamma p \rightarrow p\pi^+\pi^-$ data of this work, the open squares are the $\gamma p \rightarrow \pi^-\Delta^{++}$ data from [1].

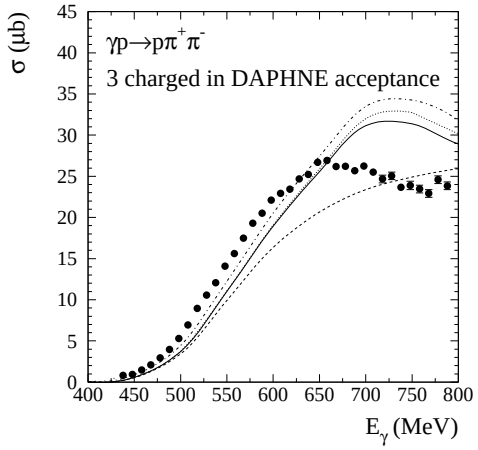

Figure 7.3: $\gamma p \rightarrow p\pi^+\pi^-$ with the three charged particles inside DAPHNE acceptance: Unpolarised cross section as a function of photon energy with calculations for the different mechanisms via $\pi\Delta$ or ρN production. Dashed curve: $\pi\Delta$ production via π exchange. Full curve: non-resonant $\pi\Delta$ via π exchange + D_{13}-resonant $\pi\Delta$. Dotted curve: non-resonant $\pi\Delta$ via π exchange + D_{13}-resonant $\pi\Delta$ + D_{13}-resonant ρN. Dashed-dotted curve: non-resonant $\pi\Delta$ via π exchange + D_{13}-resonant $\pi\Delta$ + non-resonant ρN via ρ exchange + D_{13}-resonant ρN.

ther on, is obtained through Regge trajectory exchange, i.e. when noting e.g. 'π exchange' we mean 'π Regge trajectory exchange'. From Figure 7.2 one also learns that, although both the $\pi^-\Delta^{++}$ and the $\pi^+\Delta^0$ intermediate states contribute to the total $p\pi^+\pi^-$ cross section, the former yields the main contribution. This is easily understood from the isospin factors detailed in Table 6.1 (p. 138) and Table 6.3 (p. 139). Nevertheless, for each curve shown below, the coherent sum of the $\pi^-\Delta^{++}$ and the $\pi^+\Delta^0$ contributions is calculated. For simplicity, we refer to this combination with '$\pi\Delta$'.

In the following we concentrate on the lower energy region where the data of this thesis are located. In a first step, we consider the unpolarised cross section for $\gamma p \rightarrow p\pi^+\pi^-$ in the case where the three charged particles are found inside of the DAPHNE acceptance. The acceptance is as defined in Chapter 3. The angular acceptance and the proton and pion momentum thresholds have been incorporated into the RPR calculation in order to obtain the cross sections integrated over the specified acceptance for this reaction. In Figure 7.3 the three-charged cross section data are plotted together with the RPR calculations. The largest contribution stems from the non-resonant $\pi\Delta$ production via π exchange. This mechanism is responsible for the strong increase of the $p\pi^+\pi^-$ cross section from threshold up to about 600 MeV photon energy. Above 600 MeV, extra strength is obtained from the resonant pro-

duction of $\pi\Delta$ through the D_{13} resonance. The mechanisms with an intermediate ρ add relatively small contributions. The D_{13}-resonant ρN production evidently contributes only at the resonance position of the D_{13}, whereas the non-resonant ρN production mechanism adds a smooth background. We use here the $D_{13} \rightarrow \pi\Delta$ and $D_{13} \rightarrow \rho$N couplings as determined by the analysis of Manley and Saleski [91], based on $\pi N \rightarrow \pi\pi N$ data. It is evident, however, from the large range quoted by the Particle Data Group [105] for the decay widths $D_{13} \rightarrow \pi\Delta$ and $D_{13} \rightarrow \rho$N, that the present knowledge of these resonance couplings is only very approximate. As discussed in the introductory chapter, the aim of different analyses of precise double pion photoproduction data through the resonance region is to pin down these couplings better.

The fact that the data are not perfectly described, is ascribed to the fact that, in spite of the used extrapolation prescription, the description remains an extrapolation in this energy range (see discussion below).

The measured invariant mass distributions $d\sigma/dW_{\pi^+\pi^-}$ and $d\sigma/dW_{\pi^\pm p}$ for $\gamma p \rightarrow p\pi^+\pi^-$ with the three charged particles in the DAPHNE acceptance are also compared with the RPR results. The pion-pion invariant mass spectra in Figure 7.4 exhibit a rather uniform behaviour, close to the phase space distribution. There is no indication for a strong correlation between the two pions at these invariant masses. The calculations are in agreement with this observation. The ρN contributions are too small to alter the uniform behaviour.

As discussed in Chapter 3, the pion-nucleon invariant mass distributions $d\sigma/dW_{\pi^+ p}$ and $d\sigma/dW_{\pi^- p}$ cannot be separated with DAPHNE. Therefore the presented data are a superposition of the two. The theoretical curves, on the other hand, represent a calculation for $d\sigma/dW_{\pi^+ p}$. In Figure 7.5, the measured pion-nucleon invariant mass distributions are compared to the calculations with the $\pi\Delta$ and ρN (both non-resonant and D_{13}-resonant) mechanisms. The observed peak around the Δ mass is clearly due to the predominance of the $\pi\Delta$ production and in particular it corresponds to the decay $\Delta^{++} \rightarrow \pi^+ p$ in the dominant isospin channel $\gamma p \rightarrow \pi^- \Delta^{++}$. The $\pi^+\Delta^0$ contribution does not add to the peak in $d\sigma/dW_{\pi^+ p}$ as the proton and the π^+ are not correlated in this case. It merely broadens the peak. At the lower energies, i.e. in the 500 and 600 MeV energy bins, the calculations fail to describe the observed strength at the lower invariant masses. Therefore we investigate the influence of the inclusion of the non-resonant $\pi\pi$N production via π exchange with a nucleon intermediate state, corresponding to the diagrams in Figure 6.5 (p. 141). This is illustrated with the full curve in Figure 7.6. The non-resonant $\pi\pi$N production is clearly able to explain the underestimation of the data at lower energies. At higher energies, however, they enhance the overestimation of the Δ peak. On the other hand, one should still bear in mind the uncertainty due to the extrapolation prescription used in the Regge propagator. This is illustrated in Figure 7.7, where we compare the calculations, including all mentioned mechanisms, for the s and $(s-u)/2$ prescriptions. Especially at the higher energy bins, it is again clear that the extrapolation method plays an important role.

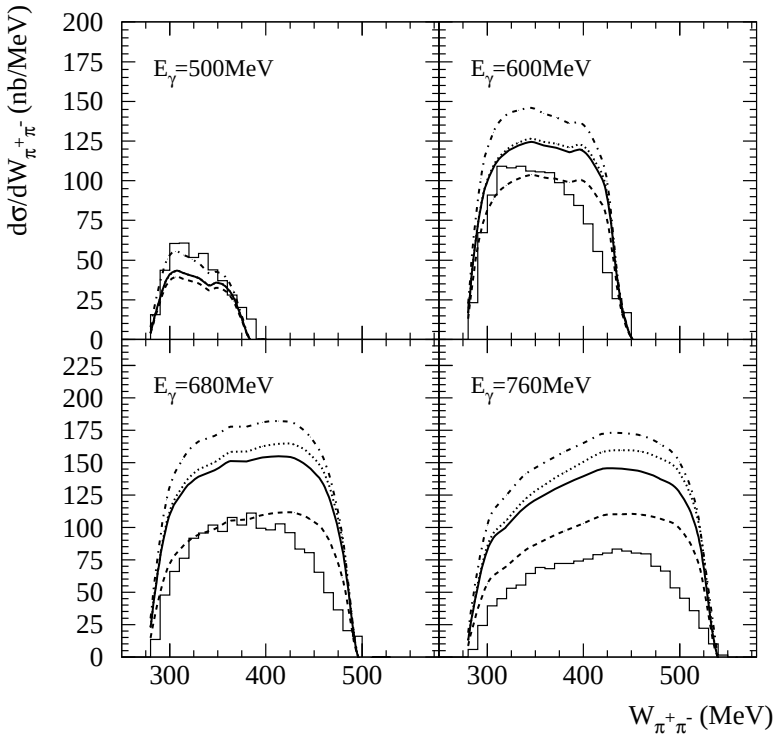

Figure 7.4: $\gamma p \rightarrow p\pi^+\pi^-$ with the three charged particles inside DAPHNE acceptance: Pion-pion invariant mass spectra at $E_\gamma = 500$, 600, 680 and 760 MeV. Curve conventions are as in Figure 7.3.

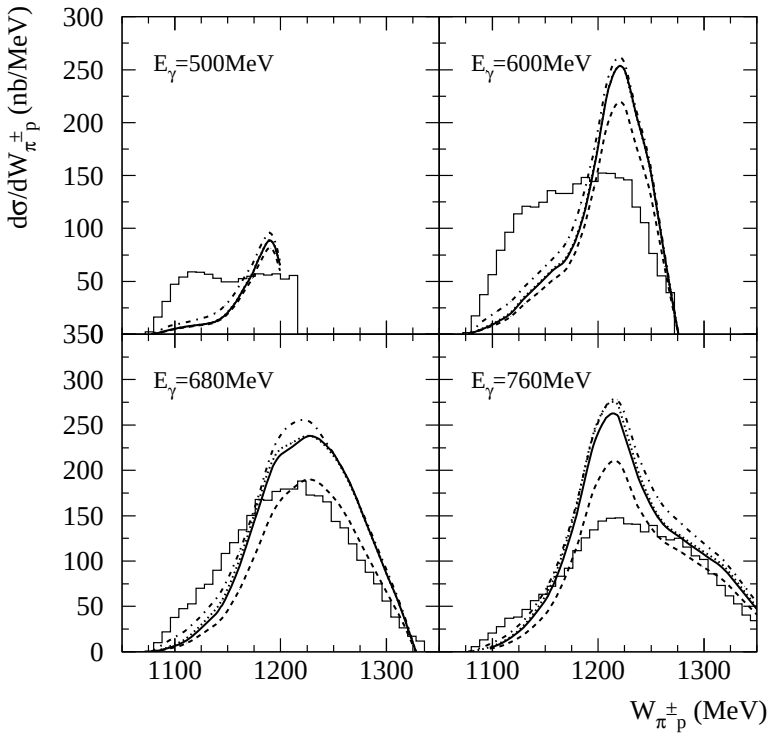

Figure 7.5: $\gamma p \rightarrow p\pi^+\pi^-$ with the three charged particles inside DAPHNE acceptance: pion-nucleon invariant mass spectra at $E_\gamma = 500$, 600, 680 and 760 MeV. Curve conventions are as in Figure 7.3.

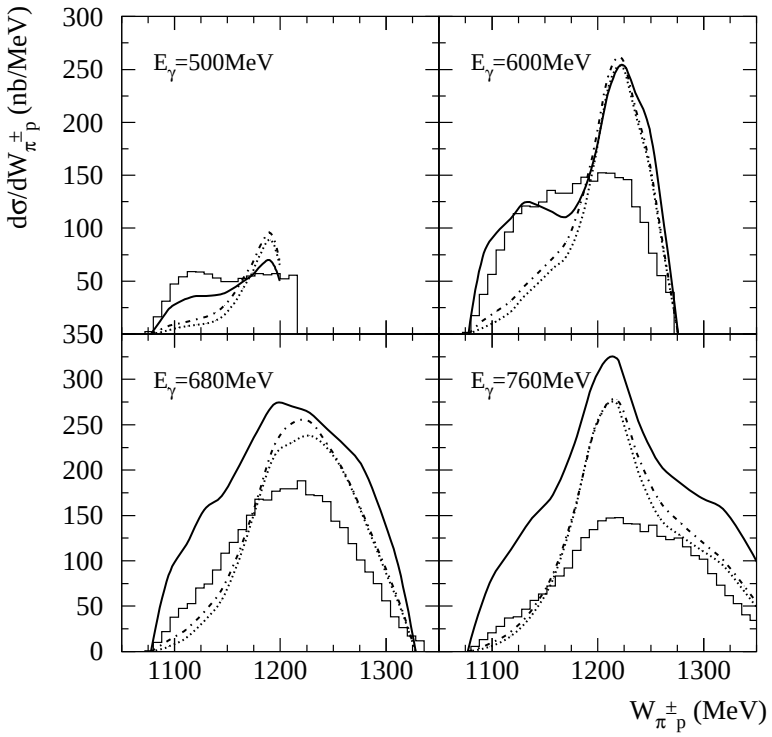

Figure 7.6: $\gamma p \rightarrow p\pi^+\pi^-$ with the three charged particles inside DAPHNE acceptance: pion-nucleon invariant mass spectra at $E_\gamma = 500$, 600, 680 and 760 MeV. Dotted curve: non-resonant $\pi\Delta$ via π exchange + D_{13}-resonant $\pi\Delta$ + D_{13}-resonant ρN. Dashed-dotted curve: non-resonant $\pi\Delta$ via π exchange + D_{13}-resonant $\pi\Delta$ + D_{13}-resonant ρN + non-resonant ρN via ρ exchange. Full curve: non-resonant $\pi\Delta$ via π exchange + D_{13}-resonant $\pi\Delta$ + D_{13}-resonant ρN + non-resonant ρN via ρ exchange + non-resonant $\pi\pi$N via π exchange.

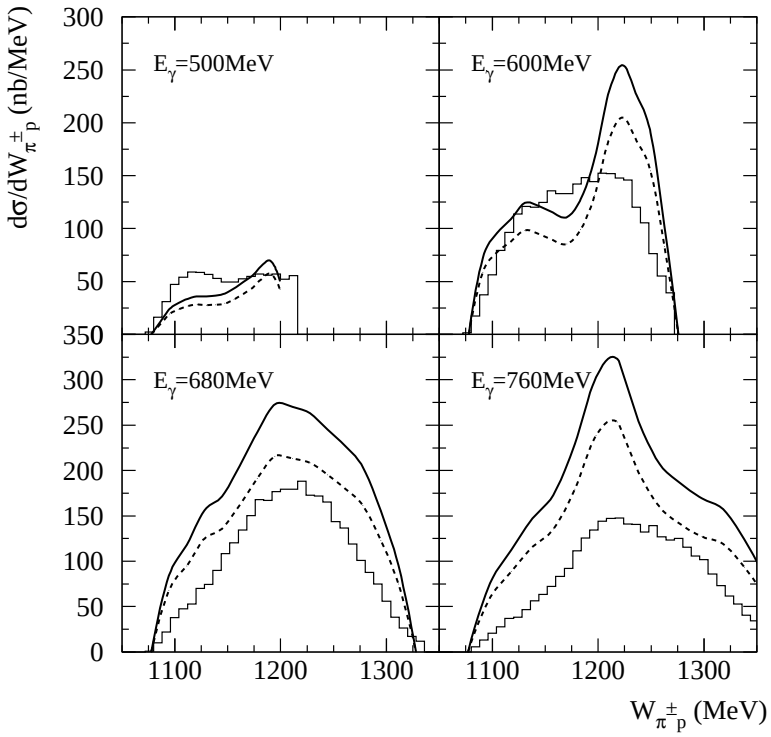

Figure 7.7: $\gamma p \rightarrow p\pi^+\pi^-$ with the three charged particles inside DAPHNE acceptance: pion-nucleon invariant mass spectra at $E_\gamma = 500$, 600, 680 and 760 MeV. All curves represent a calculation for non-resonant $\pi\pi$N via π exchange + non-resonant $\pi\Delta$ via π exchange + D_{13}-resonant $\pi\Delta$ + non-resonant ρN via ρ exchange + D_{13}-resonant ρN. Full curve: calculation with $(s-u)/2$ in the Regge propagator. Dashed curve: calculation with s in the Regge propagator.

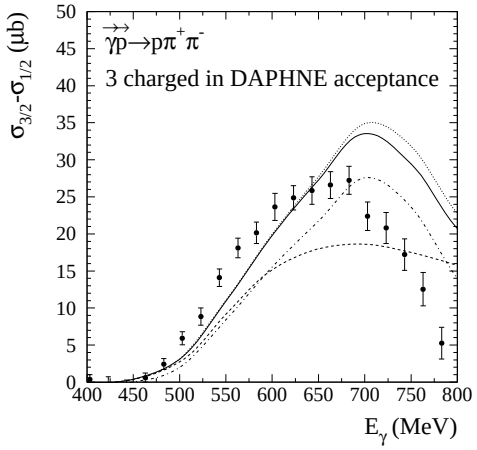

Figure 7.8: $\vec{\gamma}\vec{p} \rightarrow p\pi^+\pi^-$ with the three charged particles inside DAPHNE acceptance: Polarised cross section difference $\sigma_{3/2} - \sigma_{1/2}$ as a function of photon energy. Curve conventions are as in Figure 7.3.

Figure 7.8 shows the comparison between the data and the RPR calculation for the cross section difference $\sigma_{3/2} - \sigma_{1/2}$ for the three-charged cross section. The non-resonant and D_{13}-resonant terms for $\pi\Delta$ and ρN production are included in the calculation. Again, the non-resonant $\pi\Delta$ terms alone are responsible for the larger part of the positive cross section difference. This is understood from the $3/2$ spin state of the Δ resonance. In the initial photon-nucleon state, as well as in the intermediate $\pi\Delta$ state, all projections of the spin $-3/2$, $-1/2$, $+1/2$ and $+3/2$ are allowed. However, the observed cross section difference indicates that the $3/2$ state is favoured. The $D_{13}(1520)$, being a spin $3/2$ resonance, has a much larger photo-coupling for the excitation of the helicity $3/2$ state (see (6.29) on p. 152). The D_{13}-resonant $\pi\Delta$ and ρN contributions to $\sigma_{3/2} - \sigma_{1/2}$ are thus understandably also found to be positively peaked. The non-resonant ρN production on the other hand, reduces the cross section difference as in this case the spin $1/2$ state is prevailing. This is a good illustration of the importance of polarisation observables as they yield more information about the underlying mechanisms than unpolarised ones. The separated helicity cross sections $\sigma_{1/2}$ and $\sigma_{3/2}$ are shown in Figure 7.9. The largest contribution to $\sigma_{1/2}$ stems from the non-resonant $\pi\Delta$ production. Extra strength is added only by the non-resonant ρN production. The $\sigma_{3/2}$ cross section exhibits a peaked structure with main contributions from the $\pi\Delta$ and the D_{13}-resonant ρN mechanisms.

As discussed in Chapters 3 and 4, the data within the DAPHNE acceptance are extrapolated to 4π by means of a simulation using a phase space generator. With the aid of the RPR model one can obtain an idea of the correctness of this

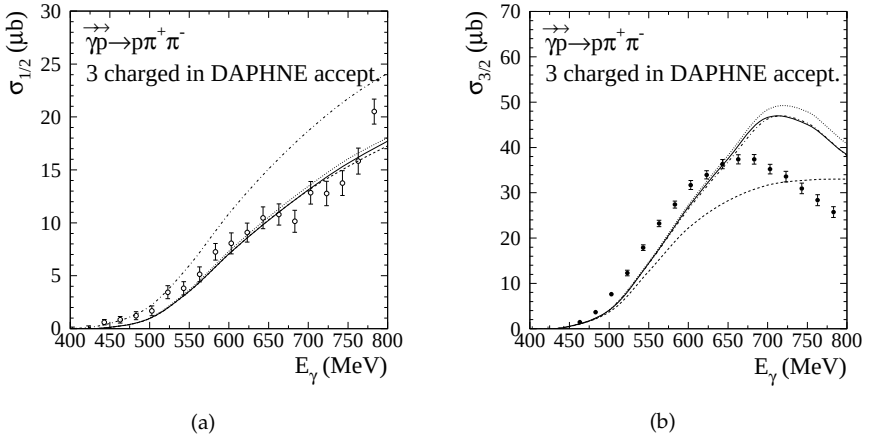

Figure 7.9: $\vec{\gamma}\vec{p} \rightarrow p\pi^+\pi^-$ with the three charged particles inside DAPHNE acceptance: Helicity cross sections $\sigma_{1/2}$ (a) and $\sigma_{3/2}$ (b) as a function of photon energy. Curve conventions are as in Figure 7.3.

procedure. To this end, we consider the extrapolation of the three-charged cross section to 4π. This is merely to illustrate the argument of the degree of validity of the phase space simulation. The 4π data presented further on are still obtained via the sum of two- and three-charged events, unless mentioned explicitly. The phase space extrapolation can be reproduced by means of the RPR calculation programme by omitting all dynamical information, i.e. by setting the matrix elements equal to a constant. The ratio of the obtained cross section inside the acceptance and over 4π yields the extrapolation function. Analogously, the RPR extrapolation function with dynamical information can be calculated. The two options are plotted in Figure 7.10(a) in the case of the extrapolation of the unpolarised cross section. From this figure, one learns that the RPR model predicts a non-negligible deviation from phase space. In the case of the extrapolation for the polarised cross section difference $\sigma_{3/2} - \sigma_{1/2}$, this deviation becomes larger still. These observations are an indication for the possible error on the extrapolated experimental results. However, as the RPR model does not exactly describe the energy dependence of the cross sections inside the acceptance, a definitive conclusion is not drawn yet.

Finally, the helicity cross sections $\sigma_{1/2}$ and $\sigma_{3/2}$ over the full 4π space are shown in Figure 7.11. The conclusions drawn for the cross sections inside the acceptance for the three-charged case, are also valid. The $\sigma_{1/2}$ is dominated by the non-resonant $\pi\Delta$ production via π exchange and the non-resonant ρN production via ρ exchange. On the other hand, the $\sigma_{3/2}$ cross section has an extra contribution from the D_{13}-resonant $\pi\Delta$ and ρN production and it exhibits a strongly peaked behaviour. For the comparison between the data and the model predictions, caution should be taken because of the uncertainty in

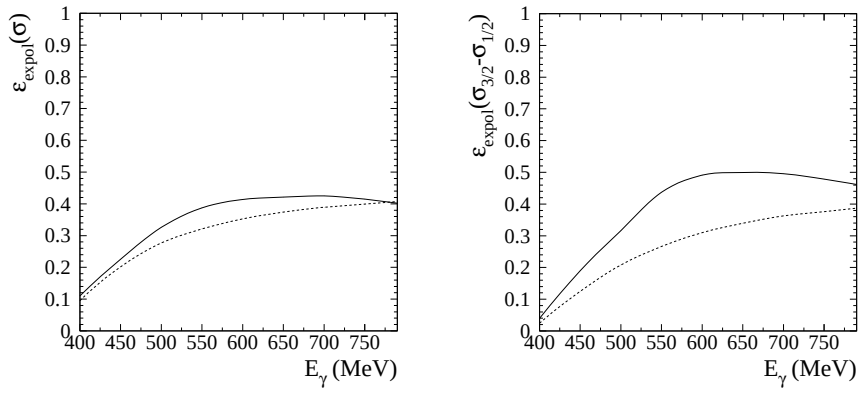

(a) (b)

Figure 7.10: $\gamma p \rightarrow p\pi^+\pi^-$: Extrapolation function for the reconstruction of the cross section over the full 4π space from the three-charged cross section, as a function of photon energy: (a) For the total unpolarised cross section σ: (b) For the polarised cross section difference $\sigma_{3/2} - \sigma_{1/2}$. Full curve: calculation includes $\pi\Delta$ production. Dashed curve: calculation includes no dynamical information and corresponds to the uniform emission over phase space of the outgoing particles.

extrapolation. Therefore we illustrate what the possible effect is of the error made in the extrapolation by using the phase space approximation. In Figure 7.12, the helicity cross sections over 4π are again plotted. The difference with Figure 7.11 is that the experimental data are obtained here by extrapolating the three-charged cross sections, without using the information from the two-charged cross sections. In Figure 7.12(a) this is done by using the phase space extrapolation (corresponding to the dotted curve in Figure 7.10(b), and also corresponding to what was done for the data in Figure 7.11). For the data in Figure 7.12(b), the three-charged cross sections are extrapolated using the RPR model (full curve in Figure 7.10(b)). Comparing Figures 7.12(a) and 7.12(b) demonstrates how one should be careful in comparing the extrapolated data with the model calculations. As soon as the precision of the RPR model will be found to be satisfactory, it can be used for the extrapolation of the data from the DAPHNE acceptance to 4π.

7.2 $\gamma p \rightarrow n\pi^+\pi^0$

The question of which mechanisms are responsible for the observed strength of the $\gamma p \rightarrow n\pi^+\pi^0$ process is at present not completely answered. The contribution of the $\pi\Delta$ production —which almost fully explains the $p\pi^+\pi^-$ cross section— is much smaller in this isospin channel. This is immediately understood from the isospin factors given in Tables 6.1 (p. 138), 6.3 (p. 139) and 6.4

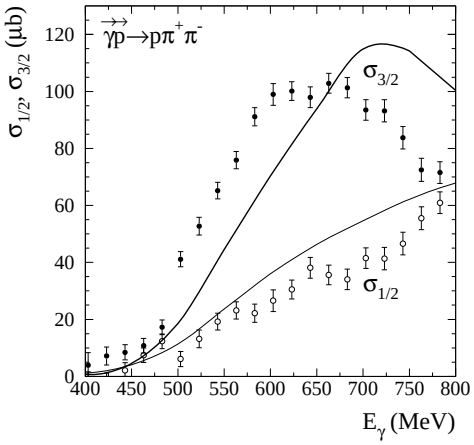

Figure 7.11: $\vec{\gamma}\vec{p} \rightarrow p\pi^+\pi^-$: Helicity cross sections $\sigma_{1/2}$ and $\sigma_{3/2}$ as a function of photon energy. The curves represent a calculation with non-resonant $\pi\Delta$ via π exchange + D_{13}-resonant $\pi\Delta$ + non-resonant ρN via ρ exchange + D_{13}-resonant ρN.

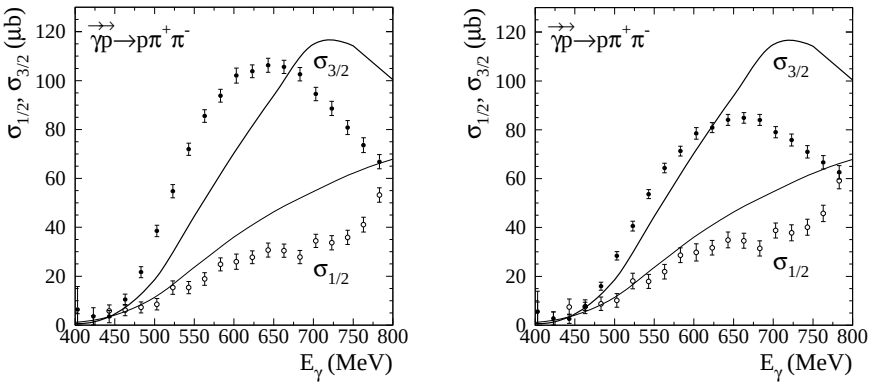

Figure 7.12: $\vec{\gamma}\vec{p} \rightarrow p\pi^+\pi^-$: Helicity cross sections $\sigma_{1/2}$ and $\sigma_{3/2}$ as a function of photon energy. The experimental 4π cross sections are obtained by extrapolating the three-charged cross section use a phase space approximation (a) and using the RPR model (b), respectively. The curves are as in Figure 7.11.

(p. 155) in Chapter 6. Recent experimental results have yielded some interesting indications. From the polarised data obtained in this thesis, one learns that the $\sigma_{3/2}$ helicity cross section for this process is much larger than the $\sigma_{1/2}$ helicity cross section. Moreover, the $\sigma_{3/2}$ has a strong resonant structure, with a peak at about 750 MeV. This points to a strong 3/2 resonant intermediate state playing an important role. On the other hand, the TAPS collaboration has recently published precise data for the invariant mass spectra for the $n\pi^+\pi^0$ process. The $\pi^+\pi^0$ invariant mass distributions are skewed towards higher invariant masses which points to the presence of an intermediate ρ meson. Also recently published are invariant mass spectra for the isospin-symmetric channel $\gamma n \rightarrow p\pi^-\pi^0$ measured with DAPHNE in 1992. Also from these one can infer that the ρ may play a role in these processes.

The $\pi\Delta$ isospin channels contributing to $\gamma p \rightarrow n\pi^+\pi^0$ are $\pi^+\Delta^0$ and $\pi^0\Delta^+$, the former being relatively more important. Again, all calculations below contain the coherent sum of the two contributions, denoting the combination simply by $\pi\Delta$.

We first consider the pion-pion and pion-nucleon invariant mass distributions. The data available for these observables are from the TAPS collaboration [81]. Figure 7.13 shows $d\sigma/dW_{\pi^+\pi^0}$ for different photon energies. Below 600 MeV, the distributions are quite uniform and do not point to any correlation between the two pions. Above 600 MeV, a skewing towards higher invariant masses is observed in the data from which one can infer that, at these energies, mechanisms in which the two pions are correlated, play a role. Calculations include the non-resonant $\pi\pi$N production and the non-resonant and D_{13}-resonant $\pi\Delta$ and ρN mechanisms. The strongly skewed shape, especially at the $E_\gamma = 657$, 720 and 760 MeV energy bins, is not reproduced by the calculations. The clearest tendency towards a skewing at higher invariant masses stems from the D_{13}-resonant ρN channel. However, its strength is not sufficient to explain the data. This could be an indication for the imprecision of the used $D_{13} \rightarrow \rho$N decay width —taken from [91]— which is known with quite some uncertainty, as discussed above.

The π^0-n invariant mass spectra $d\sigma/dW_{\pi^0 n}$ are shown in Figure 7.14 and the $d\sigma/dW_{\pi^+ n}$ in Figure 7.15. The π^0-n distributions show a peak around the Δ mass which corresponds to the Δ^0 decay to π^0n of the $\gamma p \rightarrow \pi^+\Delta^0$ channel. The second $\pi\Delta$ channel, $\gamma p \rightarrow \pi^0\Delta^+$, is smaller and merely broadens the peak a bit. The ρN mechanisms do not significantly alter the shape of invariant mass spectra. The peak at the Δ mass is shifted towards lower invariant masses in the π^0-n invariant mass distributions. This is especially true at the lower photon energies. Above 600 MeV, a broader peak around the Δ mass is found.

In Figure 7.16 the unpolarised cross section for $\gamma p \rightarrow n\pi^+\pi^0$ inside the DAPHNE acceptance is plotted. From the plotted RPR curves, it is immediately clear that the non-resonant $\pi\Delta$ production via π exchange and the D_{13}-resonant $\pi\Delta$ production are not sufficient to explain the full strength of the cross section. The D_{13}-resonant ρN production and the non-resonant ρN pro-

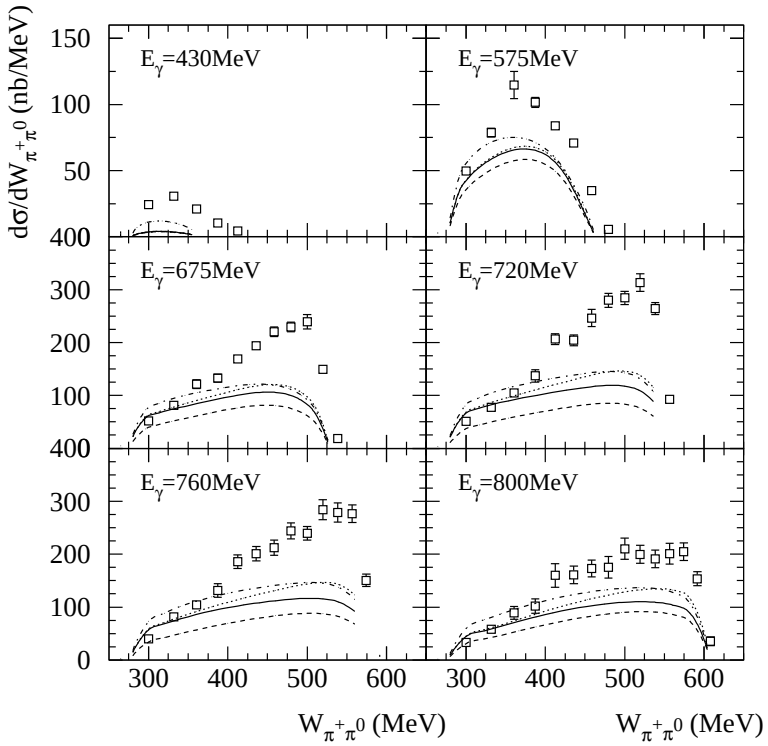

Figure 7.13: $\gamma p \rightarrow n\pi^+\pi^0$: pion-pion invariant mass distributions at different photon energies. Dashed curve: non-resonant $\pi\pi N$ via π exchange + non-resonant $\pi\Delta$ via π exchange. Full curve: non-resonant $\pi\pi N$ via π exchange + non-resonant $\pi\Delta$ via π exchange + D_{13}-resonant $\pi\Delta$. Dotted curve: non-resonant $\pi\pi N$ via π exchange + non-resonant $\pi\Delta$ via π exchange + D_{13}-resonant $\pi\Delta$ + D_{13}-resonant ρN. Dashed-dotted curve: non-resonant $\pi\pi N$ via π exchange + non-resonant $\pi\Delta$ via π exchange + D_{13}-resonant $\pi\Delta$ + D_{13}-resonant ρN + non-resonant ρN. The data are from the TAPS collaboration [81].

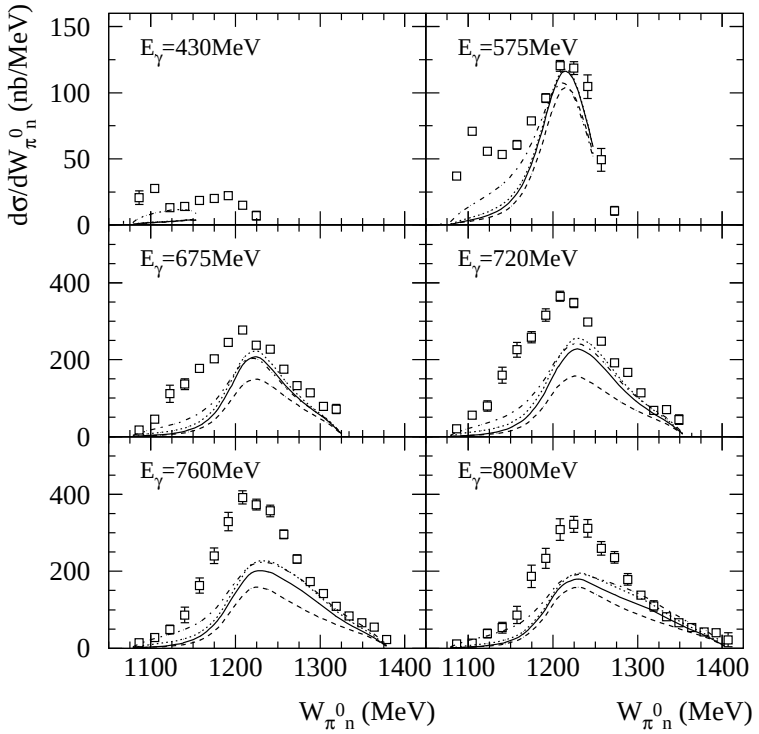

Figure 7.14: $\gamma p \rightarrow n\pi^+\pi^0$: π^0-n invariant mass distributions at different photon energies. Curve conventions are as in Figure 7.13. The data are from the TAPS collaboration [81].

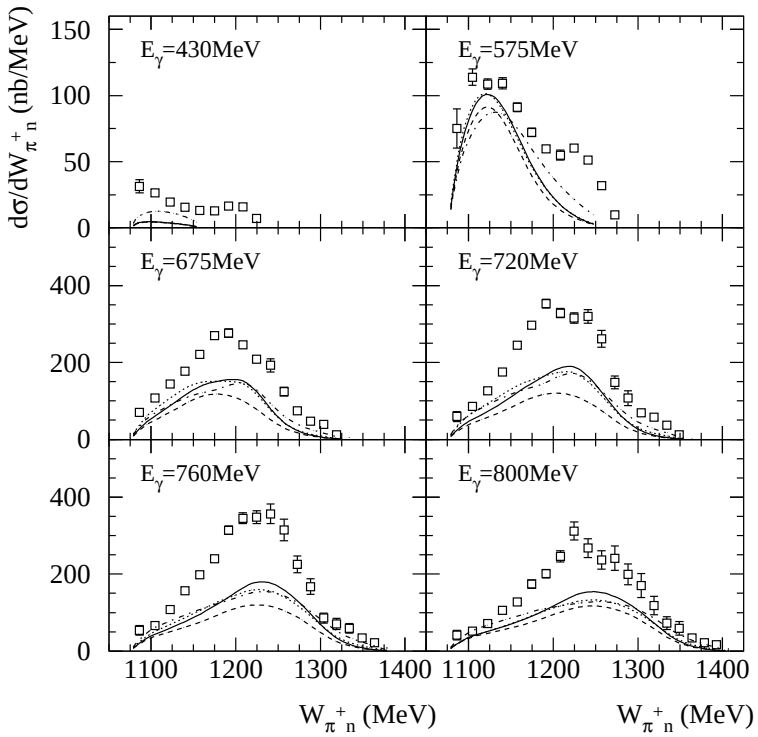

Figure 7.15: $\gamma p \rightarrow n\pi^+\pi^0$: π^+-n invariant mass distributions at different photon energies. Curve conventions are as in Figure 7.13. The data are from the TAPS collaboration [81].

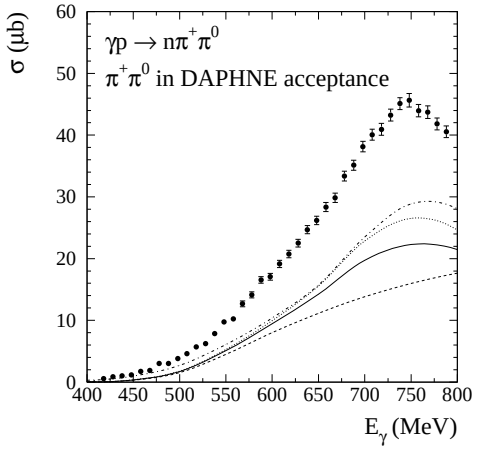

Figure 7.16: $\gamma p \rightarrow n\pi^+\pi^0$ with π^+ and π^0 inside DAPHNE acceptance: Unpolarised cross section as a function of photon energy. Curve conventions are as in Figure 7.13.

duction via ρ exchange add significant contributions. However, it is clear that some strength is missing to completely describe the observed cross section.

When verifying the cross section difference $\sigma_{3/2} - \sigma_{1/2}$ in Figure 7.17, one finds that strong positive contributions stem from the $\pi\Delta$ (non-resonant and especially D_{13}-resonant) and the D_{13}-resonant ρN production. Again the 3/2 spin of the Δ and D_{13} resonances is primarily responsible for this. The non-resonant ρN mechanism via ρ exchange has a negative contribution to $\sigma_{3/2} - \sigma_{1/2}$ and reduces the final calculated result. The separate helicity cross sections are shown in Figure 7.19. From these one learns that $\sigma_{3/2}$ and, to a lesser extent also $\sigma_{1/2}$, are underestimated by the calculations. The non-resonant ρN contribution is quite important in the $\sigma_{1/2}$ cross section. In the case of $\sigma_{3/2}$ the underestimation may point towards an insufficient knowledge of the D_{13} decay widths or towards another mechanism that strongly contributes to the 3/2 intermediate spin state.

Similarly as for the $p\pi^+\pi^-$ channel, we study the validity of the phase space extrapolation of the data inside the DAPHNE acceptance to 4π. In Figure 7.18(a) the phase space and RPR extrapolation functions for the unpolarised cross section are compared, while in Figure 7.18(b) this is done for the polarised cross section difference $\sigma_{3/2} - \sigma_{1/2}$. In contrast with what we found for $p\pi^+\pi^-$, the phase space approximation seems to be rather good as the two curves are quite similar. This is even the case for the cross section difference. The origin of the different conclusion for the two reaction channels may be the following. For the $n\pi^+\pi^0$ only an angular extrapolation is necessary. In the case of $p\pi^+\pi^-$ the acceptance function also contains effects due to momentum thresholds of the particles.

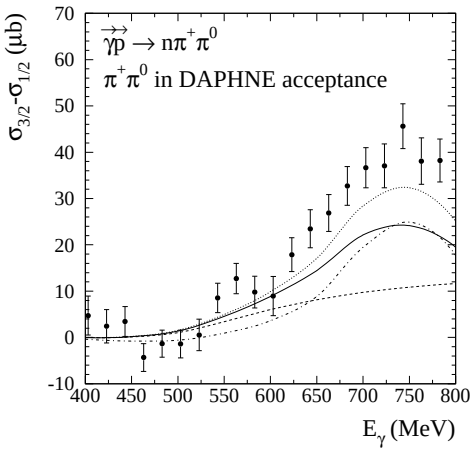

Figure 7.17: $\vec{\gamma}\vec{p} \rightarrow n\pi^+\pi^0$ with π^+ and π^0 inside DAPHNE acceptance: Polarised cross section difference $\sigma_{3/2} - \sigma_{1/2}$ as a function of photon energy. Curve conventions are as in Figure 7.13.

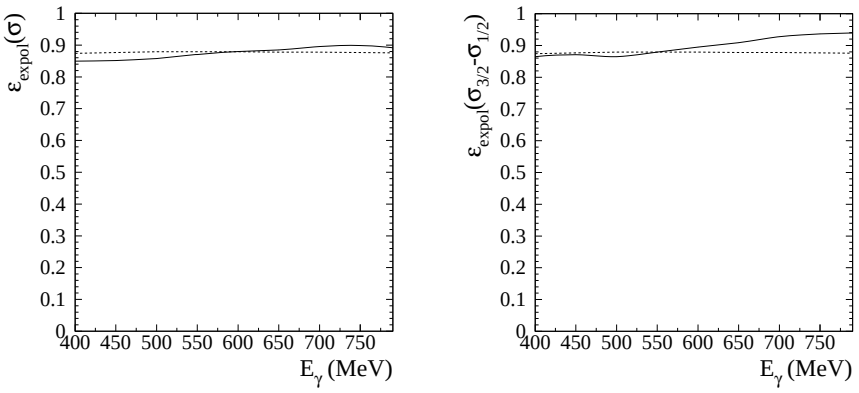

(a) (b)

Figure 7.18: $\gamma p \rightarrow n\pi^+\pi^0$: Extrapolation function for the reconstruction of the cross section over the full 4π space from the cross section with the π^+ and the π^0 inside the acceptance, as a function of photon energy: (a) For the total unpolarised cross section σ: (b) For the polarised cross section difference $\sigma_{3/2} - \sigma_{1/2}$. Full curve: calculation includes $\pi\Delta$ production. Dashed curve: calculation includes no dynamical information and corresponds to the uniform emission over phase space of the outgoing particles.

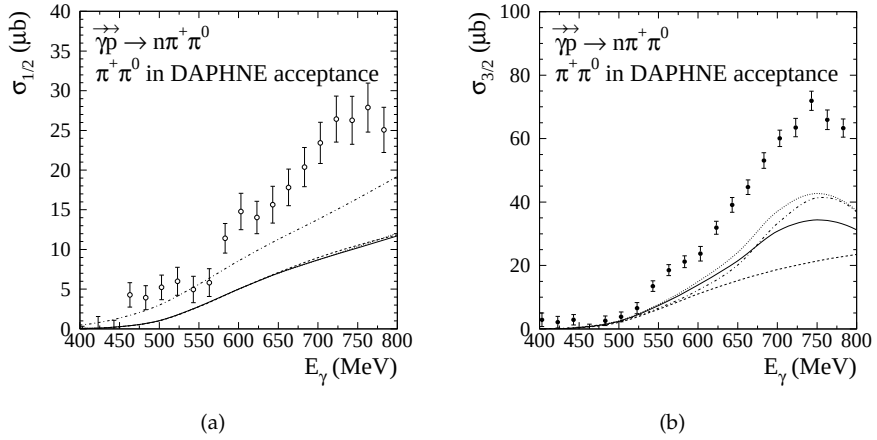

Figure 7.19: $\vec{\gamma}\vec{p} \to n\pi^+\pi^0$ with π^+ and π^0 inside DAPHNE acceptance: Helicity cross sections $\sigma_{1/2}$ (a) and $\sigma_{3/2}$ (b) as a function of photon energy. Curve conventions are as in Figure 7.13.

Finally, in Figure 7.20, we present the helicity cross sections $\sigma_{3/2}$ and $\sigma_{1/2}$ extrapolated to 4π. Again one can draw similar conclusions as in the unextrapolated case.

7.3 $\gamma p \to p\pi^0\pi^0$

The contribution of the non-resonant $\pi\Delta$ production via π exchange to the $\gamma p \to p\pi^0\pi^0$ is negligible. The only intermediate state is $\pi^0\Delta^+$. To this isospin state, only the small sN and $u\Delta$ terms contribute. The only sizeable effect stems from the D_{13}-resonant $\pi\Delta$ production. This is illustrated in Figure 7.21(a) for the total unpolarised cross section. The data are from the TAPS collaboration [119]. It is expected that the missing mechanism at lower energies corresponds to the non-resonant diagrams obtained from the s- and u-channel nucleon diagrams for $\gamma p \to p\pi^0$ by coupling an additional π^0 to the initial and final proton. The calculated helicity cross sections $\sigma_{1/2}$ and $\sigma_{3/2}$ are shown in Figure 7.21(b). Unfortunately the GDH data for this channel have not become available, they are still under analysis [122]. Evidently the strength of the D_{13}-resonant contribution is found completely in $\sigma_{3/2}$, whereas the $\sigma_{1/2}$ cross section contains the tiny non-resonant background terms.

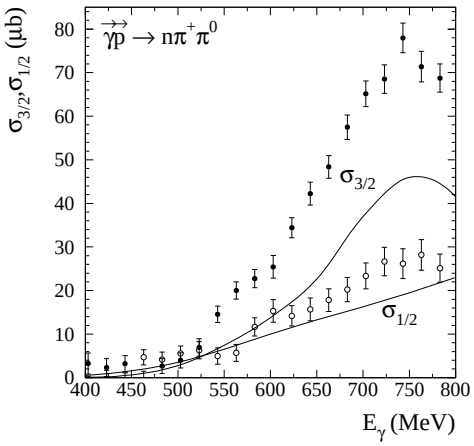

Figure 7.20: $\vec{\gamma}\vec{p} \rightarrow n\pi^+\pi^0$: Helicity cross sections $\sigma_{1/2}$ and $\sigma_{3/2}$ as a function of photon energy. The curves represent a calculation with non-resonant $\pi\pi$N via π exchange + non-resonant $\pi\Delta$ via π exchange + D_{13}-resonant $\pi\Delta$ + non-resonant ρN via ρ exchange + D_{13}-resonant ρN.

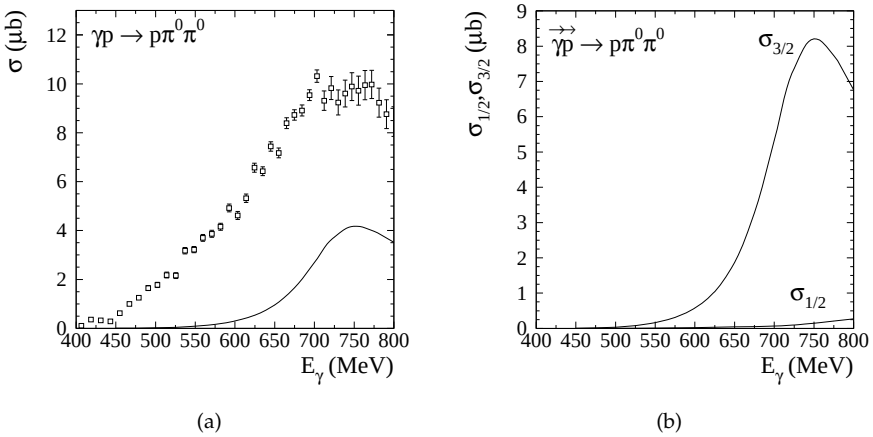

Figure 7.21: $\gamma p \rightarrow p\pi^0\pi^0$: (a) Unpolarised cross section as a function of photon energy, (b) Helicity cross sections $\sigma_{1/2}$ and $\sigma_{3/2}$ as a function of photon energy. The curves represent a calculation with non-resonant $\pi\Delta$ via π exchange + D_{13}-resonant $\pi\Delta$.

	$I^{\mathrm{p}}_{\mathrm{GDH}}$ (μb)	I_{γ_0} (10^{-4} fm^4)
$\mathrm{p}\pi^+\pi^-$	-35.9	-0.072
$\mathrm{n}\pi^+\pi^0$	-16.8	-0.027
$\mathrm{p}\pi^0\pi^0$	-2.7	-0.004
Sum $\gamma\mathrm{p} \to \mathrm{N}\pi\pi$	-55.4	-0.103

Table 7.1: RPR predictions for the contributions of double pion production to the GDH sum rule on the proton and the forward spin polarisability up to 2.6 GeV. The calculations contain non-resonant $\pi\Delta$ production and D_{13}-resonant $\pi\Delta$ and ρN production.

7.4 Contribution of double pion production to the GDH sum rule and the forward spin polarisability

An important feature of the RPR model is that it provides a good high energy behaviour, i.e. it leads to the cross sections which drop with a power of the energy at higher energies. Consequently, we can use this model to investigate the trends of the double pion photoproduction processes at high photon energies. In particular, this allows to calculate the contribution of the double pion channels to the GDH sum rule and the forward spin polarisability. The results shown here are the model calculations including non-resonant $\pi\Delta$ production via π exchange and the D_{13}-resonant $\pi\Delta$ and ρN production. The regge-isation of the non-resonant ρN production via ρ exchange still needs to be further investigated which makes this contribution uncertain at higher energies. Therefore, the non-resonant ρN production is at present not included in the predictions for the sum rule and the spin polarisability shown here. As we have found in the previous sections that this mechanism reduces the cross section difference $\sigma_{3/2} - \sigma_{1/2}$, one should keep in mind that the values given here are not the final ones.

The results are shown for the three isospin channels on the proton in Figures 7.22, 7.23 and 7.24 for photon energies up to 2.6 GeV. The GDH integral and the integral of the forward spin polarisability are as defined in (4.3) and (4.4) (p. 107) and both are plotted as a function of the upper integration limit. For the $\mathrm{p}\pi^+\pi^-$ and $\mathrm{n}\pi^+\pi^0$ channels the data obtained in this work are also shown. In the case of $\mathrm{p}\pi^+\pi^-$ the data obtained with both extrapolation methods —phase space or RPR model— are shown in order to illustrate the effect of the uncertainty concerning the extrapolation from DAPHNE acceptance to 4π. In Table 7.1 we gather the predictions of the RPR model for the contribution of the double pion channels to the GDH sum rule and the forward spin polarisability for the proton up to 2.6 GeV. The values obtained for each channel are listed separately and also their sum is given. Of the theoretical value for the GDH sum rule, -204 μb, the three double pion photoproduction together contribute about 25%. For the forward spin polarisability, $\gamma_0 = -(0.86 \pm 8 \pm 13)\ 10^{-4}$ fm^4 in accordance with Table 1.2 (p. 11), the double pion channels account for about 12%.

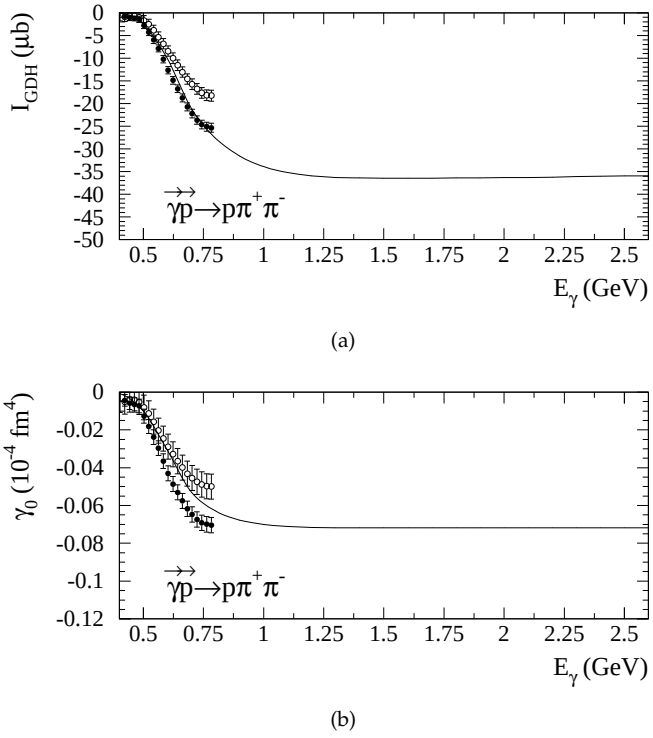

Figure 7.22: $\vec{\gamma}\vec{p} \to p\pi^+\pi^-$: (a) Contribution to the GDH integral I_{GDH} as a function of the upper integration limit, (b) Contribution to the forward spin polarisability γ_0 as a function of the upper integration limit. The curves represent a calculation with non-resonant $\pi\Delta$ via π exchange + D_{13}-resonant $\pi\Delta$ + D_{13}-resonant ρN. The data represented by the full circles correspond to those in Figure 7.11, i.e. extrapolated from DAPHNE acceptance to 4π using a phase space approximation. The open circles correspond to those in Figure 7.12(b), i.e. extrapolated using the RPR model.

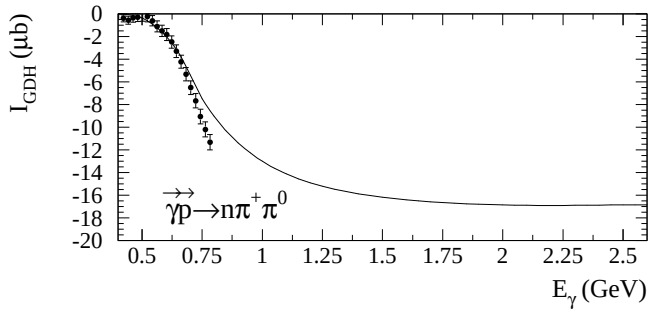

(a)

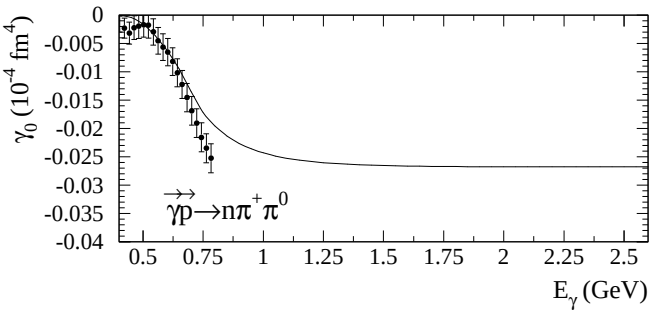

(b)

Figure 7.23: $\vec{\gamma}\vec{p} \rightarrow n\pi^+\pi^0$: (a) Contribution to the GDH integral I_{GDH} as a function of the upper integration limit, (b) Contribution to the forward spin polarisability γ_0 as a function of the upper integration limit. The curves represent a calculation with non-resonant $\pi\Delta$ via π exchange + D_{13}-resonant $\pi\Delta$ + D_{13}-resonant ρN.

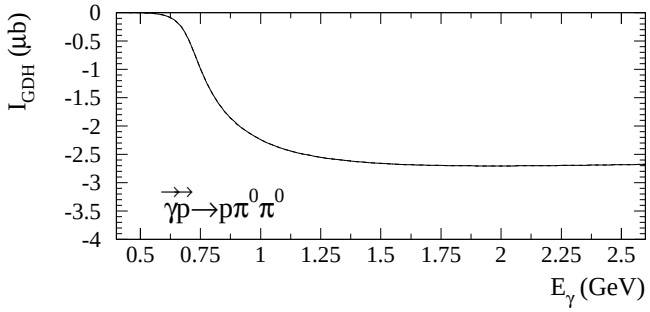

(a)

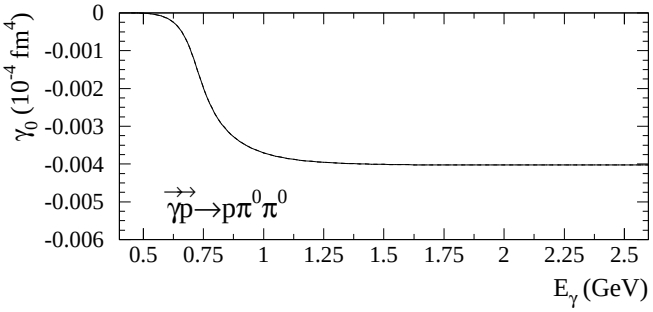

(b)

Figure 7.24: $\vec{\gamma}\vec{p} \to p\pi^0\pi^0$: (a) Contribution to the GDH integral $I_{\rm GDH}$ as a function of the upper integration limit, (b) Contribution to the forward spin polarisability γ_0 as a function of the upper integration limit. The curves are calculated with non-resonant $\pi\Delta$ via π exchange + D_{13}-resonant $\pi\Delta$.

8

Summary and outlook

8.1 Summary

The subject of this PhD thesis was the study of the helicity dependence of double pion photoproduction on the proton. The work consisted of an experimental and a theoretical part. In the experimental part, data from the recently completed GDH experiment on the proton at MAMI have been analysed. This has yielded the helicity cross section difference $\sigma_{3/2} - \sigma_{1/2}$ as a function of photon energy for the double pion production processes $\vec{\gamma}\vec{\mathrm{p}} \to \mathrm{p}\pi^+\pi^-$ and $\vec{\gamma}\vec{\mathrm{p}} \to \mathrm{n}\pi^+\pi^0$ from threshold up to 800 MeV. These observables had not been measured before. On the theoretical side, a Regge Plus Resonances (RPR) model has been developed for the description of the double pion photoproduction reactions. This model has provided a means to interpret the measured data and to predict the cross sections of the studied processes in those kinematical regions that were not accessible in the experiment.

The analysis of the GDH data was performed in two steps. The first one was a calibration analysis of unpolarised data to obtain the total cross sections for $\gamma\mathrm{p} \to \mathrm{p}\pi^+\pi^-$ and $\gamma\mathrm{p} \to \mathrm{n}\pi^+\pi^0$. This allowed the verification of the newly developed analysis methods and the understanding of the new detector setup. The analysis methods were carefully optimised to minimise statistical and systematical errors. They were also developed to be immediately portable to the analysis of the doubly polarised data from the GDH experiment. Several internal checks have been performed and, where possible, the obtained results were compared with existing data. From this it could be concluded that the developed analysis methods are reliable.

In a second step the doubly polarised data from the GDH experiment were analysed. This has resulted in the helicity cross section difference $\sigma_{3/2} - \sigma_{1/2}$ as a function of photon energy for the $\vec{\gamma}\vec{\mathrm{p}} \to \mathrm{p}\pi^+\pi^-$ and $\vec{\gamma}\vec{\mathrm{p}} \to \mathrm{n}\pi^+\pi^0$ processes. For both studied channels, $\sigma_{3/2} - \sigma_{1/2}$ is positive over the measured energy range. In case of the $\mathrm{p}\pi^+\pi^-$ process a broad peak around 600–650 MeV is observed. For the $\mathrm{n}\pi^+\pi^0$ reaction, a strong peak around 750 MeV is found for the cross section difference. By combining the measured cross section

difference with the total unpolarised cross section, also the helicity asymmetry $E = \frac{\sigma_{3/2}-\sigma_{1/2}}{\sigma_{3/2}+\sigma_{1/2}}$ and the separate helicity cross sections $\sigma_{1/2}$ and $\sigma_{3/2}$ have been obtained. Finally, the contribution of the studied channels to the GDH sum rule on the proton and its forward spin polarisability in the measured energy range have been evaluated. The measured contributions to the GDH sum rule, from threshold up to 800 MeV, are $-(25.4 \pm 1 \pm 1.5)$ μb (statistical and systematical error, respectively) from the $p\pi^+\pi^-$ process and $-(11.3 \pm 0.7 \pm 0.7)$ μb from the $n\pi^+\pi^0$ reaction. The GDH sum rule predicts a total value of -204 μb. Consequently, both channels together —in the measured energy range— contribute about 18% to the GDH sum rule. The contributions in the measured energy range to the proton forward spin polarisability amount to $-(0.070 \pm 0.004 \pm 0.004)\ 10^{-4}$ fm^4 and $-(0.025 \pm 0.003 \pm 0.002)\ 10^{-4}$ fm^4 for the $p\pi^+\pi^-$ and the $n\pi^+\pi^0$ process, respectively. Summed, these contributions are estimated to represent about 11% of the forward spin polarisability in the energy range up to 800 MeV.

The RPR model developed in order to describe double pion photoproduction processes is a Regge model to which explicit resonance mechanisms are added. The goal was to obtain a unitary and gauge invariant description over a large photon energy range, starting from threshold up to several GeV. The high energy behaviour of the model has been verified with unpolarised high energy data from the literature for the $\gamma p \rightarrow \pi^-\Delta^{++}$ reaction. In the resonance region, the RPR calculations have been compared with the unpolarised and polarised data obtained in this work for $\gamma p \rightarrow p\pi^+\pi^-$ and $\gamma p \rightarrow n\pi^+\pi^0$. Predictions for the $\gamma p \rightarrow p\pi^0\pi^0$ reaction have been compared with previously published data.

As a main conclusion for the $p\pi^+\pi^-$ channel, it was found that the non-resonant $\gamma p \rightarrow \pi\Delta \rightarrow p\pi^+\pi^-$ mechanism dominates the observed cross sections. Extra strength stems from the non-resonant $\pi\pi$N production via π exchange, the D_{13}-resonant $\pi\Delta$ and ρN production and the non-resonant ρN production via ρ exchange. These mechanisms are responsible for the observed behaviour for $\sigma_{3/2} - \sigma_{1/2}$. By means of the RPR model, the method used in the analysis to extrapolate the measured data outside of the detector acceptance was also tested. It was found that the assumption that the three particles in the final state are uniformly emitted over phase space may not be accurate.

In the case of the $n\pi^+\pi^0$ reaction, the above mentioned $\pi\Delta$ production mechanisms are not sufficient to explain the observed cross sections. It was found that mechanisms in which an intermediate ρ meson is present, play an important role. Although these account for an important part of the missing strength, some uncertainty remains. The combination of the mentioned $\pi\Delta$ and the ρN mechanisms partly explains the observed $\sigma_{3/2}-\sigma_{1/2}$ behaviour. Invariant mass distributions for the pion-pion system and for the pion-nucleon systems have also been investigated. The former are a good indication for the presence of the ρ mechanisms. Finally, also for this $n\pi^+\pi^0$ reaction, the extrapolation method used in the data analysis was checked. In this case the phase

space approximation was found to be a better one than for the $p\pi^+\pi^-$ case.

The RPR prediction was also compared to the previously published unpolarised data for the $\gamma p \to p\pi^0\pi^0$ channel. The only included mechanism that significantly contributes in this case is the D_{13}-resonant $\pi\Delta$ production. The missing strength at lower photon energies that remains here, is expected to correspond to the non-resonant diagrams obtained from the s- and u-channel nucleon diagrams for $\gamma p \to p\pi^0$ by coupling an additional π^0 to the initial and final proton. No polarised data have become available for this channel so far.

Finally, the RPR model was used to predict the contribution of the double pion channels to the GDH sum rule over the full energy range, i.e. also for photon energies above 800 MeV. In these calculations the non-resonant and D_{13}-resonant $\pi\Delta$ production is included as well as the D_{13}-resonant ρN production. A value of -55.4 μb for the contribution of all three double pion production channels to the GDH sum rule on the proton is found. This corresponds to about 25%. For the proton forward spin polarisability, a total value of $-0.103\ 10^{-4}$ fm^4 is found. This amounts to about 12% of the total.

8.2 Outlook

In first instance, this work could be continued by the further refinement of the RPR model. A more precise extrapolation of the Regge model to the resonance region and the inclusion of duality corrections are some of the possibilities. The missing mechanisms to fully explain the $\gamma p \to n\pi^+\pi^0$ process are also an important further step. Once a higher precision is obtained, the properties of the D_{13} resonance can be verified and possibly pinned down more precisely.

On the experimental side, a first next step is to use the model calculations to extrapolate the measured data outside of the detector acceptance in order to avoid the phase space approximation. Other observables, such as polarised invariant mass distributions could also be studied and can give further information for the improvement the theoretical model.

Once the GDH experiment on the neutron is performed, these data can be analysed to yield the helicity dependence of the double pion photoproduction on the neutron. The results can then again be studied in detail by means of the RPR model.

Bibliography

[1] AACHEN-BERLIN-BONN-HAMBURG-HEIDELBERG-MÜNCHEN COLLABORATION. *Phys. Rev.* **175**, 5 (1968) 1669–1696.

[2] M. AIELLO, M. FERRARIS, M. GIANNINI, M. PIZZO and E. SANTOPINTO. *Phys. Lett. B* **387** (1996) 215–221.

[3] S. ALTIERI ET AL. e-print nucl-ex/9911001 (submitted to NIM A).

[4] J. R. M. ANNAND ET AL. *Nucl. Instr. Meth. A* **368** (1996) 385.

[5] M. ANSELMINO ET AL. *Sov. J. Nucl. Phys.* **49** (1989) 1.

[6] I. ANTHONY ET AL. *Nucl. Instr. Meth. A* **301** (1991) 230.

[7] H. ARENDS ET AL. *Few Body Systems* **26** (1999) 213.

[8] P. ARGAN ET AL. *Nucl. Instr. Meth.* **228** (1984) 20.

[9] R. A. ARNDT ET AL. *Phys. Rev. C* **53** (1996) 430. (Solution SP00K).

[10] G. AUDIT ET AL. *Nucl. Instr. Meth. A* **301** (1991) 473–481.

[11] G. AUDIT ET AL. *Nucl. Phys. A* **614** (1997) 461.

[12] K. AULENBACHER ET AL. *Nucl. Instr. Meth. A* **391** (1997) 498.

[13] D. BABUSCI ET AL. *Nucl. Instr. Meth.* **305** (1991) 19.

[14] R. BECK ET AL. *Phys. Rev. Lett.* **78** (1997) 606.

[15] N. BIANCHI and E. THOMAS. *Phys. Lett. B* **450** (1999) 439–447.

[16] J. D. BJORKEN. *Phys. Rev.* **148** (1966) 1467.

[17] R. BLANCKENBECLER and M. L. GOLDBERGER. *Phys. Rev.* **126** (1962) 766–786.

[18] J. M. BLATT and V. F. WEISSKOPF. *Theoretical Nuclear Physics*. Wiley, New York (1952).

[19] A. M. BOYARSKI ET AL. *Phys. Rev. Lett.* **22** (1969) 148.

[20] C. BRADTKE, H. DUTZ ET AL. *Nucl. Instr. Meth. A* **436** (1999) 430–442.

[21] A. BRAGHIERI. *Misure esclusive di fotoreazioni su ^2H e ^2He per la verifica di nuvi gradi di libertà nucleonici*. Ph.D. thesis, Università di Pavia, Italia (1991).

[22] A. BRAGHIERI, L. MURPHY, G. AUDIT, J. LAGET, J. AHRENS, N. D'HOSE, V. ISBERT, S. KERHOAS, M. MACCORMICK, P. PEDRONI, T. PINELLI, G. TAMAS and A. ZABRODIN. *Phys. Lett. B* **363** (1995) 46–50.

[23] A. BRAGHIERI, P. PEDRONI and S. ALTIERI. *Private communciation* (2000).

[24] A. BRAGHIERI, P. PEDRONI, T. PINELLI, G. AUDIT, N. D'HOSE, V. ISBERT, S. KERHOAS, M. MC.CORMICK, L. Y. MURPHY, G. TAMAS and R. CRAWFORD. *Nucl. Instr. Meth. A* **343** (1994) 623–628.

[25] A. BRAGHIERI ET AL. *Few Body Systems* **Suppl. 8** (1995) 173.

[26] R. BRUN ET AL. *GEANT3 User's guide*. CERN DD/EE 84-1 (1987).

[27] V. BURKERT and Z. LI. *Phys. Rev. D* **47** (1993) 46.

[28] J. A. CAMPBELL, R. B. CLARK and D. HORN. *Phys. Rev. D* **2**, 1 (1970) 217–224.

[29] S. CAPSTICK and B. KEISTER. *Phys. Rev. D* **51** (1995) 3598–3612.

[30] CERN. *Program library*. http://wwwinfo.cern.ch/asd/index.html.

[31] G. F. CHEW and S. C. FRAUTSCHI. *Phys. Rev. Lett.* **7** (1961) 394–397.

[32] G. F. CHEW and S. C. FRAUTSCHI. *Phys. Rev. Lett.* **8** (1962) 41–44.

[33] G. F. CHEW, S. C. FRAUTSCHI and S. MANDELSTAM. *Phys. Rev.* **126** (1962) 1202–1208.

[34] T. COERSMEIER (1993). Diplomarbeit, Universität Bonn.

[35] P. D. B. COLLINS. *An introduction to Regge theory and high energy physics*. Cambridge University Press (1977).

[36] R. CRAWFORD ET AL. *Nucl. Phys. A* **603** (1996) 303.

[37] J. R. CUDELL, V. EZHELA, K. KANG, S. LUGOVSKY and N. TKACHENKO. *Phys. Rev. D* **61**.

[38] R. M. DAVIDSON, N. C. MUKHOPADHYAY and R. S. WITTMAN. *Phys. Rev. D* **43** (1991) 71.

[39] M. DE SANCTIS, E. SANTOPINTO and M. GIANNINI. *Eur. Phys. J. A* **2** (1998) 403–409.

[40] A. DONNACHIE and P. LANDSHOFF. *Phys. Lett. B* **296** (1992) 227.

[41] D. DRECHSEL, O. HANSTEIN, S. S. KAMALOV and L. TIATOR. *Nucl. Phys. A* **645** (1999) 145.

[42] D. DRECHSEL and G. KREIN. *Phys. Rev. D* **58** (1998) 116009.

[43] S. D. DRELL and A. C. HEARN. *Phys. Rev. Lett.* **16**, 20 (1966) 908–911.

[44] H. DUTZ ET AL. *Nucl. Instr. Meth. A* **340** (1994) 272–277.

[45] E-142, P. ANTHONY ET AL. *Phys. Rev. Lett.* **71** (1993) 959.

[46] J. ELLIS and R. L. JAFFE. *Phys. Rev. D* **9** (1974) 1444.

[47] EMC, J. ASHMAN ET AL. *Phys. Lett. B* **206** (1988) 364.

[48] H. EMMERICH. Licentiate's thesis (1995).

[49] S. N. ET AL. *Nucl. Instr. Meth. A* **424** (1998) 93–106.

[50] S. C. FRAUTSCHI, M. GELL-MANN and F. ZACHARIASEN. *Phys. Rev.* **126** (1962) 2204–2218.

[51] M. FROISSART. *Phys. Rev.* **123** (1961) 1053.

[52] H. GARCILAZO and E. M. DE GUERRA. *Nucl. Phys. A* **562** (1994) 521.

[53] GDH-COLLABORATION, J. AHRENS ET AL. *Phys. Rev. Lett.* **84** (2000) 5950–5954.

[54] GDH-COLLABORATION, J. AHRENS ET AL. Submitted to Phys. Rev. Lett.

[55] H. GENZEL, P. JOOS and W. PFEIL. *Photoproduction of Elementary Particles (Landolt-Börnstein series)*. Springer-Verlag (1973).

[56] S. B. GERASIMOV. *Yad. Fiz.* **2** (1965) 598–602.

[57] S. B. GERASIMOV. *Sov. J. Nucl. Phys.* **2** (1966) 430–433.

[58] M. GUIDAL, J.-M. LAGET and M. VANDERHAEGHEN. *Nucl. Phys. A* **627** (1997) 645–678.

[59] M. GUIDAL, J.-M. LAGET and M. VANDERHAEGHEN. *Phys. Lett. B* **400** (1997) 6–11.

[60] S. J. HALL ET AL. *Nucl. Instr. Meth. A* **368** (1996) 698.

[61] K. HANSSGEN and J. RANFT. *Comp. Phys. Comm.* **31** (1984) 411–418.

[62] K. HANSSGEN and J. RANFT. *Comp. Phys. Comm.* **39** (1986) 37–51.

[63] K. HANSSGEN and J. RANFT. *Comp. Phys. Comm.* **39** (1986) 57–70.

[64] O. HANSTEIN, D. DRECHSEL and L. TIATOR. *Nucl. Phys. A* **632** (1998) 561–606.

[65] K. HELBING. *Messung von totalen Photoabsorptionsquerschnitten mit dem GDH-Detektor*. Ph.D. thesis, Universität Bonn (1997).

[66] HERMES, K. ACKERSTAFF ET AL. *Phys. Lett. B* **444** (1998) 531.

[67] HERMES, K. ACKERSTAFF ET AL. *Phys. Lett. B* **464** (1999) 123–134.

[68] HERMES, A. AIRAPETIAN ET AL. *Phys. Lett. B* **442** (1998) 484.

[69] HERMES, A. AIRAPETIAN ET AL. *Phys. Rev. Lett* **84** (2000) 2584–2588.

[70] H. HERMINGHAUS. *Bau und Betrieb von MAMI, Arbeits- und Ergebnisbericht 1987-1989 (SFB 201)* (1989).

[71] H. HERMINGHAUS ET AL. *Nucl. Instr. Meth.* **138** (1976) 1.

[72] H. HOLVOET. In *Verhandlüngen der Deutchen Physicalischen Gesellschaft*. Physik-Verlag (1998) 438.

[73] H. HOLVOET. *Progr. Part. Nucl. Phys.* **44** (2000) 455.

[74] H. HOLVOET. In D. DRECHSEL and L. TIATOR, eds., *Proceedings of the Symposium on the Gerasimov-Drell-Hearn Sum Rule and the Nucleon Spin Structure in the Resonance Region*. World Scientific (2000) 119.

[75] A. C. IRVING and R. P. WORDEN. *Phys. Rep.* **34** (1977) 117.

[76] V. ISBERT ET AL. *Nucl. Phys. A* **578** (1994) 525.

[77] L. M. JONES. *Rev. Mod. Phys.* **52** (1980) 545.

[78] I. KARLINER. *Phys. Rev. D* **7** (1973) 2717.

[79] S. KERHOAS. *Etude de l'interaction $N\Delta$ dans la reaction $\gamma D \rightarrow pp\pi^-$*. Ph.D. thesis, DAPNIA/SPhN, CEA Saclay, France (1993).

[80] J.-M. LAGET. *Phys. Rep.* **69** (1981) 1.

[81] W. LANGGÄRTNER ET AL. Submitted to Phys. Rev. Lett.

[82] B. LANNOY. *Experimental verification of the Gerasimov-Drell-Hearn sum rule*. Ph.D. thesis, Universiteit Gent, België (2000).

[83] H. LEHMANN. *Nuovo Cimento* **10** (1958) 579.

[84] N. LEVY, W. MAJEROTTO and B. J. READ. *Nucl. Phys.* **55** (1973) 493.

[85] D. LOHMANN ET AL. *Nucl. Instr. Meth. A* **343** (1994) 494–507.

[86] F. LOW. *Phys. Rev.* **96** (1954) 1428.

[87] D. LÜKE and P. SÖDING. *Springer tracts in modern physics*, vol. 59. Springer Berlin Heidelberg (1971) 39.

[88] A. L'VOV and V. PETRUNKIN (1995). Private communication to the GDH collaboration.

[89] R. MACHLEIDT, K. HOLINDE and C. ELSTER. *Phys. Rep.* **149** (1987) 1–89.

[90] D. M. MANLEY, R. A. ARNDT, Y. GORADIA and V. L. TEPLITZ. *Phys. Rev. D* **30** (1984) 904.

[91] D. M. MANLEY and E. M. SALESKI. *Phys. Rev. D* **45**, 11 (1992) 4002–4033.

[92] A. MARTIN. *Strong interactions and high energy physics*. Oliver and Boyd (1963).

[93] A. MARTIN. *Nuovo Cimento* **42** (1966) 930.

[94] A. MARTIN. *Nuovo Cimento* **44** (1966) 1219.

[95] M. MC.CORMICK. *Mesure des sections efficaces totales de photoabsorption sur l'hydrogene, l'*^{3}*He dans la region des resonances*. Ph.D. thesis, DAPNIA/SPhN, CEA Saclay, France (1993).

[96] M. MC.CORMICK ET AL. *Phys. Rev. C* **53** (1996) 41.

[97] M. MC.CORMICK ET AL. *Phys. Rev. C* **55** (1997) 1033.

[98] L. MURPHY. *Double pion photon production on single nucleons from threshold up to 780 MeV*. Ph.D. thesis, DAPNIA/SPhN, CEA Saclay, France (1993).

[99] L. Y. MURPHY and J. M. LAGET DAPNIA-SPHN-95-42.

[100] J. NACHER, E. OSET and M. J. V. VACAS. e-print nucl-th/0012065.

[101] S. NOZAWA, B. BLANKLEIDER and T.-S.-H. LEE. *Nucl. Phys. A* **513** (1990) 459.

[102] H. OLSEN. *Springer Tracts in Mod. Phys.* **44** (1968) 83.

[103] H. OLSEN and L. C. MAXIMON. *Phys. Rev.* **114**, 3 (1959) 887–905.

[104] A. PANZERI. *Prima verifica sperimentale della regola di somma di Gerasimov, Drell, Hearn*. Ph.D. thesis, Università di Pavia, Italia (1999).

[105] PARTICLE-DATA-GROUP. *Eur. Phys. J. C* **15** (2000) 1.

[106] P. PEDRONI. *Simulation of the inelastic hadron collisions below 5 GeV: a modification of the GEANT3 package*. INFN/BE-88/3 (1988).

[107] I. PREOBRAJENSKI. Ph.D. thesis, Universität Mainz (2001). In preparation.

[108] T. REGGE. *Nuovo Cimento* **14** (1959) 951.

[109] T. REGGE. *Nuovo Cimento* **18** (1960) 947.

[110] A. SANDORFI ET AL. *Phys. Rev. D* **50** (1994) 11.

[111] M. SAUER, A. FUCHS, P. GRABMAYR and J. LEYPOLDT. *Nucl. Instr. Meth. A* **378** (1996) 143.

[112] L. I. SCHIFF. *Phys. Rev.* **83**, 2 (1951) 252.

[113] SMC, D. ADAMS ET AL. *Phys. Rev. D* **56** (1997) 5330.

[114] J. K. STORROW. *Electromagnetic Interactions of Hadrons, High energy photoproduction: nondiffractive processes*. Plenum Press (1978).

[115] J. K. STORROW. *Exchange mechanisms of hadronic reactions*. IOP Publishing Ltd. (1987) 1229–1310.

[116] J. A. TEJEDOR and E. OSET. *Nucl. Phys. A* **571** (1994) 667.

[117] M. VANDERHAEGHEN, K. HEYDE, J. RYCKEBUSCH and M. WAROQUIER. *Nucl. Phys. A* **595** (1995) 219.

[118] B. WAGNER ET AL. *Nucl. Instr. Meth. A* **294** (1990) 541–548.

[119] M. WOLF ET AL. *Eur. Phys. J. A* **9** (2000) 5.

[120] R. WORKMAN and R. ARNDT. *Phys. Rev. D* **45** (1992) 1789.

[121] A. ZABRODIN ET AL. *Phys. Rev. C* **55** (1997) R1617.

[122] F. ZAPADTKA. Ph.D. thesis, Universität Göttingen (2001). In preparation.

Studie van de heliciteitsafhankelijkheid van dubbelvoudige pion-fotoproductie aan het proton

Nederlandse samenvatting